Exploring and Classifying the Transient Radio Sky

Małgorzata Piętka

Department of Physics

University of Oxford

This dissertation is submitted for the degree of

Doctor of Philosophy

Brasenose College

August 2016

For M&M

Declaration

I certify that the work in this thesis is wholly my own, except where explicitly stated.

Parts of this work have been published as

Pietka M., Fender R. P., Keane E. F., 2015, MNRAS, 446, 3687

Parts of this work will soon be published as

Pietka M., Fender R.P., Staley T.D., Pretorius M.; submitted to MNRAS

Małgorzata Piętka

August 2016

Acknowledgements

First I would like to thank my supervisor Rob Fender for pulling me out of the monotonous corporation life and giving me the opportunity to work in the unpredictable world of radio transients. Thanks for patiently explaining all kinds of questions I've had over the years and all the help writing this thesis.

I would also like to thank the entire 4 Pi Sky group for creating the best possible working place; Rene for mocking me mercilessly until I finally learned python; Dan and Teo for endless jokes; Aidan my favourite officemate; and Jess, Gemma, Tim, Retha, Tony, Mari and Tom, for helping me with all my questions about LOFAR, astronomy in general, and most importantly being there to not talk about LOFAR or astronomy in general. Thanks to Alex for all the great climbs, which helped me to completely forget about work problems on account of being scared for my life. Finally, thanks to Adam for being the best friend I could ever have and making the past four years so much fun – with you I could do this PhD again!

The biggest thanks goes to my sister Magda, for always being there for me, extremely patient and understanding of my constant questions and complaints over the years and putting things into the right perspective. Thanks to Mark – I don't really know what to say, but I like you. And of course a big thanks to little Lilek for arriving in this world just in time to draw the family's attention away from me during the last few months of writing up!

Dziękuję moim rodzicom za wsparcie w ciągu długich lat nauki i pracy, pomoc w realizacji wszystkich moich planów i zachętę do rozwijania zainteresowań. Przede wszystkim jednak za to, że są najlepszymi rodzicami na świecie przy których nigdy nie jest nudno! Moim dwóm ulubionym ciociom, Bogusi i Zosi, dziękuję za wszystko co dla mnie zrobiły od dzieciństwa, aż do ostatnich lat podczas których pilnie śledziły moje naukowe zmagania. Wreszcie, ogromne podziękowania dla Danuty Mazur, która w moich szkolnych latach oprócz matematyki wpoiła mi porządek i organizację pracy, bez których nigdy nie udałoby mi się osiągnąć tak wiele.

Abstract

Observations of the transient radio sky provide an insight into the most dynamic and energetic events in the Universe. The exploration of transient and variable sources, for a long time primarily focused on higher frequencies, has recently been extended to the long wavelength regime, with the development of facilities such as the Low Frequency Array (LOFAR).

In this work I describe the general design of LOFAR as well as details of the commissioning work performed during the early stages of operation. Secondly, I perform an analysis of the first dedicated LOFAR transient survey – the Radio Sky Monitor. The investigation is focused on exploring 30 seconds time-scale images and allows us to place an upper limit on the expected areal densities of fast radio transients in the low frequency sky. It also provides spectral index constraints on the previously found, first LOFAR transient event.

I also investigate the relation between the radio luminosities and variability time-scales across a wide range of sources – from nearby flare stars to distant supermassive black holes. The results are discussed in context of the potential use as a classification method, as well as in comparison with the expected brightness temperature of the events. The relation is used as a base for building a tool which classifies (with a given probability) an observed event, depending on the measured rise/decline rates of the flare. It includes the automatic selection of flares and takes into account the estimated areal densities of different classes of objects.

Lastly, I discuss the results of the luminosity – time-scale correlation in context of the estimation of the kinetic power, as well as future prospects of implementing the presented classification method into an automated transient detection pipeline for instruments such as MeerKAT and the Square Kilometer Array.

Table of contents

List of figures

List of tables

Chapter 1

Introduction

1.1 Radio Astronomy Background

The field of observational radio astronomy was initiated over 80 years ago, when an engineer Karl Jansky accidentally detected radio emission from the Milky Way, while working on eliminating sources of radio communication interference. The realisation that astronomical objects emit radio waves launched the development of facilities designed to observe the radio sky.

Because the angular resolution Θ of the observation is directly related to the diameter of the telescope D as well as the observed wavelength λ ($\Theta \propto \lambda/D$), and, the radio band makes up a significant fraction of the electromagnetic spectrum, separate antenna designs are necessary in order to explore the full range of radio wavelengths. While at higher, gigahertz frequencies a relatively good resolution can be obtained with a traditional single dish telescope, the diameter of the required instrument quickly becomes unreasonably large when observing radiation at metre wavelengths. The largest single dish radio telescope – Arecibo – has a diameter of just over 300 metres, while the Green Bank Telescope (GBT) – the largest steerable telescope – is 100 metres in diameter. Other single aperture telescopes include Parkes, Jodrell Bank and Effelsberg. All these instruments have provided a wealth of data and information about the radio sky over the years, however, even at higher frequencies the technical limitations of the size of dish that can be built are quickly reached by both the costs of construction as well as design constraints.

These problems can be solved by introducing the interferometry technique. It allows us to replace a single dish telescope with a number of smaller and easier to produce antennas, which, combined into a network, act as one instrument with the effective diameter equal to the size of the array. Thanks to the aperture synthesis method (described in Ryle and Hewish 1960 and further discussed in Section 1.2) the resulting angular resolution of the telescope can be greatly improved, with the main cost shifted from the expensive constructions into the transport and processing of vast amounts of data. Therefore, the development of interferometric arrays relies heavily upon the progress of technology. Examples of such interferometers operating in the high frequency regime include: the Karl G. Jansky Very Large Array (JVLA; Perley et al., 2011), the Arcminute Microkelvin Imager (AMI; Zwart et al., 2008), the Westerbork Synthesis Radio Telescope (WSRT; Baars and Hooghoudt, 1974) and the Australia Telescope Compact Array (ATCA; Frater et al., 1992).

While the higher frequency regime has been explored in detail over the past decades, much of the effort in recent years has been focused on the development of instruments observing at metre wavelengths. This includes the Low Frequency Array (LOFAR; van Haarlem et al., 2013) – the northern hemisphere interferometer built across the European countries (discussed more extensively in Section 2.1) and the Murchison Widefield Array (MWA; Tingay et al., 2013), located in the western part of Australia. Both of these instruments use dipole antenna arrays and cover the low frequency range of the radio band, (30–240 MHz, LOFAR; 80–300 MHz, MWA), and, together with telescopes such as MeerKAT (currently under construction; Booth et al., 2009) and Australian Square Kilometre Array Pathfinder (ASKAP; Johnston et al., 2007) contribute to both technical developement as well as provide scientific input to the Square Kilometre Array (SKA; Dewdney et al., 2009) – the largest and most advanced radio telescope, located jointly in South Africa and Australia, expected to be operational in the early 2020s.

Radio observations of astronomical objects provide great opportunities to study various areas of astrophysics, such as the evolution of galaxies, examining the behaviour of galactic and extragalactic objects or exploring the cosmic microwave background (CMB; Penzias and Wilson, 1965). Studies of radio emission allow us to probe the interstellar and intergalactic medium, measure the kinetic energy output associated with explosions, and, thanks to the high angular resolution of radio telescopes, offer a good localization of the events. In the area of transient and variable radio sources, which is the main focus of the work presented in this thesis, most of the observations performed to date come from the follow up monitoring of events discovered at other wavelengths. This is mainly due to the narrow field of view of most radio telescopes, which does not favour serendipitous detections of these (relatively rare) types of objects. However, with their wide fields of view and potentially high sensitivities, facilities such as LOFAR, MWA or SKA open up great possibilities of discoveries of new objects in blind radio surveys. Part of the work presented in this thesis concentrates on searching for transient and variable sources in LOFAR observations. The events of interest originate from a wide range of objects, from Galactic stars (Osten and Bastian, 2006) and binary systems (Audard et al. 2005, Fender 2006), through supernovae (SN; Kulkarni et al. 1998, Weiler et al. 2002), up to the most distant and luminous events such as gamma-ray bursts (GRBs; Frail et al. 1997, Chandra and Frail 2012) and bright flares from supermassive black holes in the centers of distant galaxies (Ryle et al. 1978; Volvach et al. 2010). They also include a recently discovered class of fast radio bursts (FRBs; Lorimer et al., 2007) – bright flares of unknown origin – which could potentially point to some of the exotic, so far only theoretical events such as, for example, evaporating black holes (Rees, 1977). Figure 1.1 shows a number of radio flares observed from a range of synchrotron emitting sources which occur on time-scales from minutes to years, and, will be further discussed in Chapter 4.

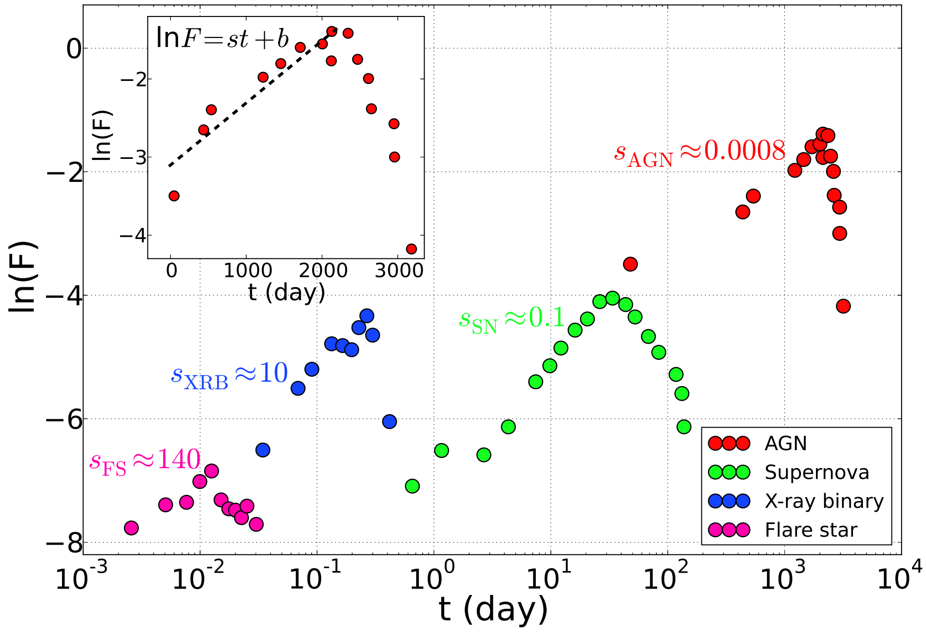

Fig. 1.1 Examples of incoherent synchrotron flares originating from a range of classes of objects, illustrating different time-scales of the events which can range from minutes to years. The exponential rise time τ of the event is related to the fitted parameter s as $\tau = s^{-1}$. From Pietka et al. (2015) – see Chapter 4 for more details.

As the expected rates of newly discovered radio sources increase, our ability to select them from the vast datasets and swiftly classify is greatly challenged. The first problem, although simple in its concept, requires innovative techniques which allow us to store, search and analyse huge amounts of data in shortest time possible. There are number of pipelines developed specifically for radio data searches, e.g. the Transient Detection Pipeline (TRAP; Swinbank et al., 2015), discussed in more detail in Section 3.6.1. The problem of rapid classification, although not immediately crucial to transient surveys, gains importance as the scheduling of follow up observations is required. If the number of detected candidates exceeds the amount which is likely to be analysed and classified by humans on the available time-scale, an automatic tool might be necessary. This issue has been undertaken at other wavelengths (see Section 1.6), but the early classification of radio-selected detections remains relatively unexplored. Therefore, the second part of the work presented in this thesis is dedicated to taking a broad look at the properties of known radio flares and using them as the basis of an early method of classification.

1.2 Radio Interferometry and Aperture Synthesis

In a simple case of a two element interferometer (Figure 1.2) a pair of antennas A and B (which form the so called baseline) located on an east – west (E–W) line monitors the sky in direction ϕ. Due to the separation D between the antennas, the signal received at location A travels an extra path length compared to B. This difference is compensated by adding the geometric delay of $\tau_{\mathrm{g}} = D\ \sin\phi/c$ to the signal received at antenna B, following which the two signals are correlated. The output of this correlation – the complex visibility V – is the component of the Fourier transform of the sky brightness distribution at a particular spatial frequency and orientation determined by the baseline. Therefore, the visibility is described in terms of the orientation of the baseline as seen from the source. As shown in Figure 1.2, the projected length of the baseline u is different to the physical distance D between the antennas. In order to express the orientation of the baseline as seen from the source, a separate u, v, w coordinate system is introduced, where u, v define the projected eastern and northern directions respectively and w is directed towards the observed object. The measurement of the visibility $V(u,v)$ for a pair of discussed antennas provides a single point in the uv space. Because the antennas in the discussed example are located on an east-west line, the projected length and orientation of their baseline (and so the values of u and v) will gradually change with the rotation of Earth. Correlating the signal from the antennas at different stages of the rotation will provide additional visibility measurements and slowly fill in the uv plane, eventually synthesising the aperture of the diameter equal to the size of the array.

The inverse Fourier transform of the visibility measurements gives the sky brightness distribution convolved with the response of the array to the point source. The true brightness distribution can be recovered by the deconvolution process – a description of the possible

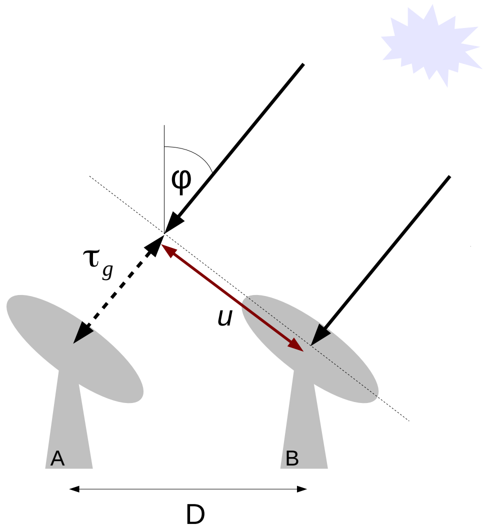

Fig. 1.2 Illustration of the two component East – West interferometer, where the two antennas separated by distance D form a baseline. The signal from the source observed in the direction ϕ arrives at a different time at each of the antennas – this difference can be corrected by adding the time delay of $\tau_{\rm g} = D \sin\phi / c$. The correlated signal from both antennas, expressed as a function of the projected baseline length (u) gives a component of the Fourier transform of the sky brightness distribution.

methods can be found in Högbom (1974) and Clark (1980). Completeness of the *uv* plane sampling is directly related to the quality of the final map – the better *uv* coverage, the closer our result is to the true sky brightness distribution. By extending the array from 2 to N antennas we can create $N(N-1)/2$ baselines and increase the number of visibility measurements.

Figure 1.3 shows the comparison of array design, snapshot *uv* coverage and the full synthesis (12 hours) sampling for the Westerbork Synthesis Radio Telescope (WSRT) and the Very Large Array (VLA). In the case of the WSRT, which is an E–W interferometer, the difference between an instantaneous *uv* coverage and the full synthesis (12 hour long observation) shows that the performance of an array with all the antennas lined up strongly depends on the rotation of the earth. For the VLA the *uv* sampling is improved over time, however, the snapshot coverage is still relatively complete. The angular resolution of the

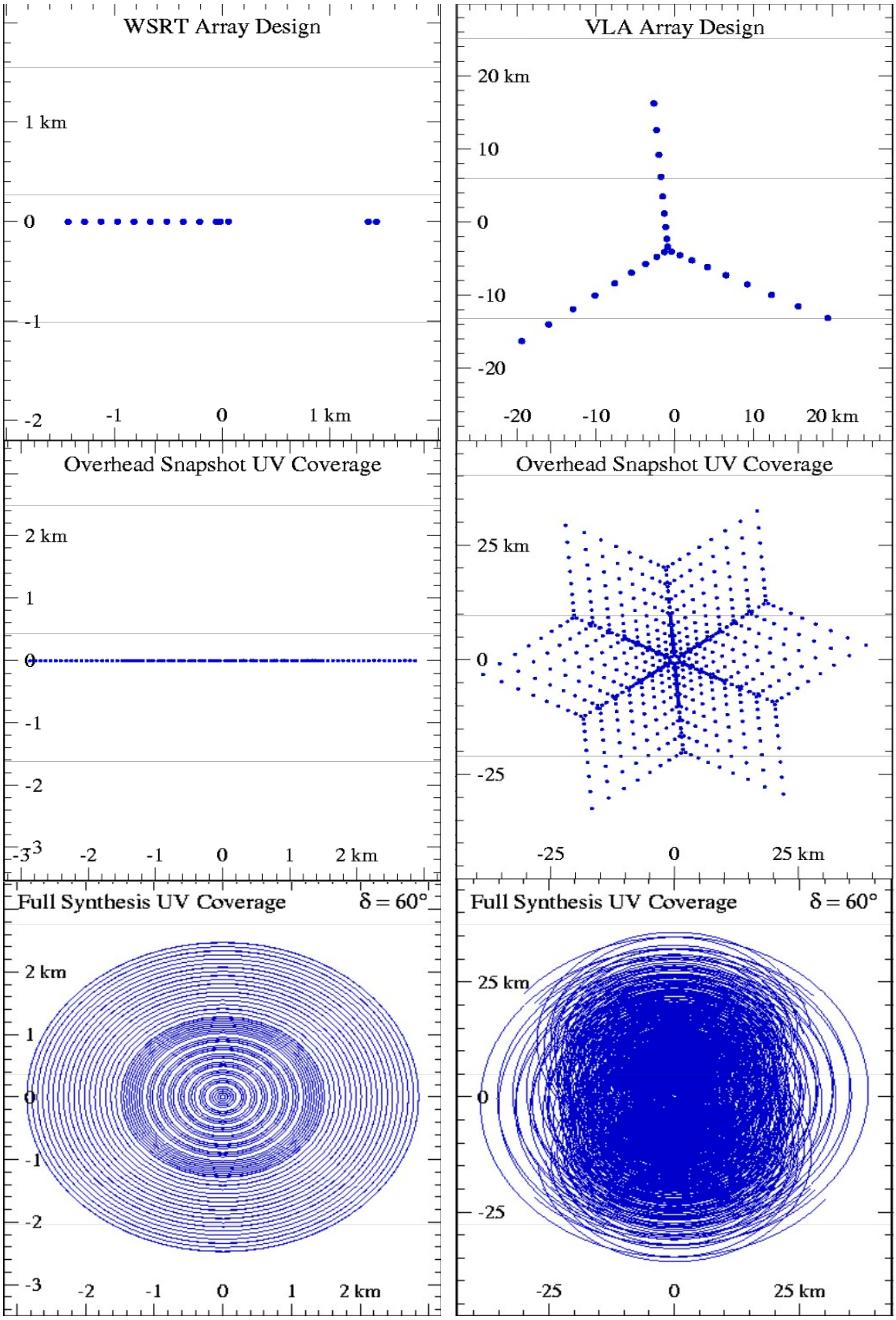

Fig. 1.3 Comparison of the design and *uv* coverage for the WSRT E–W array (left) and VLA (right). Top panels show the antenna distribution for both telescopes. Middle panels show their instantaneous *uv* coverage – while the VLA sampling provides good snapshot coverage, the corresponding *uv* sampling for WSRT is quite poor. The full synthesis coverage shown in the bottom panel improves the sampling for both arrays, although it is much more crucial for the WSRT which depends strongly on Earth's rotation. (Figure credit: `http://192.96.5.2/synthesis_school/Miod_Array_Design.pdf`)

interferometer is defined by the diameter of the array, and, consequently, including the longest baselines in the observations makes the instrument most sensitive to point sources, while short baselines are used to map large scale structures.

1.3 Types of Radio Emission

This section gives an overview of different types of radio emission mechanisms. From this point, the frequency dependence of the flux density F_ν at the frequency ν is defined as $F_\nu \propto \nu^\alpha$, where α is the spectral index.

1.3.1 Synchrotron

Emission Mechanism

Synchrotron emission arises from relativistic charged particles, usually electrons, accelerated in magnetic fields. It is a type of non-thermal radiation, i.e. the distribution of emitting particles is non-Maxwellian. When propagating in a magnetic field, electrons experience a Lorentz force which causes their acceleration around the magnetic field lines. As a result, electrons emit photons with energy proportional to the velocity of the emitting particle. Due to the relativistic velocities, the radiation is strongly beamed – i.e. emitted in a narrow cone in the direction of motion. A population of N electrons in a synchrotron emitting cloud is described by the power law distribution of energies, E, of individual electrons $N(E)dE = N_0E^{-p}dE$ (Figure 1.4), where p is the energy distribution index. Closely related to synchrotron are cyclotron and gyro-synchrotron emission mechanisms, both of which also originate from acceleration of charged particles in magnetic fields, however, the velocities of their emitting electrons are non-relativistic and mildly relativistic respectively.

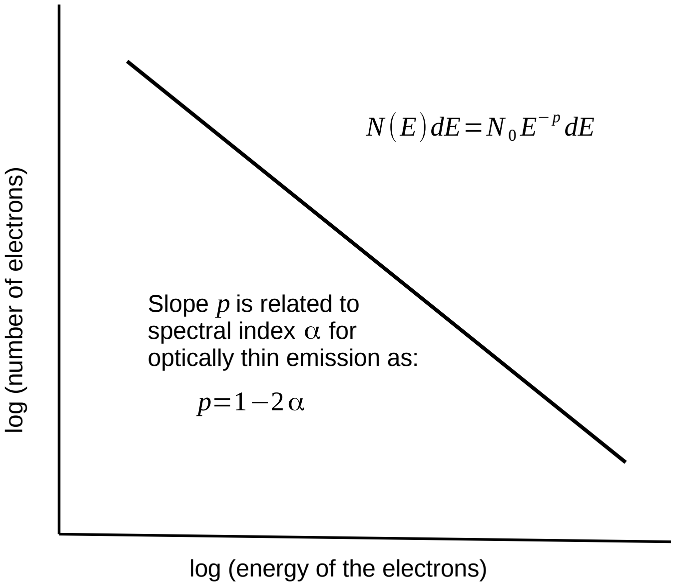

Fig. 1.4 Power law energy distribution of the synchrotron emitting electrons. Smaller number of high energy electrons is responsible for higher frequency emission, while the lower frequency radiation originates from the larger number of lower energy electrons.

Spectrum

A single relativistic electron accelerated in a magnetic field radiates at a range of frequencies, with the peak at the so called 'critical frequency', ν_0. The observed spectrum of the synchrotron emitting source is formed by summing the contributions from its individual electrons, which is schematically shown in the left panel of Figure 1.5. For the optically thin regime of synchrotron emission, the resulting dependence of the flux density F on the frequency is $F_\nu \propto \nu^\alpha$, where α is the spectral index, usually between $-2 \leqslant \alpha \leqslant 0$. Furthermore, the spectral index is related to the power law index of the energy distribution p as $p = 1 - 2\alpha$. This relation allows us to estimate the energy distribution of the electrons in the observed synchrotron emitting sources by measuring their spectral evolution.

As the observing frequency decreases, the brightness temperature T_B of the source is approaching – although can never exceed – the temperature of its particles T_e. Therefore, at a given frequency the spectrum reaches its peak before being inverted. This effect is known

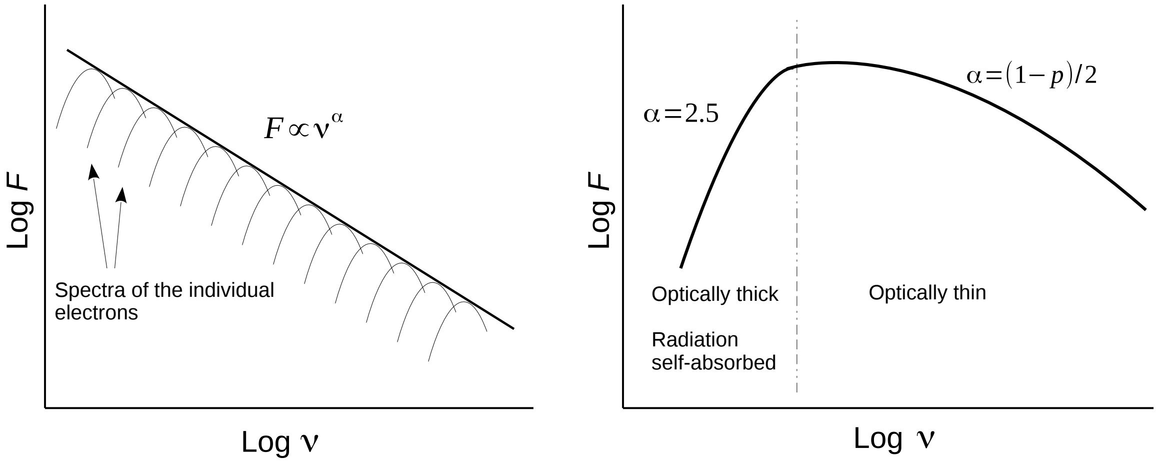

Fig. 1.5 *Left*: Illustration of the spectral distribution of the optically thin, synchrotron emitting source, where the overall profile originates from the superposition of the spectral distributions of the individual electrons. *Right*: The spectrum of a partially self-absorbed synchrotron source. For the low frequency, optically thick part of the spectrum, where the emission is self-absorbed the flux density F changes with the frequency as $F \propto \nu^{2.5}$. At the turnover frequency the plasma becomes transparent to the radiation and the spectral index depends on the energy distribution of the electrons as $F \propto \nu^{(1-p)/2}$.

as synchrotron self-absorption, where the spectral index is independent from the energy distribution p and flux density changes as $F \propto \nu^{2.5}$. It corresponds to the optically thick part of the spectrum, which describes a source that became opaque to the radiation and the only emission observed comes from its surface. The right panel in Figure 1.5 shows a schematic spectrum of a synchrotron emitting source.

A more detailed description of the physical processes and models of synchrotron emission from compact radio sources will be given in Section 4.1.

Minimum Kinetic Energy

Radio observations of synchrotron emission can also provide a general estimation of the kinetic energy associated with the event – i.e. the lower limit of the energy required to produce the detected radiation. Simplistically, the observed radio luminosity of the synchrotron emitting region contained in a given volume of space can be produced in two ways: either by the emission from low energy electrons accelerated in strong magnetic field, or, with high energy electrons radiating in a weak magnetic field. Figure 1.6 shows the energy in magnetic field $E_{\rm B} \propto B^2$ as well as the energy in the particles $E_{\rm e} \propto B^{-3/2}$ as a function of the magnetic field strength B, plotted in green and blue respectively, for a synchrotron-emitting source of a given size and luminosity. The black curve corresponds to the total energy of the system, which is defined as $E_{\rm tot} = E_{\rm B} + E_{\rm e}$ (as this is a minimum energy estimate we ignore the contribution from protons and any non-relativistic particles). Although it is not possible to find the precise ratio between the two components (and therefore the exact energy output) based on the measured luminosity, we can place the lower limit on the energy associated with the event by differentiating $E_{\rm tot}$ with respect to the magnetic field B. As shown in Figure 1.6 the minimum of the $E_{\rm tot}$ corresponds to the state where $E_{\rm B} \approx E_{\rm e}$, and the value of B for which it occurs is known as the equipartition magnetic field. This estimation of the minimum energy is useful in measuring the kinetic energy and power ejected in the observed event

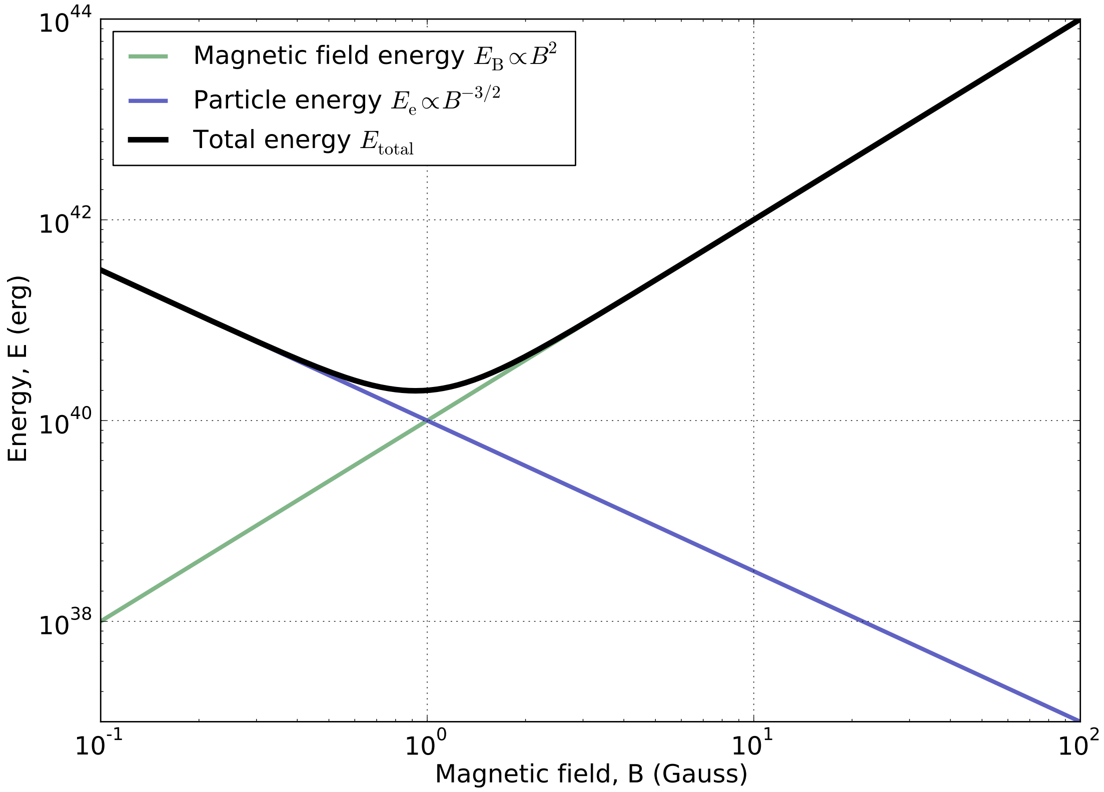

Fig. 1.6 Plotted here is the energy of a synchrotron emitting plasma as a function of the magnetic field strength. The overall energy (shown in black) is the sum of the energies of the magnetic field (green) and that in the particles (blue). The minimum energy required for the synchrotron emission corresponds to the state where the contribution from both of these components is approximately equal.

such as relativistic jets or expanding synchrotron shells from isotropic explosions. Details of this analysis can be found in Burbidge (1959).

1.3.2 Black Body

Black body radiation originates from vibrations of charged particles in an object which is in thermal equilibrium with its environment. It is a type of thermal emission, which means that the temperature of an object, T provides enough information to describe both the intensity of the observed radiation and the shape of the spectral distribution of the emitting source. The amount of radiated energy increases with the temperature of the source as $P \propto T^4$ (Stefan-Boltzmann law), and, as the temperature gets higher, the frequency at which the maximum energy is emitted increases ($\nu_{\max} \propto T$, Wien's law). At low frequencies, the spectrum of the black body is described by the Rayleigh-Jeans law and follows $F \propto \nu^2$, which is slightly less steep compared to that of synchrotron self-absorbed emission ($\alpha = 2.5$). As the frequency increases the spectrum peaks and cuts off as $F_\nu \propto e^{-\mathrm{h}\nu/\mathrm{kT}}$ at the short wavelength regime.

Examples of radiation via black body emission include planets, stars, accretion discs and the cosmic microwave background. The spectrum of the latter is the closest to that of an ideal black body found in nature.

1.3.3 Bremsstrahlung

Bremsstrahlung radiation is another thermal emission mechanism in which free (unbound to an atom) electrons emit photons once accelerated by a collision with more massive, ionised particles of the plasma. After the collision the electrons stay unbound, which is why this type of emission is often referred to as free-free radiation. The spectrum of the free-free emission at lower frequencies, where the source is optically thick, follows that of black body radiation with a spectral index of $\alpha = 2$ and becomes flat ($\alpha \approx 0$) at higher frequencies. At radio wavelengths bremsstrahlung emission can be detected from regions of hot ionised plasma.

An overview of different spectral shapes corresponding to the discussed emission mechanisms is shown in Figure 1.7.

1.3.4 Coherent Emission

Coherent emission is another type of non-thermal radiation processes. In general, the difference between incoherent (such as thermal or synchrotron) and coherent radiation lies in the properties of the emitted photons. Coherent emission originates from photons which are

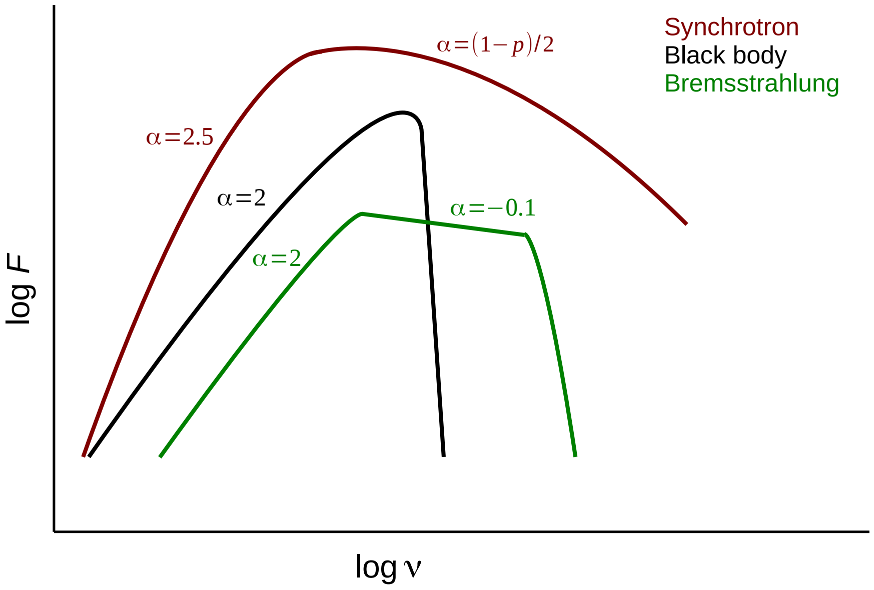

Fig. 1.7 The comparison between the spectral shapes for all of the discussed emission mechanisms.

emitted with the same frequency, phase and direction, as opposed to, for example, synchrotron radiation where the photons are out of phase and cover a range of frequencies.

An example source of coherent emission is an astrophysical maser (Microwave Amplification by Stimulated Emission of Radiation). It arises in regions where – triggered by an external energy source – more atoms are found in the excited states compared to low energy level molecules. The emission of photons from the excited molecules is not spontaneous – the process is initiated by an ’incident photon’, which stimulates emission of another photon at the same frequency and phase. Both photons propagate together, in phase and the process is repeated, increasing the number of photons emitted in phase with every photon-molecule interaction, leading to chain reaction and emission of a coherent signal. The effect of maser is observed in star forming regions. The pulsar emission mechanism is another prominent example of a coherent astrophysical mechanism, although in this case the detailed physics is not well understood.

1.4 Propagation Effects

Before reaching the telescopes, the radio signal emitted by a source travels through the inhomogeneous interstellar medium (ISM) consisting of various types of matter (e.g. ionised or magnetised plasma) distributed between the stars. The interaction with the ISM can cause a distortion of the original signal and affect its detection. This section describes the main types of propagation effects associated with the ISM.

1.4.1 Dispersion

The effect of dispersion is caused by the shift of arrival time of the different frequency components of the signal, resulting in significant reduction of the total amplitude detected.

Because the velocity of signal propagation depends on the refractive index of the ISM, which in turn is the function of frequency, the lower frequency components of the signal will arrive later than those emitted at higher frequencies. This delay is described as a function of the dispersion measure (DM), which is the column density of free electrons along the line of sight, and the frequency of the signal

$$\Delta t_{\mathrm{DM}} = \frac{\mathrm{DM}}{2.41 \times 10^{-4} \nu^2}. \tag{1.1}$$

The upper panel in Figure 1.8 shows an example time of arrival of the different frequency components of a dispersed signal (Lorimer et al., 2007). This effect is especially significant in the case of short duration signals, where the delay from the DM for individual frequency channels is larger than the duration of the signal, and the amplitude obtained by directly summing the frequency channels is reduced to the level of the noise. The lower panel in Figure 1.8 shows the effect of dispersion on a simulated short duration signal for a range of increasing DMs.

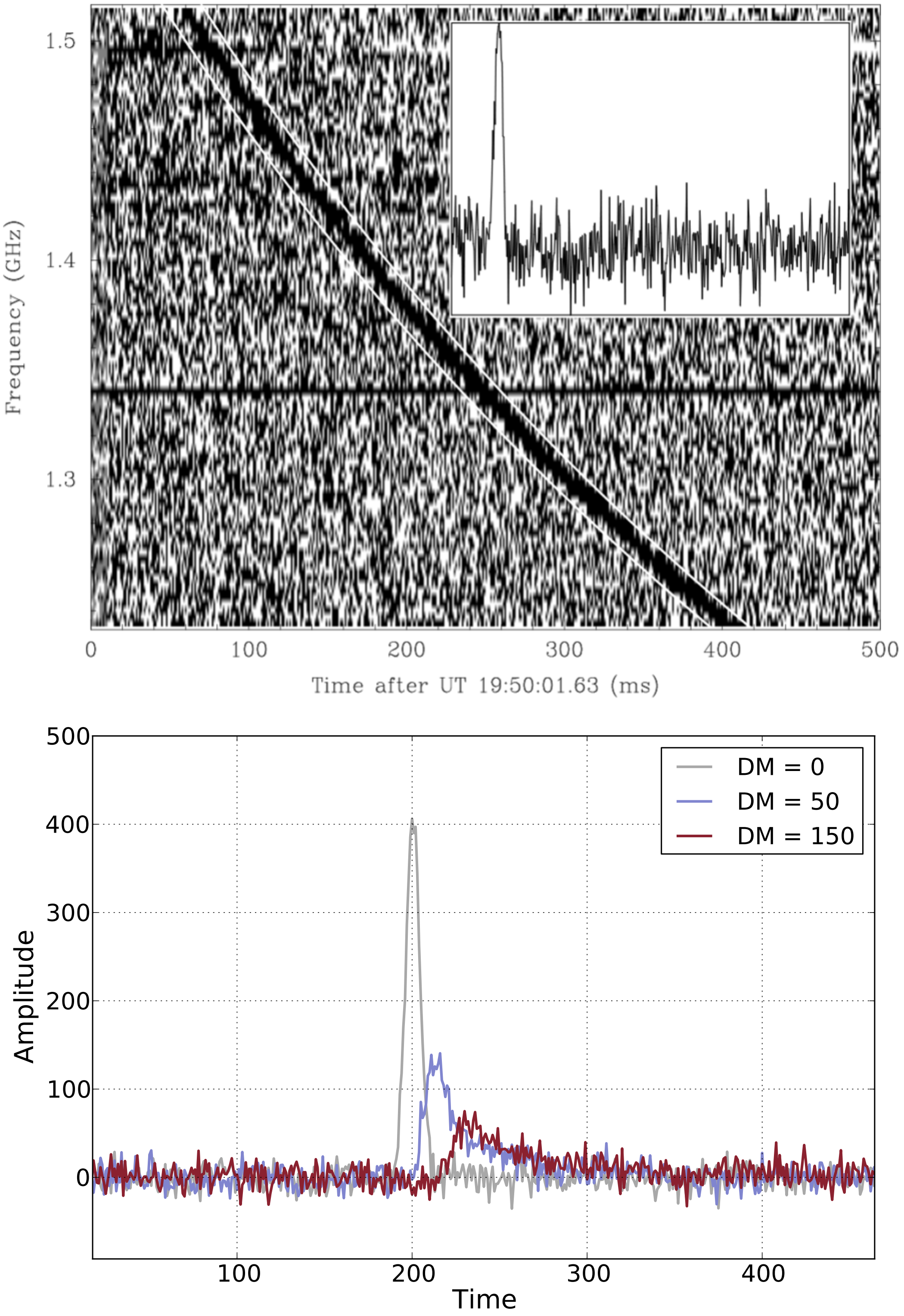

Fig. 1.8 *Upper*: The shift in arrival time of the different frequency components of a short duration radio flare, caused by the dispersive delay of the ISM. The inset plot shows the profile of the recovered original pulse. Figure from Lorimer et al. (2007) corresponds to the first ever detected fast radio burst. *Lower*: Illustration of the effect of the DM on the detection of a short duration signal in time series data. In grey is the simulated short duration burst as it would appear without experiencing any dispersion prior to the detection. In blue and red is the same signal affected by the dispersion of 50 and 150 respectively, where the resulting amplitude is significantly reduced and the chances of the detection decreased if the signal is not de-dispersed.

The recovery of the original signal is performed using the dedispersion technique, in which the time series of the individual frequency channels are shifted relative to each other by Δt_{DM} (Equation 1.1) before being combined. This process is repeated for a large sample of DMs, one of which gives the strongest signal to noise ratio and the corresponding amount of dispersion measure associated with the detection. The process of dedispersion also helps to identify signals originating from terrestrial interference, which are expected to have DM=0.

1.4.2 Scattering

Scattering is caused by changes in the electron densities in an ionised plasma. As the signal travels through a thin scattering screen located between the source and the observer, the paths of different rays are diverted with different angles. This causes the delay in their time of arrival at the observer. Scattering can change intrinsically short and bright burst into fainter and longer signal with characteristic exponential decay. The detected amplitude $F(t)$ of the pulse changes as

$$F(t) \propto \exp\left(-\frac{t}{\tau_{\mathrm{s}}}\right), \tag{1.2}$$

where τ_{s} is the scattering time, and the original width of the pulse τ_0 is increased to $\sqrt{\tau_0^2 + \tau_{\mathrm{s}}^2}$. Figure 1.9 illustrates the shape and intensity of the original signal compared to that affected by interstellar scattering. The scattering time is strongly dependent on the observing frequency ν

$$\tau_{\mathrm{s}} \propto \nu^{-4}, \tag{1.3}$$

which means that the broadening of the signal due to scattering is much larger at lower frequencies, where at the same time, the observed amplitude of the burst is also more significantly decreased.

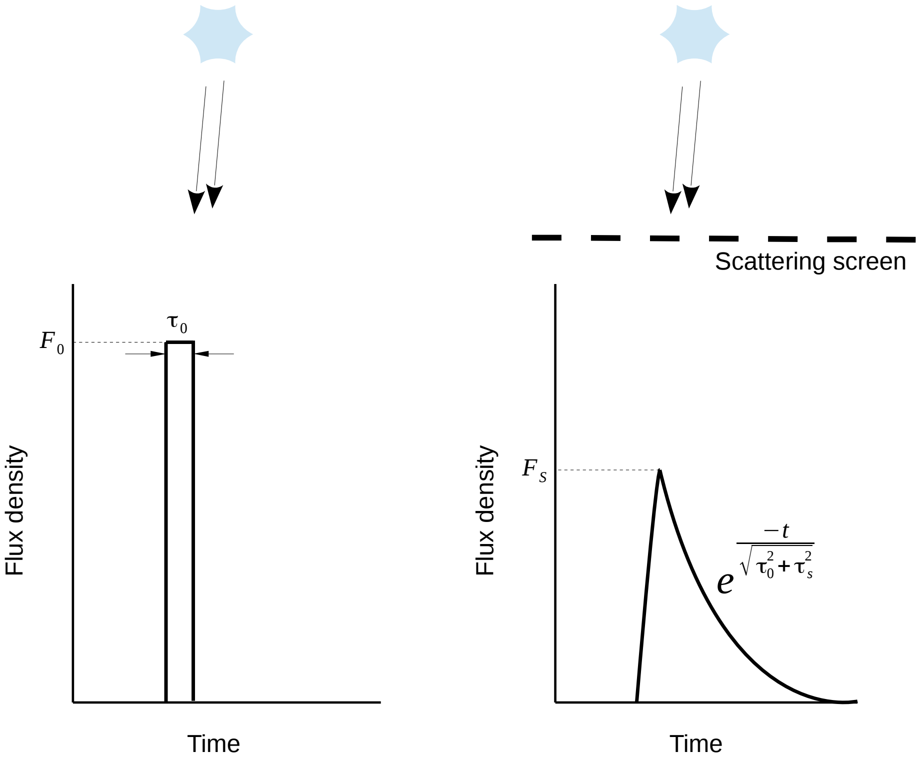

Fig. 1.9 *Left*: A short duration burst with an intrinsic time width of τ_0 and a flux density F_0 observed directly from the source. *Right*: The same signal as observed when propagating through the scattering screen. The scattering increases duration of the signal to $\sqrt{\tau_0^2+\tau_s^2}$ where τ_s is the frequency dependent scattering time. As a result the intrinsically sharp pulse gains a slowly decaying exponential tail and the final amplitude is reduced. Based on Figure 1 in Hassall et al. (2013)

1.4.3 Scintillation

Interstellar scintillation (ISS) is the variation in the intensity of the observed signal caused by the propagation through the turbulent, inhomogeneous ISM. Scintillation can be divided into two types. Diffractive scintillation is caused by an interference between different parts of the signal, which, scattered on a thin screen between the source and the observer, travel through different paths. It affects only extremely compact sources such as pulsars. Refractive scintillation is associated with large scale inhomogenities in the scattering screen which can cause variations in the intensity observed from compact extragalactic sources like quasars (Rickett, 2002).

1.5 The Radio Transient Sky

The radio sky can show dynamic changes in the brightness of observed sources, which arise from a wide range of astrophysical phenomena including both intrinsic processes as well as propagation effects. In this section I will briefly discuss the different types of events which display radio variability.

1.5.1 Intrinsic Variability

If originating from intrinsic processes, the observed variability in radio brightness points to objects displaying the most extreme physical phenomena. The sample population of known transient and variable radio sources is shown in Figure 1.10, where the radio luminosity of the observed flares is plotted against their time-scale. It can be divided into two main groups of incoherent and coherent events (marked with blue and white regions respectively) – based on the type of radio emission they originate from (Section 1.3). Flares originating from synchrotron emission show variability on time-scales longer than ~ 1 second and are separated from coherent events by the constant brightness temperature line of 10^{12} K, which

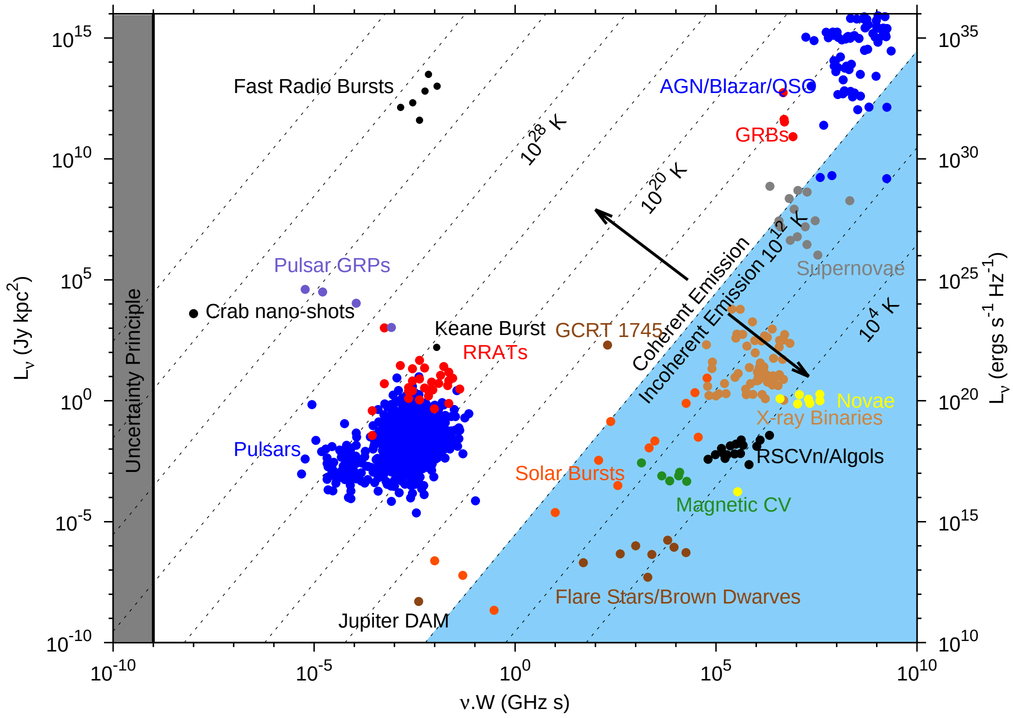

Fig. 1.10 The phase space of the known transient and variable radio sources for a wide range of astrophysical events, where the radio luminosity is plotted against the product of the observing frequency ν and the time-scale of the flare/pulse width W. These events originate from two different emission mechanisms: coherent (short duration) and incoherent (long duration), and, are separated by the constant brightness temperature line corresponding to the value of 10^{12} K – the theoretical upper limit for the brightness temperature of the incoherent emission. Figure from Pietka et al. (2015).

represents the upper limit of the brightness temperature for the synchrotron emitting matter (Kellermann and Pauliny-Toth, 1969). On the other hand, the duration of coherent flares (white part of Figure 1.10) can be as short as nano seconds, with the brightness temperatures reaching 10^{40} K. The origin of Figure 1.10 will be presented in Chapter 4.

Incoherent Events

Incoherent emission gives rise to so called 'slow' variability and can cause changes in radio brightness for a wide range of sources, on time-scales from seconds to longer than years. For active galactic nuclei (AGN) the optically thin synchrotron emission is observed from long jets extending from the central supermassive black hole into a surrounding medium, as well as large radio bright lobes at their ends. On the smaller scale, similar behaviour is observed in X-ray binaries – stellar mass black holes or neutron stars which accrete matter from their companion stars and produce relativistic outflows of matter (Fender, 2006). Relativistic jets are also formed in tidal disruption events (TDE; Zauderer et al., 2011) systems, where a star passing nearby a massive black hole is being disrupted by tidal forces. Another class of objects displaying highly collimated jets are gamma-ray bursts (GRBs), however, most of the radio detections of GRBs to date come from the radio afterglow of the 'off-axis' bursts rather than main explosive event (e.g. van der Horst et al., 2008). In those cases the observed emission is associated with the spherically expanding shell. The isotropic emission from an expanding cloud is also observed from supernovae (SN), where an explosion of a massive star accelerates electrons through the circumstellar medium giving rise to incoherent radio emission (Weiler et al., 2002).

The main emission mechanism of all the above events is synchrotron radiation. In the case of cataclysmic variables (CVs; O'Brien, 2009) – binary systems in which white dwarf accretes matter from a companion star – it is thought to be a combination of thermal and non-thermal radiation arising from spherically ejected matter. For nearby objects such as flare stars and active binaries, the dominant radiation mechanism is the gyro-synchrotron emission from electrons accelerated in magnetic loops (Osten et al., 2005).

Coherent Events

Radio flares originating from coherent type of emission are usually found in time series data. Due to their short duration, they are strongly affected by propagation effects such as dispersion, which makes them difficult (but not impossible as will be shown later in Chapter 3) to be discovered in the image plane. The best studied class of objects showing flares originating from coherent emission are pulsars – rotating neutron stars with strong magnetic fields (Hewish et al. 1968, Lorimer et al. 2006). Pulsars emit radiation beamed in a narrow cone in the direction of the magnetic field axis. If that is not aligned with the rotation axis, the beam of light is visible every time it crosses the line of sight of the observer. A subclass of pulsars – rotating radio transients (RRATs; McLaughlin et al., 2006) – show single bright flares separated by hours to days.

Potentially the most exciting class of coherent radio transients was revealed by the discovery of a highly dispersed milisecond burst by Lorimer et al. (2007). The observed frequency delay of this fast radio burst indicates a DM value which significantly exceeds that expected from the Galactic contribution along the line of sight, pointing towards an extragalactic origin. Following this discovery there have been a number of similar detections of dispersed FRB candidates (Keane et al. 2011, Thornton et al. 2013, Burke-Spolaor and Bannister 2014, Ravi et al. 2015, Petroff et al. 2015), however, due to no counterparts at other wavelengths, the origin of the signals remains uncertain.

1.5.2 Extrinsic Variability

Scintillation and Intraday Variability

It has been shown that changes in flux densities observed on time-scales from days to months for sources such as pulsars and quasars (Rickett, 1986), as well as GRB afterglows (Frail et al., 1997), can be associated with interstellar scintillation (ISS). In particular, some of the distant quasars show strong intraday variability (IDV) at gigahertz frequencies with flux density changes as high as ≈ 40 per cent. Due to the short variability time-scales and large distances, the corresponding brightness temperature of such sources would have to exceed the 10^{12} K limit. Therefore, the IDV can only be explained by propagation effects caused by the changes in the electron densities of the ISM (Section 1.4.3) rather than the intrinsic properties of sources. Scintillation from quasars is expected to be a commonly detected variability in future radio transient surveys performed by sensitive instruments such as the SKA.

Extreme Scattering Events

Extreme scattering events (ESEs) are variations in the radio light-curves of bright quasars observed at gigahertz frequencies. Similarly as the IDV described above, they can not be explained by the intrinsic processes. However, as discussed by Fiedler et al. (1994), the properties of ESEs do not match the variability caused by the interstellar scintillation either. They can show strong frequency dependence, with bright flares observed at 2.7 GHz having no 8.1 GHz counterpart. The origin of ESEs is not well understood, however, they are thought to be caused by the refraction of the signal by ionised clouds in the Galaxy (Walker 2007, Senkbeil et al. 2008).

1.5.3 Overview of Radio Transient Surveys

The majority of image plane radio transients observed to date have been found through follow up monitoring of objects discovered at other wavelengths. However, a number of blind searches using both archival data as well as dedicated surveys has also been undertaken.

An extensive search of archival VLA observations has been performed by Bower et al. (2007), where 994 epochs, covering a period of 22 years were analysed. In total, 10 transient candidates were detected at frequencies of 4.9 and 8.4 GHz, indicating high sky densities of these types of events. However, a re-analysis of the same data by Frail et al. (2012) confirmed the reality of just one of these sources, with three other candidates being marginal detections and the remaining assigned to rare imaging artefacts.

The investigation of archival 330 MHz VLA data has also led to a discovery of three transient sources described by Hyman et al. (2002, 2005, 2006, 2009). The discussed events have been found in the direction of the Galactic center, with flux densities between 1 mJy – 1 Jy, showing variability on time-scales from minutes to several months. At lower frequencies, no transient sources have been found outside the solar system in the all sky transient survey carried out with the Long Wavelength Demonstrator Array (LWDA). This survey had a flux density limit of 500 Jy and was conducted at the frequency of 73.8 MHz (Lazio et al., 2010). Following that, Bannister et al. (2011) reported 53 highly variable (possibly scintillating) objects, and, 12 previously unidentified transient events detected with the Molonglo Observatory Synthesis Telescope (MOST) at 843 MHz. The analysed data spanned 22 years of observations with a total area of 2776 deg^2 covered.

A total of 1627 objects showing variability on time-scales from minutes to years have been identified by Thyagarajan et al. (2011), who analysed 55 000 snapshot images from Faint Images of the Radio Sky at Twenty-Centimeters (FIRST). Another archival search of 325 MHz VLA observations (Jaeger et al., 2012) resulted in the discovery of one, day – long transient event and several variable sources, with no counterparts at other wavelengths associated with any of those detections. Bell et al. (2014) analysed the observations of 1430 deg^2 from a dedicated transient survey performed with the Murchison Widefield Array at 154 MHz. The study of 105 radio sources showed high variability in several of the light-curves, the origin of which could be either intrinsic or associated with scintillation. No transient events were found. While searching for prompt low frequency emission from GRBs with the Long Wavelength Array (LWA), Obenberger et al. (2014a) found two (not related to GRBs) bright transient events: a 2.4 kJy outburst at 37.9 MHz, 75 seconds in duration, and, a 100 seconds long flare at 29.9 MHz with peak flux density of 3.2 kJy. Later on, the analysis of 11 000 hours of all sky images from 25–75 MHz LWA observations showed 49 long duration transients, 10 of which have been associated with large meteors (Obenberger et al., 2014b).

There have been substantial efforts to find transient sources with LOFAR. Carbone et al. (2016) analysed observations of four fields monitored at 115–190 MHz, covering an area of 2275 deg^2. No transients were found, with the explored time-scales ranging from 15 minutes to months, at the flux density limit of 0.5 Jy. Several months of LOFAR observations of the field centered on the tidal disruption event Swift J1644+57 field also resulted with no detections (Cendes et al., 2014). The first transient candidate discovered with LOFAR has been reported by Stewart et al. (2016). A bright (20 Jy) source, up to 15 minutes in duration was found in observations of the North Celestial Pole at 60 MHz, in which an area of 175 deg^2 was surveyed.

Compilations of rates obtained with the blind searches for radio transients at MHz and GHz frequencies are presented in Figures 1.11 and 1.12 respectively. In addition, Figure 1.12 shows expected rates of transient detections with the future SKA surveys. Detailed information about the estimated rates of radio transient sources can be found in Fender et al. (2015).

1.6 Transients Classification

In recent years the problem of near real time transient classification has become an important and complex challenge. Recognising the type of source that has been detected is essential in terms of planning follow up observations with limited instruments available. First however, the real transient detections need to be selected from various false alerts – a process which has usually been done by visual inspection of the images. In an era of extensive surveys carried out at optical wavelengths such as the Sloan Digital Sky Survey (SDSS) the number of snapshot maps needed to be analysed can reach hundreds per night, and is expected to exceed a million for the Large Synoptic Survey Telescope. Identifying real sources in vast amounts of data like this can no longer be done by humans on a reasonable time-scale.

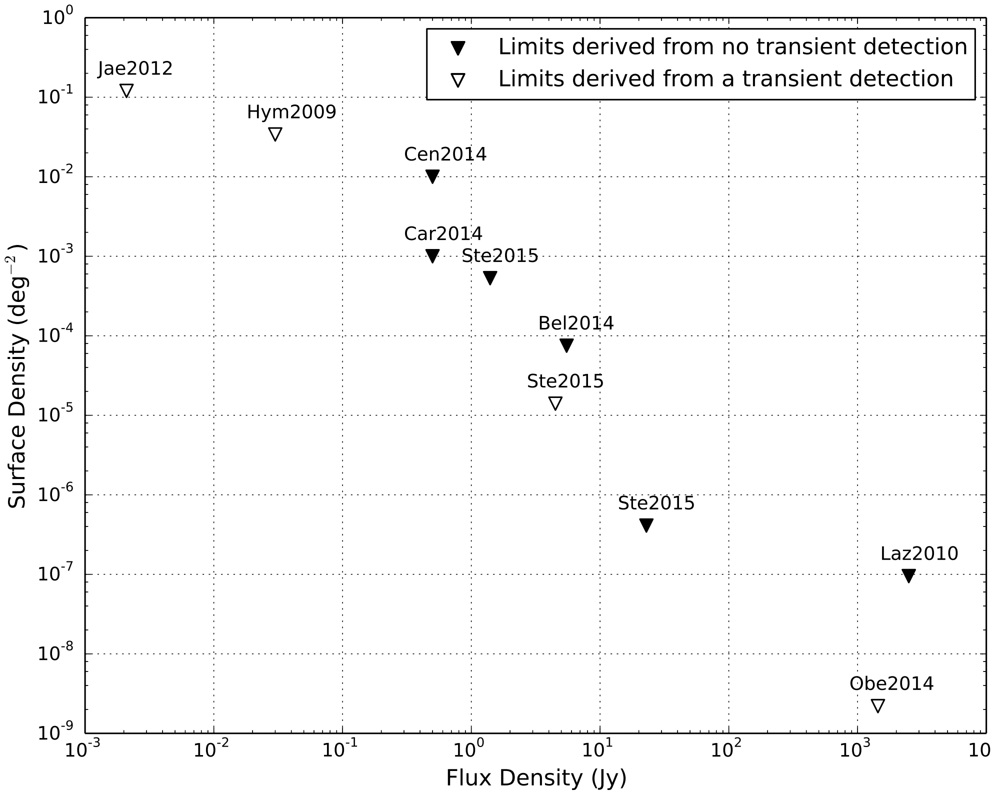

Fig. 1.11 A compilation of rates and upper limits for blind searches for radio transients at MHz frequencies including discussed low frequency surveys. Figure from Fender et al. (2015).

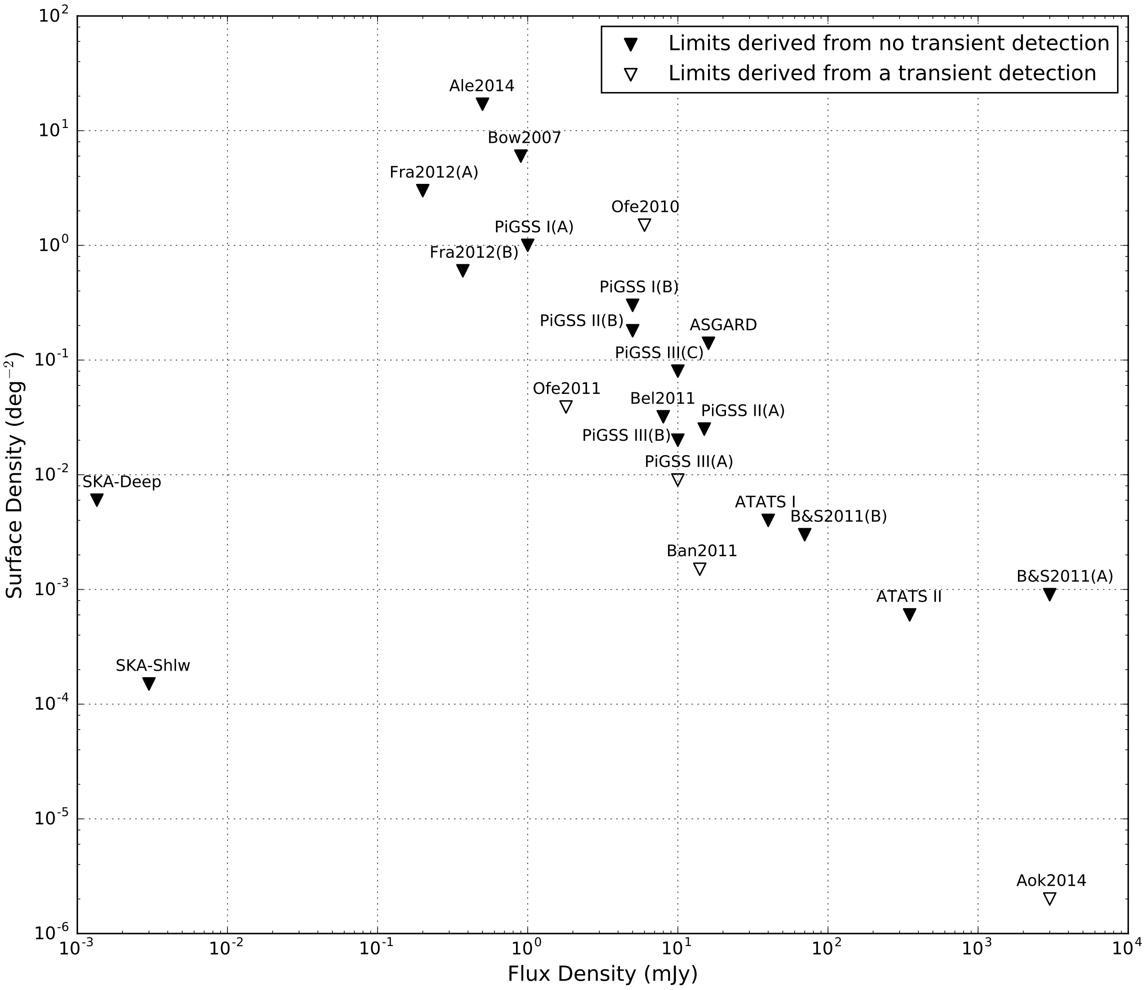

Fig. 1.12 A compilation of rates and upper limits for blind searches for radio transients at GHz frequencies, including discussed high frequency surveys. Additionally, marked with SKA-deep and SKA-shlw are planned SKA-1 narrow-and-deep and wide-and-shallow surveys respectively. Figure from Fender et al. (2015).

Automatic classification methods have been implemented for, for example, the Palomar Transient Factory (PTF; Rau et al., 2009). Bloom et al. (2012) showed that given at least two epochs of observations, the measurements of the variability time-scales and magnitude can provide an early classification of the detected source. Further generalisation of this method presented by Brink et al. (2013) can also be adopted for future surveys. Figure 1.13 shows a phase space of optical transients observed by the PTF (Kasliwal, 2011), which allows us to classify sources based on their magnitude and variability time-scales. A classifier for sources detected in the Catalina Realtime Transient Survey (Djorgovski et al., 2011) is described by Mahabal et al. (2011). The method of identifying sources from the properties of their light-curves proved to be successful in selecting objects for further spectroscopic follow up with instruments such as Palomar or Keck. Another machine learning based algorithm, designed to separate the artefacts from the actual events was presented by du Buisson et al. (2015). The performance of the classifier, which was tested on a sample of SDSS datasets, matched the results obtained manually. Further techniques for automatic selection and classification into subcategories of supernovae events from Gaia observations have been described by Blagorodnova et al. (2014).

1.7 This Work

The work presented in this thesis explores several aspects of the radio transient sky, from searching for new sources in the relatively unexplored low frequency domain, to methods of early classification of the events.

Chapter 2 describes the LOFAR radio telescope and the early imaging work I was involved in during the commissioning stage of the project.

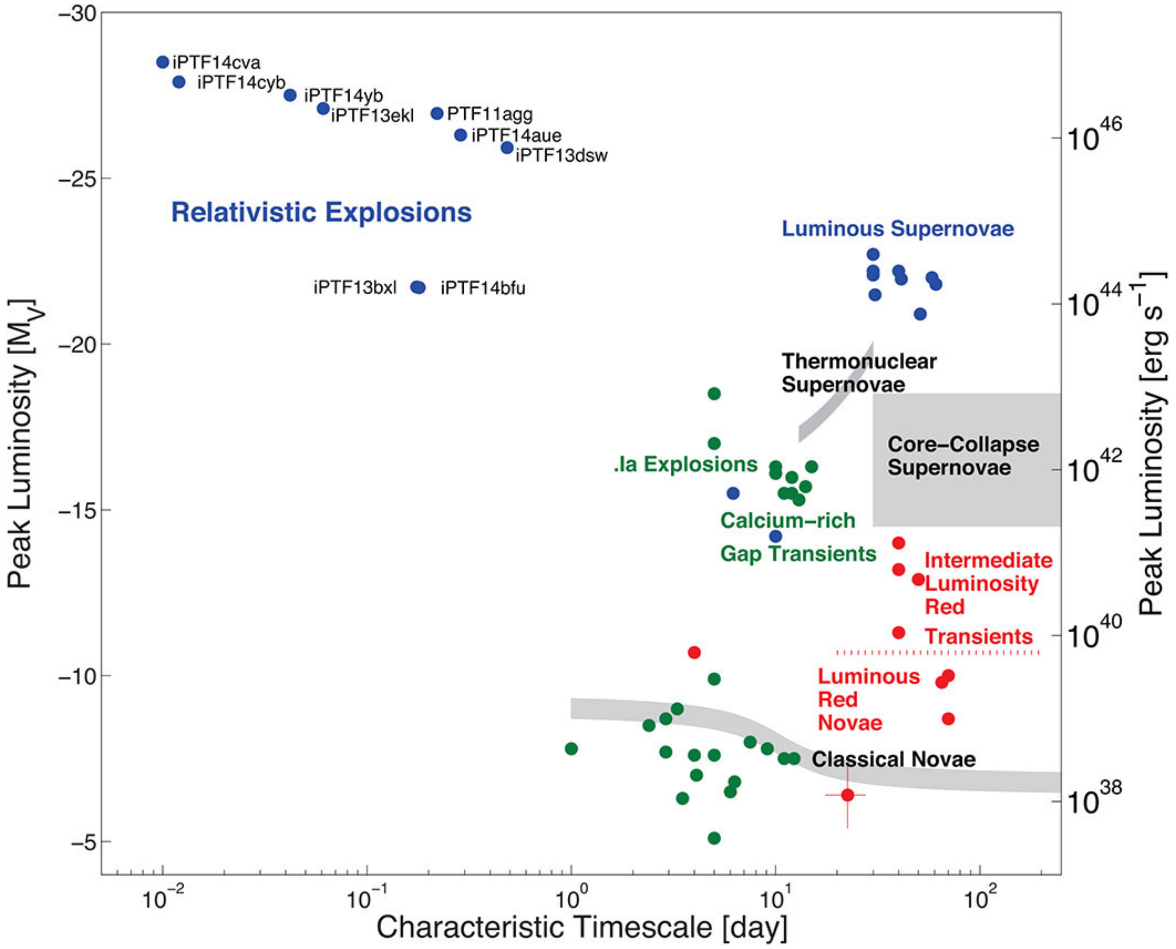

Fig. 1.13 The phase space of optical transients (Kasliwal, 2011), where the magnitude is plotted against the time-scale of the observed events. Grey areas represent classes of transients known prior to the PTF survey which identified the remaining, previously unobserved classes of sources. Figure from http://spie.org/newsroom/technical-articles/5738-searching-for-optical-transient-and-variable-sources-with-the-palomar-transient-factory, which expanded on the results presented in Kasliwal (2011).

Chapter 3 presents the analysis of the observations carried out during LOFAR's largest dedicated transient search survey.

Chapter 4 shows the analysis of basic properties of radio synchrotron flares which leads to the discovery of a previously unknown correlation covering a wide range of events.

Chapter 5 expands on the results shown in Chapter 4. An automatic software reproducing the results from Chapter 4 is built and the final outcome leads to the development of an early radio transients classification technique.

Chapter 6 summarises the work presented in the thesis. It also highlights the potential direction in which further development can be made in the future.

Appendix A provides example parset files used in the analysis (imaging and processing of LOFAR data) presented in Chapter 3.

Chapter 2

LOFAR and Commissioning

2.1 The Low Frequency Array

2.1.1 LOFAR Design

The Low Frequency Array (LOFAR) is an interferometric radio telescope built across European countries with the central component based in the Netherlands. It operates in the frequency range of 30–240 MHz and, with the wide field of view and high resolution, offers an excellent opportunity to explore the low frequency sky. It is built using simple dipole antennas rather than classic parabolic dishes and contains few, if any, moving parts. Therefore, instead of steering the dish towards the chosen location of the sky, the direction of observation is set up electronically, where multiple beams are formed by introducing a delay to the signals received at individual antennas prior to adding them. As a result, LOFAR is often described as a next generation ’software’ telescope, and is capable of performing simultaneous observations in several different directions.

Observations are carried out by two types of antennas, the Low Band Antenna (LBA), operating at 30–80 MHz and the High Band Antenna (HBA) covering the range of 120–240 MHz, with the gap in between due to the radio broadcasting band. Figure 2.1 shows

Fig. 2.1 *Upper*: The international LOFAR station at Chilbolton, UK formed with 96 single low band dipole antennas and 96 HBA tiles. *Lower*: Examples of the two types of antennas: LBA and HBA shown on the left and right respectively (picture credit: ASTRON).

Fig. 2.2 The central part of the core of LOFAR – the so called ’superterp’. It is formed by 6 stations placed on an area of $\sim$ 300 m in diameter, with the remaining 18 core stations arranged across 3 km around it (picture credit: ASTRON)

an example of the LBA which is a single dipole antenna, and the HBA, which is formed by 16 dipoles arranged into a tile. A single LOFAR station is built with a number of LBA and HBA antennas (48 or 96 depending on the location) grouped together. The core of LOFAR, situated in The Netherlands (near Exloo) is formed by 6 stations placed within an area of $\sim$ 300 m in diameter, called the "superterp", and an additional 18 stations arranged across 3 km around it (Figure 2.2). With the remote stations distributed around the Netherlands and the international stations across the European countries (Figure 2.3), LOFAR is capable of baselines up to $\sim$ 1000 km in length.

The processing of the signal received by LOFAR starts at the level of the station, where signals from individual antennas are combined to form a station beam. Data from each LOFAR station are then transported to the supercomputer in Groningen where they are correlated together. The full LOFAR bandwidth (48 MHz in 16-bit and 96 MHz in 8-bit modes) can be distributed in numerous ways. Multiple beams, limited by the number of sub-bands (244 in 16- and 488 in 8-bit mode), can be used to tile up a large area of sky,

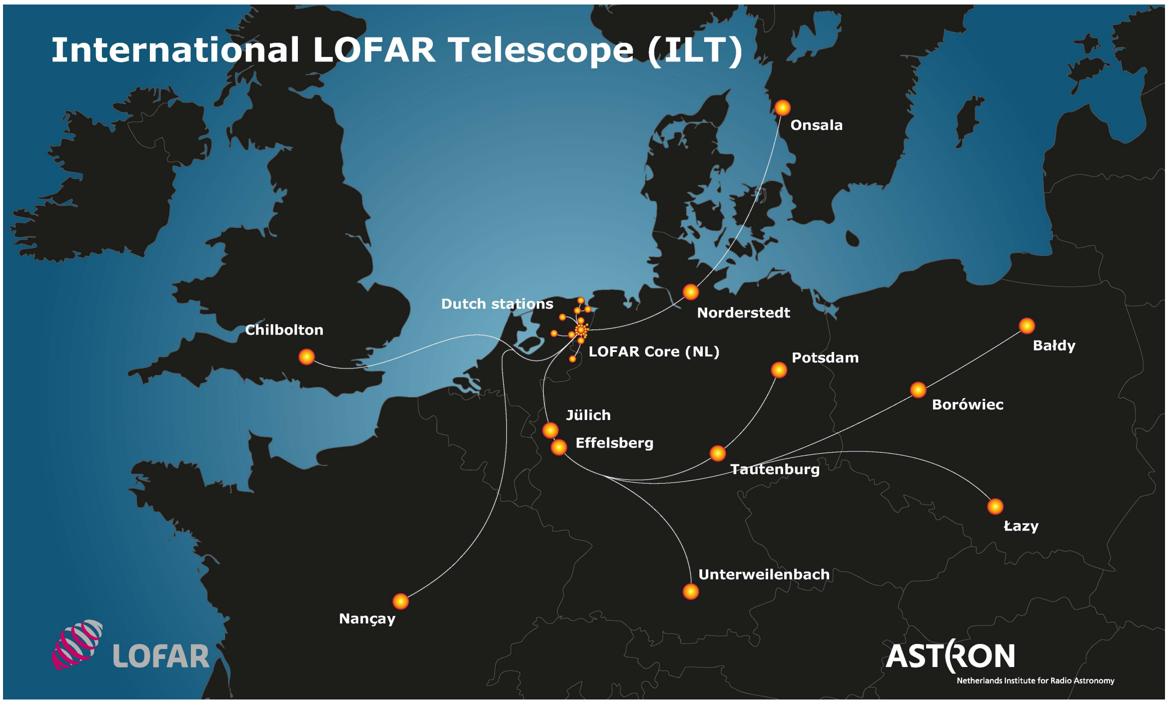

Fig. 2.3 The location of the LOFAR stations across Europe – with the central core as well as remote stations in the Netherlands. The distant international stations distributed across European countries bring the maximum baseline of the interferometer to $\sim$ 1000 km (picture credit: ASTRON).

trading the sensitivity for a wide field of view. Alternatively, LOFAR can allocate the full (or nearly full) bandwidth into one beam, increasing the sensitivity of the observed (however smaller) field, with any remaining sub-bands directed towards different target fields in the sky. An extensive overview of LOFAR can be found in van Haarlem et al. (2013).

2.1.2 Transients Key Science Project

Among six LOFAR key science programmes covering different areas of radio astronomy is the Transients Key Science Project (TKP; Fender et al., 2008b). It is focused on monitoring and studying all transient and variable events found by LOFAR, as well as developing and improving the process of detecting new sources.

The range of transient and variable sources which can potentially be found by LOFAR is wide and extends from fast ($\sim$ seconds and less) events originating from coherent processes, to incoherent flares which can last years or even decades. These two groups of transients require separate detection methods and are investigated by different scientific groups. Identification of coherent, short duration events (e.g. pulsars), depends strongly upon the accurate compensation for the propagation effects in high time resolution data (Section 1.5.1). On the other hand, slower evolving synchrotron flares (e.g. jets from X-ray binaries or gamma ray bursts) are usually found in the image plane. Because various processing and imaging artefacts, as well as radio frequency interference (RFI) can mimic the behaviour of a radio source, any detections have to be carefully validated before their astrophysical origin can be confirmed. The process of verifying newly discovered transient candidate is especially important in the case of a new instrument such as LOFAR.

One of the main surveys performed by LOFAR and dedicated to searching for image plane transients is the Radio Sky Monitor (RSM), which makes use of the wide field of view in order to observe a large part of northern hemisphere. During each RSM scan, multiple beams tile up a fraction of the sky, covering the entire zenith strip through the course of the day. An example of such zenith scan is shown in Figure 2.4. Although the primary focus of the RSM search was on slowly evolving incoherent transients, later work showed that in some conditions the detection of coherent events in image plane is also likely. As a result, the work described in this thesis is partially focused on inspecting the (image-plane) RSM observations to search for Fast Radio Bursts and will be discussed in detail in Chapter 3.

As well as performing dedicated transient searches, the TKP team made use of the data collected during the commissioning stage of LOFAR operations, such as the Multifrequency Snapshot Sky Survey (discussed in the following section). This search resulted in the first – and, to date, the only – image plane transient source discovered by LOFAR. This result is published in Stewart et al. (2016), and the candidate will be mentioned in the context of expected LOFAR transient rates later in Sections 3.6.3 and 3.8.2.

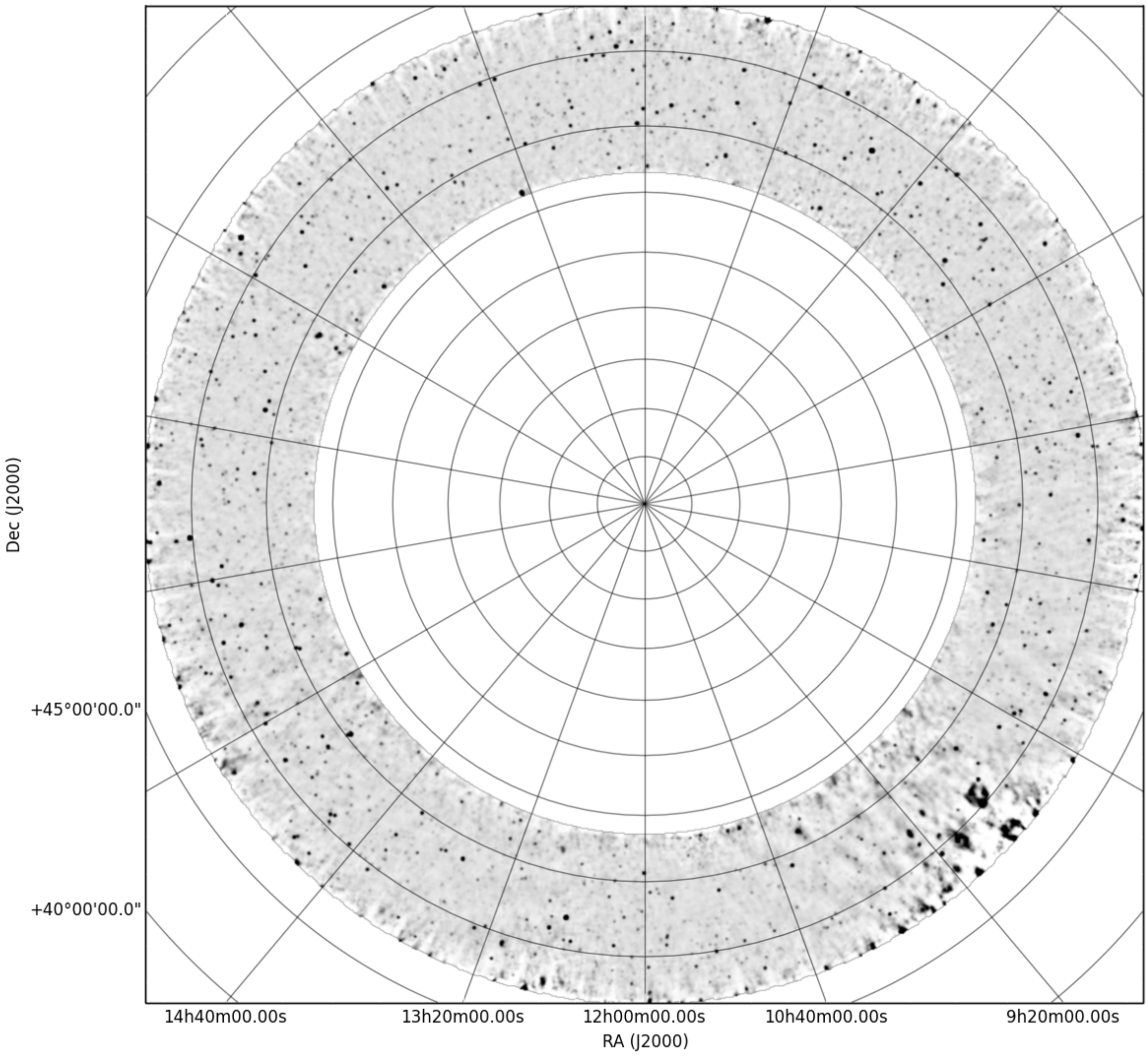

Fig. 2.4 The mosaic of the full Zenith strip observed by LOFAR HBA in February 2013, with the total field of view of ≈ 1500 deg^2. Declination is marked with concentric circles, with the two outer circles corresponding to $+40°00'.00.0''$ and $+45°00'.00.0''$ labelled on the vertical axis. Straight lines correspond to RA values, marked on the horizontal axis (image credit: Rene Breton).

The transient search in LOFAR images is performed with the Transient Pipeline (TraP; Swinbank et al., 2015) – software developed by the TKP team, capable of processing hundreds of LOFAR maps (or other radio telescopes images). It compares every extracted source against previous extracted detections, ultimately building a global database comprising broad information for every source – the light-curve, spectral information and variability statistics across the monitoring epochs.

During the six years of extensive transient searches performed by the TKP team, from commissioning observations to dedicated surveys, the number of discovered image plane transients is unexpectedly low compared to predicted rates. There are numerous explanations which can account for this discrepancy (e.g. Metzger et al., 2015), however, it should be noted that the timeline at which LOFAR achieved the expected functionality was delayed due to a variety of technical difficulties. Therefore, it can not be ruled out that further analysis of LOFAR data (from either new or archival observations), using the most recent advances in software, will bring to the surface new discoveries currently hidden by the processing issues.

2.2 Multifrequency Snapshot Sky Survey – Commissioning Work

2.2.1 Introduction

The Multifrequency Snapshot Sky Survey (MSSS) is the first major LOFAR sky survey covering the entire northern hemisphere, which amounts to a total area of 20 000 deg^2. It is divided into two frequency ranges: 30–75 MHz, using the Low Band Antenna (LBA), and 119–158 MHz, using the High Band Antenna (HBA). In both observing modes three beams are formed, each consisting of 8 $\times$ 2 MHz bands. Every band consists of 10 sub-bands, and every sub-band is split into 64 channels, with a total bandwidth of $\approx$ 200 kHz. In the LBA, the entire area of the survey is formed by 660 individual fields. Each observation of every field lasts 99 minutes and consist of 9 × 11 minute snapshots. During the observation, one of the three beams is monitoring the calibrator source, while the other two are pointed at the two target fields. For the HBA mode, in which the field of view is smaller than the LBA, the observations of the same 20 000 deg^2 area are formed by 3616 fields. Unlike for the LBA, monitoring of the calibrator source and target fields is not simultaneous – the calibrator source is observed prior to pointing all three beams at three target fields. Every field is observed in two 7 minute snapshots, with only one minute required for the calibrator source beforehand. A detailed overview of the MSSS survey is presented by Heald et al. (2015), where initial results are reported based on the analysis of the so-called 'MSSS Verification Field'. This field, centered at $\left(15^{\mathrm{h}}, +69^{\circ}\right)$, covers a region of 100 deg^2 and is used as a representative sample of all observations, to show the general strategies and first results of the survey.

Between February and October 2012, during the commissioning weeks of the MSSS project, I have been involved in the analysis of several LBA observations, which is summarised in later sections. The next section details the calibration strategy, which is applied to all observations.

2.2.2 Processing Methods

The first step of processing the data was removing any radio frequency interference (RFI). This was done automatically, using AOFLAGGER (Offringa et al., 2010) software. The demixing technique (van der Tol et al., 2007) was also applied in order to remove the contributions from the brightest radio objects in the sky: Cygnus A, Cassiopeia A, and – where necessary – Taurus A and Virgo A. In order to reduce the volume of the extensive data sets, prior to calibration, each single sub-band measurement set has been compressed in frequency and time. This resulted in an integration time of 10 seconds per time-step and the frequency compressed to one channel per sub-band (frequency bandwidth of 200 kHz).

Observations of the calibrator source were then used to calibrate the flux density in the target fields. The phase calibration was performed in a separate step using the global sky model (GSM; Scheers, 2011) based on the VLSS catalogue, using sources with a flux density above 0.1 Jy, found within 10 degrees from the center of the field. These sources were cross-correlated with the 325 MHz Westerbork Northern Sky Survey (WENSS; Rengelink et al., 1997) and the 1400 MHz NRAO VLA Sky Survey (NVSS; Condon et al., 1998) in order to estimate the spectral index α. The association radius for cross-matching sources between catalogues was set to 10 arcsec – in cases where no match was found, the value of $\alpha = -0.7$ was used[1]. Bad stations, which were identified by checking if the amplitudes for the baselines including those stations showed large scatter, were manually flagged. This was necessary because various aspects of LOFAR were still unstable during commissioning. Finally, after the datasets were fully calibrated and flagged, they were imaged with the AWIMAGER – software designed specifically for imaging LOFAR data (Tasse et al., 2013).

2.2.3 Single-band Analysis of Two MSSS LBA Fields

This section presents the analysis of two MSSS LBA fields, L227+69 and L243+69, which I have been involved in during the early stage of the commissioning work. The analysis described here was focused on the following aspects:

- Investigation of the gain amplitudes of the calibrator source.
- Analysis of the evolution of the flux density measurements for the brightest sources in the field across snapshots.
- Comparison of the flux density values of sources in the field with the corresponding sources in the VLSS catalogue.

---

[1] The exception was the analysis described in Section 2.2.3 where the estimation of the spectral index was not included by default in GSM. The sky model used in this work included VLSS sources above 4 Jy found in the 10° radius from the center of the field.

At this stage, due to the still slow processing time, the analysed data were limited to one frequency band for both sets of observations.

Data Processing and Imaging

The discussed observations were carried out in January 2012. Both the L227+69 and L243+69 fields have been observed in 9 x 11 minute snapshots, separated by one hour intervals. The 60 MHz band was chosen for the following analysis, as it corresponds to the peak of the bandpass and offers the best data quality. Data were processed as described in Section 2.2.2, including demixing in order to remove the contributions from Cyg A and Cas A. The calibrator source used for the flux calibration in both of the discussed fields was 3C 295. Prior to imaging, ten sub-bands were combined to form one 2 MHz band. This resulted in obtaining a final set of nine images for each of the analysed fields (one image for every 11 minute snapshot). A deep map for each of the fields was created by combining the measurement sets from all nine snapshots and imaging the final concatenated dataset. For both L227+69 and L243+69 fields, the rms noise level at the centre of the field varied from 600–700 mJy beam^{-1} in the early snapshots to 900–1000 mJy beam^{-1} in the later snapshots. We ascribed the increase in the observed noise level to the interference from the rising Sun. Figure 2.5 shows the deep images for both fields and the summary of the observations can be found in Table 2.1.

Investigating the Calibrator Gain Amplitudes

During the processing it was noticed that outlying amplitudes were present in the calibration of the 3C 295 observations. Therefore, we tested a range of parameters for clipping these outliers in the gain solutions of the calibrator. Using a set of tools developed by John Swinbank (University of Princeton) as a part of the earlier MSSS work, we tested different cut off levels, ranging from 1–3σ (rms). A set of diagnostic plots generated for these clipping values suggested that 2.5σ was the safest choice for the threshold level. This meant that outliers

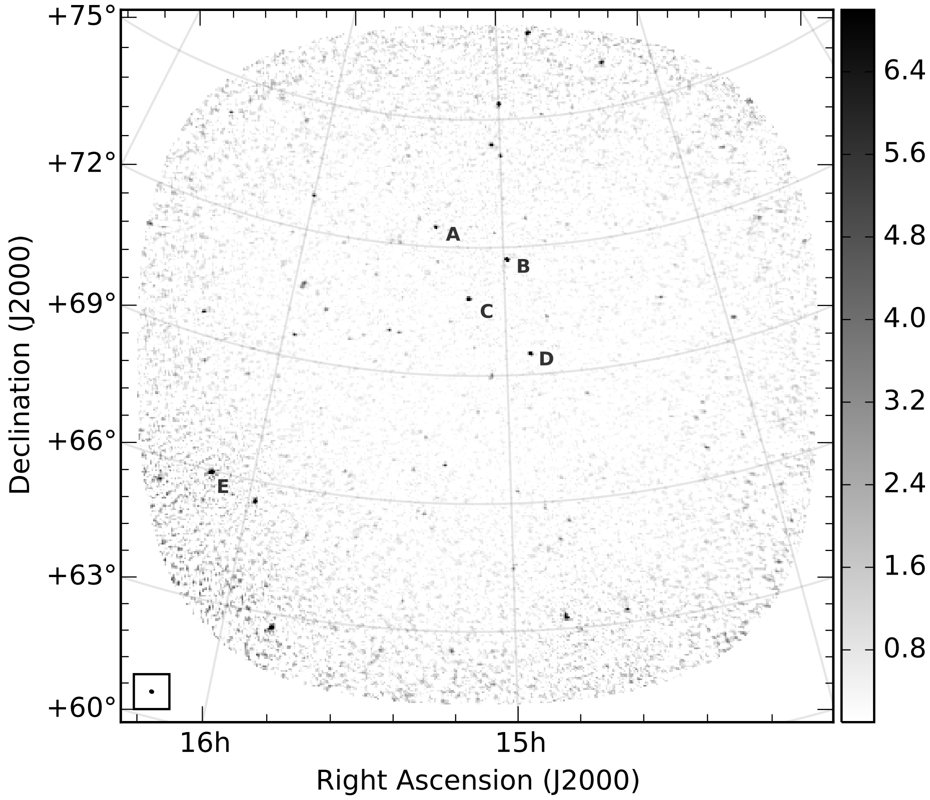

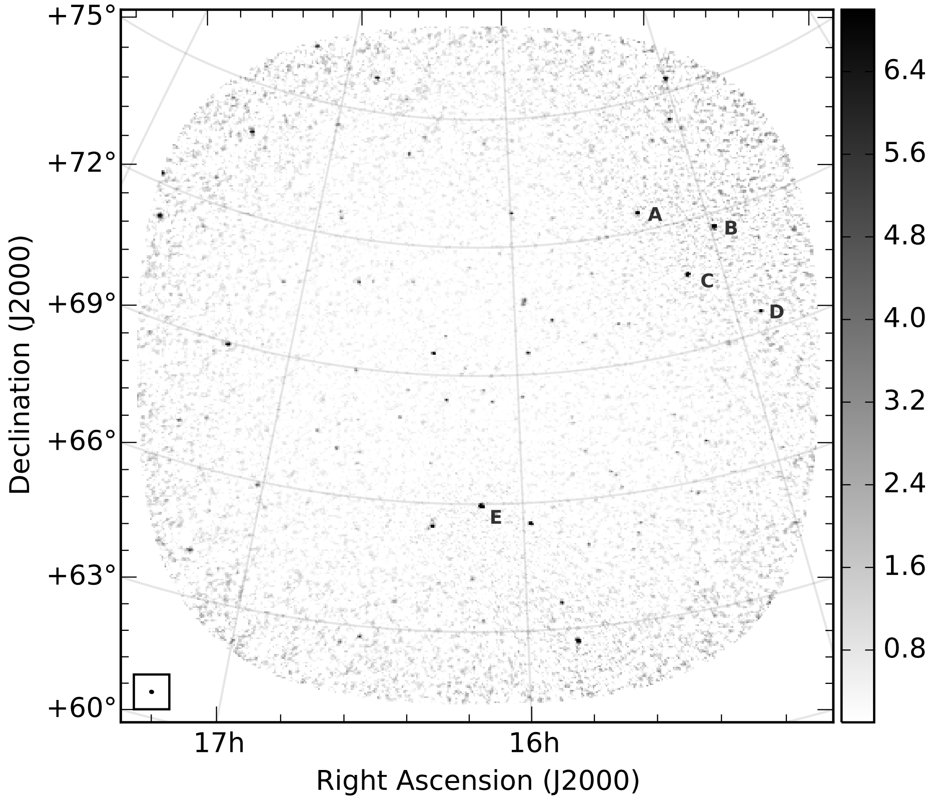

Fig. 2.5 Deep images for the two studied fields: L227+69 (*upper*) and L243+69 (*lower*). The angular resolution is ≈ 240 arcsec × 170 arcsec, and the rms noise level at the centre of the image is ≈ 260 mJy beam^{-1}. The five brightest sources in the overlapping region of the fields (marked A–E) were chosen for further comparison.

Table 2.1 Details of the data analysed for two overlapping MSSS LBA fields. Both fields have been observed in January 2012 as a part of the MSSS commissioning programme.

	L227+69	L243+69
RA (hh:mm:ss)	15:07:49.5652	16:10:26.0870
Dec (dd:mm:ss)	+69:14:24.0000	+69:14:24.0000
Observation start	04:18 UT, Jan 07	03:48 UT, Jan 14
Observation end	12:18 UT, Jan 07	11:48 UT, Jan 14
Core stations	24	24
Remote stations	9	9
Center frequency	60 MHz (LBA)	60 MHz (LBA)
Bandwidth	2 MHz	2 MHz
Calibrator	3C 295	3C 295

were removed, yet it was the least likely to exclude possibly real amplitude fluctuations. Hence, these settings were then applied to the processing of the analysed fields. Figure 2.6 shows example plots for one of the 11 minute snapshots, with the amplitudes clipped at the level of 2.5σ.

Flux Density Measurements Between Snapshots

For the comparison of the flux density measurements across the nine 11 minute snapshots, we chose the five brightest sources in the overlapping region of the analysed fields (marked A–E in Figure 2.5). The integrated flux densities of these sources were manually measured using KVIS. Figure 2.7 shows the light-curves for each of the five sources, as measured in the L227+69 field. While all the sources located in the center of the image show relatively low fluctuations in the measured flux density from snapshot to snapshot, source E, being very close to the edge of the image, varies significantly due to the increased noise level in that region. The comparison of the flux densities of the same sources (A–E) between two fields

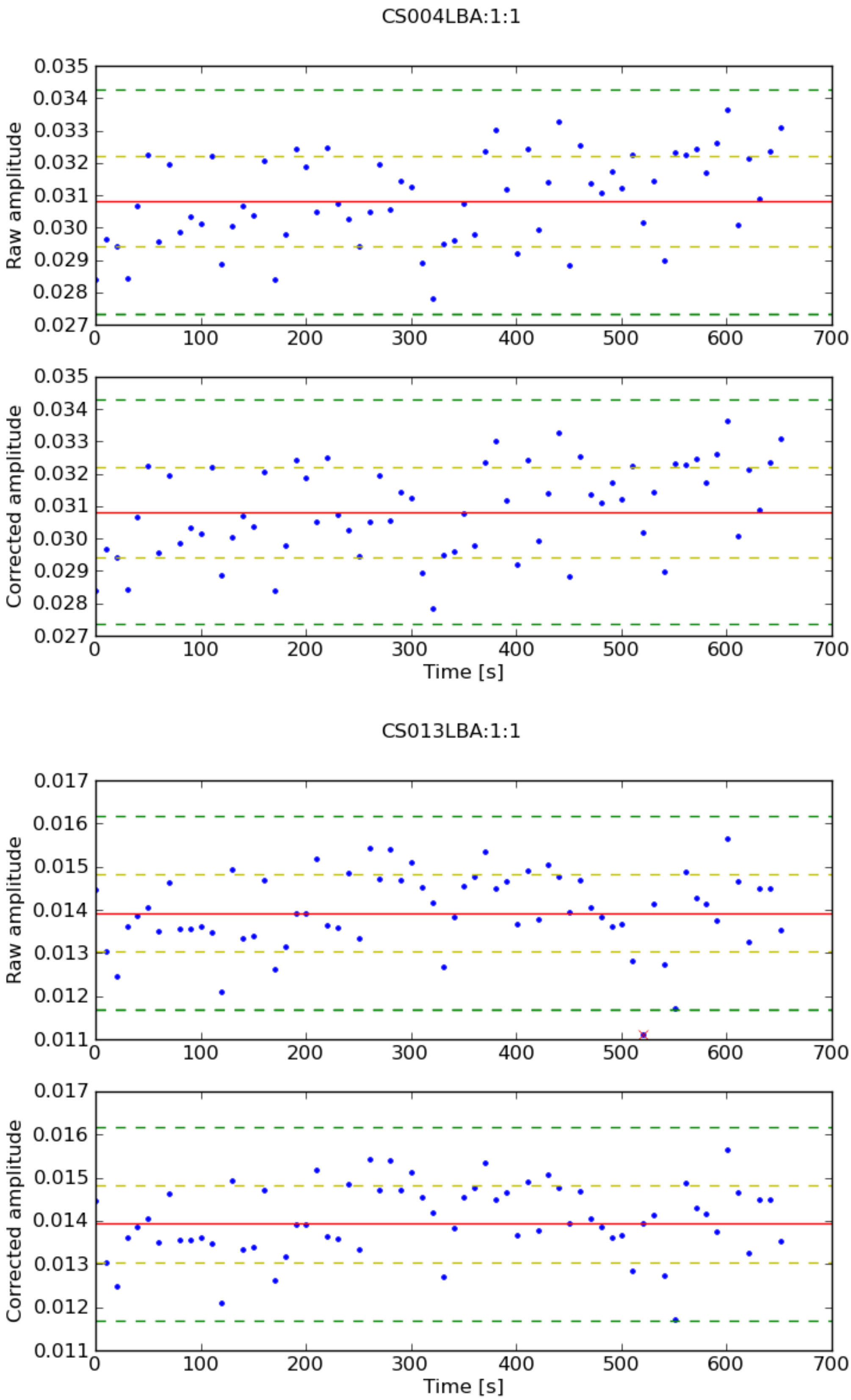

Fig. 2.6 Gain amplitudes of the calibrator source 3C 295 plotted against time, for one of the 11 minute snapshots. The median is marked with a red line and the rms (σ) is indicated by dashed yellow lines. Dashed green lines correspond to the chosen cut off threshold for the amplitudes, in this case 2.5σ.

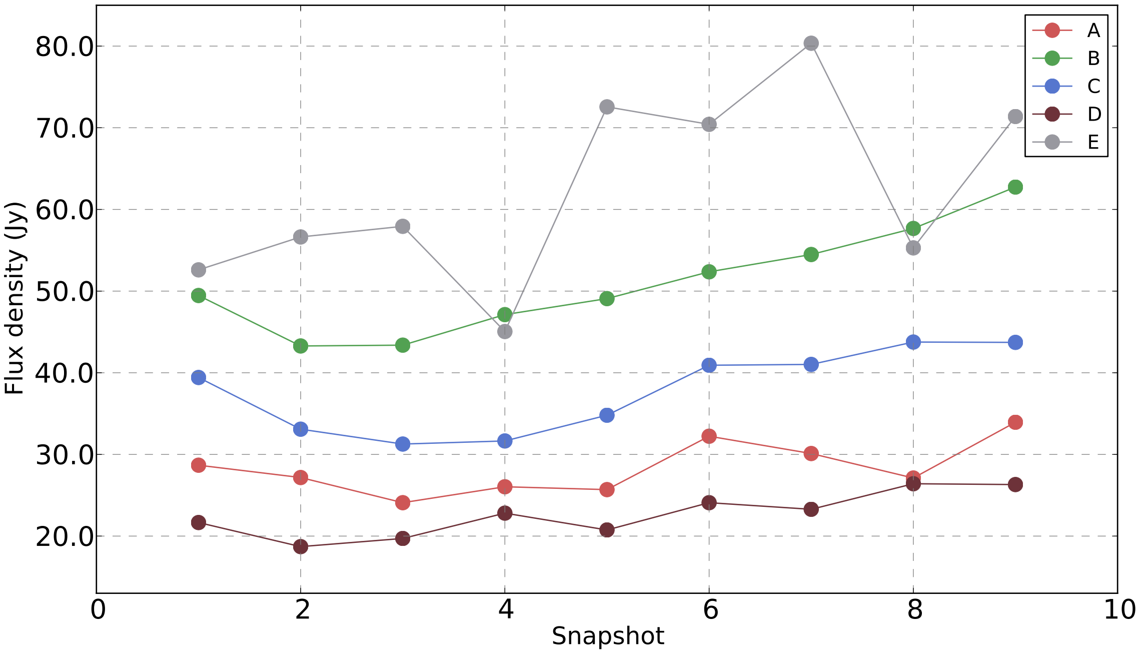

Fig. 2.7 Plotted here is the comparison of the flux density values for five brightest sources (marked A-E in Figure 2.5) in the L227+69 field, across nine snapshots.

showed a general agreement, with a standard deviation of ≈ 20 per cent.

LOFAR vs VLSS Flux Densities

We have compared the flux density values of sources in the analysed LOFAR fields with the VLSS catalogue. For each of the fields we used PYBDSM[2] software to extract sources from the corresponding deep image and fit them with Gaussians. Due to the shape of the map it was not possible to extract all of the sources in the field – in particular, some of the sources near the edges were not detected by PYBDSM. In those cases, flux densities manually measured using KVIS were used instead. Those 60 MHz LOFAR flux density measurements were then compared with the corresponding sources in the 74 MHz VLSS catalogue. The analysis has been limited to the brightest sources in the field, with a lower flux density cut off of 4 Jy, which gave a total number of ≈ 30 sources for flux comparison. For both fields,

---

[2] http://www.astron.nl/citt/pybdsm

the measured LOFAR/VLSS flux density ratio was ≈ 1.4. This difference can be partially explained by the spectral evolution of synchrotron emitting sources – i.e. for a source with spectral index -0.7, we expect the flux density measured at 60 MHz to be 16 per cent higher than at 74 MHz. However, the observed discrepancy was too high to be explained simply by this effect and required further investigation, which – at the time – had to be postponed.

Summary

The analysis of single band MSSS LBA observations of two fields showed an acceptable agreement between the flux densities measured for four brightest sources in their overlapping region, as well as across the 9×11 minute snapshots. The comparison of the LOFAR flux density measurements (60 MHz) with the VLSS catalogue (74 MHz) also gave a reasonable agreement, however, the discrepancy was slightly higher than what could be expected due to the spectral evolution.

2.2.4 Full Bandwidth Analysis of Selected MSSS LBA Fields

At the time of the work presented in this section, processing of LOFAR data was advanced enough to allow relatively quick imaging of multiple fields across the whole MSSS LBA bandwidth. The main focus of the commissioning work described here was on the following analysis done for several of the MSSS fields:

- Spectral analysis of sources detected across the LBA bands.
- Cross-matching sources across the eight LBA bands.
- Cross-matching sources detected in LOFAR images with the VLSS catalogue.

Source Detection

For the following analysis, we have chosen six MSSS LBA fields[3] imaged across all eight bands (31–74 MHz). The extraction of sources from images has been performed with the PYBDSM software. After testing several approaches for the detection and flux measurement of the sources, we decided to implement the following steps.

Detection. In order to identify sources, a deep map was used as the detection image for the source extraction. The deep map was created by combining eight images of the individual bands. By averaging single band images we ensure a better signal to noise ratio in the final map, which makes faint sources in the field more likely to be detected by the software. Images for which the primary-beam correction has been applied have a higher level of noise near the edges, therefore, we decided to use the non primary beam corrected maps and decrease the risk of false detections.

Analysis. For every source detected in the deep map, the flux density measurement was taken in each of the single band images at the location of the detection. For this measurement, we used the primary beam corrected images, which give more accurate flux density level. Force fitting of the data has not been implemented, i.e. if the signal to noise ratio for a given source detected in a deep image was too low in a given band, no flux measurement was taken at this location for the respective band.

The output files generated by PYBDSM provide catalogues of sources detected across the bands, which can later on be used to perform the spectral evolution analysis and cross matching with other catalogues.

Cross-matching and Spectral Analysis

Using the PYBDSM based routine for the source analysis described above, we have created catalogues comprising of flux density measurements across the full bandwidth for sources in each of the six selected fields. The analysis described here has been done using the

---

[3] L045+63, L070+69, L071+23, L078+23, L086+40 and L086+69.

cross-matching tool developed by Rene Breton (University of Manchester) during the commissioning work. The tool constructs a set of diagnostic plots, which include: a comparison of the extracted sources with the sky model catalogue used in the data processing step, spectral indices distribution and, a summary of the measurements taken for every analysed source. Firstly, it creates maps illustrating the PYBDSM detection of sources across the bands. An example map obtained for the L070+69 field is presented in Figure 2.8, where the sources are colour coded by the number of bands in which they were found. Figure 2.9 is a variation of that plot, where each colour corresponds to a different band in which the source was detected. Small crosses mark sources in the provided sky model (in this case VLSS based catalogue), while positive matches between the catalogue sources and LOFAR images are marked by large crosses. Figure 2.10 (upper panel) shows an example of the spectral index distribution for sources in one of the fields (L070+69). The relation between the measured spectral indices and the reduced χ^2 values of those measurements is shown in lower panel of Figure 2.10. Finally, several examples of the summary plots for individual sources detected in a given field are presented in Figures 2.11 and 2.12. These figures give an overview of the spectral evolution across the bandwidth (error of each data point is estimated by 15 per cent of its measured flux density) as well as the images of the source as it appears in each band.

Discussion

For half of the analysed fields, approximately 80 per cent of the catalogue sources from the corresponding VLSS based sky models have been successfully detected, with the number of positive cross-matches increasing towards the central regions of the images (e.g. Figures 2.8, 2.9). For the remaining fields, possibly due to the poor quality of images, the extracted source count was much lower and a significant fraction of the catalogue sources has not been found.

The most unexpected result, however, was the spectral indices distribution, which seemed to peak at $\approx$ -1.0 for four out of the six considered fields. We have recognised this value to

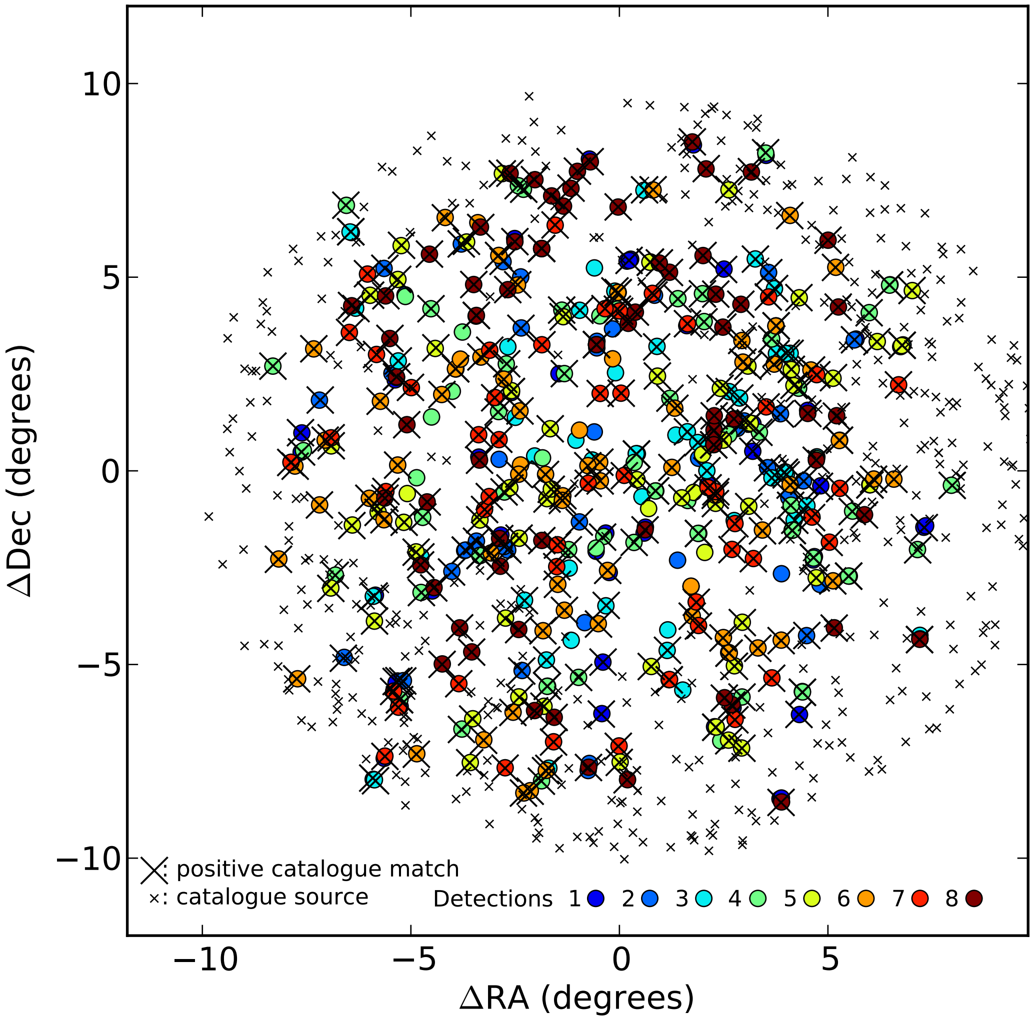

Fig. 2.8 The sources found in the L070+69 field. The detections have been colour coded by the number of detections across eight bands.

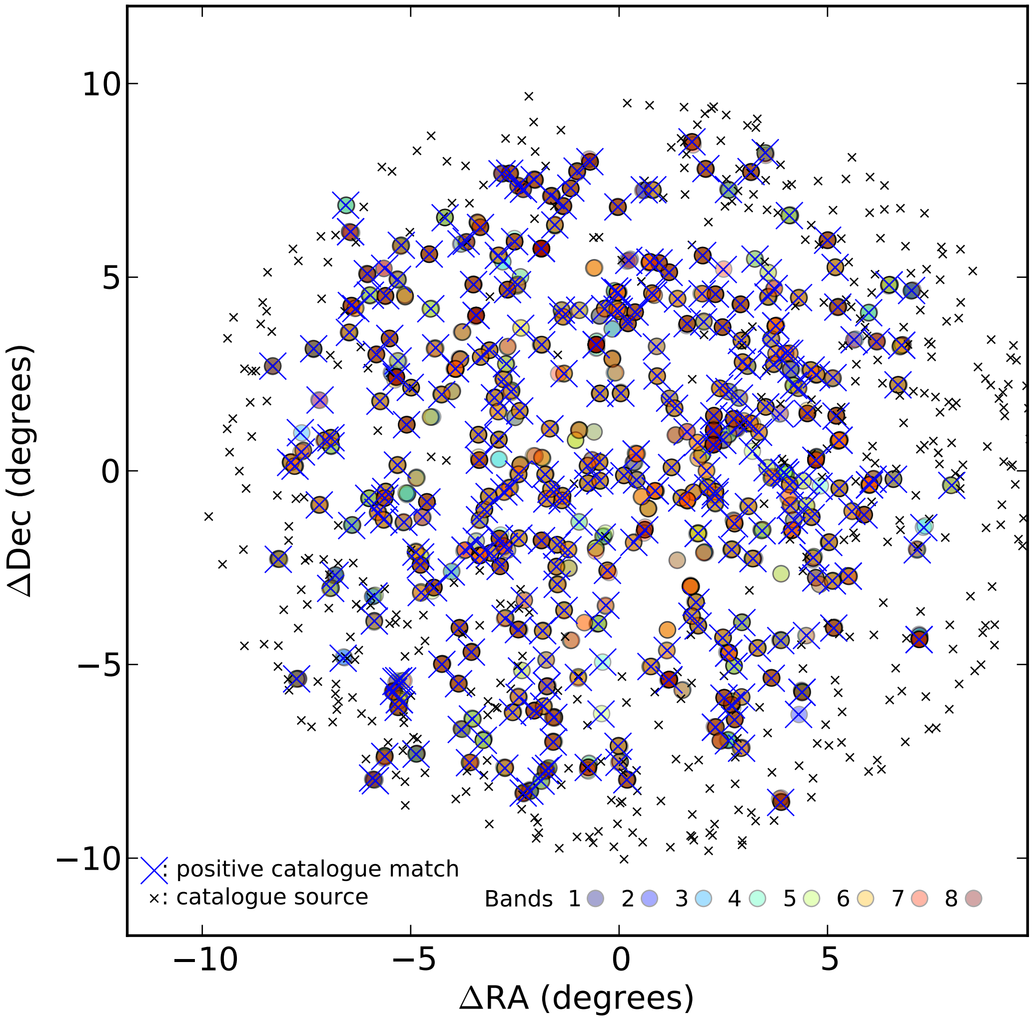

Fig. 2.9 The sources found in the L070+69 field colour coded by the band in which the source has been found.

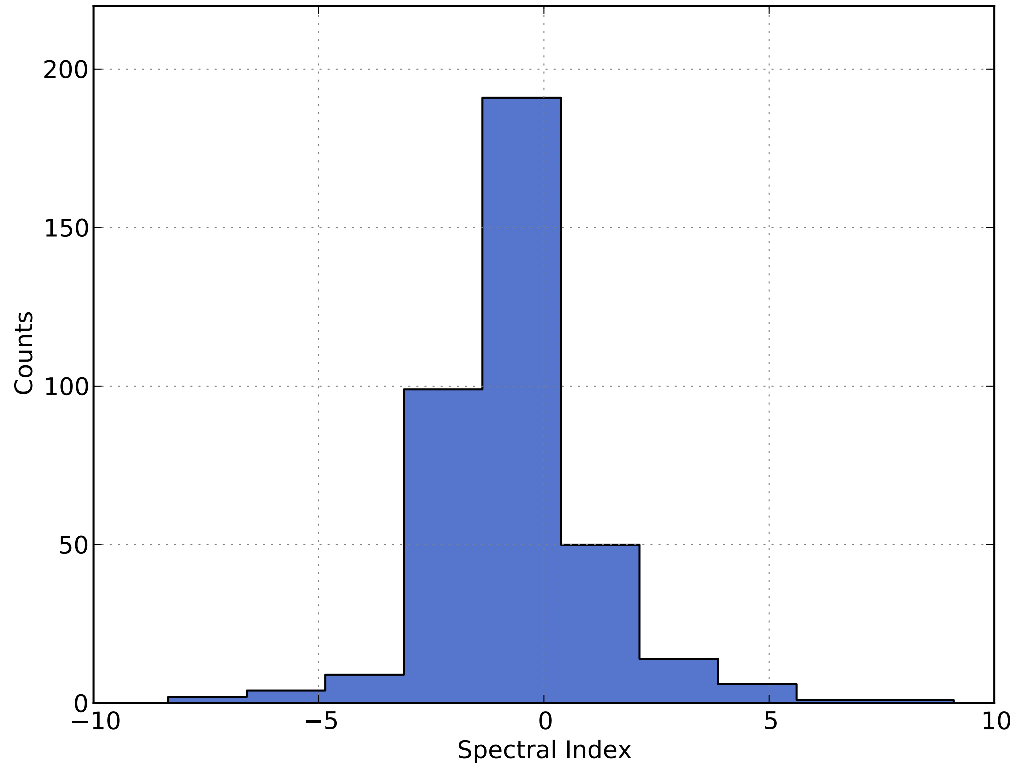

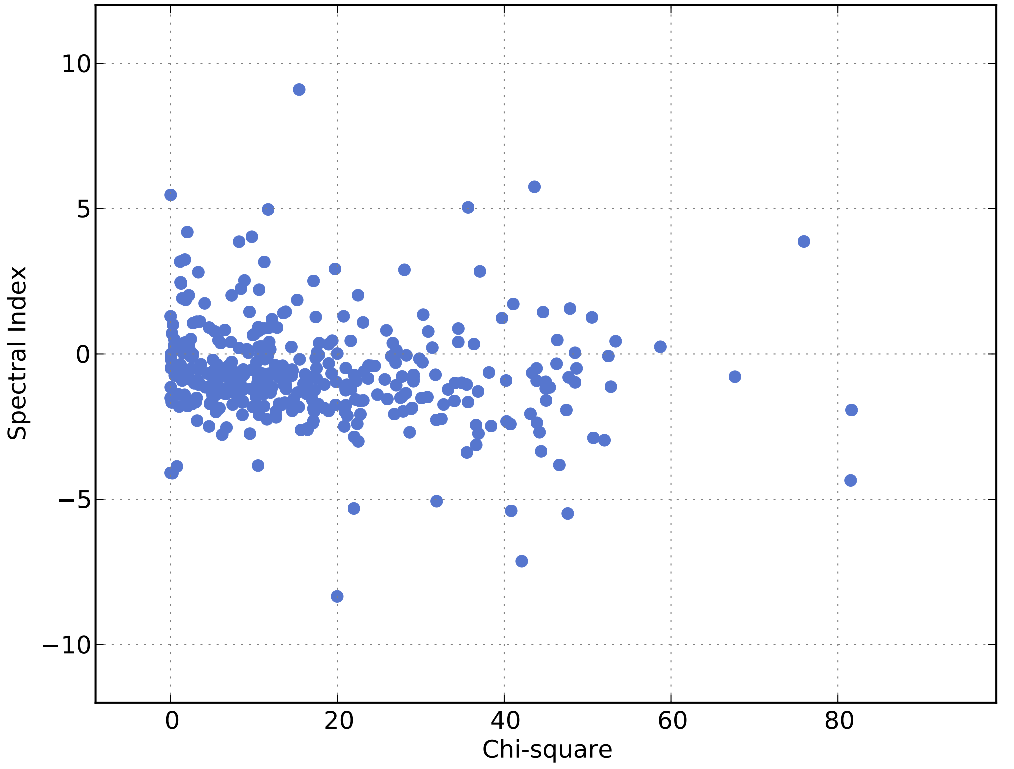

Fig. 2.10 *Upper*: the distribution of measured spectral indices for the sources detected in L070+69 field. *Lower*: spectral indices plotted against the reduced χ^2 values of the fit done across the bands with detections.

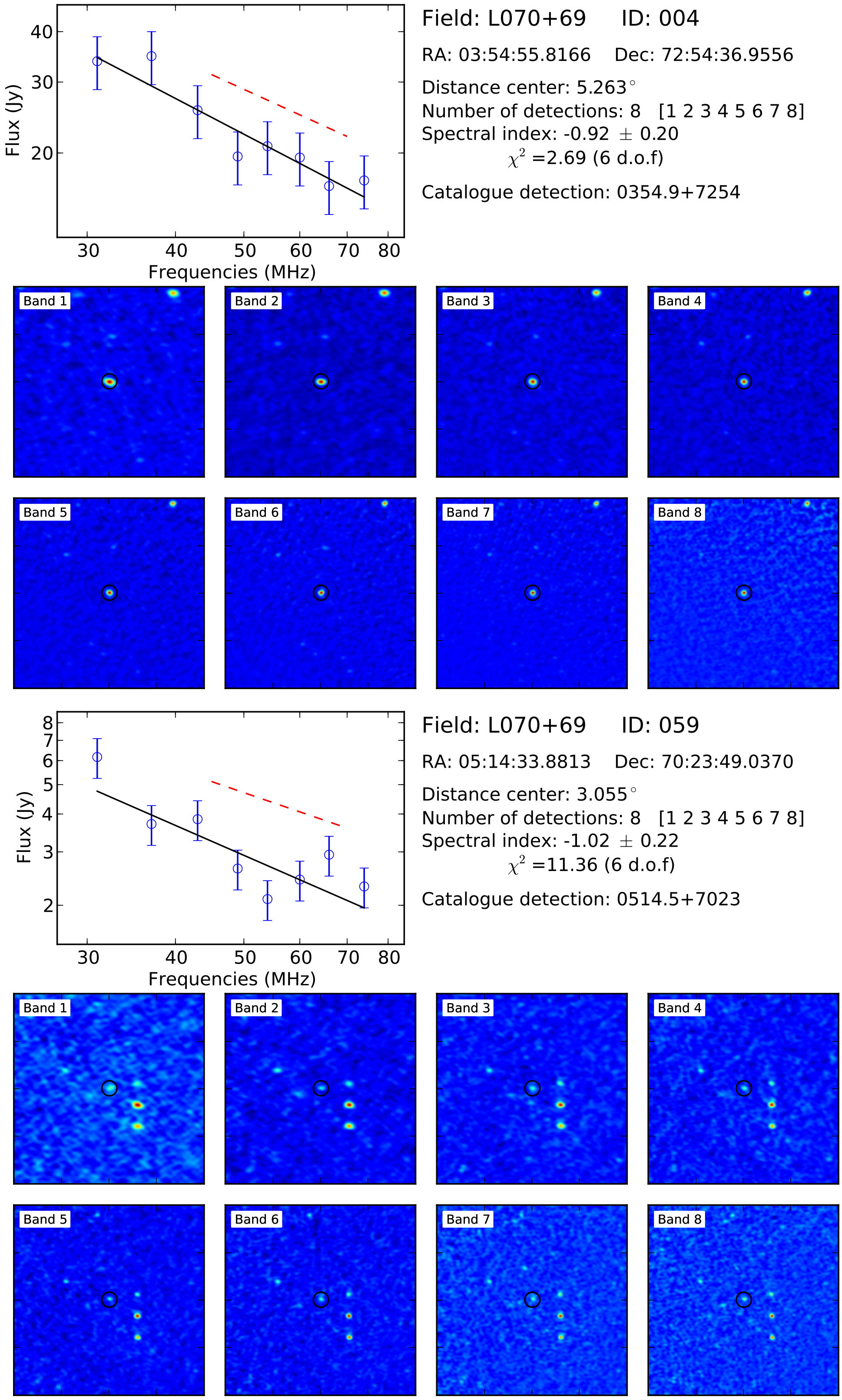

Field: L070+69 ID: 004
RA: 03:54:55.8166 Dec: 72:54:36.9556
Distance center: 5.263°
Number of detections: 8 [1 2 3 4 5 6 7 8]
Spectral index: -0.92 ± 0.20
χ^2 =2.69 (6 d.o.f)
Catalogue detection: 0354.9+7254

Field: L070+69 ID: 059
RA: 05:14:33.8813 Dec: 70:23:49.0370
Distance center: 3.055°
Number of detections: 8 [1 2 3 4 5 6 7 8]
Spectral index: -1.02 ± 0.22
χ^2 =11.36 (6 d.o.f)
Catalogue detection: 0514.5+7023

Fig. 2.11 Example summary plots for two sources detected in the L070+69 field in all eight bands. The upper left part of each figure shows the spectral energy distribution. The best fit to the data is shown with the black line. The red dashed line plotted for reference corresponds to the slope of -0.8. A summary of the measurements for the source is displayed above the snapshots of the eight bands, which show the extracted source in the center.

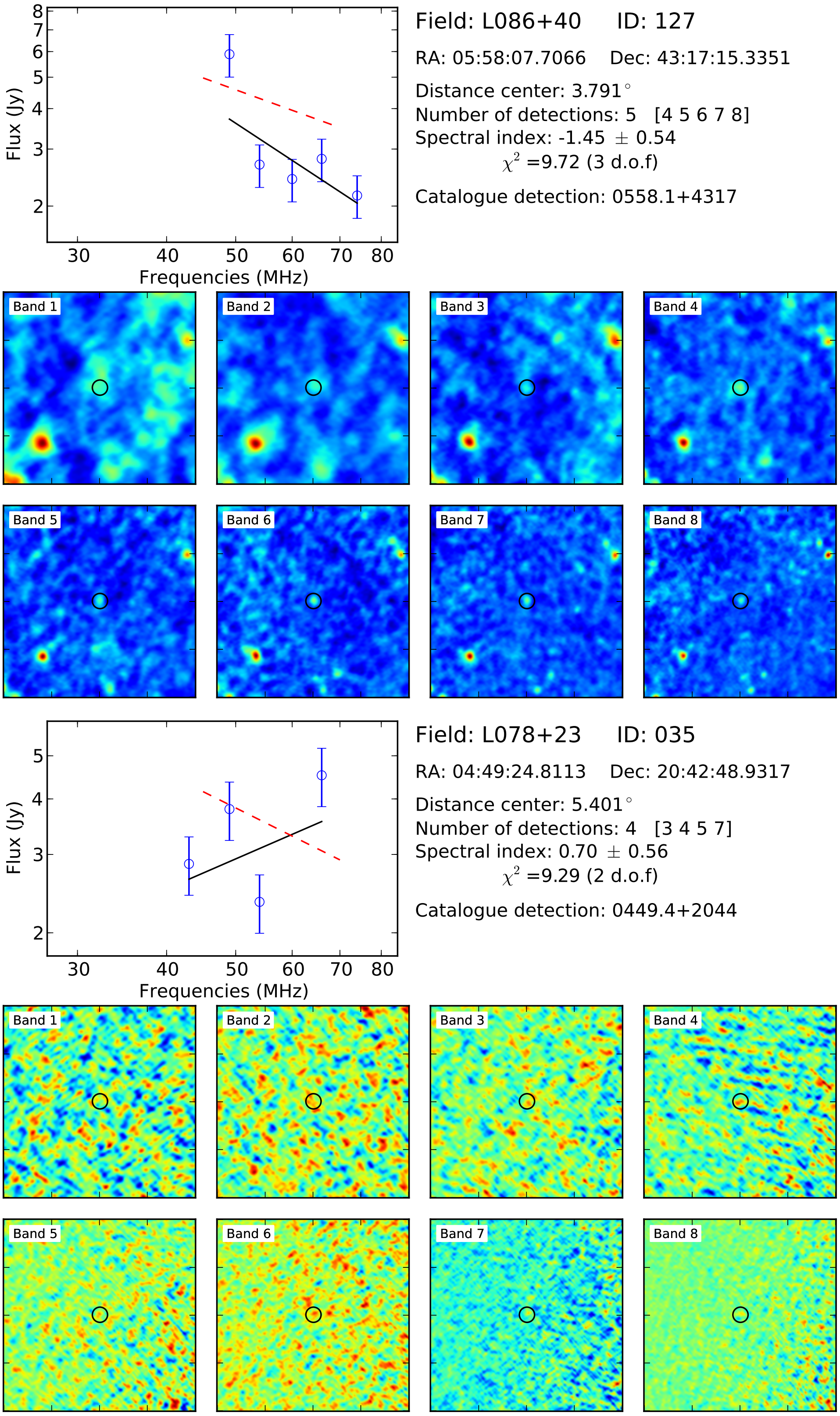

Field: L086+40 ID: 127

RA: 05:58:07.7066 Dec: 43:17:15.3351

Distance center: 3.791°

Number of detections: 5 [4 5 6 7 8]

Spectral index: -1.45 ± 0.54

χ^2 =9.72 (3 d.o.f)

Catalogue detection: 0558.1+4317

Field: L078+23 ID: 035

RA: 04:49:24.8113 Dec: 20:42:48.9317

Distance center: 5.401°

Number of detections: 4 [3 4 5 7]

Spectral index: 0.70 ± 0.56

χ^2 =9.29 (2 d.o.f)

Catalogue detection: 0449.4+2044

Fig. 2.12 Example summary plots as described in the caption of Figure 2.11 for two sources which were not detected in all bands.

be too steep comparing to the spectral index of $\approx$ -0.7 expected for the synchrotron emitting objects, like AGN, which make up a large fraction of the field sources. Detections with poor signal to noise ratio (e.g. Figure 2.12) could have contributed to the observed scatter in the spectral distribution, which seems to be too broad comparing to the expected values of the spectral index between -2 and 1 (De Breuck et al., 2000). However, the reason for the steep spectral distribution measured here has later on been assigned to the error in the way the LOFAR primary beam correction has been applied. Once this problem was resolved, the flux density measurements were corrected and the peak of the observed spectral distribution of detected sources shifted towards the expected -0.7 value. The primary beam correction error also explains the discrepancy between the VLSS and LOFAR flux measurement discussed in Section 2.2.3.

The commissioning work presented in this chapter was carried as part of the MSSS commissioning programme and, at the time, has contributed to the progress of the survey. Due to the work done during the commissioning stage of LOFAR, I have been listed as a co-author in the following papers:

Buitink S., et al., 2016, Nature, 531, 70
Carbone D., et al., 2016, MNRAS, 459, 3161
Garsden H., et al., 2015, A&A, 575, A90
Heald G. H., et al., 2015, A&A, 582, A123
Jelić V., et al., 2014, A&A, 568, A101
Marcote B., et al., 2016, MNRAS, 456, 1791
Morosan D. E., et al., 2014, A&A, 568, A67
Nelles A., et al., 2015, APh, 65, 11
Noutsos A., et al., 2015, A&A, 576, A62
Orrù E., et al., 2015, A&A, 584, A112

Pilia M., et al., 2016, A&A, 586, A92

Sobey C., et al., 2015, MNRAS, 451, 2493

Stewart A. J., et al., 2016, MNRAS, 456, 2321

van Weeren R. J., et al., 2014, ApJ, 793, 82

2.3 LOFAR Observations of IC 342

This section presents the analysis of the High Band Antenna (HBA) LOFAR monitoring of IC 342 – a face-on spiral galaxy located at the distance of $\approx$ 3 Mpc. The observations discussed here have been taken in February 2013 as part of the LOFAR Nearby Galaxies monitoring project. Our interest in these data was due to the possibility of searching for the radio counterparts of ultra-luminous X-ray sources (ULXs).

The analysed dataset consists of a three hour observation of the field centered at 03:46:48.50 +68.05.46.92, carried out at the frequency range between 115-178 MHz. Data pre-processing has been done by Cameron Van Eck (Radboud University) – this consisted of RFI flagging using AOFLAGGER and data compression in frequency and time to four channels per sub-band and ten seconds per time-step. Using the pre-processed data, flux calibration was then done using 3C 147 as a flux calibrator, and the phase calibration was performed using the VLSS based sky model created with GSM. Prior to imaging, 324 sub-bands were combined into 18 bands, each consisting of 18 sub-bands. Those single bands were then imaged using baselines up to a projected length of 6 km. The deep map was created by combining 18 single band images, which resulted in the average noise level in the final map of $\approx$ 3 mJy beam^{-1}. The upper panel of Figure 2.13 shows the deep map, where IC 342 is clearly visible in the center of the image, with a more detailed view of the galaxy shown below. Marked with the white circle is the position of the known ultraluminous X-ray source (ULX) IC 342 X-1 (Feng and Kaaret, 2008). ULX are a class of extragalactic sources for which a high observed luminosity

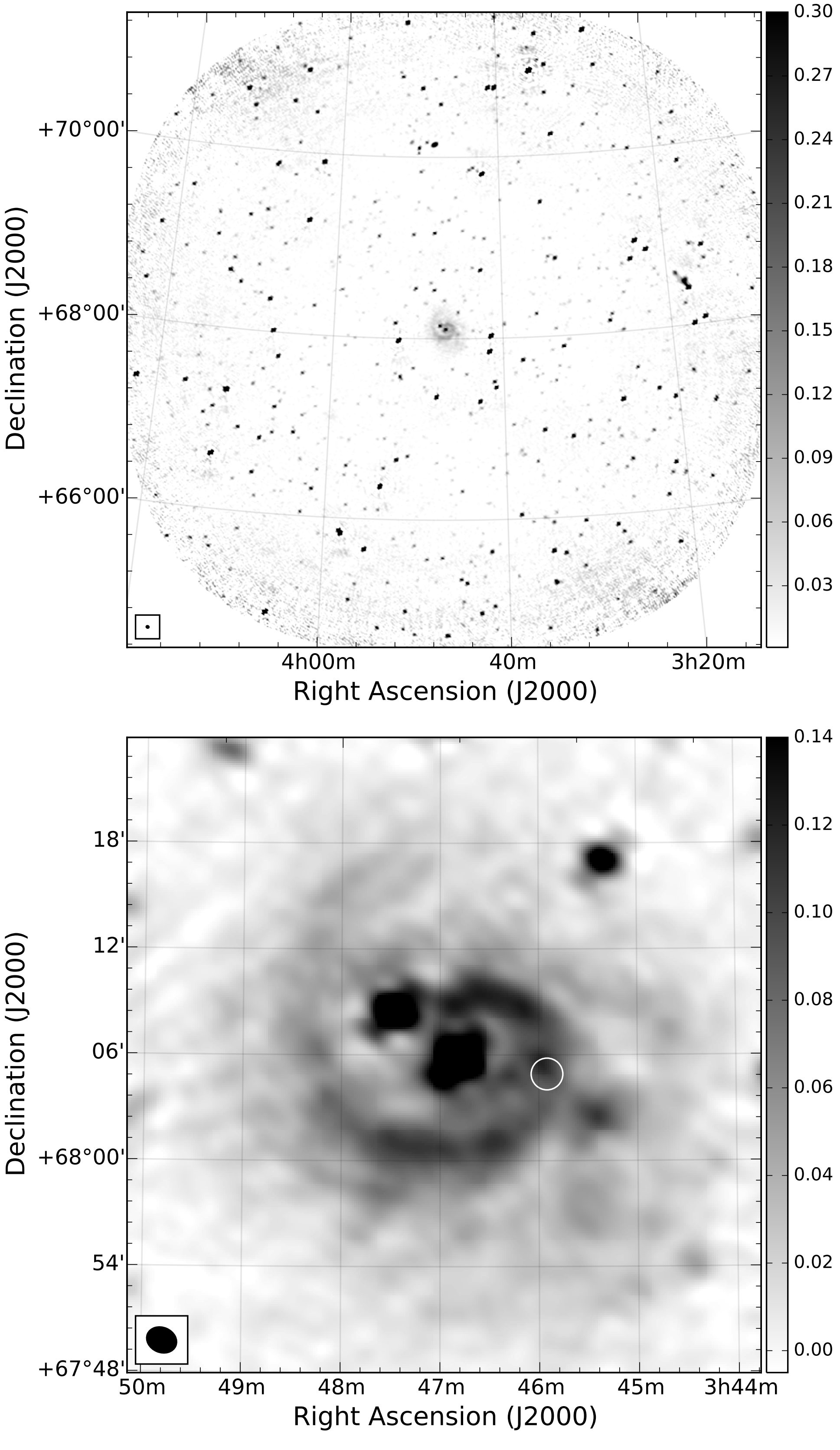

Fig. 2.13 This figure shows 3 hour long observation of the IC 342 field at the frequencies between 117 and 180 MHz, with the spiral galaxy clearly visible in the centre of the image (upper panel). In the lower panel, a closer view of the galaxy is shown, where the position of the known ultraluminous X-ray source IC 342 X-1 is marked with a white circle. The average noise level in the deep map is 3 mJy beam^{-1} and the resolution is 1.81×1.51 arcmin.

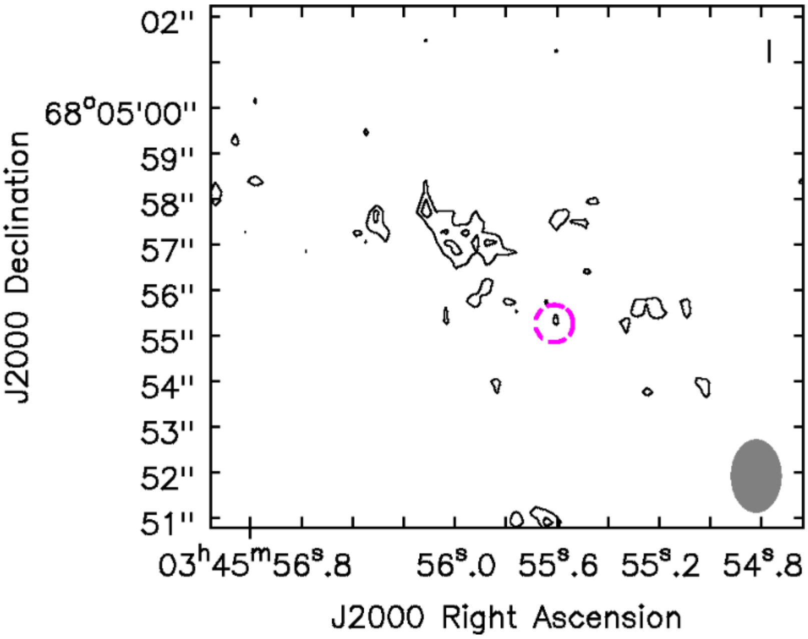

Fig. 2.14 This figure shows 5.5 GHz JVLA observations of ULX source IC 342 X-1 (Marlowe et al., 2014). No radio counterpart was found within the ULX region (marked with a pink circle) at the 3σ detection threshold (rms ≈ 5 µJy). Figure credit: Marlowe et al. (2014).

can be explained either by beamed radiation from the relativistic jet from the stellar mass black hole, or, emission from an intermediate-mass black hole. IC 342 X-1 is one of a few ULXs for which the radio counterpart was identified.

Previous attempts to detect the radio emission from the IC 342 X-1 central compact source placed upper limits on its flux density: observations with the Very Large Baseline Interferometry (VLBI) at 1.6 GHz showed no detections at the limit of ≈ 20 µJy (Cseh et al., 2012) and, no emission was found with JVLA at the 3σ detection threshold of 14 µJy at 5.5 GHz (Figure 2.14; Marlowe et al., 2014). However, Cseh et al. (2012) reported on the detection of a large radio nebula associated with IC 342 X-1. The observations, carried out with the VLA at 5 GHz, showed a nebula with a total flux density of 2 mJy and an estimated diameter of 225 pc (Figure 2.15). In comparison, the other known radio nebulae linked to the ULX objects, such as, for example, Holmberg II X-1 (Miller et al., 2005) or NGC 5408 X-1 (Kaaret et al., 2003) have much smaller diameters of 60 and 40 pc respectively,

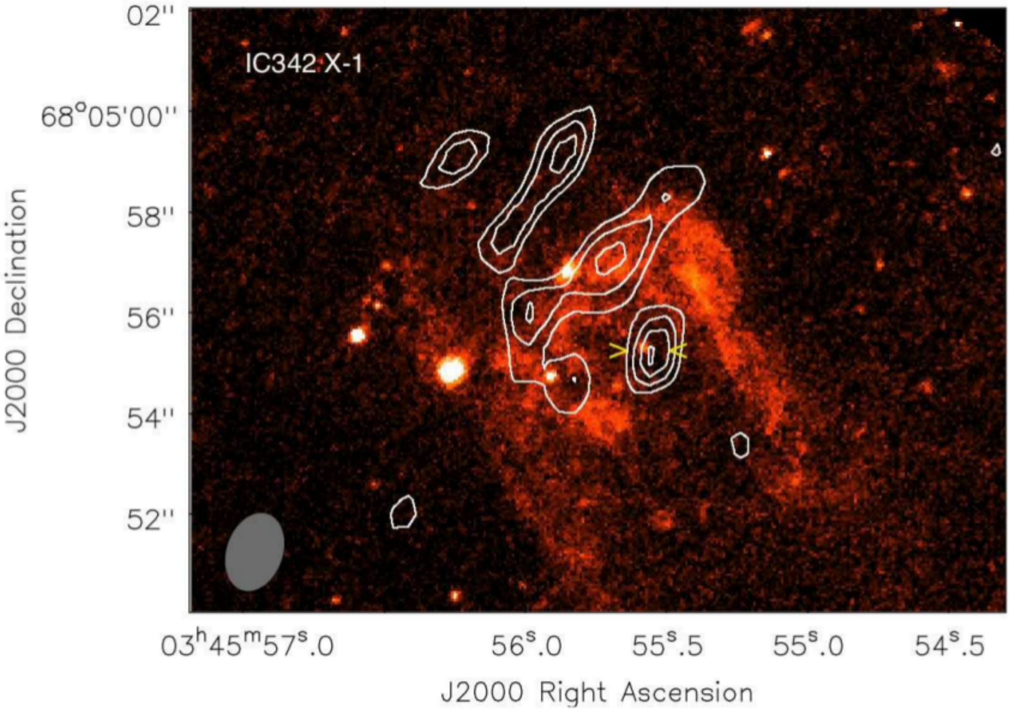

Fig. 2.15 VLA 5 GHz radio contours of the IC342 X-1 region overlaid with the Hubble Space Telescope image Cseh et al. (2012). The X-ray location of the ULX is marked with yellow arrows and the maximum flux density of the radio emission is ≈ 95 µJy. Figure credit: Cseh et al. (2012)

.

and, their estimated minimum energy required to produce the observed emission is an order of magnitude lower than that of IC 342 X-1. All of these sources are located in galaxies at the distance of ≈ 3–5 Mpc and show spectra consistent with optically thin synchrotron emission. On the other hand, a recently discovered ULX, found in VLA observations of M31 galaxy and described by Middleton et al. (2013) indicate an optically thick emission ($\alpha \approx 0.3$). Detection of a bright (≈ 340 µJy), unresolved source, displaying variability on time-scale of tens of minutes suggests that the emission originates from a compact object rather than extended nebula. Further analysis showed that the observations are consistent with the compact object being a stellar mass black hole.

It is clear that the resolution of the LOFAR map presented in the lower panel of Figure 2.13 (≈ 1.7 arcmin) is not sufficient to resolve individual sources in that region. In an attempt to

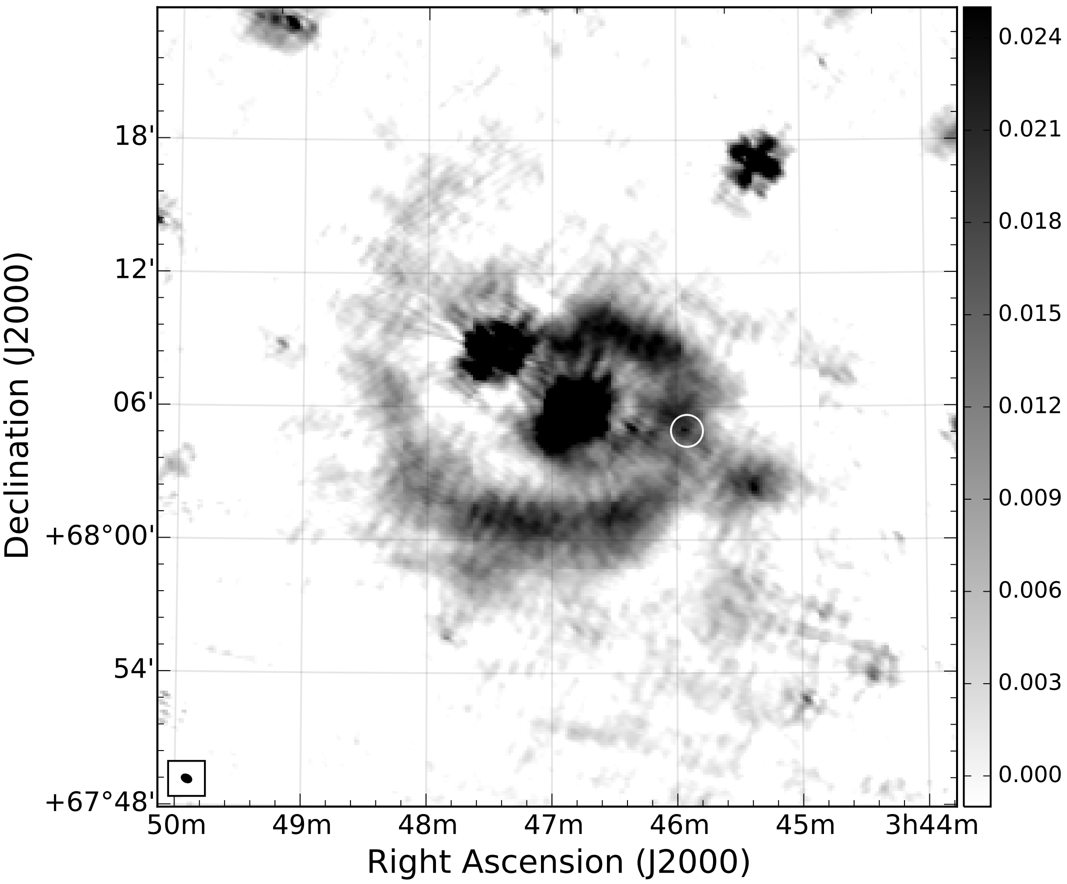

Fig. 2.16 A deep LOFAR map of the IC 342 galaxy, created with baselines ranging from 150 m up to 22 km, giving a resolution of 0.46 × 0.32 arcmin. A point source visible in the center of the white circle is a 5σ ($\approx$ 25 mJy) detection above the noise level and could be associated with the ultraluminous X-ray source IC 342 X-1.

increase the resolution, the range of included baselines was increased from 6 km to 22 km, excluding the shortest baselines (less than 150 m) in order to reduce the visibility of the extended emission. Figure 2.16 shows the higher resolution ($\approx$ 0.4 arcmin) deep LOFAR map of the IC 342 field, created using the extended range of baselines. In the middle of the white circle we detected a point source at 5σ above the noise level, with a peak flux density of $\approx$ 25 mJy. Comparing this result to the 2 mJy source at 5 GHz (Cseh et al., 2012) gives the estimated spectral index of the emitting region of -0.7, which makes the discussed detection likely to be associated with the IC 342 X-1. However, more extensive tests should be carried out in order to confirm whether this detection is real.

Chapter 3

Radio Sky Monitor Fast Transient Search

3.1 Introduction

3.1.1 LOFAR Radio Sky Monitor

The LOFAR Radio Sky Monitor (RSM) is one of the largest ever low frequency surveys dedicated to searching for radio transients (Fender et al., 2008a). During each observation LOFAR monitors the entire zenith strip (centered on the declination of +52:54:00), covering an area of approximately 1500 square degrees of the sky. In this chapter I describe the analysis of the RSM HBA observations carried out between February 2013 and April 2015 consisting of eight full zenith scans. Figure 3.1 shows an example image of a full RSM LOFAR HBA scan.

In the HBA, each scan of the zenith strip is formed by 48 pointings. Each of the pointings is formed by six, simultaneously observing, overlapping beams (Figure 3.2). The total observation time of 30 minutes per pointing is allocated between the calibrator and target in the following way: 2 minutes on the calibrator, 1 minute switch time, 11 minutes on

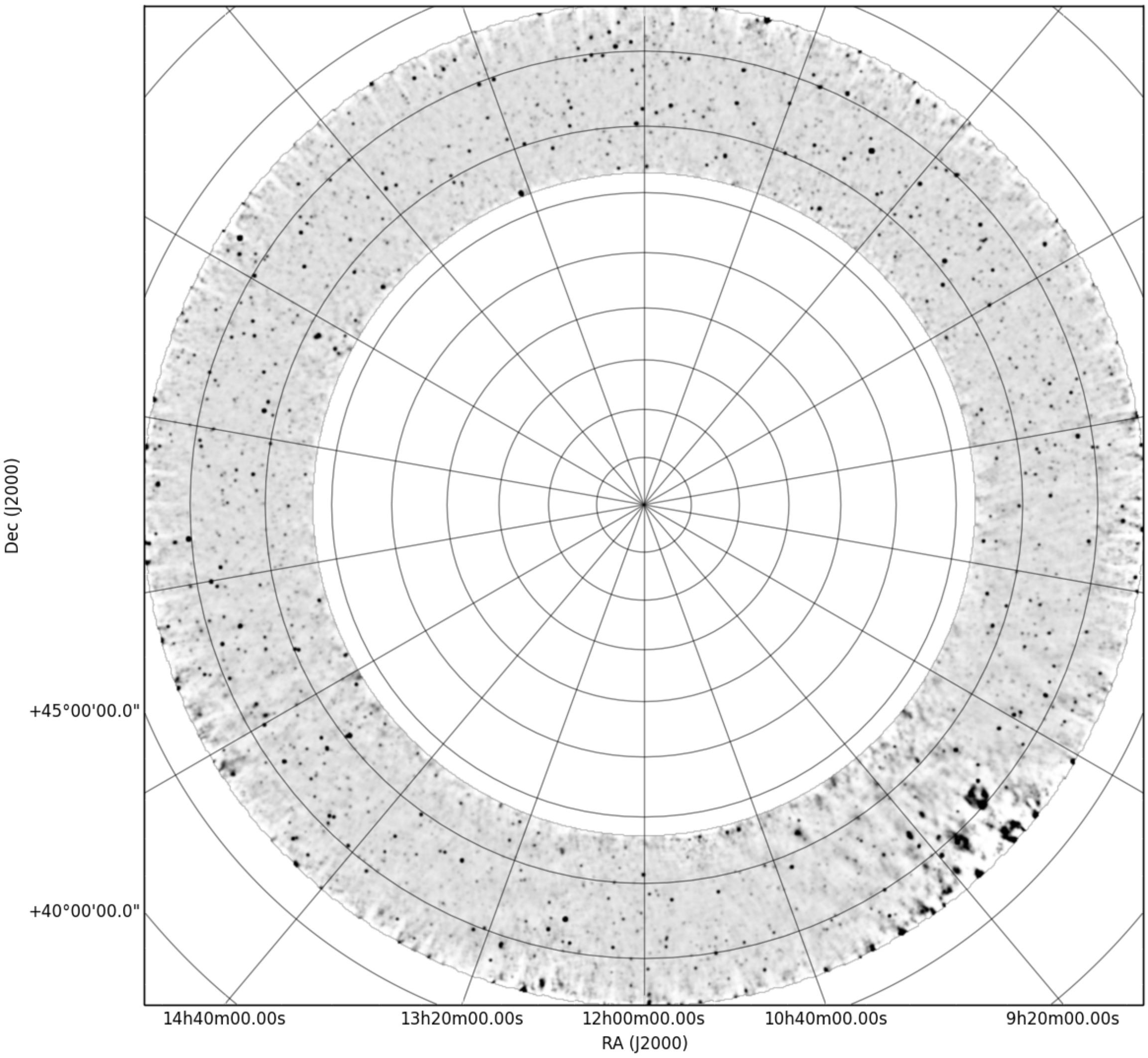

Fig. 3.1 The mosaic of the full Zenith strip observed by LOFAR HBA in February 2013, with the total field of view of ≈ 1500 deg^2. Declination is marked with concentric circles, with the two outer circles corresponding to $+40°00'.00.0''$ and $+45°00'.00.0''$ labelled on the vertical axis. Straight lines correspond to RA values, marked on the horizontal axis (image credit: Rene Breton).

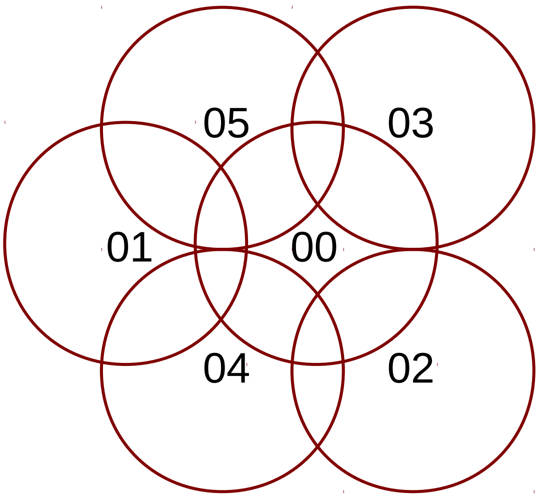

Fig. 3.2 Illustration showing a single pointing observation formed by six (00–05) overlapping beams, covering approximately 60 deg^2 of the sky.

the target, 1 minute switch time. This sequence is repeated twice for every pointing before moving on to the next one, which gives a total time of 22 minutes on the target. Each beam is formed by four frequency bands centered on 124, 149, 156 and 185 MHz. Each band consists of 10 sub-bands (240 total). The remaining four sub-bands not included in the monitoring of the Zenith strip are used to form an additional beam which is pointed at extra targets, for example M31 and LS I +63°303. Full details of the RSM HBA observations are summarized in Table 3.1.

3.1.2 Fast Radio Transients in Image Plane?

Radio transients originating from coherent processes are commonly found in high time resolution data rather than image plane (see Section 1.5.1). However, the recent independent re-discovery of the eclipsing pulsar J2215+5135 in the LOFAR RSM images (Broderick et al., 2016) showed that some of these types of objects are also likely to be found in images.

Table 3.1 Details of the RSM HBA observations.

Declination	+52:54:00.0 (dd:mm:ss)
Number of pointings	48
Number of beams per pointing	6
Total number of beams	288
Number of bands per beam	4
Central frequencies of the bands	124, 149, 156 and 185 MHz
Sub-bands per band	10
Channels per sub-band	64
Integration time	2 seconds
Compression in time	5 (10 seconds per time-step)
Compression in frequency	16 (4 channels per sub-band)
Total observing time per pointing	30 minutes
Calibrator observation	2 × 2 minutes
Target observation	2 × 11 minutes
Switch time	4 × 1 minute
Number of cycle 0 scans	6[1]
Number of cycle 1 scans	1
Number of cycle 2 scans	1
Number of cycle 3 scans	2

[1] Two of these observations were of poor quality and were excluded from the analysis.

The following example illustrates the variability of a bright radio pulsar captured in short time-scale imaging.

Figure 3.3 shows a single snapshot chosen from a set of 10 second images of one of the RSM HBA fields (map on the left side of the figure) in which a bright pulsar PSR B0329+54 is located (highlighted in a green frame). Along with the pulsar, a persistent field source (marked with a red frame) has been selected as a point of reference. A close up view of both sources is shown on the right hand side of the figure. The lower panel shows light-curves corresponding to both of the discussed sources, as measured across the set of 65 images, 10 seconds in duration each. Plotted in red is the light-curve of a steady field source, which shows that the flux calibration in the individual snapshots is stable, with a coefficient of variability value (defined as the ratio of the rms and the mean) of $\approx$ 10 per cent. Overplotted in green is the light-curve corresponding to the pulsar B0329+54, which clearly shows variability in the observed flux density (with a variability coefficient of $\approx$ 30 per cent).

Although this illustration shows that coherent radio variability can indeed be measured in the imaging data, it should be noted that (as discussed in Section 1.4) the propagation of short duration bursts is strongly affected by the ISM. In particular, for highly dispersed sources, the delay caused by the DM is so significant that the original signal can be recovered only by de-dispersing the data (Section 1.4.1). In those cases, the imaging technique in which the flux density is obtained simply by adding up the individual frequency components without correcting for the shift in their time of arrival, could reduce the observed amplitude below the detection threshold. On the other hand, if the duration τ of the event is dominated by scattering (Section 1.4.2) it will depend on the observing frequency ν as

$$\tau \propto \nu^{-4}. \tag{3.1}$$

Using this relation, we can extrapolate the time-scale of, for example, a 5 ms FRB observed at 1.4 GHz (Lorimer et al., 2007) to the 149 MHz of the BAND 01 (B01) of the RSM

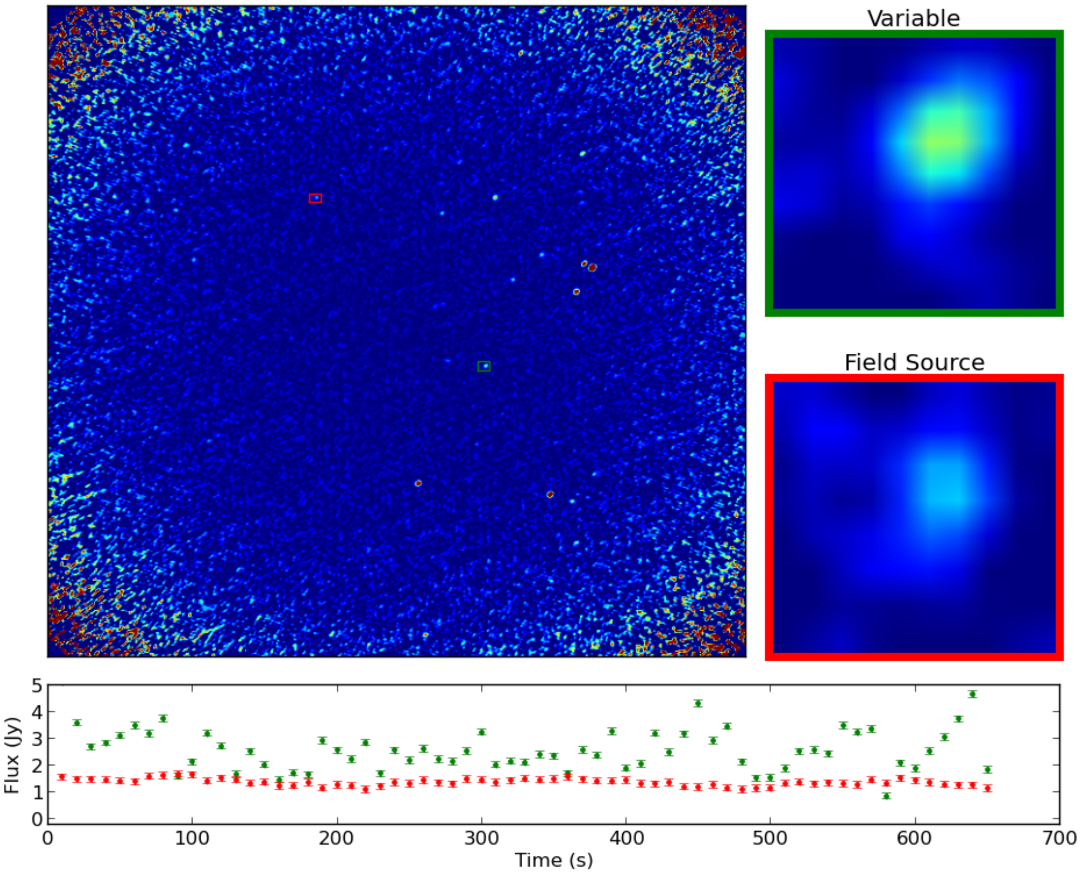

Fig. 3.3 An example of the variability of the pulsar (PSR B0329+54) measured in the RSM short time-scale images. In this 10 second snapshot the green frame marks the position of the discussed pulsar. The red frame shows a steady field source chosen as a reference point. The plot below shows the light-curves for both pulsar and the field source (green and red respectively) as observed across 65 × 10 second snapshots. The variability coefficient of the field source is 10 per cent and the variability coefficient of the PSR B0329+54 is 30 per cent (image credit: Tom Hassall).

LOFAR observations, which gives ≈ 40 seconds. This shows that the effect of scattering might significantly increase the duration of the signal and boost the probability of the image plane detection. Therefore, our ability of finding a fast radio transient in the image plane depends on the source being in a lucky direction of the sky, where the DM is low and the scattering is high. Figure 3.4 shows the scattering time ($\tau_{\rm s}$, solid lines) and dispersive delay ($\tau_{\rm DM}$, dashed lines) plotted as a function of frequency for a sample of fast radio bursts. These relations were obtained by extrapolating the 1 GHz measurements following Equations 1.1 and 1.3. The sample of presented sources includes all the FRBs for which the scattering times have been measured (Petroff et al., 2016). The shaded area represents the parameter space where the scattering time dominates over the dispersive delay. At the RSM B01 frequency of 149 MHz this corresponds to time-scales of 100 seconds and higher, which means that at those frequencies the variability from coherent events can be detected in images on a time-scale of tens of seconds. More detailed discussion of the possibility of detecting dispersed bursts in radio images can be found in Hassall et al. (2013).

3.1.3 This Work

The work presented in this chapter is focused on searching for short duration ($\sim$ tens of seconds) radio transients in the RSM field. This choice of time-scale was greatly motivated by the prospects of finding Fast Radio Bursts (FRBs; Thornton et al. 2013, Petroff et al. 2015) – the most widely discussed class of radio transients in recent years. With the large area of sky covered in the survey and the demonstrated ability of monitoring short time-scale variability in imaging data, the possibility of finding FRBs is worth exploring. Additionally, a broad frequency coverage of the survey offers an opportunity of a detailed spectral analysis of any potential candidates.

Considering the impact of the propagation effects on our ability to detect short duration outbursts in the image plane, we decided to focus our analysis on the observations performed

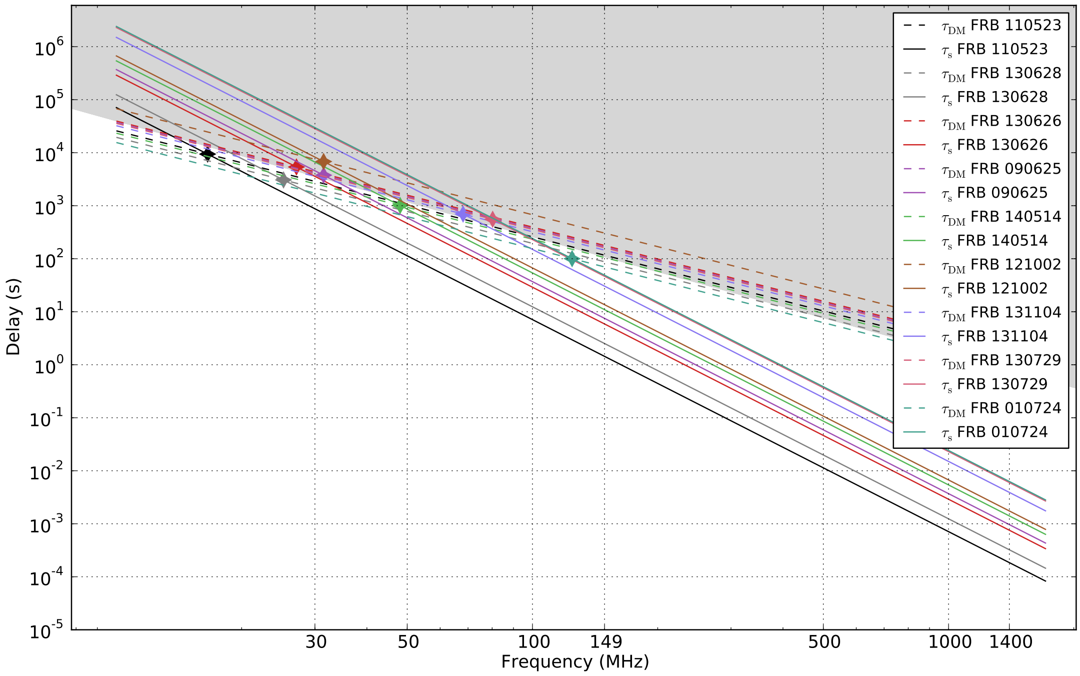

Fig. 3.4 The dispersive delay (dashed lines) and scattering times (solid lines) as a function of frequency for a number of FRB sources. The results were obtained by extrapolating the 1 GHz measurements (Petroff et al., 2016) following Equations 1.1 (dispersion) and 1.3 (scattering time). At higher frequencies the dispersive delay dominates, while at lower frequencies the scattering time is more significant, with the transition point marked with a star for each FRB. The grey region of the plot corresponds to the area where the scattering time is more significant than the dispersion time for at least one of the FRBs. The lower limit of that region is equal to the power law fit to the points marked with stars.

in the direction of the sky which is expected to have a low contribution from the Galactic DM. Details of selecting the relevant observations are summarised in the following section.

3.2 Data

Figure 3.5 shows the distribution of the Galactic DM, based on the Cordes-Lazio NE2001 model (Cordes and Lazio, 2002) of the free electron distribution in the Galaxy. The colour coding corresponds to the expected DM values (low – blue, high – yellow to red) along a given line of sight. The white circles represent pointings of a hypothetical survey designed to monitor low DM areas of the sky. Because the RSM survey covers the zenith strip centered at declination of +52:54:00, we can estimate that the best low DM regions of the sky fall between the RA values of 09:30:00–16:00:00. In RSM HBA these directions correspond to pointings 01–14. Therefore, the analysis discussed in this chapter is limited to those 14 out of 48 pointings in total, which gives a final field of view of ≈ 440 deg^2 . Detailed values of the dispersion measure estimated for the chosen lines of sight are listed in Table 3.2.

Because of the large size of short time-scale images, the initial search has been performed on a dataset limited from four bands (B00–B03) to single band observations. I chose the frequency of 149 MHz (corresponding to B01) due to the highest sensitivity in this band. The full bandwidth data of a given observation were imaged only if a transient candidate had been identified in the respective measurement set. Finally, due to the poor quality of the data, two out of six observations carried out during cycle 0 have been excluded from further analysis. A list of all the RSM HBA runs used in the analysis, together with the start and end times of the observations of the included pointings can be found in Table 3.3.

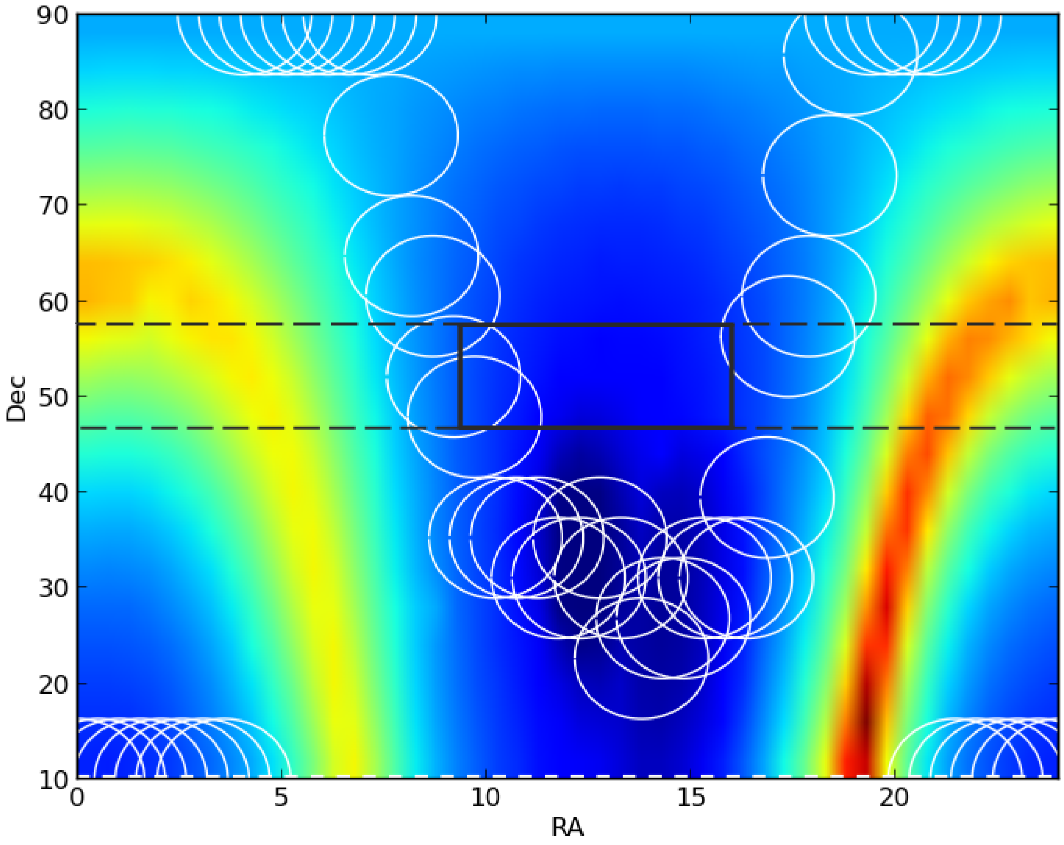

Fig. 3.5 Distribution of the DM in the sky plotted based on the Cordes-Lazio NE2001 model. Coloured with blue are the regions in the sky corresponding to low DM values, while yellow and red indicate directions with progressively higher DM. For the RSM survey, centered at the declination of +52:54:00, the lowest values of dispersion measure fall between the RA of 09:30:00 and 16:00:00. The low DM region of the sky for the RSM survey is marked with the grey box (solid lines). The dashed grey lines together with horizontal solid lines show the range of the declination values for the entire RSM survey. Circles mark the positions of the pointings for a hypothetical survey aiming at monitoring low DM directions of the sky (image credit: Tom Hassall).

Table 3.2 List of the RA coordinates for the central beam (beam 00), together with calibrators used, for each of the analysed pointings. Declination for the central beam in every pointing is +52:54:00.0. The dispersion measure values have been estimated according to the Cordes-Lazio NE2001 model (Cordes and Lazio, 2002), integrated up to distance of 30 kpc.

Pointing	RA (h:m:s)	DM[1](cm pc^{-3})	Calibrator
01	09:30:00.00	39.96	3C 196
02	10:00:00.00	37.36	3C 196
03	10:30:00.00	35.14	3C 196
04	11:00:00.00	33.39	3C 196
05	11:30:00.00	31.84	3C 295
06	12:00:00.00	30.55	3C 295
07	12:30:00.00	29.94	3C 295
08	13:00:00.00	30.00	3C 295
09	13:30:00.00	30.34	3C 295
10	14:00:00.00	30.55	3C 295
11	14:30:00.00	31.26	3C 295
12	15:00:00.00	32.24	3C 295
13	15:30:00.00	33.72	3C 295
14	16:00:00.00	35.28	3C 295

[1] DM values have been estimated using the software available at: http://www.nrl.navy.mil/rsd/RORF/ne2001/index.html.

Table 3.3 Summary of the RSM observations used in the short time-scale transient search. All of the listed observations have been limited to low DM pointings (1–14) corresponding to RA range of 09:30:00–16:00:00. Cycle refers to the LOFAR science cycle in which the observation took place.

Cycle	Observation	Pointings (UTC)	Start time (UTC)	End time
0	Feb 10–11 2013	03 – 14	00:30:07	06:26:07
		01 – 02	23:30:07	00:26:07
0	Mar 10–11 2013	07 – 14	00:38:01	04:34:02
		01 – 06	21:38:02	00:34:02
0	Mar 24–25 2013	08 – 14	00:11:54	03:37:54
		01 – 07	20:41:54	00:07:54
0	Jul 13 2013	01 – 14	13:22:22	20:18:22
1	Jan 15–16 2014	11 – 14	06:09:59	08:06:03
		01 – 10	01:09:59	06:06:03
2	Jul 23 2014	01 – 14	12:45:48	19:41:48
3	Mar 11–12 2015	01 – 14	21:33:08	04:29:09
3	Apr 10–11 2015	01 – 14	19:35:26	02:31:26

3.3 Processing

The work presented in this chapter was done using calibrated data and did not include the processing itself, which was done by Adam Stewart (University of Oxford). The main steps of processing are described in this section for a reference.

Processing was done in two major blocks: the pre-processing and the calibration. The standard pre-processing of the data was done by the observatory. The initial flagging of RFI was done with the AOFLAGGER. The original data, recorded with a 2 second integration time and 64 channels per sub-band, was averaged by factor of 5 in time (resulting in the integration time of 10 second per time-step) and 16 in frequency (which gives 48 kHz frequency channels; 4 channels per sub-band). Additionally, for targets less than 20 degrees away from Cyg A and/or Cas A, demixing was applied.

In the HBA, observations of the target fields and the respective calibrator source are not simultaneous. The calibrator is observed for 2 minutes before LOFAR switches to monitor the target. The list of calibrators used for the analysed pointings can be found in Table 3.2. Following the calibration of the calibrator source, the resultant gain amplitudes were transferred to the visibilities of the target field. For each snapshot, the individual sub-bands were concatenated into their respective band measurement sets. After the sub-bands were combined, a phase-only calibration of the target fields was performed. The sky model used in this step was created with GSM (Section 2.2.2) based on the VLSS catalogue and included ≈ 250 sources with a flux density above 0.1 Jy, found within 5 degrees from the center of the field (as there were six beams, six different models were constructed for each pointing).

The final calibrated data used in this analysis consist of the following measurement sets. For two, single-band, 11 minute observations of a single pointing, there are 2×6 measurement sets – one for each beam forming the pointing. For eight zenith scans this gives 96 measurement sets per pointing, and, 1344 in total for the whole analysed area of the sky.

3.4 Deep Images

For every individual pointing (i.e. the area of the sky), a deep map was created, which provided a catalogue of sources used as a point of reference in the transient search. Every transient candidate found in the short time-scale images was compared against this catalogue, which helped to decrease the number of false detections. The deep images were made by imaging the 11 minute single-band measurement sets and creating the mosaic formed by six overlapping beams.

3.5 Short Time-scale Imaging

Taking into account all the aspects discussed in Section 3.1.2 we decided to image the low DM observations of the RSM on a time-scale of 30 seconds. This choice provided a reasonable balance between keeping the rms level relatively low and increasing chances of finding fast radio transients.

To obtain 30 seconds images each of the 11 minute observations is split into 21 $\times$ 30 seconds measurement sets. These 30 second measurement sets of the individual beams are then imaged and combined into a mosaic representing single, short time-scale snapshot of the entire pointing. The total field of view of the final single epoch map is ≈ 60 deg^2, with the rms value of about 50 mJy and the number of visible sources of up to ≈ 70 (example 30 second images are shown in Figure 3.6). A complete AWIMAGER parset including the parameters used in creating 30 seconds images was created with help from Jess Broderick (ASTRON) and can be found in Appendix A.

The following section describes the process of searching for transient and variable sources in the discussed observations.

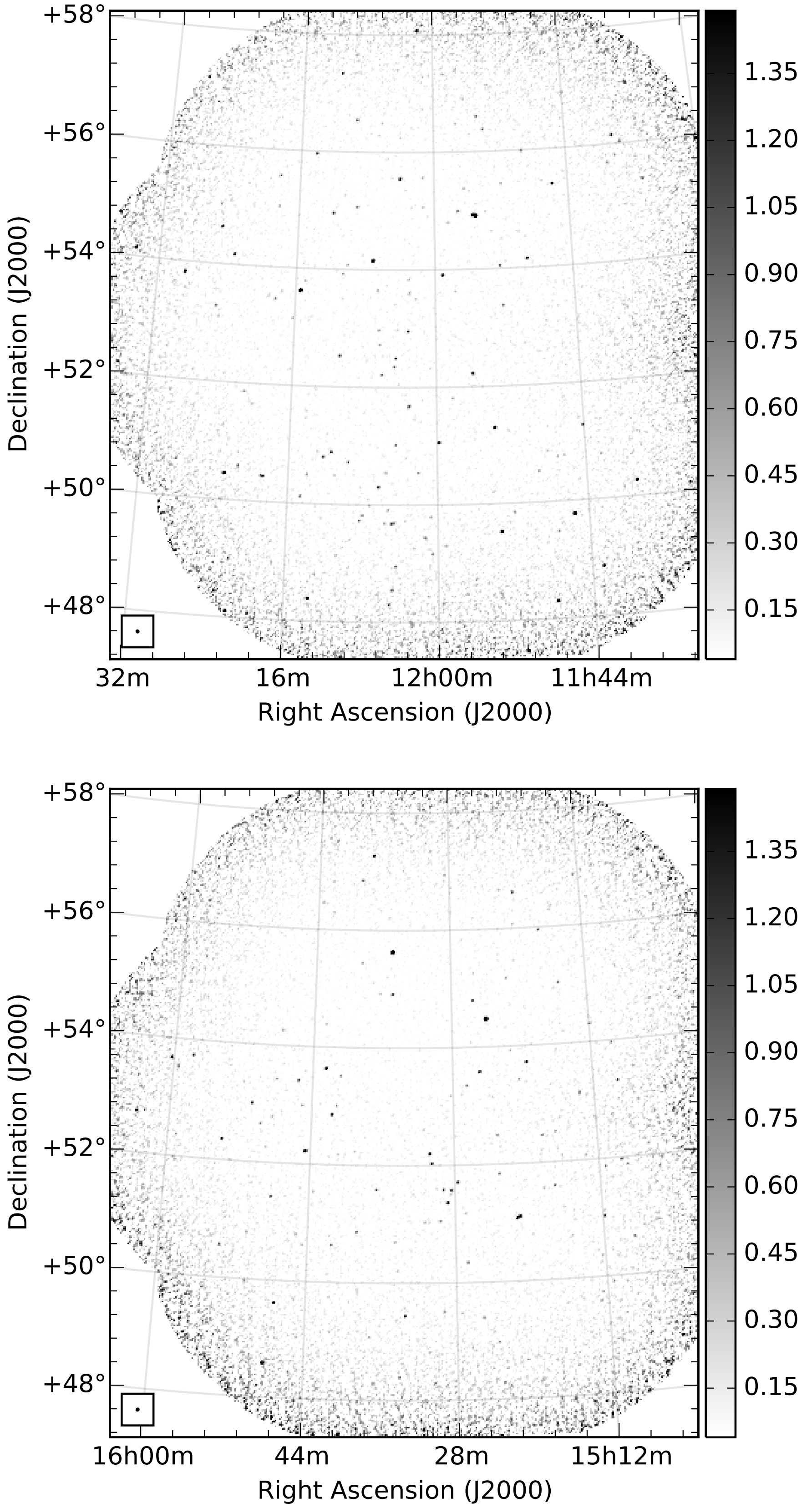

Fig. 3.6 Examples of 30 second RSM HBA images. Both of the images show a low DM field observed at the frequency of 149 MHz. *Upper*: The first RSM run (Feb 10 2013), Pointing 06, time window 17, rms at the center of the image ≈ 45 mJy. *Lower*: Cycle 3 RSM run (Mar 11 2015), Pointing 13, time window 14, rms at the center of the image ≈ 40 mJy. Each image is a six-beam mosaic created using the pattern illustrated in Figure 3.2.

3.6 Transient Search

3.6.1 Transients Pipeline

The Transients Pipeline (TraP) is software developed by the LOFAR TKP, designed to search for transient sources in image plane data. In the most general view, the TraP creates a database of sources extracted from the provided radio images and selects potential transient candidates based on the properties of their light-curves. This section gives a brief overview of the software properties – detailed description of the TraP can be found in Swinbank et al. (2015).

Firstly, all images processed by TraP have to pass the Quality Control step (QC, discussed in more detail in Section 3.6.2), which checks them against the criteria describing whether the quality of the maps is sufficient for further analysis. The extraction of sources from the maps which passed the QC step is done with PYSE – a source extractor developed specifically for TraP (Spreeuw 2010; Carbone et al. in prep). Two user-defined parameters control how deep the analysis is performed: an island threshold (also called an analysis threshold) and a detection threshold. The analysis threshold specifies the region in which the source fitting is performed, i.e. sets the flux density level above which the sources are extracted from the image. The detection parameter sets the peak flux density value above which sources are considered in further analysis. An additional option allows the user to set a different flux density threshold for the detection of new sources to reduce the amount of selected transient candidates in lower quality images to a more manageable number. Additionally, TraP allows to constrain the area of the map considered in the analysis. Due to the increased noise level and poor flux calibration towards the edges of the image, extracting sources from the outer parts of the map would increase the number of false detections. By limiting the extraction radius these outer regions can be eliminated which makes the detections more reliable.

The flux density measurement taken for every detection in a given snapshot is compared against the previous measurements taken at this location, which allows a light-curve to be generated for each of the extracted sources. In cases where there were no previous detections at a given location, the source is flagged as a potential transient candidate and monitored in all the following epochs. Two parameters characterising the variability of every detected source are calculated based on the light-curve recorded to date. The coefficient of variation, V_ν, which describes the level of variability of the light-curve, and the significance of the flux density variability, η_ν, which is based on the χ^2 calculation and describes how well the light-curve is modelled by a constant value. V_ν is defined as

$$V_\nu = \frac{1}{\overline{I_\nu}} \sqrt{\frac{n}{n-1}\left(\overline{I_\nu^2} - \overline{I_\nu}^2\right)}, \tag{3.2}$$

where $\overline{I}$ is the mean flux density of the sample and n is the number of flux density measurements. The significance of the flux density variability is defined as

$$\eta_\nu = \frac{n}{n-1}\left(\overline{\omega I_\nu^2} - \frac{\overline{\omega I_\nu}^2}{\overline{\omega}}\right), \tag{3.3}$$

where ω is a weight of a flux density measurement defined as a function of the error of a flux density measurement σ_{I_ν}: $\omega = 1/\sigma_{I_\nu}^2$. The following section describes the details of the TraP setup used in the analysis of the RSM data.

3.6.2 Running TraP

Quality Control

Before the images can be run through the TraP and searched for the transient candidates, we need to separate the good quality maps from those with high rms. In order to exclude images with a low signal to noise ratio, without having to look at every snapshot individually, I use

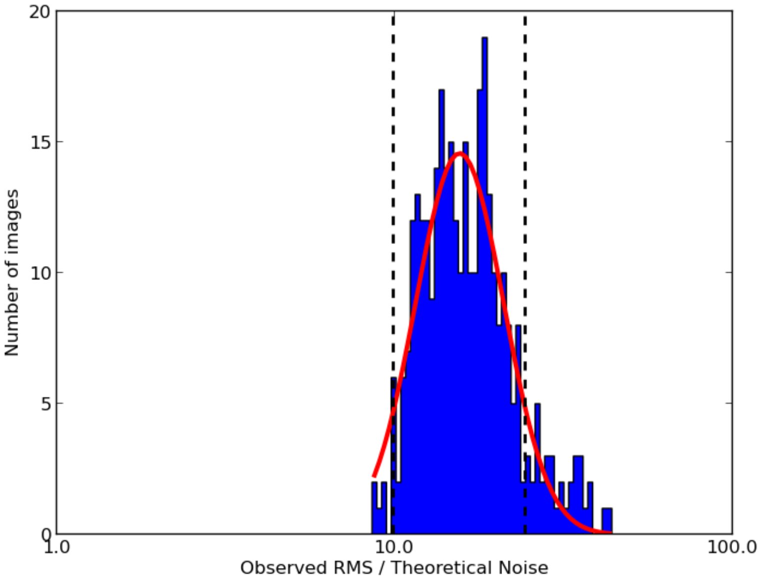

Fig. 3.7 Example diagnostic plot produced by the QC script, showing the distribution of the measured-to-theoretical noise ratio across the 30 second images, for pointing 10. The red line shows the Gaussian distribution fit to the data, while dashed black lines mark the 1.5σ cut off region, outside of which the images are rejected.

the Quality Control tool (QC) developed by Antonia Rowlinson (University of Amsterdam)[1]. The quality control method is based on the measurement of the parameter describing the ratio of the measured to theoretical noise

$$\beta = \frac{\text{Observed rms}}{\text{Theoretical noise}}. \tag{3.4}$$

Calculating this ratio for every image in the sample allows to fit Gaussian function to the distribution of the obtained values of β (example shown in Figure 3.7). Based on that result, we can define the minimum/maximum values of the measured-to-theoretical noise ratio, below/above which the images will be rejected. The default value for LOFAR images is 2σ, where σ is standard deviation of the Gaussian distribution. However, in this case a slightly lower limit of 1.5σ was set, as the tests done with the 2σ cut off showed too many noisy

---

[1] Details of the QC script can be found at
https://github.com/transientskp/scripts/tree/master/TraP_QC_diagnostics

images have passed the quality control stage. The entire sample of images to be analysed is run through the TraP in smaller sets, corresponding to individual pointings. Therefore, the QC script is also run on a sample of images for one pointing at the time.

An example parset file with the TraP settings used in the analysis can be found in Appendix A.

Setting TraP Parameters

Having defined the bad quality images that will be rejected, the short time-scale maps are ready to be analysed by the TraP. As mentioned above, I have divided the sample of images into 14 sets, each corresponding to a single pointing/area of the sky. Initially, I attempted to analyse single beam images rather than the mosaic of the full pointing. However, because the fields of view for single beams overlap strongly, the output of the TraP would often create multiple light-curves for sources in overlapping regions. Additionally, because the location of the same source varies across the images in different beams, in relation to the center of the map, measured flux density would often be slightly different depending on which beam the source was detected in. For this reason, the analysis was performed on the 30 second mosaics of single beams for all the images instead.

I have used the PYBDSM source extraction software to evaluate the size of the box for the rms level estimation at different parts of the image (PYBDSM automatically finds optimal rms box settings for a given image). Several values of the detection and analysis thresholds for source extraction were tested and finally set to 10 and 5 sigma respectively. With those parameters, the number of transient candidates selected by TraP was manageable, yet the inspection of the results by eye showed that all obvious sources in the field have been recognised by the software. Due to the increase of the noise closer to the edge of the image, I have constrained the source extraction area to the circle with a radius of 4.5 deg from the center of the image, which effectively excluded the most noisy regions of images from further analysis.

Due to the rms in short time-scale images being higher compared to the deep images, the number of detected sources might not only be smaller, but also vary depending on the quality of a single snapshot. This means that a faint source which was not picked up in the first, but was detected in any of the following snapshots, could be classified as a potential transient candidate. In order to avoid such false positive detections, the first image run through the TraP for every pointing is the deep map of the field (Section 3.4). This 'catalogue' becomes a point of reference for all the next short time-scale snapshots, where every potential candidate can be associated with a possible counterpart in the respective deep image, and classified either as a new, or, previously known source.

3.6.3 Estimating Expected RSM Transients Rate

The first radio transient found by LOFAR has been detected in 400 hours of monitoring of the North Celestial Pole (NCP) and reported by Stewart et al. (2016). These observations have been carried out as part of the MSSS survey (Chapter 2, Section 2.2), where a single sub-band centered at the frequency of 60 MHz has been pointed at the NCP during each MSSS run. While the nature of the NCP transient has not been confirmed, the two possible origins discussed by Stewart et al. (2016) include a flare star and an FRB. In the following analysis I use the NCP detection as an indication of the number of transient candidates expected to be found in the RSM search. One of the reasons for extrapolating the NCP result to this work is the potential origin of the source. If we consider the case where the time-scale of the NCP transient (which was found in an 11 minute snapshot, with the upper limit of the duration of 15 minutes) was dominated by scattering, we can use the Equation 3.1 to scale this result up to the frequency of 149 MHz. This gives an estimated time-scale of $\approx$ 25 seconds, which makes the 30 second RSM images potentially sensitive to finding NCP-like events.

Number of the 30 Second RSM Epochs

In order to extrapolate the NCP transient search results to the analysis of RSM data, we need to compare the sensitivity, frequency, field of view and number of epochs for both surveys. The RSM data sample consists of 8 observations of the zenith strip. For every pointing, there are two 11 minute snapshots within each observation, and, 14 out of 48 pointings are used in total. Imaging every 11 minute snapshot on a 30 second time-scale gives 21 images (due to a small time shift in between measurement sets we get 21 instead of 22). This gives the final number of 30 second images of

$$N_{\text{total}} = 14(\text{pointings}) \times 8(\text{runs}) \times 2(11\text{min}) \times 21(30\text{s}) = 4704. \tag{3.5}$$

In the ideal case, this means that for every considered pointing we have 336 snapshots, each of them 30 seconds in duration. However, due to the quality control step (Section 3.6.2), the total number of images was reduced to 3553. As a result, the actual number of 30 second epochs within each pointing is ≈ 253. Table 3.4 provides a summary of the short time-scale RSM images.

Extrapolating the Expected Rates from the NCP Transient to RSM Survey

Having estimated the number of 30 second RSM epochs, we can now summarise the properties of the NCP and RSM images (Table 3.5). By comparing those parameters we can estimate the number of NCP type transient candidates expected to be found in the RSM data (N_{RSM}), based on the NCP detection. The nature of the NCP survey means that there is no spectral information about the source found in the data. In order to simplify calculations, I start with the case of the spectral index $\alpha = 0$. In other words, I assume that the flux density of the source will not change with the observing frequency (NCP vs RSM). We can

Table 3.4 Details of the RSM HBA 30 second mosaiced (6 beams) images.

Snapshots per pointing per observation	2 × 11 min
Number of 30 second images within 11 minute snapshot	21
Number of RSM runs	8
Number of pointings	14
Total number of images	4704
Number of QC rejected images	1151
Total number of accepted images	3553

Table 3.5 A summary of the parameters of the images from the RSM and NCP surveys. The left column contains details of the 11 minute images of the NCP field, in which the first LOFAR transient candidate has been detected. In the right column are corresponding parameters of the 30 seconds RSM images.

Survey	NCP	RSM
Frequency (MHz)	60	149
Image time-scale	11 min	30 s
rms (Jy)	0.79	0.05
Detection threshold	10 σ	10 σ
FoV (deg^2)	175	440
Number of epochs	1897	253

estimate the N_{RSM} by comparing the field of view and number of epochs for both surveys, and correcting for their respective sensitivities

$$N_{\mathrm{RSM},\,\alpha=0} = N_{\mathrm{NCP}} \times \frac{\mathrm{FoV}_{\mathrm{RSM}} \times \mathrm{Epochs}_{\mathrm{RSM}}}{\mathrm{FoV}_{\mathrm{NCP}} \times \mathrm{Epochs}_{\mathrm{NCP}}} \times \left(\frac{S_{\mathrm{RSM}}}{S_{\mathrm{NCP}}}\right)^{-3/2}, \tag{3.6}$$

where N_{NCP}=1 is the NCP transient; $\mathrm{S}_{\mathrm{RSM}}$ = 0.5 Jy and $\mathrm{S}_{\mathrm{NCP}}$ = 7.9 Jy are the detection thresholds set in the analysis for the RSM and NCP fields respectively. This gives the expected number of $\approx$ 21 transient sources to be found in the set of 3553 RSM images. However, if we consider the spectral index α of the source different than 0, Equation 3.6

Table 3.6 Correction factor f for the expected number of RSM field NCP-like transients calculated for different values of the spectral index and the corresponding number of expected candidates found in the RSM N_{RSM}.

α	f	N_{RSM}
-3	0.017	0.35
-2	0.065	1.4
-1	0.255	5.4
0	1	21
1	3.913	82
2	15.314	322
3	59.932	1262

needs to be corrected for the factor f, which takes into account changes in the measured flux density of the source with the observing frequency

$$f = \left(\left(\frac{\nu_{\mathrm{NCP}}}{\nu_{\mathrm{RSM}}} \right)^{\alpha} \right)^{-3/2}, \tag{3.7}$$

where ν_{NCP}, ν_{RSM} are the frequencies of the surveys. Including this correction, we can calculate the rate of RSM transients depending on the spectral index α

$$N_{\mathrm{RSM}} = N_{\mathrm{RSM},\,\alpha=0} \times f. \tag{3.8}$$

Table 3.6 lists several values of the factor f calculated for a range of spectral indices, together with the corresponding expected transient rates for the analysed RSM data.

The next section gives an overview of the transients selected by TraP and a more detailed analysis of several of the strongest candidates.

3.7 Results

3.7.1 Overview of Candidates Selected by TraP

Overall, from the 14 pointings ($\approx$ 253 epochs each), 121 sources were flagged by TraP as new events. An initial manual inspection of those candidates showed that the majority of them were in fact the result of association errors. This means that the sources in question had been previously detected by the TraP in earlier epochs, but the correct association with those detections had not been properly made, hence the sources were flagged as 'new'. In several cases false detections were caused by the structured noise in bad quality images. This initial investigation allowed us to reject most of the candidates, leaving 13 sources which could not be immediately disproved.

Up to this point, due to the large volume of the short time-scale images data, the search was focused on single band (149 MHz) observations. However, for the selected transient candidates, the remaining bands centered at 124, 156 and 185 MHz were also imaged (as described in Section 3.5). Imaging the lowest band in most cases produced noisy, bad quality maps which had to be excluded from the analysis. Images of the higher frequency bands (156 and 185 MHz) showed no detections at the location of any of the 13 candidates, which puts the limit on their spectral indices of $\approx$ -35. This result eliminates the intrinsic variability as the origin of the observed emission. The remaining explanations include extreme scattering events (Section 1.5.2) which often show strong spectral variability, or, RFI and imaging related artefacts. In the first case, the extrinsic variability is caused by propagation of the emission from a compact object through the turbulent ISM. This means that – usually – we expect to see a background source from which the radiation originates, which was not the case for any of the detected candidates. However, it is possible that the background source is very faint and brightens significantly only when magnified by the ISM, therefore we can not exclude this scenario. On the other hand, it is not unlikely that some (or all) of the candidates were artificially created during the processing rather than linked to astrophysical sources. Taking it all into account it is necessary to perform further tests, verifying whether the discussed detections are real.

Stewart et al. (2016) describe a number of different methods which can help to determine whether the radio source detected in the image plane is real. Based on their approach I have performed the following tests:

- Using an automated tool to remove bad LOFAR stations from the observations.
- Running additional RFI flagging with AOFLAGGER.
- Subtracting bright sources from the visibilities using the sky model and re-imaging the visibilities. The sky model was based on sources extracted from the 11 minute snapshot corresponding to the detection of a given transient candidate. The extraction was done using PYBDSM software.
- Splitting the full bandwidth and imaging narrow frequency bands individually.
- Imaging the data using different weighting schemes.

Based on the properties of the 13 candidates, such as, for example, detection in multiple beams and/or epochs, I chose the three most interesting and potentially real sources. If the location of the candidate is common to multiple RSM beams, and, the source is visible in more than one, it is more likely to be a real detection. These three candidates were then further checked against the tests listed above. It should be noted that all three sources remained unaffected by the first test – no bad stations have been found for any of the analysed datasets. Details of the selected sources as well as the results of the validity checks are discussed in the following sections. The ID numbers of the transient candidates (#1644, #668 and #1190) correspond to the IDs they were assigned by the TraP when flagged as new events. The verification tests described in the following sections were done with help from Adam Stewart (University of Oxford).

3.7.2 Transient Candidate #1644

The candidate #1644 was detected in two individual RSM epochs of the Pointing 08 observations, separated by 11 months. In the first epoch (Feb 10, 2013) the peak and integrated flux density of the detection are 1.21 ± 0.11 Jy and 1.22 ± 0.2 Jy respectively. The source then disappeared and was detected again only in the fifth analysed zenith scan (Jan 16, 2014) at the level of 1.47 ± 0.15 Jy (peak flux) and 1.48 ± 0.26 Jy (integrated flux). The source does not appear in the deep RSM map or the catalogues of previous radio surveys such as the Very Large Array Low-frequency Sky Survey Redux (VLSSr; Lane et al., 2014) and WENSS. The upper panel in Figure 3.8 shows the 149 MHz light-curve of the source monitored between February 10, 2013 and July 23, 2014. In the lower panel, the 149, 156 and 185 MHz light-curve of the same source is shown across the two epochs in which it was detected. The upper panel in Figure 3.9 shows the snapshot of the original (February) detection, and the epoch immediately following it. The lower panel in Figure 3.9 shows the snapshot prior to the second (January) detection, and the following epoch where the source reappears.

Although #1644 was found in the region of the mosaic where the beams are not overlapping, its recurrence in observation carried out nearly a year later made it interesting. The following analysis was focused on testing the two observations in which the source was found.

Additional RFI flagging and Sky Model Subtraction

I have run an additional round of AOFLAGGER on the calibrated 11 minute measurement set. The data was then imaged in the same way as originally (Section 3.5). The final images of the time-steps in which #1644 was previously detected showed that flagging removed the source in both epochs, indicating that the detection was an RFI related artefact. Additionally, I have tested subtracting the brightest source in the field from the visibilities prior to imaging. This also resulted in the #1644 candidate disappearing from the respective detection epochs. Figure 3.10 shows the Feb 2013 detection snapshot of the transient candidate (marked ’T’)

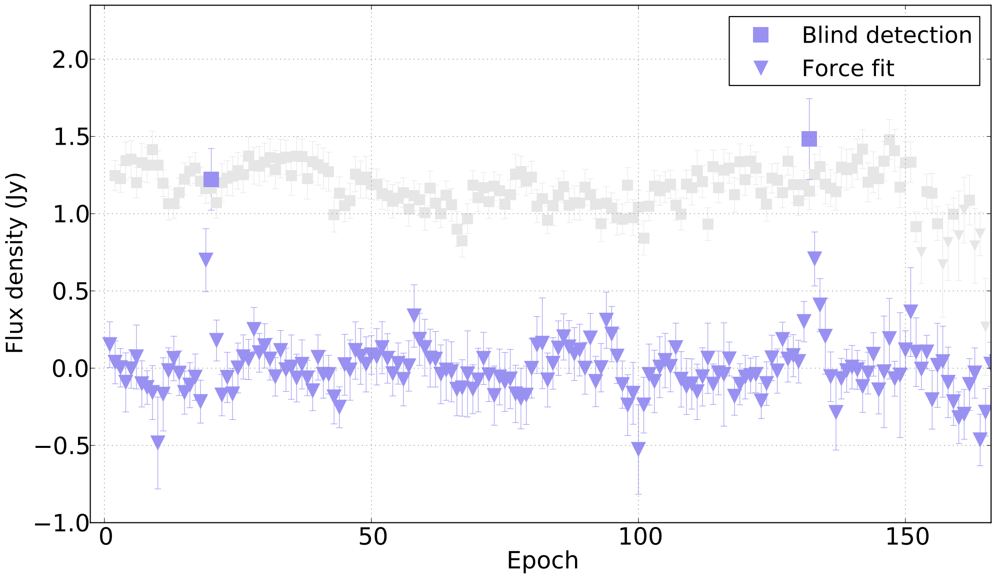

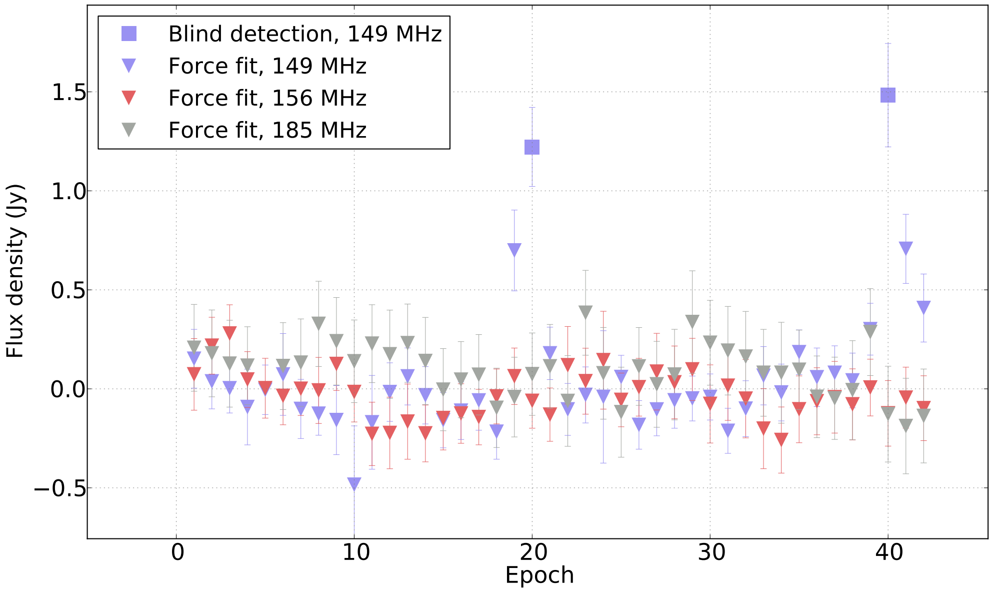

Fig. 3.8 *Upper*: The 149 MHz light-curve of the transient candidate #1644 covering observations from February 2013 to July 2014 (the last two zenith scans are not included to make the light-curve clearer). Marked with squares are data points corresponding to TraP detections (above 10σ limit), while triangles correspond to forced extractions at the position of the source. Overplotted in grey is the light-curve of a steady field source shown for comparison. *Lower*: The same light-curve limited to two epochs in which the candidate was detected with additional measurements at 156 and 185 MHz, in which there are no detections.

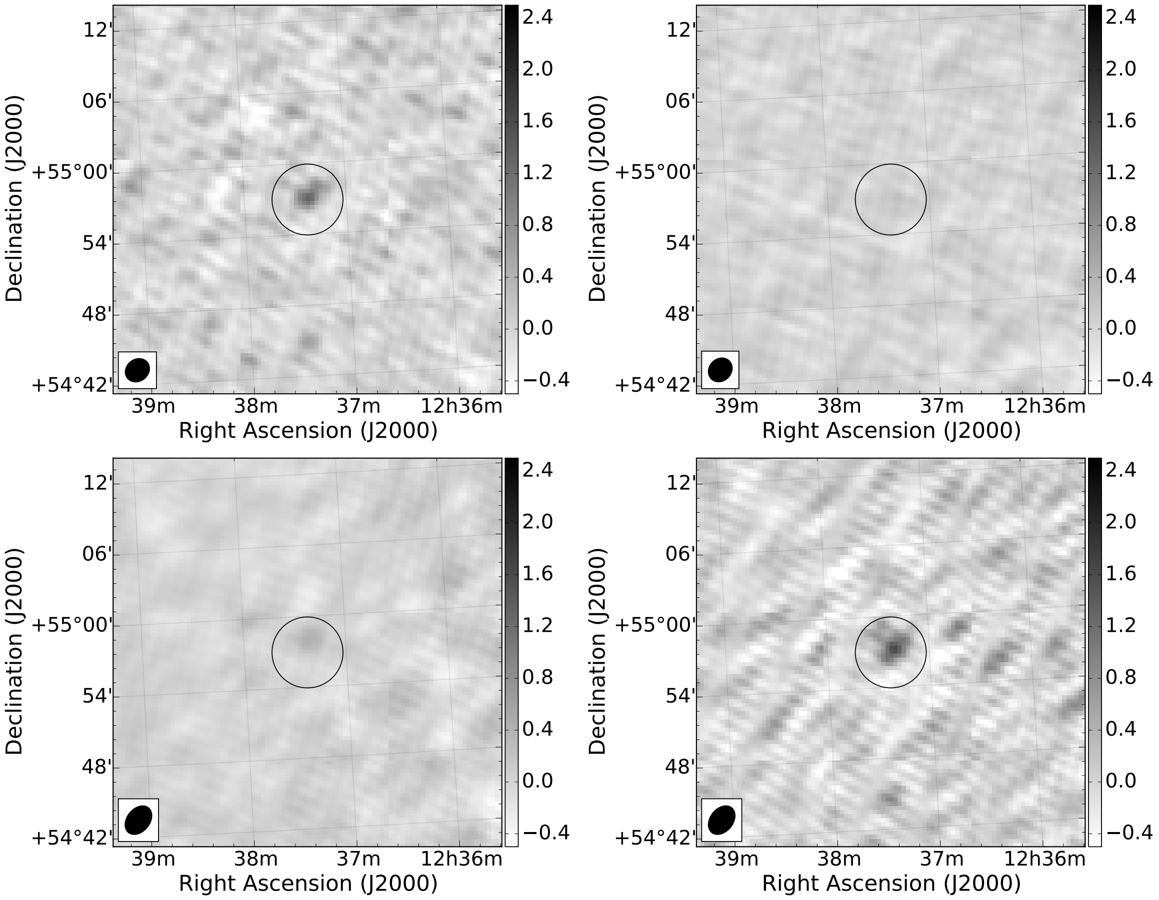

Fig. 3.9 *Upper:* Two 30 seconds snapshots of the #1644 candidate in the epoch in which source was detected (Feb 10, 2013) and the subsequent epoch in which it disappeared (left and right respectively, with the corresponding rms level of approximately 100 mJy and 60 mJy). *Lower:* Two 30 seconds snapshots of the #1644 candidate corresponding to the epoch prior to and at the second detection (Jan 16, 2014, left and right respectively, with the corresponding rms level of approximately 60 and 120 mJy).

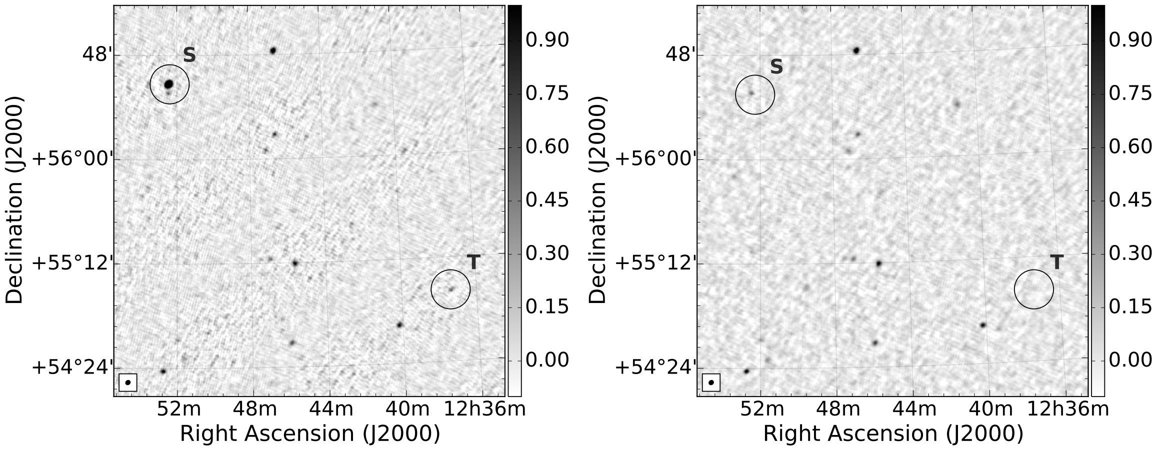

Fig. 3.10 The image on the left shows the original snapshot of the #1644 candidate (marked '**T**'). Circled and labelled with '**S**' is the brightest source in the field. Figure on the right shows the same snapshot, with source '**S**' subtracted prior to imaging, which also resulted in removing the #1644 candidate from the final map.

before (left) and after the source 'S' was subtracted (right). While the additional flagging performed on calibrated data might lead to removing real sources, having cancelled the source with two independent methods we can confidently classify it as a processing related artefact.

3.7.3 Transient Candidate #668

The candidate #668 was detected on July 13, 2013 in Pointing 13, with the peak and integrated flux density of 0.62 ± 0.05 Jy beam^{-1} and 0.62 ± 0.08 Jy respectively (upper panel in Figure 3.11). The source does not appear in the deep RSM map or catalogues of previous radio surveys (WENSS, VLSSr), and, has no counterparts in the remaining RSM bands. Additionally, because of the generally poor quality of the data in the July 2013 zenith scan, the remaining 30s images created from the discussed dataset have been rejected by the quality control step (Section 3.6.2). However, the source is clearly visible in two out of three overlapping beams (00, 02; middle and lower panels in Figure 3.11), with no detection in the remaining beam (04). The measurement sets corresponding to these two beams were

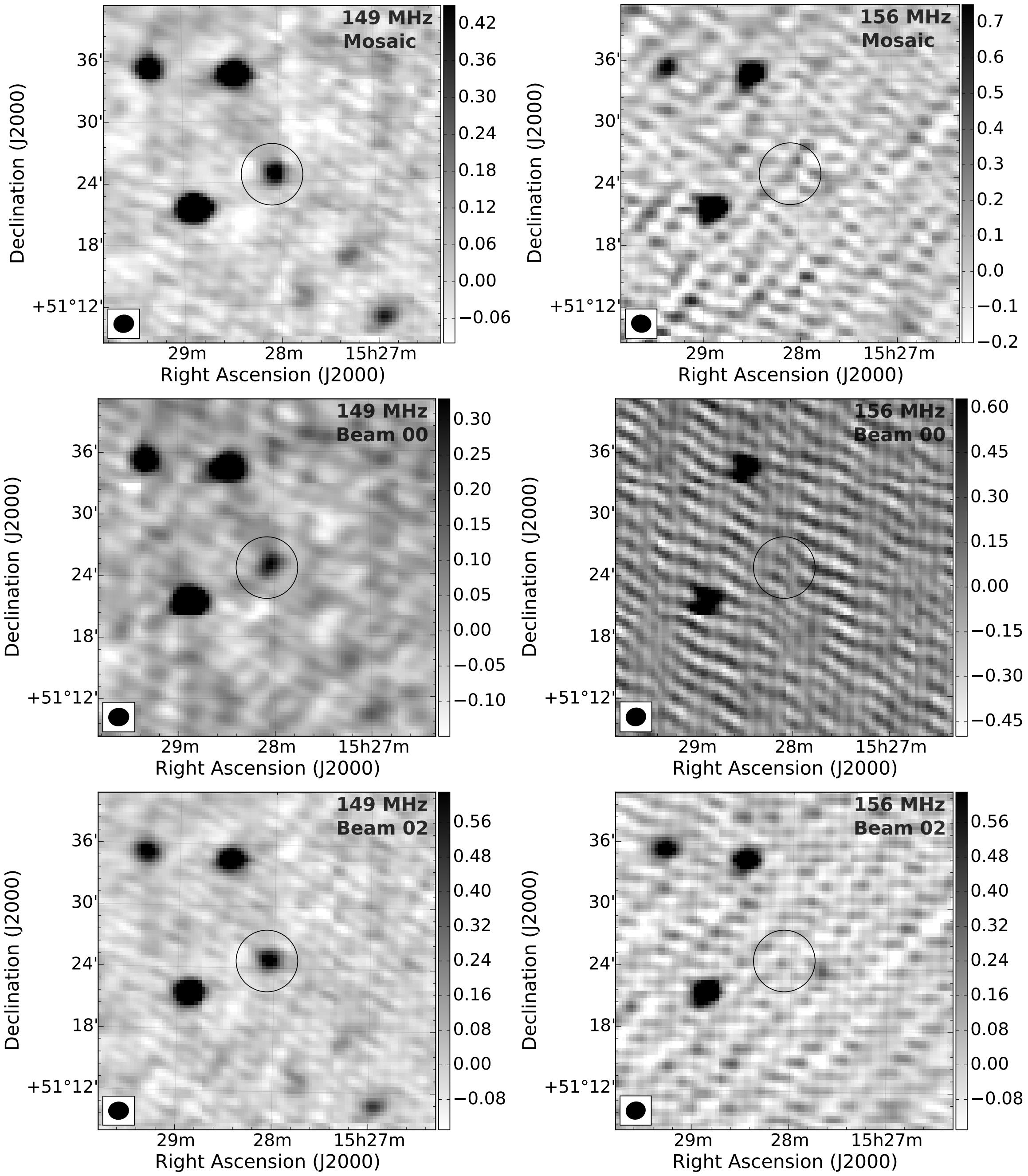

Fig. 3.11 *Left:* Snapshots of the 149 MHz epoch in which candidate #668 was found, showing the source detected in the mosaic of the entire pointing (upper panel) and the same detection in two overlapping beams forming the pointing (beam 00 and 02 in middle and lower panels respectively). *Right:* The same epochs imaged at the frequency of 156 MHz, showing no higher frequency counterparts at the location of #668.

re-analysed and checked against the tests listed in Section 3.7.1.

Additional RFI Flagging

Performing an extra round of RFI flagging did not have an impact on the final 30 second images in neither of the analysed beams, with the candidate #668 consistently visible in both of them.

Subtracting the Sky Model

As mentioned previously, the sky models used in this step were extracted from the 11 minute maps of beams 00 and 02. For each beam, the subtraction of sources was done one by one, from brightest to faintest. With each subtracted source, the measurement set was imaged on 30s time-scale and the location of #668 was checked. This method allowed to identify a bright, three component source, most likely responsible for the appearance of the #668. This source alone was then subtracted from the original measurement sets for beams 00 and 02 respectively in order to confirm its connection to #668.

In beam 00 the subtraction of the 3 component source successfully removed the #668 candidate, as shown in Figure 3.12. The comparison of 30 second snapshots before and after subtraction showed that no other real sources have been removed.

The same subtraction of the 3 component source in beam 02 data also removed the #668 candidate. However, in this case the subtraction resulted in poor quality of the final image, with only 7 detected sources, compared to 21 in the original 30 second snapshot. Therefore, we were not able to confirm whether the subtraction caused real sources to disappear and the test can not be considered fully conclusive.

Imaging Narrow Frequency Bands

For each of the two considered beams I have split the full bandwidth (≈ 2 MHz) measurement

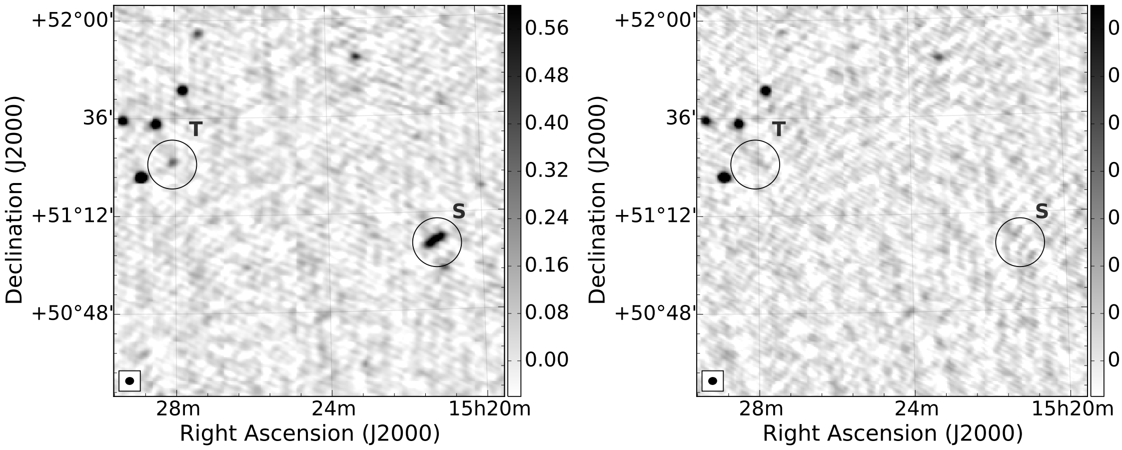

Fig. 3.12 The image on the left shows the beam 00 snapshot with the #668 transient candidate marked '**T**'. Circled and labelled with '**S**' is a bright, nearby field source. The figure on the right shows the same snapshot, with source '**S**' subtracted prior to imaging, which also resulted in removing the #668 candidate from the final map.

set in which the #668 was found into five sub-bands, $\approx$ 400 kHz each. Those individual sub-bands were then imaged and the respective 30 second snapshots were inspected. For beam 00 the candidate is visible only in one out of five 400 kHz sub-bands (the rms around the source is consistent across the sub-bands). This result points to the source being some kind of narrow band RFI. However, this is not matched by the results of imaging sub-bands for beam 02: the #668 is still clearly visible in 4 out of 5 images (with the remaining map being too noisy to be considered).

Imaging with Different Weighting Scheme

As a final test, I imaged the snapshots of beams 00 and 02 in which the #668 source appears with two weighting schemes: uniform and normal. In both cases, the source remained visible in both beams.

Discussion

The candidate #668 was successfully removed by the validity tests from one out of two beams. The detection in beam 02 which seems to have survived the tests might require further investigation. However, the overall properties of the source point towards an RFI or imaging related artefact rather than astrophysical origin, with the latter expected to survive all the above checks.

3.7.4 Transient Candidate #1190

The candidate #1190 was detected in observations taken on February 10, 2013 in Pointing 10, with the peak and integrated flux density of 0.61 ± 0.05 Jy beam^{-1} and 0.62 ± 0.09 Jy respectively. The source has no counterpart in the deep RSM map or catalogues of previous radio surveys (WENSS, VLSSr). Figure 3.13 shows the light-curve of the source at 149, 156 and 185 MHz plotted across the snapshot in which it was detected. The candidate was detected at the position where two of the beams (03 and 05) forming the pointing are overlapping, and is visible in both of them. The upper panel in Figure 3.14 gives a zoomed in view of the originally detected source in the mosaiced image, with the middle and lower panels showing the detection in beams 03 and 05. Below I discuss the results of the validity checks.

Additional RFI Flagging

Performing additional flagging with the AOFLAGGER did not have an impact on the final 30 second images in either of the analysed beams, with candidate #1190 consistently visible in both of them.

Subtracting the Sky Model

The subtraction of individual field sources was done as discussed in Section 3.7.3. After each subtracted source, the measurement set was imaged on 30s time-scale and the location of #1190 checked.

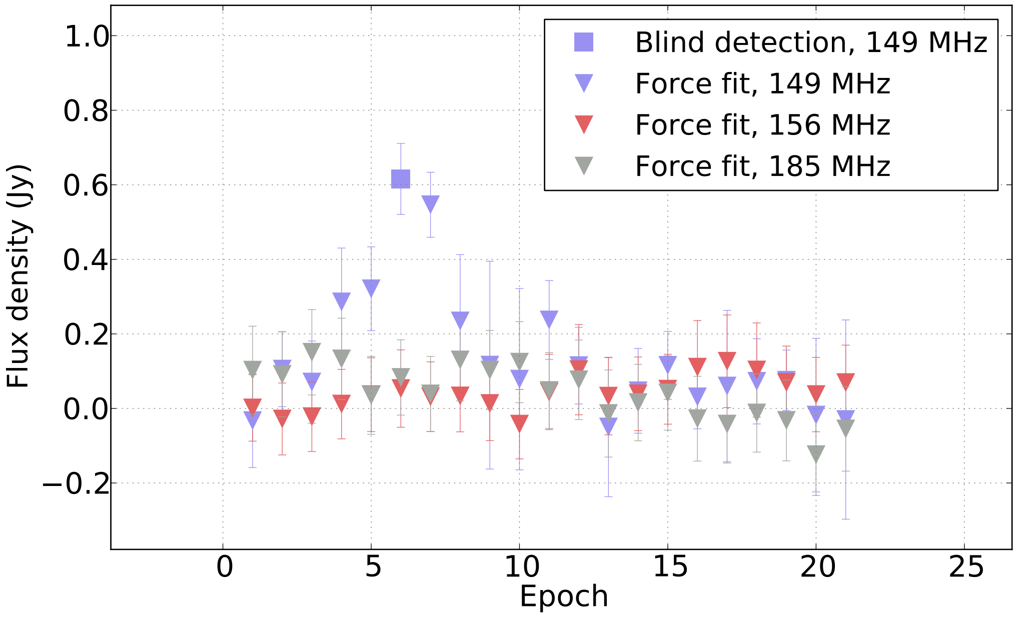

Fig. 3.13 Light-curve of the #1190 candidate in the detection epoch (Feb 10, 2013), monitored at the frequencies of 149, 156 and 185 MHz.

In beam 03 the candidate seemed to be fading away with subtraction of the 8th brightest field source. However, subtracting the 8th source alone, as well as further tests including subtracting different combinations of sources did not result in removing the #1190 from the final image. In beam 05 the candidate survived gradual subtraction of the first 20 brightest sources.

Imaging Narrow Frequency Bands

For each of the two considered beams I split the full bandwidth ($\approx$ 2 MHz) measurement set in which the #1190 was found into five sub-bands, with a width of $\approx$ 400 kHz each. Those individual sub-bands were then imaged and the respective 30 second snapshots were inspected. In both beams the source is visible in most of the sub-bands, however, its position is consistently drifting away from the original location, and, in beam 05 the source is also fading away. With all the other sources in the field being stable, this test gives the strongest

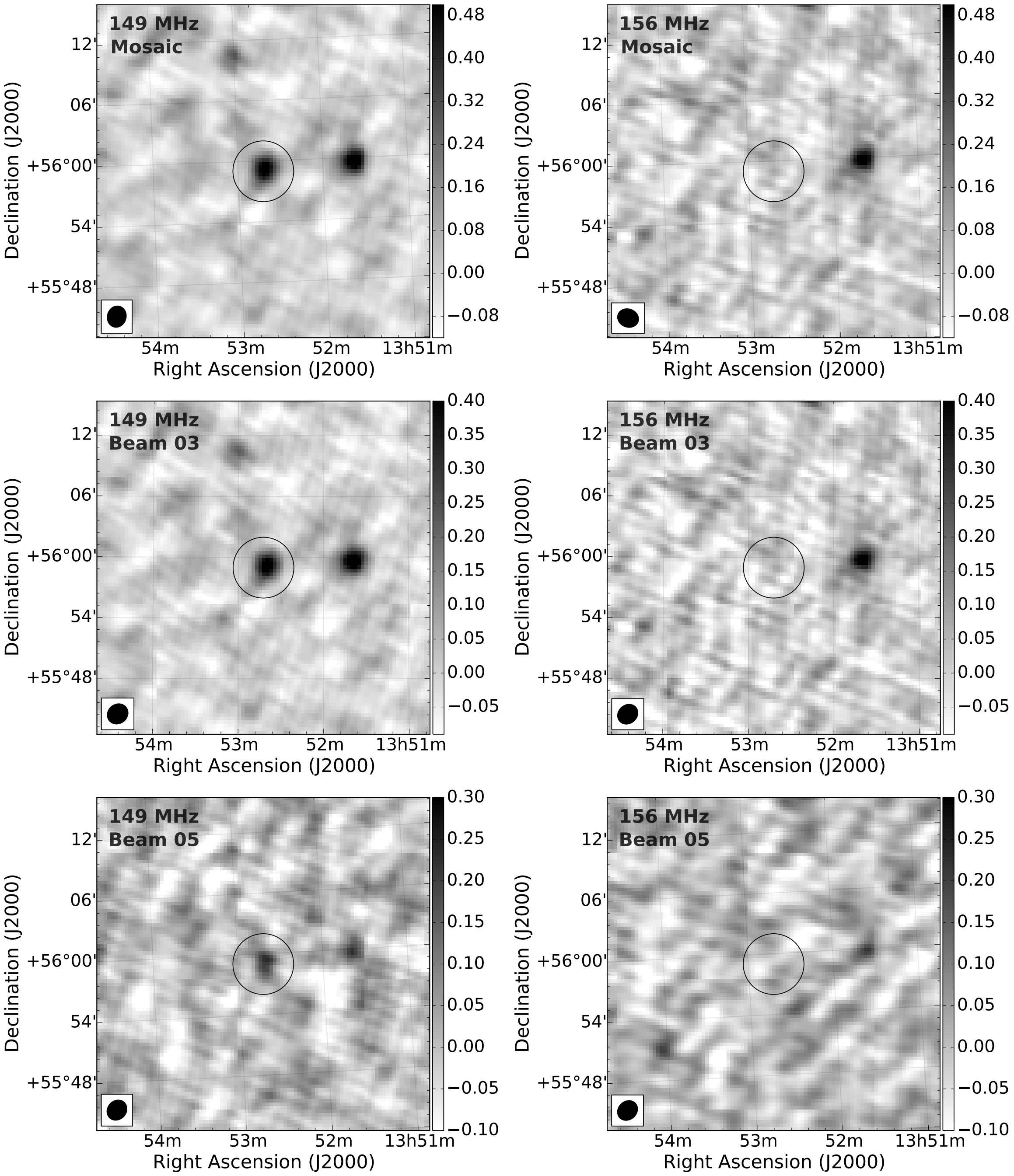

Fig. 3.14 *Left:* Snapshots of the 149 MHz epoch in which candidate #1190 was found, showing the source detected in the mosaic of the entire pointing (upper panel) and the same detection in two overlapping beams forming the pointing (beam 03 and 05 in middle and lower panels respectively). *Right:* The same epochs imaged at the frequency of 156 MHz, showing no higher frequency counterparts at the location of #1190.

proof so far that the detection of #1190 is related to RFI.

Imaging with Different Weighting Scheme

As it was done in Section 3.7.3, I used two different weighting schemes in imaging the #1190 snapshots: uniform and natural. However, this did not alter or remove the source from either beam.

Discussion

Based on the single sub-band images, where the position of the source appeared to be drifting through the sub-bands, it was concluded that the detection of #1190 is due to RFI. This example shows how an artefact can pass various authentication tests, which needs to be carefully considered in future transient searches.

A summary of the results of all the discussed tests for the selected transient candidates is given in Table 3.7.

3.8 Rates and Limits

3.8.1 Estimating Rates of Low Frequency Fast Radio Transients

Even though we have selected a number of potential transient sources from the analysed RSM data (Section 3.7), none of them can be fully confirmed to be real (at least at this stage). Therefore, it was decided to take a conservative approach and estimate the upper limit on the expected transients rate, which can be placed using the Poisson distribution

$$P = e^{-\rho A\,(N_{\mathrm{e}}-1)}, \tag{3.9}$$

Table 3.7 Summary of the validity tests and results for the three RSM short time-scale transient candidates discussed in Sections 3.7.2–3.7.4. The ✓ sign for a given candidate means that the source remained unaffected by the respective test listed in column 1.

	#1644[1]		**#668**[2]		**#1190**[2]	
	Feb 2013	**Jan 2014**	**Beam 00**	**Beam 02**	**Beam 03**	**Beam 05**
Removing bad stations	✓	✓	✓	✓	✓	✓
Additional RFI flagging	candidate removed	candidate removed	✓	✓	✓	✓
Sky model subtraction	candidate removed with subtraction of the brightest field source	candidate removed with subtraction of the brightest field source	candidate removed with bright nearby source subtracted	test inconclusive	test inconclusive	✓
Imaging sub-bands	–	–	candidate visible only in 1 out of 5 sub-bands	✓	candidate present in all sub-bands but position of the source systematically drifting	candidate present in all sub-bands but position of the source systematically drifting
Different imaging settings	–	–	✓	✓	✓	✓

[1] Tests for the candidate #1644 were done on the single beam measurement sets (#1644 was found at the location were no beams are overlapping) for two detection epochs: February 2013 and January 2014.

[2] Because the single epoch candidates #668 and #1190 were both detected in two overlapping beams, tests were performed on the two measurement sets corresponding to those beams (00, 02 and 03, 05 respectively).

where ρ is the areal density of transients (per square degree), N_e is the number of epochs and A is the analysed area of the sky. Assuming no transient events were detected, the 2σ confidence level of the Poisson distribution is $P = 0.05$. For the 253 analysed epochs, covering an area of 440 deg^2, the upper limit of transient sources at 149 MHz is $\rho_{\mathrm{RSM}} < 2.7 \times 10^{-5}$ deg^{-2}.

This result is similar to that obtained by Bell et al. (2014), where the area of 802 deg^2 observed at 154 MHz with MWA was searched. With no transient events found on time-scales of 26 min and 1 year at the flux density limit of 5.5 Jy, the analysis defined an upper limit of $\rho_{\mathrm{MWA1}} < 7.5 \times 10^{-5}$ deg^{-2}. A more recent survey described in Rowlinson et al. (2016) gives further constraints on the expected surface density of radio transients of $\rho_{\mathrm{MWA2}} < 4.1 \times 10^{-7}$ deg^{-2}, based on the analysis of 182 MHz MWA observations, searched on time-scale of 28 seconds.

3.8.2 Constraining the Spectral Index of the NCP Transient

In Section 3.6.3 I estimated the number of transient candidates expected to be found in the analysed set of 30 second RSM images for a range of spectral indices. These rates have been obtained by extrapolating the detection of the transient found in the single sub-band LOFAR LBA observations of the NCP (Stewart et al., 2016). Due to the poor frequency range of this dataset (with a total bandwidth of 200 kHz) the spectral index of the NCP transient could not be estimated. However, reversing the analysis presented in Section 3.6.3 allows for upper limits to be placed on its value. With no transients found in the RSM survey, we can place the upper limit on the number of sources using the Poisson distribution

$$P(k) = \frac{\lambda^k e^{-\lambda}}{k!}, \tag{3.10}$$

where k is the number of detected transients and λ is its upper limit. Assuming there are no transients found in the RSM search (k=0), at the 95% confidence level (2σ, $P = 0.05$) this gives the upper limit $\lambda = 3$. Using Equations 3.6 – 3.8 we can now place an upper limit

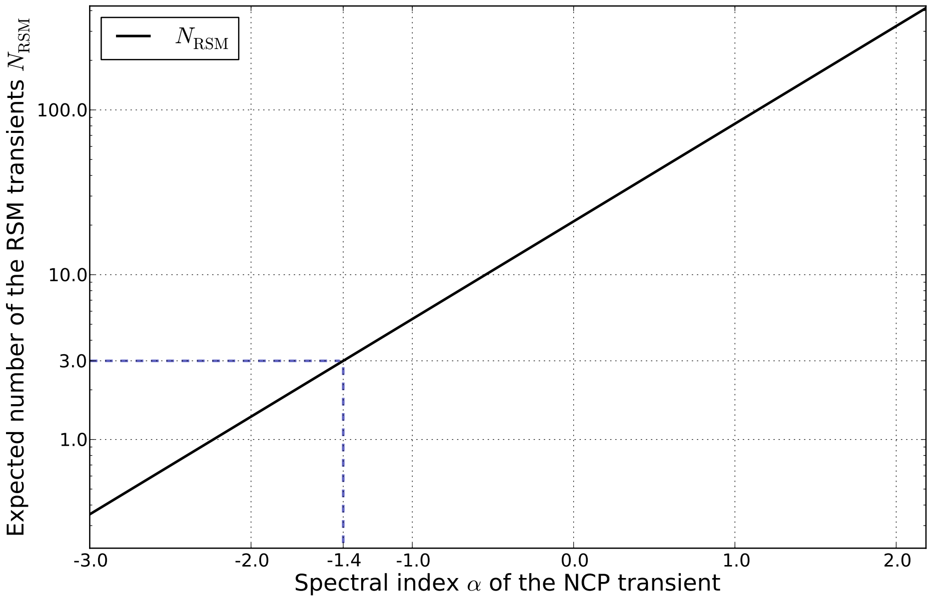

Fig. 3.15 The solid line shows the expected number of NCP-like events to be found in the RSM 30 s images depending on the spectral index α of the NCP transient (as calculated in Section 3.6.3, Equations 3.6 – 3.8). Marked with the dashed line is the upper limit of the spectral index $\alpha = -1.4$ of the NCP transient, estimated based on the assumption that no transient events were found in the low DM RSM survey at the 95% confidence level.

on the spectral index α of the NCP transient of $\alpha < -1.4$ (Figure 3.15). In comparison, the upper limit for the NCP transient spectral index estimated by Rowlinson et al. (2016) based on the transient search carried out with MWA is $\alpha < -2$. Both of these estimates are consistent with the NCP source originating from a coherent emission processes.

3.9 Conclusions

In this chapter I described the search for fast radio transients in the LOFAR RSM field, at 149 MHz. A total number of 253 epochs were analysed on 30 seconds time-scale, covering an area of 440 deg^2, with the average rms of 50 mJy in a single image. The search was limited to observations performed in the directions of low dispersion measure, which were favoured as the ones offering the best chance of finding fast radio transients.

Within this dataset, I have performed the transient search using the Transient Detection Pipeline (TraP), with the detection threshold of 10σ. From 121 candidates selected by TraP I have chosen 13 detections which were not immediately recognized as RFI related artefacts or false associations with catalogue sources. Imaging the remaining frequency bands for these candidates showed that none of them were supported by detections in the other bands, which allowed us to estimate their spectral index $\alpha \approx -35$. This result suggests that the detected sources could originate from propagation effects such as extreme scattering events. However, this type of variability is caused by the ISM amplifying signal from bright, compact object, which should be visible in a corresponding deep map. Although the analysis showed that no background source was found at the location of any of the discussed transient candidates, we can not rule out the presence of faint object below the detection threshold.

Out of the 13 candidates, the three most interesting and potentially real sources (one two-epoch event and two single epoch multi beam detections) were subjected to a number of tests aiming to verify their reality. The checks included subtraction of the sky model, imaging individual sub-bands and running additional, post-calibration RFI flagging. Two out of three sources have been confidently removed by the tests listed above, confirming that they were RFI or imaging related artefacts. The remaining candidate was successfully removed from one out of two beams, with the tests performed on the other beam being inconclusive.

Considering those results, it was conservatively concluded that no transients were detected in the performed search. This allowed us to estimate the upper limit for the areal density of transient events of $\rho_{\rm RSM} < 2.7 \times 10^{-5}$ deg^{-2} at the flux density limit of 0.5 Jy, as well as set the constraints on the spectral index of the NCP transient of $\alpha < -1.4$.

The analysis of the RSM survey presented in this chapter was limited to the area of sky corresponding to low Galactic DM directions. This search could be extended to the remaining

RSM pointings in addition to searching at different time-scales. Although searching the areas of sky expected to have higher Galactic DM contribution decreases our chances of detecting coherent events, exploring different time-scales, from minutes to months, provides opportunities to discover other types of transients. As for the discussed short time-scale transient candidates, a detailed analysis of selected sources was focused on the three most promising detections, however, the remaining ten sources should also be checked against the verification tests.

Chapter 4

Variability Timescales and Brightness Temperatures of Synchrotron Sources

The work presented in this chapter has been published as

Pietka M., Fender R. P., Keane E. F., 2015, MNRAS, 446, 3687

4.1 Introduction

4.1.1 Synchrotron Emitting Sources

It has been known for 50 years that synchrotron-emitting radio sources can vary dramatically, undergoing flaring events. These events are associated with particle acceleration and/or compression of magnetic fields during phases of rapid injection of kinetic energy into the ambient medium. Sources from the stellar scale to supermassive black holes, a range of over 10^9 in mass, can exhibit this behaviour, often associated with large amplitude variations at other (e.g. optical, X-ray) wavelengths. Radio emission can be used as an identifier and locator of interesting events for study at other wavelengths. It can also provide a measure of the degree of kinetic feedback associated with a given phenomenon – having estimated the volume of the emitting region from, e.g. measuring the radio variability time-scale of the event, we can place a lower limit on its kinetic energy by minimizing the total energy associated with the outburst as a function of the magnetic field (as shown by Burbidge 1959, and discussed in more detail in Section 1.3.1). The processes associated with this feedback are not a homogeneous set, however, and cover a wider range of geometries and physical regimes. In accreting black holes (of all masses, stellar to supermassive) and neutron stars, as well as gamma-ray burst afterglows the radio emission is often associated with highly collimated flows. These are characterised by opening angles of degree scale or smaller and significant bulk Lorentz factors (at least in the initial phases). In novae and supernovae, however, the feedback is in the form of much more slowly moving (1000s of km s^{-1} or less) ejecta moving in a much more isotropic geometry. Intermediate geometries and regimes also exist.

4.1.2 Van der Laan Model

One of the earliest models for the evolution of variable extragalactic radio sources was that of van der Laan (1966), in which an astrophysical explosion is described as a uniform, spherical cloud of relativistic particles and magnetic field, expanding adiabatically into a surrounding medium. The relativistic electrons, with isotropic energy distribution $N(E) \propto E^{-p}$ (where p is related to the spectral index α as $p = -2\alpha + 1$ in optically thin regime) are accelerated in the magnetic field B and radiate via the synchrotron mechanism (Section 1.3.1). In this model two competing effects determine the light-curve at a given frequency as the cloud expands: decreasing optical depth causes an increase in the flux for those frequencies which are initially self-absorbed, but adiabatic expansion losses reduce the internal energy and therefore the synchrotron emission. A schematic of the evolution of the light-curve is shown in Figure 4.1 and details of the process are described below.

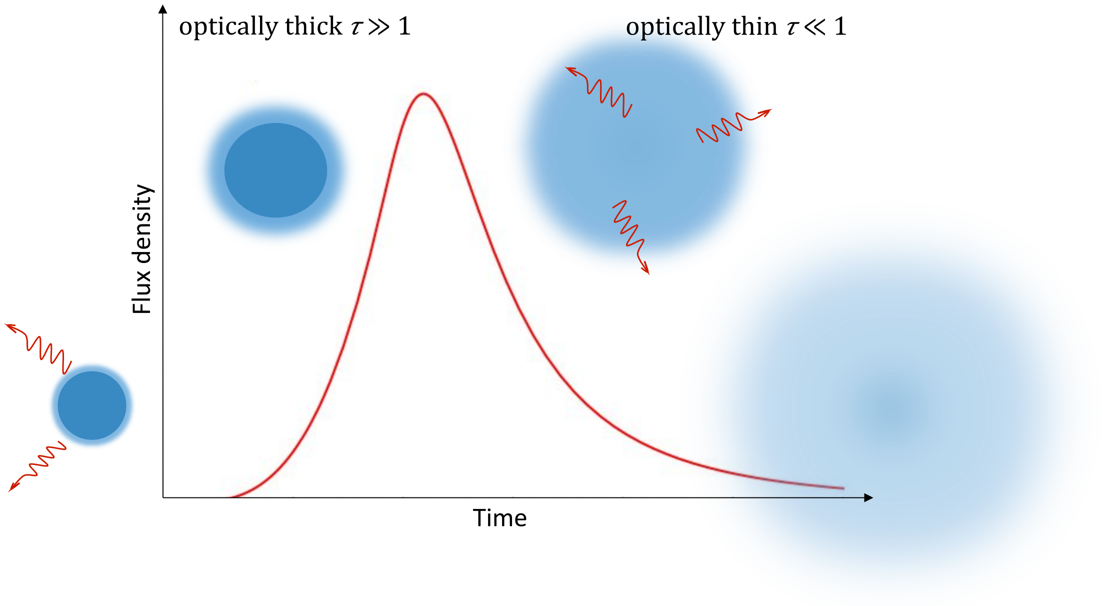

Fig. 4.1 Illustration of the flux density evolution for an expanding cloud of relativistic electrons, radiating via a synchrotron mechanism. As the size of the bubble increases, the optical depth decreases and the cloud becomes transparent to the radiation. The maximum flux density corresponds to the transition between optically thick and optically thin phases. The peak flux is followed by a slow decline of the flux, reflecting the loss of energy of the cloud due to expansion.

Evolution of the Light-curve in Time

At the initial, optically thick stage, the shape of the light-curve is determined by the synchrotron self-absorption (Section 1.3.1). At the beginning the optical depth τ is high enough to prevent the radiation at most radio frequencies from escaping the cloud. Observing the changes of the flux density in time at one set frequency will show that as the cloud expands, decreasing optical depth progressively makes it transparent to the radiation, causing an increase in the observed flux. The intensity of the flux rises steeply with time until it reaches its peak, where the source becomes completely transparent to the radiation at the given frequency, after which it enters the optically thin stage. From that moment, the shape of the light-curve is dominated by adiabatic expansion losses, and characterised by a slow decrease in the flux intensity (Figure 4.1). The slope of the decline phase of the light curve is frequency independent, since it is transparent to the photons at all energies and decreases only due to the expansion energy losses (in the absence of significant synchrotron and inverse Compton loses), which are energy independent.

Spectral Evolution

At the self-absorbed part of the spectrum, the relation between the flux density F and the observed frequency ν is described by

$$F \propto \nu^{2.5}, \tag{4.1}$$

while at the optically thin stage it depends on the spectral index α

$$F \propto \nu^{\alpha}, \tag{4.2}$$

where $\alpha = -(p-1)/2$ and p is the power law index of the energy distribution (Section 1.3.1). In his model, van der Laan shows that the flux density can be related to the observed frequency

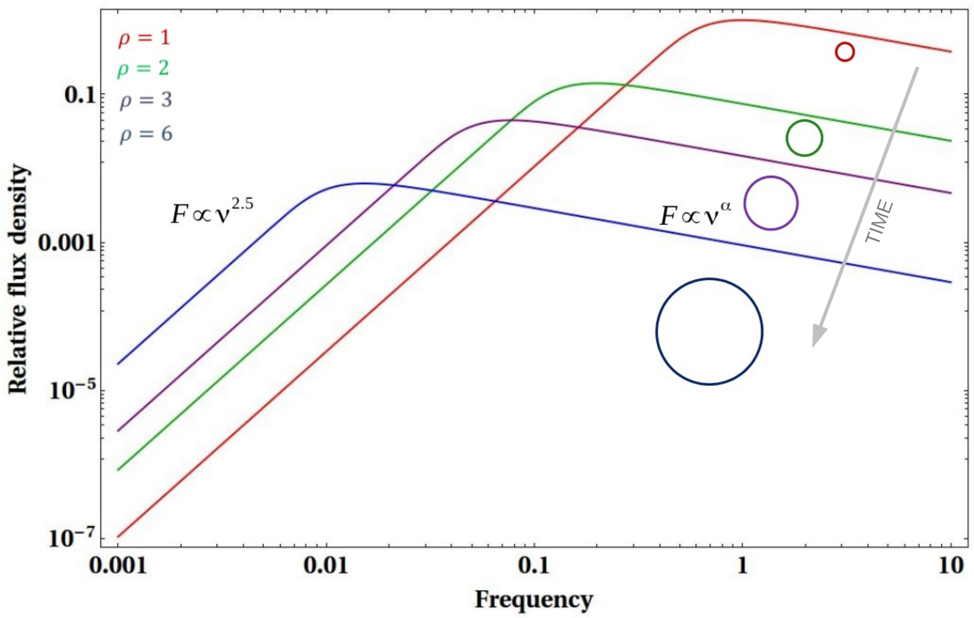

Fig. 4.2 Spectral evolution of the synchrotron emitting expanding radio source calculated for several values of the relative size of the source ρ.

ν and the fractional size of the source $\rho = r/r_0$ (where r_0 is the radius of the cloud at some reference time) in the following way

$$F(\nu,\rho) = F_0(\nu)\,\rho^3 \tag{4.3}$$

for the optically thick part of the spectrum (where F_0 corresponds to the value of the flux density at given instance), and

$$F(\nu,\rho) = F_0(\nu)\,\rho^{-2p} \tag{4.4}$$

for the optically thin part of the spectrum. Figure 4.2 shows examples of the spectral evolution of the radio source, calculated for several values of the relative radius of the source ρ. Because the optical depth to synchrotron self absorption decreases with increasing frequency, higher

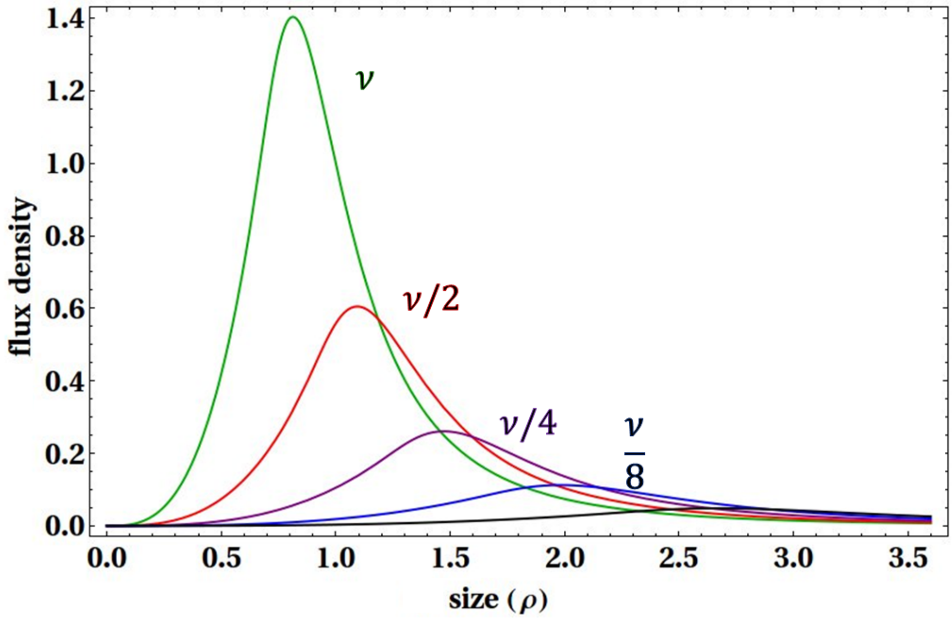

Fig. 4.3 Illustration of the changes in the shape of the synchrotron flare with observed frequency as a function of sources relative size, ρ. With the decreasing frequency (from top to bottom), the peak of the observed flare is lower, and its overall duration extended. The ratio of eight in frequency illustrated here is comparable to that between the 1.4 GHz and the high band of LOFAR. Light-curves have been calculated based on the van der Laan model.

frequencies peak earlier and stronger, although in the later, optically thin, phase the lowest frequencies are strongest. Van der Laan (1966; and many others since) clearly demonstrates the contrast between the sharply peaked light curves at high radio frequencies and the much smoother events at lower frequencies. Figure 4.3 shows the change in the shape of the flare observed at different frequencies (re-created based upon van der Laan's paper, similar to his Figure 1).

4.1.3 Other Models

Many modifications have been made to the simple van der Laan model, in order to give an accurate explanation for the behaviour observed from different classes of radio transients. The main differences between those models come from highly variable geometry depending on the originating astrophysical phenomena. For supernovae, the explosion is followed by spherically symmetric expansion (Chevalier 1982a,b; Weiler et al. 2002). However, the radio emission from X-ray binaries and active galactic nuclei is believed to come from highly collimated outflows, with additional acceleration of matter along the jet, causing bright spots (Hjellming and Johnston 1988, Livio 1999, Fender 2006). This is also the case for recently observed tidal disruption events (TDE; Giannios and Metzger 2011). For gamma ray bursts, we observe both beamed radiation from the initial collimated explosion, as well as more spherical radio afterglow at later stages (Chevalier and Li 1999, Li and Chevalier 1999, Sari et al. 1999, Kumar and Panaitescu 2000). Additionally, more complex models include internal and external shocks at later times which can re-energise particles, constrained expansion of the ejecta, deceleration from highly to mildly relativistic bulk flows.

4.1.4 This Work

We are currently in an era in which wide-field blind surveys for radio transients are beginning (e.g. with LOFAR: van Haarlem et al. 2013, Fender and Bell 2011 for a general overview) and are going to be a major factor for future larger radio facilities such as MeerKAT (Booth et al., 2009), ASKAP (Johnston et al. 2007, 2008) and the Square Kilometre Array (SKA; Fender et al. 2015). As in the X-ray and optical fields, in which such blind searches for transients have been undertaken for some time (e.g. Sesar et al. 2007), early identification and classification of a new variable or transient, even if crude, can be invaluable in optimising the science delivered from a finite set of resources (observing time). The simplest and earliest such diagnostic is the variability time-scale of the event (see e.g. Rau et al. 2009, Ofek et al. 2014, Cao et al. 2012 for the time-scale – magnitude plot for optical transients used in Palomar Transient Factory literature). There is no strong *a priori* reason to believe that a simple relation should exist between event type and the most basic characteristics of radio variability, given the wide range of geometries and physical regimes present, as outlined above. In this work, we analyse a large number of known synchrotron emitting sources, and reveal an overall correlation between variability time-scales and luminosities of their flares, which, in spite of different physical phenomena explaining their origin (Section 4.1.3), exists for these events. The considered sample of radio light-curves spans a wide range of astrophysical objects observed in outburst, from nearby galactic sources to the most distant objects in the Universe. Additionally, it only includes sources for which the distances are known, so the peak radio luminosities of the flares can be calculated. It should be noted however, that this compilation was based on the range of available archival data, and it is possible that other types of objects might be populating the parameter space. Furthermore, the steepness of the observed relation between luminosity and time-scales implies, rather unexpectedly, that the minimum brightness temperature, of a given event is an increasing function of source luminosity. Finally, the result offers hope that the relation could be used as a very early time diagnostic of radio flaring events and transients (see Chapter 5).

4.2 Exploring the Variability Time-scales Correlations

4.2.1 Lightcurves Sample

The entire data sample used in this analysis consists of $\approx$ 200 flare events from $\approx$ 90 distinct objects. Due to the strong frequency dependence of the shape of the light curve (Section 4.1.2, Figure 4.3), the sample was limited to sources that were observed at 5-8 GHz – the frequency range for which the largest set of observational data was available. Data for 70 objects/events, mostly observed at $\approx$ 5 GHz, have been compiled from the literature, which offers a range of pre-selected flares for objects such as supernovae or X-ray binaries, as well as long-term monitoring light-curves of AGN. The remaining part of the sample (27 objects) has been compiled from the online Green Bank Interferometer (GBI) database[1], which provides archival data for AGN, RSCVn, Algol and X-ray binary sources monitored on a time-scale

---

[1] ftp://ftp.gb.nrao.edu/pub/fghigo/gbidata/gdata/

of several years, at frequencies 2.25 GHz and 8.3 GHz. Because better defined light-curves were available at higher GBI frequencies, I have decided to use the 8.3 GHz data for the analysis. Five objects in the considered sample have been present both in the literature as well as the GBI sample, which gives 92 distinct objects in the analysed dataset. While GBI offers complete datasets for the archived radio light-curves, this was not the case for most of the data compiled from the literature where only schematic light-curves were available, with no data values. For this reason, data points of the light-curves selected from the published results have been extracted for further analysis using the WebPlotDigitizer[2] software. The sample has been limited to astrophysical synchrotron flares only, and does not include scintillating events (they are considered in the work described in Chapter 5) or those originating from coherent emission (discussed briefly in Section 4.3.3). For objects that undergo recurrent outbursts (XRBs, AGN, etc.) I have analysed multiple flare light-curves, if such were available. Although the selection of single flares from the light-curves used in the analysis in this chapter has been done by eye, a more robust and human independent method was later developed and will be discussed in Section 5.2.2. Here, for the purpose of the analysis, I have only included events with the best possible time coverage, for which the clear identification of rise/decline phases was possible. For objects with multiple flares, measurements have been done on different time-scales, including both longer time-scale variability and shorter outbursts superimposed on it. Examples of selecting flares from the noisy data are shown in Figure 4.4. Summaries of the data sample and the references are listed in Tables 4.2–4.11 at the end of this chapter.

4.2.2 Method

As mentioned in Section 4.1.4, the time-scale of the radio variability of synchrotron sources can be an early indication of their nature. However, when a transient candidate is detected in

---

[2] Web based tool to extract data from maps and images, created by Ankit Rohatgi. (http://arohatgi.info/WebPlotDigitizer)

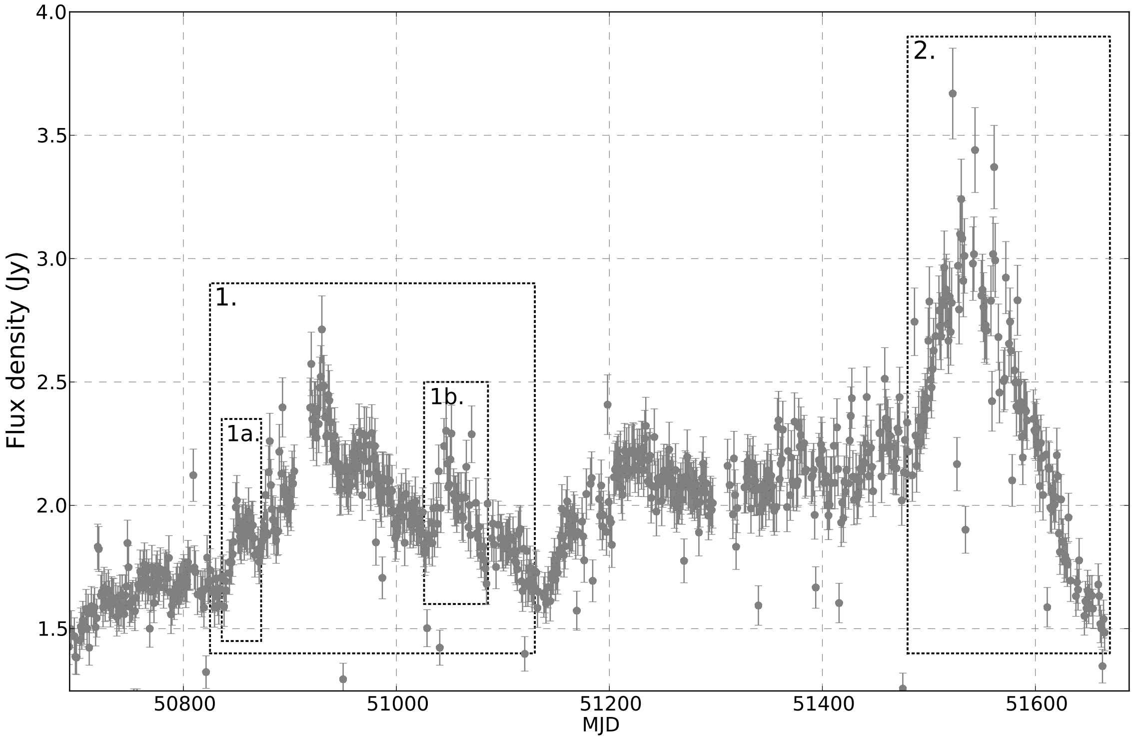

Fig. 4.4 An example of a light-curve (blazar 0851+202; GBI, 8.3 GHz) from which several flares have been selected for the analysis. Apart from two main long time-scale flares (*1.,2.*), we have also included two shorter flares that took place during the rise (*1a.*) and decline (*1b.*) phases of the first outburst. Selection of all the flare events has been done by eye.

a radio observation, in many cases only a partial light-curve rather than the complete data covering the duration of the outburst is available. Additionally, as discussed in Section 4.1.2, the rising part of the light-curve, determined by decreasing optical depth, in most geometries will show steeper increase in the intensity of the observed flux density with time, compared to the slower decline, dominated by the expansion losses. Considering this, in order to explore the distribution of variability time-scales for synchrotron flares, each flare from the sample described in Section 4.2.1 was divided into rising and declining phases which were then analysed separately. This section presents the method chosen to uniformly measure the variability time-scales across the sample, as well as the motivation for that choice. The following discussion is focused on the example of the rising phase of the flare, however, the exact same steps apply to the decline of the outburst.

If we consider a flaring synchrotron source observed at distance d_1, its light-curve will show a steep rise with the slope s_1 on a time-scale $t_{\rm rise}$ (left panel in Figure 4.5). If the same source is observed at the further distance d_2, it appears much fainter. Therefore, the peak flux density will be lower, and the measured slope s_2 will differ from s_1. This illustration shows that simply measuring the slope of the light-curve gives different results depending on the distance to the source. This problem can be solved by plotting the logarithm of the flux density against linear time instead (right panel in Figure 4.5). Because $F \propto L/d^2$, where F is the flux density, d is the distance to the source and L is the luminosity of the source, the slope s of the light-curve becomes distance independent

$$s = \frac{\ln F_2 - \ln F_1}{t_2 - t_1} = \frac{\ln\left(L_2/L_1\right)}{\Delta t}. \tag{4.5}$$

The rate s defined this way is related to the e-folding time τ as

$$s = \frac{1}{\tau}, \tag{4.6}$$

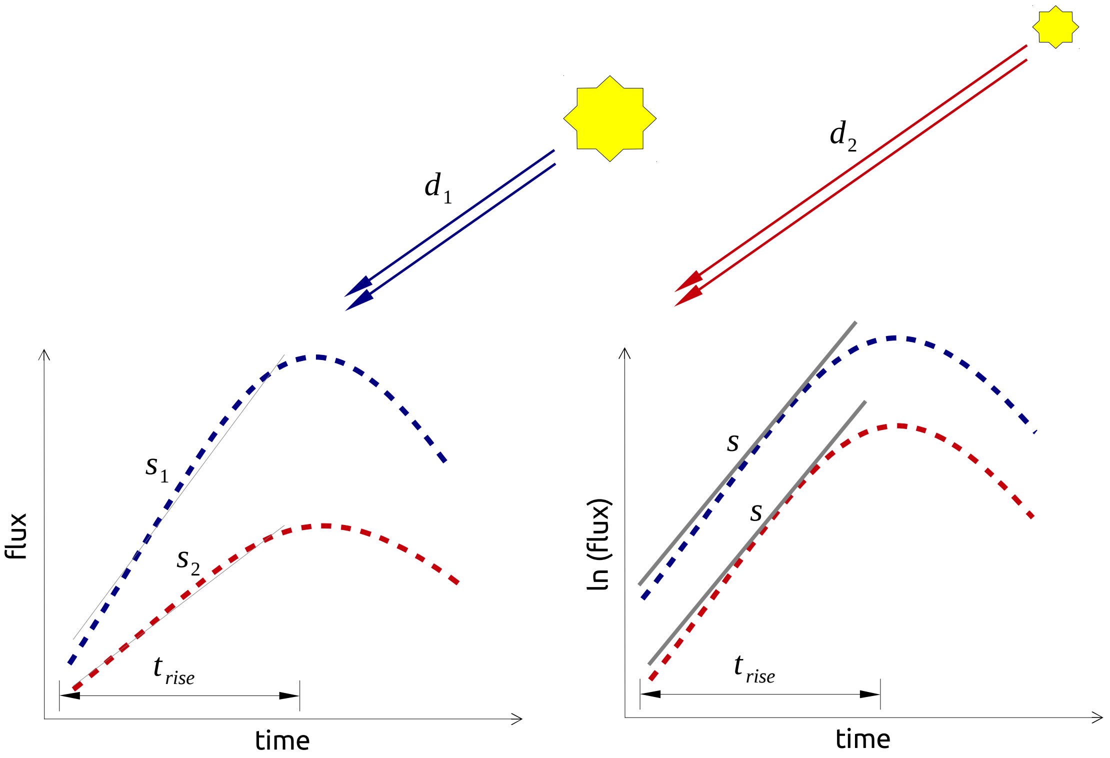

Fig. 4.5 Schematic illustration of the measurements of the rise rate for a radio light-curve. Left panel shows two light-curves of the same source, observed at different distances. For the source observed at smaller distance (figure left, blue light-curve) the flare appears much brighter when compared to the same source observed at the larger distance (figure left, red light-curve). Both light-curves, although representing the flare from the same source, will give different results if the slope of their rise/decline rates is measured. The figure on the right shows how by plotting the logarithm of the flux against linear time instead, removes distance dependence from the measurement of the slope.

where τ (previously used to define the optical depth) describes the characteristic time-scale. Therefore the fractional change of the flux density in time Δt can be defined as

$$\frac{F_2}{F_1} = \exp\left(\frac{\Delta t}{\tau}\right). \tag{4.7}$$

Apart from being distance independent, this choice of the measurement is physically motivated. In the van der Laan model (1966), the radio flux density of a source is described by an exponential function that depends on the optical depth. As the optical depth decreases with the size of the source increasing over time, the flux density can be seen to change exponentially. It is true that some alternative models favour power-law decays. These power-law fits (linear fits to log flux vs log time) were also attempted but exponential fits gave the most robust and reproducible results. As well as for measuring rise rates of the events, the same method can be used in order to measure decline rates of synchrotron flares.

4.2.3 Analysis

Following the reasoning above, a linear fit was made to the natural logarithm of the flux as a function of linear time, which effectively corresponds to fitting exponential functions. One thing that should be remembered during this fitting conversion is the number of free parameters. If we consider fitting the exponential function to the data, the model consists of three free parameters, a - amplitude, b - background and τ - time-scale

$$F(t) = a \times \exp\left(\frac{t}{\tau}\right) + b. \tag{4.8}$$

Therefore, if we decide to calculate the logarithm of the flux density instead and fit the linear model to the data, the background emission has to be subtracted from the flux density measurements prior to fitting

$$\ln\left(F\left(t\right)-b\right)=\frac{1}{\tau}t+const. \tag{4.9}$$

While these two methods (Equations 4.8 and 4.9) are equivalent in complexity, in this work I decided to use the latter one. At this stage, the estimation of the background has been done by eye, however, an automated method was later developed and will be discussed in Sections 5.2.2 and 5.4.2. Figure 4.6 shows examples of light-curves for several classes of object and the measurement method. Slope measurements were made on a case by case basis in MATHEMATICA once the start and end points of an event had been chosen by eye. The steps described above were applied to the sample of light curves presented in Section 4.2.1. Peak radio luminosities have been calculated using

$$L_{\mathrm{peak}}=\nu L_{\nu,\mathrm{peak}}=4\pi d^2\nu F_{\mathrm{max}}, \tag{4.10}$$

where $L_{\nu,\mathrm{peak}}$ is the peak monochromatic luminosity, ν is the observed frequency, F_{max} is the maximum flux density and d is the luminosity distance to the source (listed in Tables 4.2–4.11). No attempt to correct for any beaming or anisotropy was included in the analysis.

4.3 Results

The main objective of the analysis described in Section 4.2.3 was to find a relation between the variability time-scales and luminosities of synchrotron events, which could provide a separation between different classes of objects. Additionally, having measured rise/decline rates for a sample of synchrotron events with well defined luminosities, we can put a lower limit (corresponding to maximum physical size of the source) on their brightness temperatures. In the following sections I will present the correlation between peak radio luminosities and rise/decline rates obtained for analysed sample of events (Section 4.3.1), as well as the estimations of the minimum brightness temperatures for those sources (Section 4.3.2). This

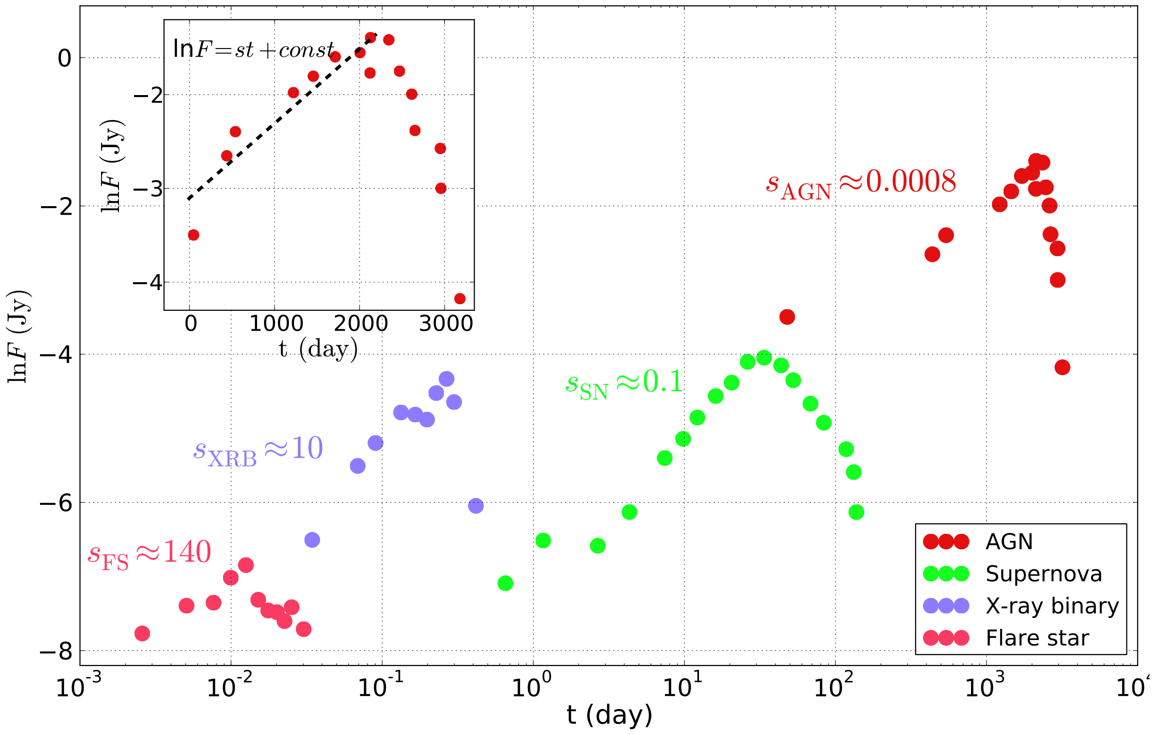

Fig. 4.6 Examples of the light-curves for several classes of objects, illustrating different time-scales of the events: flare star (AU Mic), X-ray binary (Sco X-1), supernova (SN 1994I) and AGN (NGC 4278). A schematic example of the slope measurement of the light curve for rising phase is shown for the flare from NGC 4278. The measured slope s of the fitted line corresponds to τ^{-1}, where τ is the e-folding time. All the light-curves shown have been normalized to have a similar initial flux density.

analysis, focused on incoherent events, does not include the other - coherent - flavour of radio emission. However, the phase space for these types of objects has been investigated before (Cordes et al., 2004). In section 4.3.3, we use those results for the coherent types of sources to build a complete picture of the parameter space of known radio transients.

4.3.1 Variability Time-scales Results

Figures 4.7 and 4.8 show the results of the measurements described in Section 4.2.3 for a sample of 200 (200 for rise, 200 for decline phases) light curves from 70 sources found in the literature (mostly observed at ≈ 5 GHz) plus 27 objects from the GBI database (8.3 GHz). The variability time-scale parameters τ calculated for rising/declining phases of light-curves are plotted against the corresponding peak radio luminosity of the source. The results show that the measured time-scales are broadly correlated with the peak radio luminosities. We see that as the peak luminosity increases, sources tend to vary on longer time scales. This is not unexpected (see Sections 4.1, 4.5) but has not been systematically measured before. AGN as the most luminous objects in the Universe can take up to several years before they reach peak flux density, while nearby and faint flare stars go into outburst and fade away within a couple of hours. The analysed sample of objects includes synchrotron emitting sources as well as those for which the origin of radio emission is gyro-synchrotron (flare star, magnetic CV, Algol and RSCVn). This different flavour of incoherent emission is explained by radiation from electrons trapped in magnetic coronal loops. Table 4.1 shows the results of fitted values for the correlation between L and τ for two cases: first, including all of the sources in our sample and second - excluding gyro-synchrotron emitting sources.

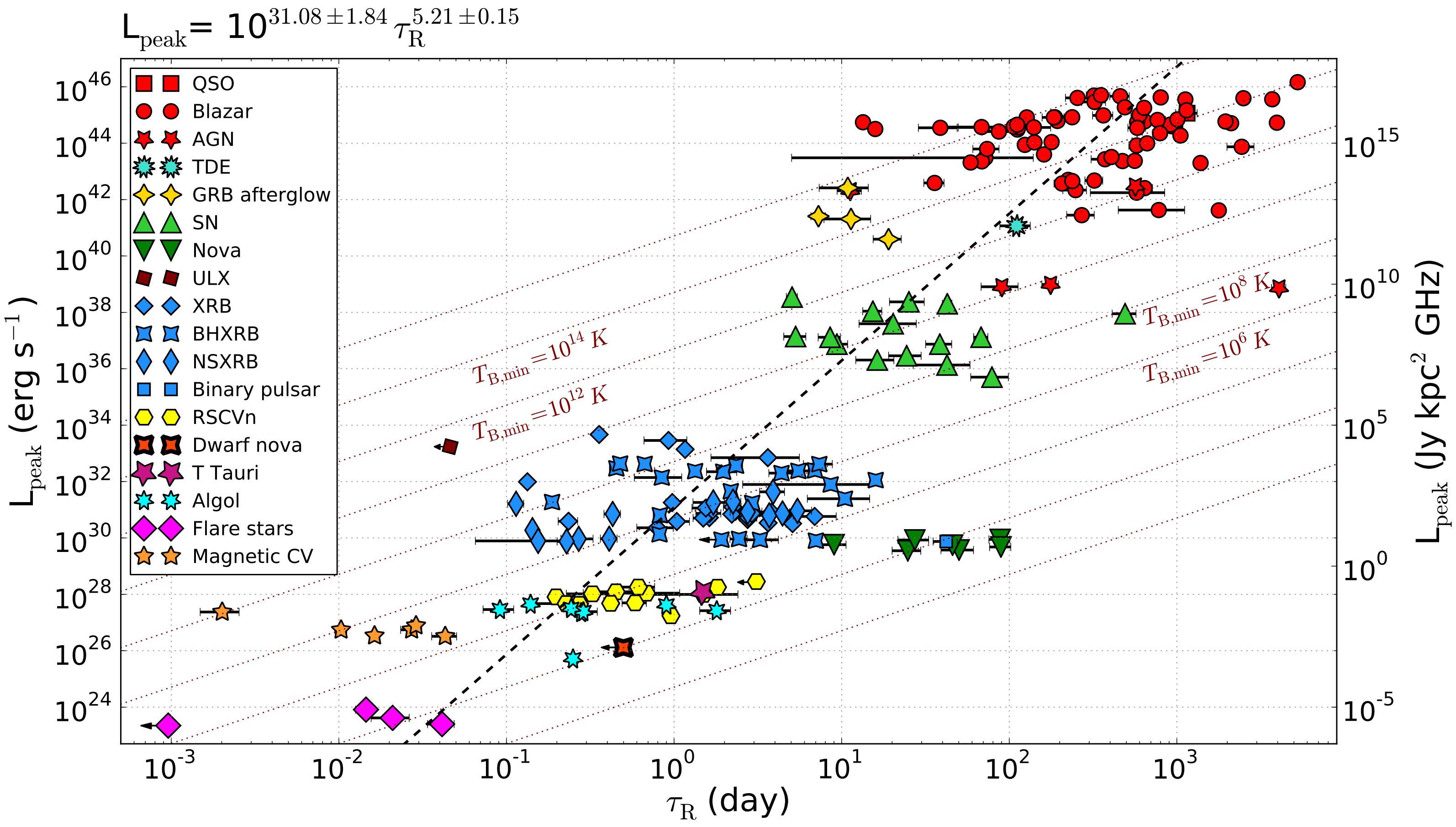

Fig. 4.7 This figure shows exponential rise time-scale as a function of peak radio luminosity for the entire set of radio flares studied. The overall relation is of the form $L \propto \tau^{5.21 \pm 0.15}$. Overplotted are lines corresponding to a fixed minimum brightness temperature ($T_{B,min}$), under the assumption that the size of the emitting region $r = c\tau$, which have a form $L \propto \tau^2$, demonstrating clearly that $T_{B,min}$ is an increasing function of luminosity, peaking just above the theoretical limit of 10^{12}K for the most luminous AGN (which are also likely to be beamed).

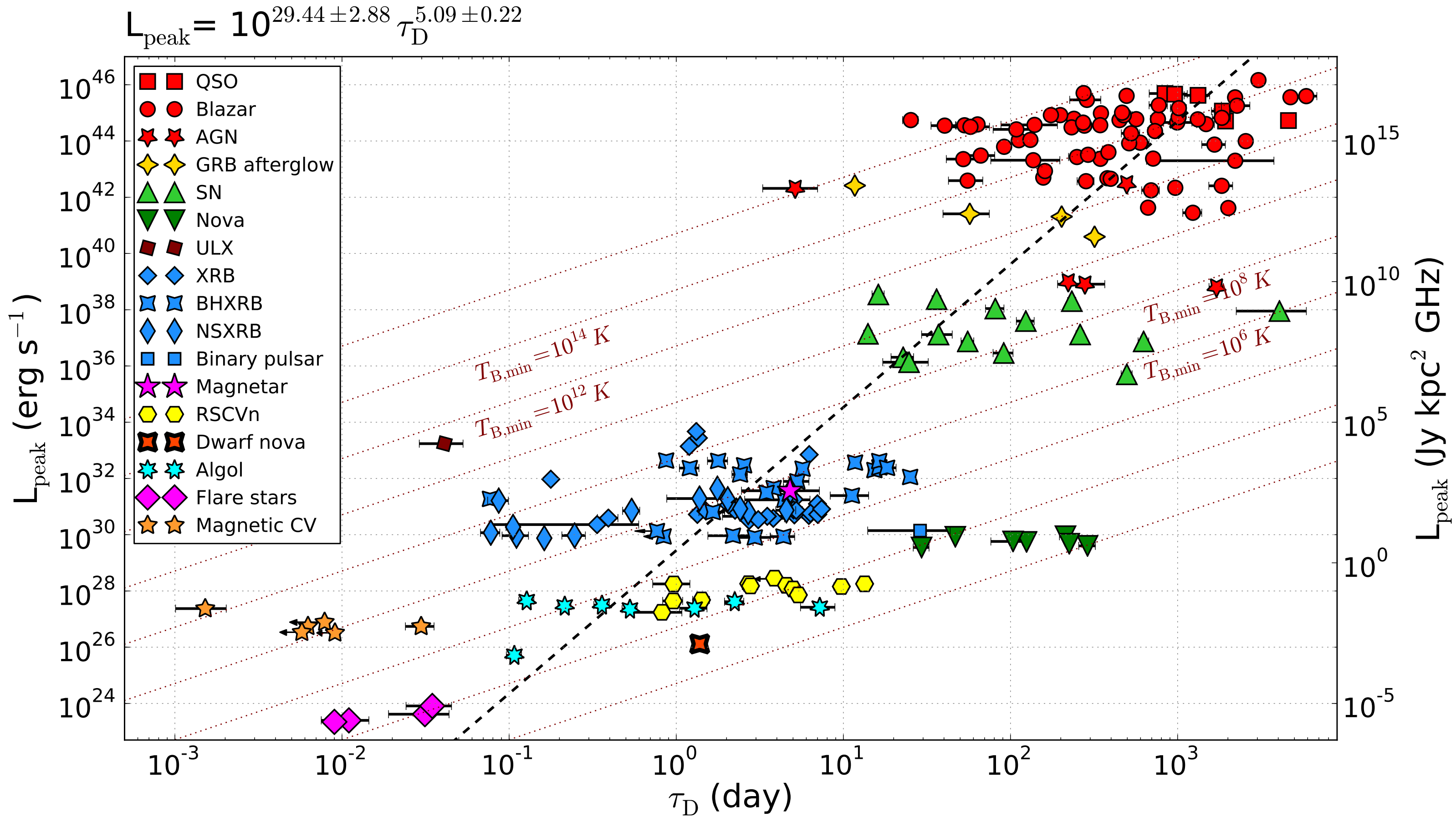

Fig. 4.8 This figure shows exponential decline time-scale as a function of peak radio luminosity for the entire set of radio flares studied. The overall relation is of the form $L \propto \tau^{5.09\pm0.22}$. Overplotted are lines corresponding to a fixed minimum brightness temperature ($T_{\mathrm{B,min}}$), under the assumption that the size of the emitting region $r = c\tau$, which have a form $L \propto \tau^2$, demonstrating clearly that $T_{\mathrm{B,min}}$ is an increasing function of luminosity, peaking just above the theoretical limit of 10^{12}K for the most luminous AGN (which are also likely to be beamed).

Table 4.1 Parameters of the fits to the rise/decline phases. Fits done with MATHEMATICA, with the following formula: $\log(L_{\mathrm{peak}}) = A \times \log\tau + B$.

	A $\pm\delta$ A	B $\pm\delta$ B	A$'$ $\pm\delta$ A$'$ [1]	B$'$ $\pm\delta$ B$'$ [1]
Rise	5.21 ± 0.15	31.08 ± 1.84	5.20 ± 0.22	31.12 ± 2.89
Decline	5.09 ± 0.22	29.44 ± 2.88	5.80 ± 0.28	27.82 ± 3.21

[1] Additional fit done for comparison on a sample excluding flares that originate from gyro-synchrotron emission mechanism (flare star, magnetic CV, algol, RSCVn).

4.3.2 Brightness Temperature

In a steady state, the brightness temperature of synchrotron emission is limited to $T_{\mathrm{B}} \sim 10^{12}$ K (Kellermann and Pauliny-Toth 1969); above this value inverse Compton losses rapidly cool the electrons. The combination of luminosity and time-scale naturally allow us to constrain the effective T_{B} for each flare event measured in this study.

In the Rayleigh-Jeans part of the blackbody spectrum, the monochromatic luminosity of a spherical source of radius r is defined as

$$L_\nu = \frac{2k_{\mathrm{B}}T\nu^2}{c^2}4\pi r^2. \tag{4.11}$$

For a source changing luminosity by ΔL_ν on time-scale τ, a minimum brightness temperature, $T_{\mathrm{B,\,min}}$ will correspond to the source having a maximum size $r = c\tau$. Since τ is the exponential rise (or decay) time-scale, the luminosity ΔL_ν should be a fraction of the monochromatic peak luminosity $L_{\nu,\mathrm{peak}}$

$$\Delta L_\nu = \frac{e-1}{e}L_{\nu,\,\mathrm{peak}}. \tag{4.12}$$

Substituting and rearranging Equations 4.11 and 4.12, allows us to calculate $T_{\mathrm{B,\,min}}$ for any source from which we have measured the luminosity and variability time-scale (note that this does not take into account relativistic beaming)

$$T_{\mathrm{B,\,min}} = \frac{\Delta L_\nu}{8\pi k_{\mathrm{B}}\nu^2\tau^2}. \tag{4.13}$$

Using this approach we calculate the $T_{\mathrm{B,min}}$ for all the events in our sample, and present a histogram of the results in Figure 4.9.

It is interesting to note that if all the sources had the same brightness temperature and relation between variability time-scale and physical size, we would expect a relation between luminosity and time-scale of the form

$$L \propto \tau^2, \tag{4.14}$$

which is considerably shallower than the relation we observe (Figures 4.7 and 4.8), which is approximately

$$L \propto \tau^5. \tag{4.15}$$

This is illustrated by the lines of constant $T_{\mathrm{B,min}}$ overplotted in Figures 4.7 and 4.8. This is an unexpected result which is further discussed in Section 4.5.2.

4.3.3 Radio Transients Phase Space

In previous sections we identified the correlation between peak radio luminosity and the variability time-scales of synchrotron events. Here we combine those results with the sample of coherent sources, from the millisecond bursts seen from most pulsars and fast radio bursts, to the nanosecond shot emission seen from the Crab pulsar (Hankins et al. 2003, Keane 2013, Thornton et al. 2013), in order to present the entire luminosity – time-scale parameter space. Transients are often classified as either ‘beamformed’, i.e. those detected in high time-resolution pulsar-like observations where dedispersion is required, or ‘imaging’, i.e. sources can be identified in images and dedispersion is not required (Hassall et al., 2013). The boundary between these classes is often taken to be ~ 1 s, so that the synchrotron

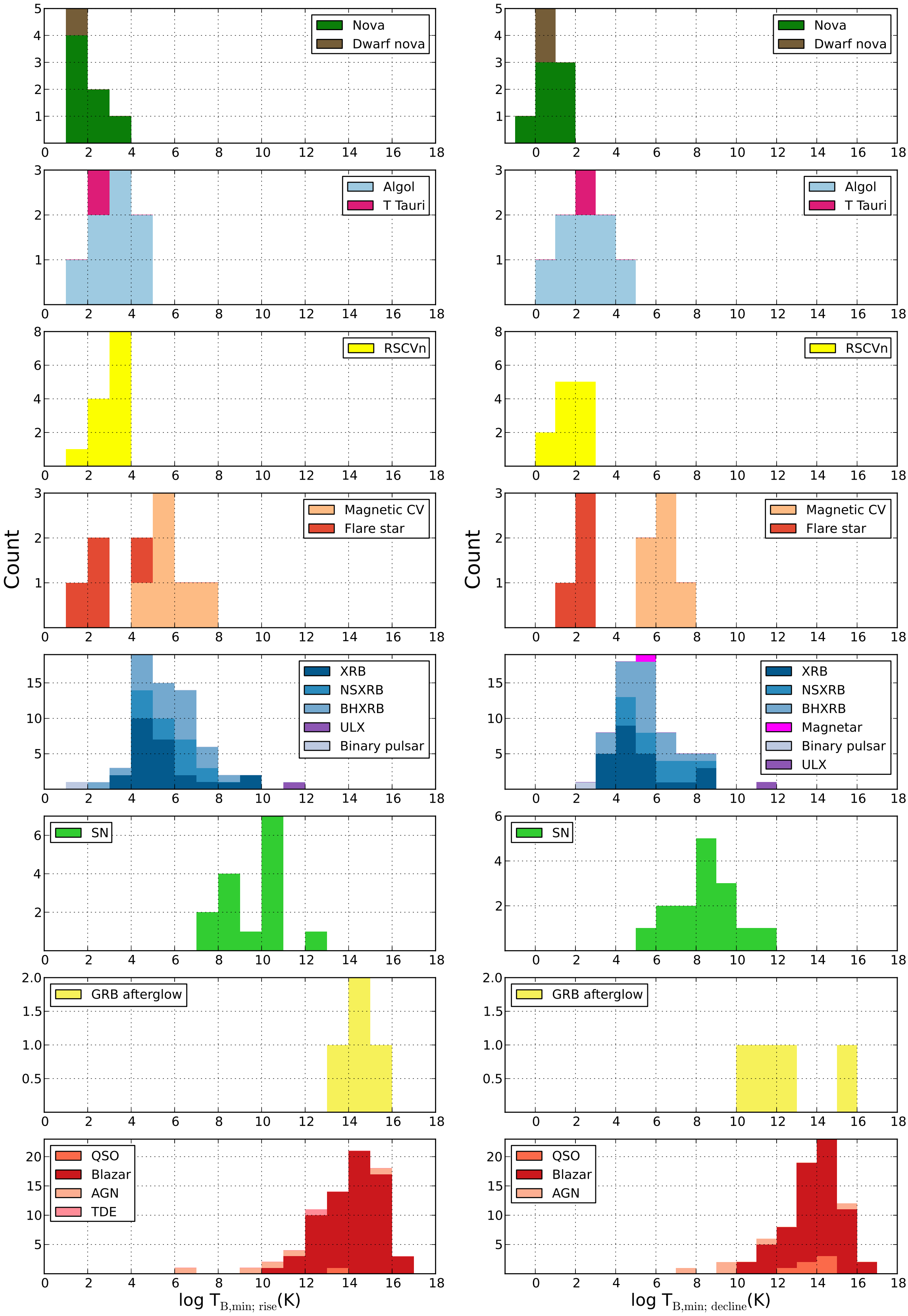

Fig. 4.9 The distribution of minimum brightness temperature, $T_{\mathrm{B,min}}$ for the flare events studied calculated for the rising (left) and declining phases (right).

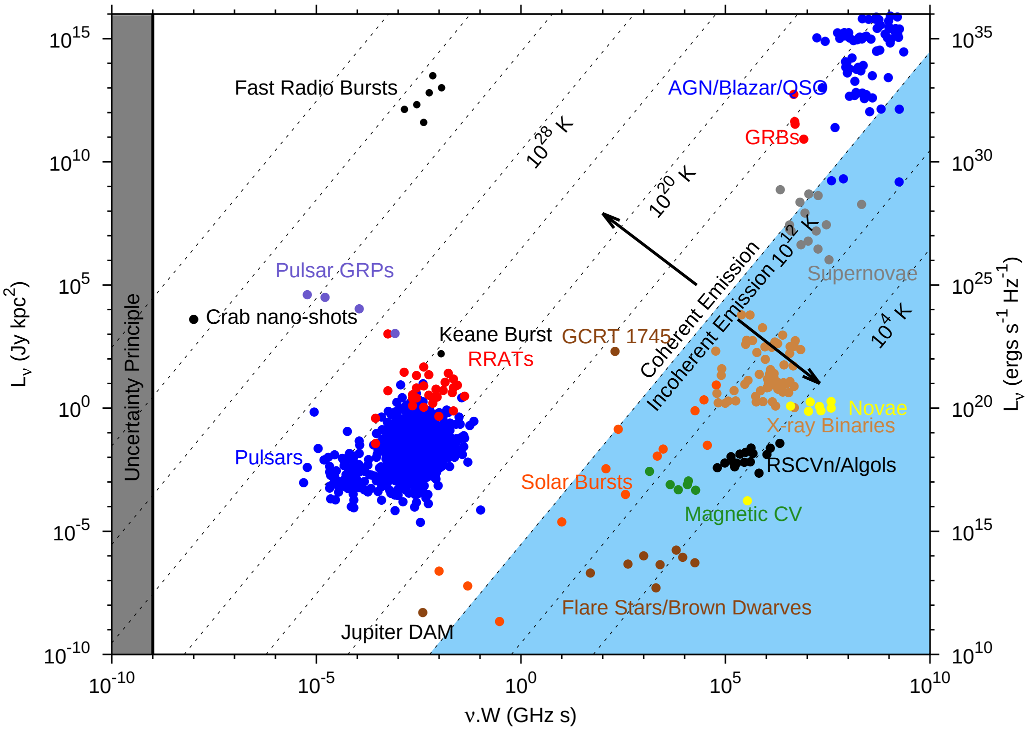

Fig. 4.10 Plotted is a variation of the Figure 4.7, with luminosity plotted against the product of the observing frequency ν and the time-scale of the flare/pulse width W over an even wider range of parameter space. This allows us to identify the sources of coherent radio emission (pulsars, fast radio bursts) for comparison with the more slowly varying synchrotron transients.

sources considered in Sections 4.2, 4.3.1 and 4.3.2 fall into the latter category. The extended parameter space is shown in Figure 4.10. We can see that, as expected, the relation we have determined (Table 4.1, Equation 4.15) does not apply to beamformed transients, which are all examples of coherent emission, but rather seems to be a manifestation of the physics underlying incoherent synchrotron emission only.

4.4 Extension to 1.4 GHz band

4.4.1 Data and Analysis

The analysis presented in this chapter is focused on the synchrotron flares observed in the frequency range of 5-8 GHz – the choice largely dictated by the availability of the data. Although the sample of sources observed at other wavelengths is – at this time – too small to make any definitive statements about the luminosity – time-scale relation, we can still explore the parameter space for the events which have been monitored and can be analysed. If we consider using the variability time-scales as an early classification technique for radio transients (Section 4.1.4), the frequency of 1.4 GHz can be especially useful in context of, for example, the upcoming MeerKAT transient surveys (Booth et al., 2009).

For the following analysis, we have compiled a sample of synchrotron events from 17 objects observed at ≈ 1.4 GHz. Detailed list of sources can be found in Table 4.12. The selection of flares, as well as the analysis, have been performed as described in Sections 4.2.2 and 4.2.3. Figure 4.11 shows the results of the measurements for rise (upper panel) and decline (lower panel) phases, plotted against the peak radio luminosities of the flares. Data points have been colour-coded in the following way. The sample of events observed at 1.4 GHz is shown in red, with the fit to the data represented by the black dashed line. The sample of 5-8 GHz sources analysed earlier has been overplotted (in light gray) for the reference, with the grey dashed line showing fit to the data. One pair of the data points has been highlighted within each of several classes of objects. These measurements (marked with a bold edge) correspond to the same flare observed at both 1.4 and 5-8 GHz (red and grey respectively) and include: GRB 030329, SN 1993J, V407 Cyg (nova), B1259-63 (binary pulsar), SS 433 (black hole X-ray binary) and SGR 1806-20 (magnetar, decline phase only).

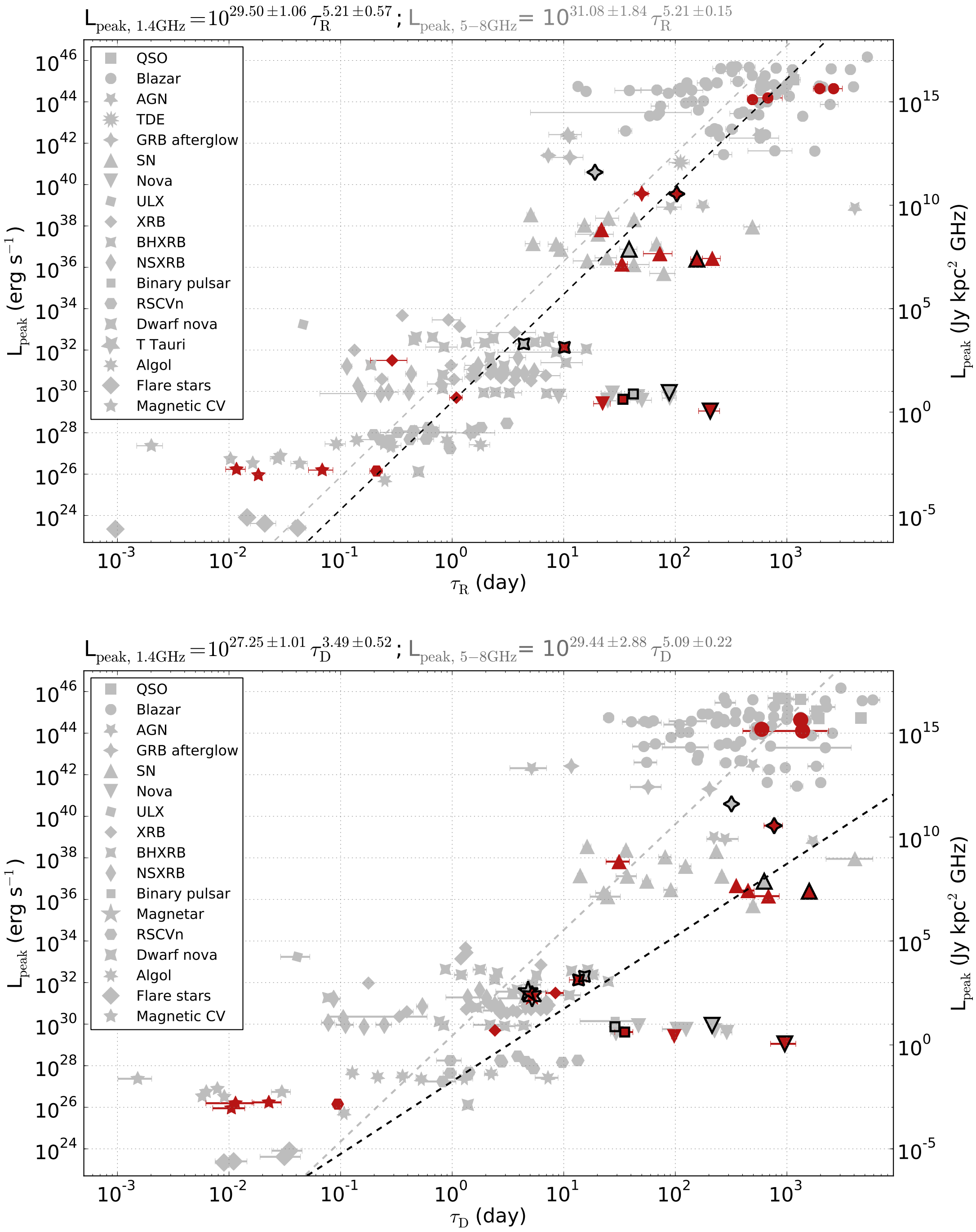

Fig. 4.11 Correlation between the luminosity and rise (upper panel) / decline (lower panel) rate for the extended sample of objects. Plotted in grey is the sample of synchrotron flares discussed in earlier sections, observed at 5-8 GHz. Overplotted in red is the additional sample of sources observed at the frequency of 1.4 GHz. Black and grey dashed lines correspond to the fit to the data for lower and higher frequencies respectively. Measurements for several individual sources have been cross-matched between the observed frequencies – those are marked with black bold edges and include: GRB 030329, SN 1993J, V407 Cyg (nova), B1259-63 (binary pulsar), SS 433 (black hole X-ray binary) and SGR 1806-20 (magnetar, decline phase only).

4.4.2 Results and Discussion

Quantitative comparison of the results obtained across the analysed frequencies is not possible due to the limited sample of flares representing the 1.4 GHz dataset. While the correlation between the luminosity and rise rate of the events is the same for both low and high frequency data ($L \propto \tau^5$), in case of decline rates the difference is more significant.

However, cross-matching of the individual outbursts shows that, in most cases, flares observed at lower frequency are fainter and their time-scale is longer compared to higher frequency – as expected for the evolution of synchrotron emitting sources (Section 4.1.2). In his paper, van der Laan gives a formula describing the evolution of the peak flux density with the observing frequency

$$F_{\mathrm{m}}(\nu_2) = F_{\mathrm{m}}(\nu_1)\left(\frac{\nu_1}{\nu_2}\right)^{-(7p+3)/(4p+6)}, \tag{4.16}$$

where $F_{\mathrm{m}}(\nu_1)$ and $F_{\mathrm{m}}(\nu_2)$ are peak flux densities at frequencies ν_1 and ν_2 respectively, and p is the energy distribution. Based on that, we can extrapolate our 5 GHz flux density measurements for a set of six sources highlighted in Figure 4.11 to the lower 1.4 GHz frequency assuming $p = 2$ for synchrotron emitting sources. Comparison of these predictions with our 1.4 GHz measurements shows that the observed values vary within a factor of 0.5–3 from what we expect based on the simple van der Laan model.

While the peak flux density of the synchrotron flare will be reached later when observed at lower frequencies, the difference in observed rise rates depends on the measurement method. The upper panel of Figure 4.12 shows light-curves for the same source observed at progressively lower frequencies. The middle and lower panels show variation of this figure where light-curves are plotted on different time and flux scales in order to illustrate different ways of measuring the rise rate. Fitting a power law function to the rise phase of the light-curve corresponds to fitting a linear function to the logarithmic flux plotted against

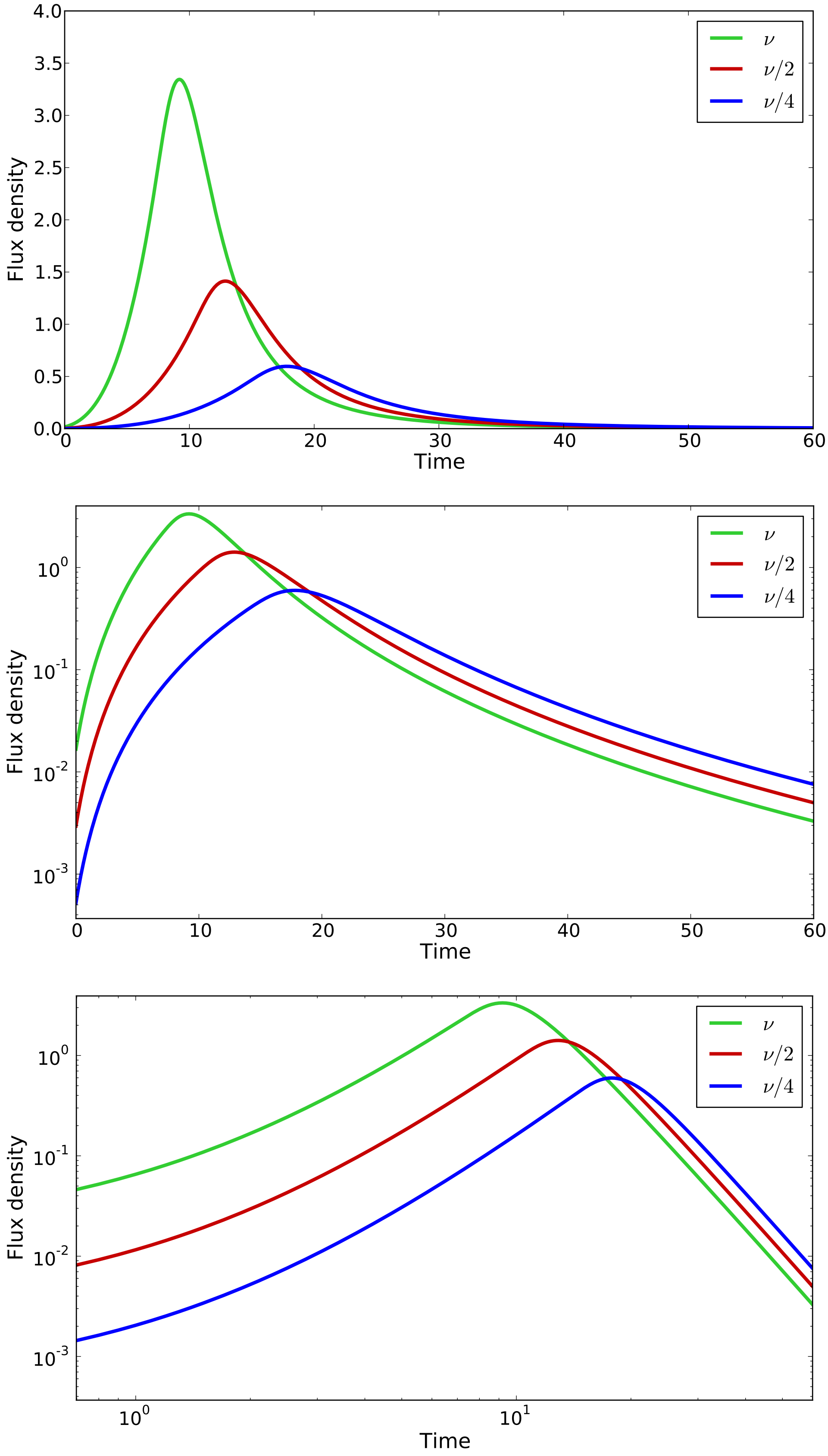

Fig. 4.12 Example radio light-curves simulated based on the van der Laan model, for the same source observed at three different frequencies (ν, $\nu/2$, $\nu/4$). Each panel shows the same set of light-curves plotted on different scales for the illustration: linear (upper figure), logarithmic flux density vs linear time (middle figure) and logarithmic (lower figure).

the logarithmic time (as shown in the lower panel of Figure 4.12). This illustration shows that the slope measured this way would be frequency independent.

The middle panel of Figure 4.12 shows the same set of light-curves, where the logarithmic flux is plotted against linear time. The rise/decline rates measured this way (as was done in our analysis) correspond to fitting an exponential function to the data. In this case, if measured close to the peak of the flare (which corresponds to the phases where optical depth $\tau \approx 1$), the rise/decline rates will be slower at lower frequencies. This agrees with the observed rise/decline rates measured for our sample of sources across 1.4 – 5 GHz frequencies. However, at very early stages of the outburst (where the optical depth is very high and the radiation at all frequencies is self-absorbed), as well as late into the decline phases (where $\tau << 1$ and the energy loss is dominated by the expansion processes), the rates we measure will be frequency independent. While the very early times of the outbursts, where the flux density is increasing rapidly, are often missed, radio transient surveys performed with sensitive instruments (such as SKA) are likely to be dominated by the detections of slowly declining synchrotron events, where the results are independent from the observing frequency. The discussed effect can also be useful in separating those detections from more recent events based on spectral information.

We have chosen a method of fitting exponential functions rather than a power law as it gave more consistent results – estimating the precise start time of the flare required for fitting power law model could not have been properly done across the entire data sample. Additionally, as shown by Canosa et al. (1997), even if the emission from the source is intrinsically a power law, the observational data can in certain cases be fit more accurately with an exponential function, due to the distortions of the signal caused by relativistic effects. Future observations could help to extend the sample of lower frequency data and make the discussion about the luminosity – time-scale correlation more conclusive.

4.5 Discussion and Conclusions

4.5.1 Time – Luminosity Correlation for Synchrotron Events

The work presented in this chapter compiled the analysis of the simplest measurable quantity of a synchrotron flare event, its rise/decline time, with its luminosity. The astrophysical objects from which the flares originate vary from flare stars to supermassive black holes in active galactic nuclei, and include both repeating phenomena and single cataclysmic events. The results show a broad correlation that exists across those classes, with peak luminosities ranging over 22 orders of magnitude and time-scales from minutes to longer than years. The following example illustrates why – as we observe – the most luminous events are expected to vary more slowly.

The main energy loss mechanism for these phenomena is the work done in expanding against the surrounding medium, and yet the maximum 3D expansion speed of a relativistic plasma is fixed at $c/\sqrt{3}$. Since the maximum (rest frame) brightness temperature (surface brightness) of a synchrotron emitting plasma (in equilibrium) is $\sim 10^{12}$ K, then the most luminous events are going to be associated with larger sources. We can describe the change of the sources size in time $r(t)$ by

$$r(t) = r_0 + \frac{c}{\sqrt{3}}t, \tag{4.17}$$

where r_0 is the initial size of the source. The scale factor ($\rho = r/r_0$ in the original model of van der Laan 1966), on which the observed flux is strongly dependent (the flux rises as ρ^3 in van der Laan during the optically thick phase), is therefore going to evolve more slowly for the most luminous sources

$$\rho(t) = 1 + \frac{c}{\sqrt{3}r_0}t. \tag{4.18}$$

In other words, a doubling in size will result – in this simple model – in the same relative flux change, but will take longer for more luminous and larger sources. The upper panel in Figure 4.13 shows the relation between the relative change in the size of the source ρ and the evolution time for several values of the initial size of the source r_0. The lower panel of the same figure shows example light-curves for three sources with the same range of initial size r_0. Of course, as discussed in Section 4.1.3, since van der Laan there have been a large number of further, more complex models for different scenarios. It was therefore not at all obvious while starting this project, that a compilation such as this would result in the rather straightforward relation between rise/decay times and radio luminosity that we have found.

The relation between variability time-scales and peak radio luminosities obtained for incoherent events can be extended to parameter space covering coherent bursts as well. Those events varying on times less than $\approx$ 1s can reach brightness temperatures of $\approx 10^{40}$ K. However, the broad correlation of $L \propto \tau^5$ obtained for the incoherent events does not apply to those classes of objects.

4.5.2 Brightness Temperature

As demonstrated in Section 4.3.2, having the variability time-scales and peak radio luminosities of the event, we can estimate its minimum brightness temperature. Results of the analysis show, that the brightness temperature estimated this way is a rising function of sources luminosity. This means that the relation we find, $L \propto \tau^5$, is much steeper than that which would be expected for a similar set of phenomena with the same brightness temperature, $L \propto \tau^2$. Two possible explanations for this effect are discussed here in more detail.

Intrinsic Properties of Sources

If the discrepancy between the observed luminosity – time-scale relation and that expected for objects with the same brightness temperature originates from the intrinsic properties of the

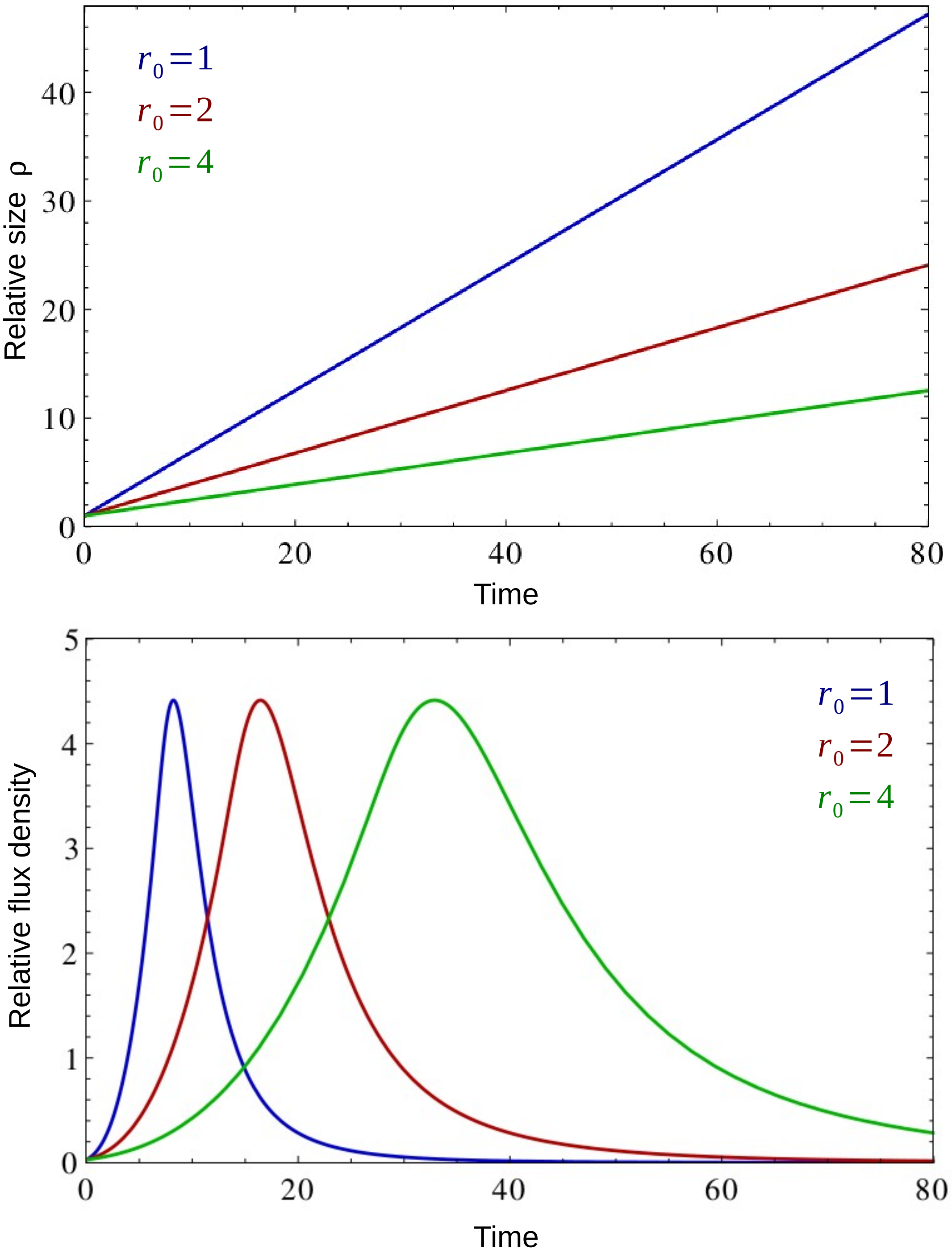

Fig. 4.13 *Upper:* The relation between the fractional change of the size of the source and the evolution time. As discussed in Section 4.5.1, more luminous, and therefore larger sources evolve on longer time-scales. The presented examples have been calculated for increasing values of the initial size r_0, with the expansion velocity of $c/\sqrt{3}$ (where c=1 to simplify the calculations). *Lower:* Example light-curves calculated for three sources with different initial size r_0 (based on van der Laan model, van der Laan 1966), showing that for larger sources their flaring time-scales are longer.

sources, it could be perhaps due to a systematically varying relation between the true radius and the variability time-scale. While estimating the minimum brightness temperatures of synchrotron events (Section 4.3.2), we assume the radius of the emitting region corresponds to the maximum possible physical size of the source $r = c\tau$. However, it is likely that for a given time-scale, the true radius of the emitting region is considerably smaller than this, and our estimation of the T_B is severely underestimated (Figure 4.14). This is the case for flare stars for example, where the Alfvén speed should be considered rather than c. This would mean a velocity of 10^6 ms^{-1} (Mitra-Kraev et al., 2005), which would change the estimated minimum brightness temperatures by factor of 10^4. Figure 4.15 schematically shows the shape of constant $T_{\mathrm{B,min}}$ lines we would expect if this effect was accounted for. As we approach the phase space populated by lower luminosity sources, for which the velocities fall into non-relativistic regime, the minimum brightness temperature is likely to be higher, therefore the direction of the constant $T_{\mathrm{B,min}}$ lines is steeper than originally shown in Figure 4.7. However, it is hard to see this explaining everything: since the sound speed of an ultrarelativistic plasma is $\sim c/\sqrt{3}$ and we believe that this condition should hold for both AGN and XRBs, both of which seem to have highly relativistic jet plasmas, it is not clear why they should be systematically two orders of magnitude different in $T_{\mathrm{B,min}}$ from each other. The actual geometry of relativistic jets is likely to be rather linear and so a 3D expansion at $c/\sqrt{3}$ is not likely, but could/should be similar for XRBs and AGN. On the other hand, an increasing energy density with luminosity does not seem obvious, either, since the jets of AGN are anticipated to be *lower* density than those of XRBs. At a given Eddington ratio the luminosity L of the source is proportional to its mass M, $L \propto M$. With the area of the jet $A \propto M^2$, we get the energy density $L/A \propto M^{-1}$, which means that it should be lower for the jets of more massive AGN.

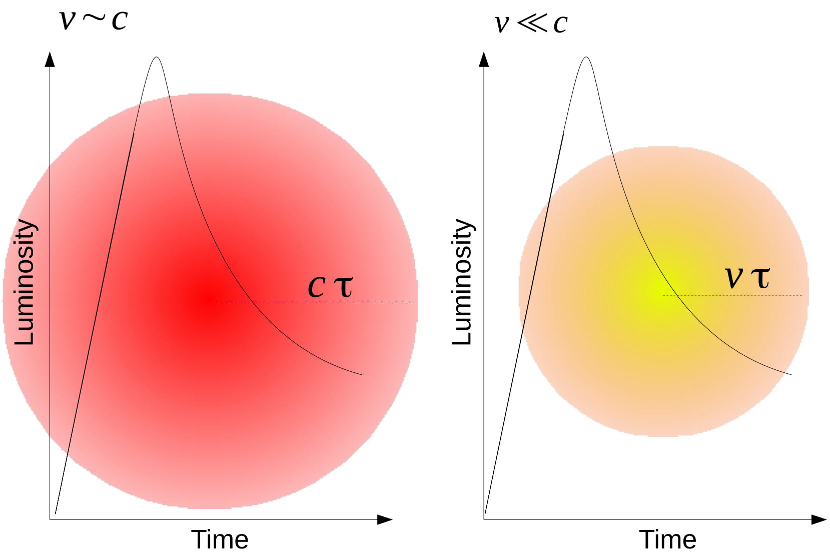

Fig. 4.14 Illustration of a possible explanation for the estimated $T_{\mathrm{B,min}}$ distribution. Figure on the left shows the case, where the minimum brightness temperature estimated at the observed peak radio luminosity corresponds to the maximum physical size of the emitting region, $r \approx c\tau$. However, if the speed at which the signal propagates through the source, v, is significantly lower than c (figure on the right), the actual size of the source is smaller. Because the estimated minimum brightness temperature $T_{\mathrm{B,min}} \propto L/r^2$, a smaller radius of the emitting region corresponds to a higher brightness temperature.

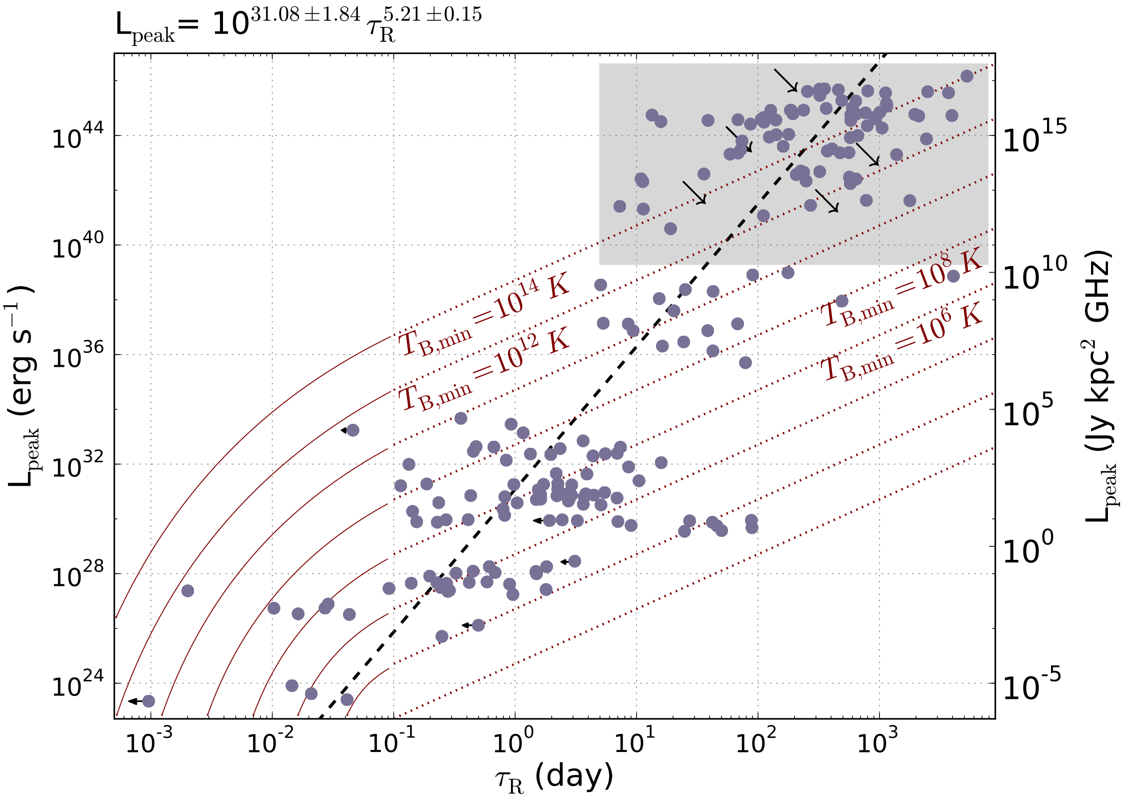

Fig. 4.15 This plot shows Figure 4.7 schematically modified to illustrate possible effects that could explain the observed increase in the estimated minimum brightness temperature with luminosity. Error bars and differentiation between classes have been removed for clarity. In the lower luminosity end of the sample, minimum brightness temperatures might be overestimated due to the smaller radius of the emitting region. Constant $T_{B,\mathrm{min}}$ lines plotted in Figure 4.7 would in fact need to turn down while approaching lower luminosity sources. At the other end of the plot the most luminous sources in the sample are expected to be relativistically beamed. The actual luminosity of these objects could be significantly lower, and the variability time-scale slower than what we observe (marked with arrows). The likely result of both effects is to reduce the actual spread in the intrinsic values of T_{B}.

Relativistic Beaming

Can relativistic beaming explain the trend perhaps? This would result in a larger apparent $T_{\mathrm{B,min}}$, and it is certainly the case that blazars and GRB afterglows, which make up a large fraction of the luminous end of the sample, are pointed towards us. Such sources will appear to be brighter and vary faster than in their comoving frames, resulting in a higher apparent minimum brightness temperature. This effect is schematically shown in Figure 4.15, where arrows in the grey box indicate the expected direction that the AGN sample would move if we could account accurately for Doppler boosting. Therefore, in a flux-limited sample of such jetted sources one would expect to see an increase in $T_{\mathrm{B,min}}$ with luminosity. This effect has been investigated for AGN in some detail (e.g. Homan et al. 2006; Vermeulen and Cohen 1994). However, it seems unlikely that this alone can explain the near-monotonic trend towards higher $T_{\mathrm{B,min}}$ with luminosity across our entire sample for at least two reasons: (i) some of the objects in the sample – e.g. supernovae, flare stars – are not expected to be significantly boosted, (ii) the lowest-luminosity population of relativistic sources – the X-ray binaries – are actually an *X-ray selected* sample which in general are de-boosted due to large angles to the line of sight.

Bringing in both these effects to the picture of the obtained time-luminosity correlation could decrease the discussed gap between the expected and fitted relation. However, neither of the considered interpretations fully explains the observed discrepancy. The real origin of the trend is likely to be a combination of both effects, but we cannot rule out a dominant effect which we have not considered here.

4.5.3 Future Work

Of course as well as being astrophysically interesting, the relation opens up the possibility of using variability time-scale as an early classifier of radio transient events which may be discovered by future wide-field monitoring in the radio band (see Fender and Bell 2011 and references therein). A faint (sub-mJy) event could be anything from a flare star to a supernovae, and yet within minutes/hours (probably) and days (certainly) it would be obvious from the rise time which class of object it was likely to have been. However, the likelihood of a given event cannot be simply read from the presented figures, since these are compiled from highly biased samples. In Chapter 5 I will present the extended analysis of the compiled data, where the process of selection of flaring events is automated and the results are convolved with estimates of the areal density (rates) of the different classes of objects.

Table 4.2 Sample of AGN, blazars (including flat spectrum radio quasars) and a compact steep spectrum radio quasar (QSO) used in the analysis.

Source	Distance (Mpc)	Reference	Distance reference
0224+671	2981	GBI	MOJAVE[1]/ NED[2]
0235+164	6142	Roy et al. (2000)	MOJAVE / NED
0336-019	5434	GBI	MOJAVE / NED
0458-020	18551	Pyatunina et al. (2006)	MOJAVE / NED
0528+134	16418	Pyatunina et al. (2006), GBI	MOJAVE / NED
0605-085	5577	Kudryavtseva et al. (2011)	MOJAVE / NED
0850-121	3281	GBI	MOJAVE / NED
0851+202	1577	GBI	MOJAVE / NED
0954+658	1951	Marchili et al. (2012), GBI	MOJAVE / NED
1237+049	13441	GBI	MOJAVE / NED
1328+254	7093	GBI	MOJAVE / NED
1413+135	1232	GBI	MOJAVE / NED
1622-297	5142	GBI	MOJAVE / NED
1749+096	1673	GBI	MOJAVE / NED
1803+784	4107	Britzen et al. (2010)	MOJAVE / NED
2004-447	1192	Gallo et al. (2006)	Gallo et al. (2006)
2005+403	13205	GBI	MOJAVE / NED
2223-052	10138	Kudryavtseva and Pyatunina (2006)	MOJAVE / NED
3C120	143	Volvach et al. (2010)	MOJAVE / NED
3C273	748		
3C279	3071		
3C345	3473		
3C454.3	5489		
BL Lacertae	305	Villata et al. (2004), GBI	MOJAVE / NED
CTA 102	6943	Kudryavtseva and Pyatunina (2006)	MOJAVE / NED
NGC 4278	14.9	Giroletti et al. (2005)	Usher et al. (2013)
NGC 7213	22	Bell et al. (2011)	Emmanoulopoulos et al. (2013)
NRAO 150	11193	Chen et al. (2001)	MOJAVE / NED
NRAO 530	5834	Lu et al. (2012), Pyatunina et al. (2006)	MOJAVE / NED
J1644+57	1845	Zauderer et al. (2013b)	Levan et al. (2011)
III zw2	403	Salvi et al. (2002)	MOJAVE / NED

[1] http://www.physics.purdue.edu/astro/MOJAVE/index.html

[2] http://ned.ipac.caltech.edu/

Table 4.3 Supernovae sample used in the analysis.

Source	Distance (Mpc)	Reference	Distance reference
SN 1980K	5.9	Weiler et al. (1992)	Milisavljevic et al. (2012)
SN 1988Z	93	van Dyk et al. (1993)	Schlegel and Petre (2006)
SN 1993J	3.6	Pérez-Torres et al. (2001)	Pérez-Torres et al. (2001)
SN 1994I	8.9	Weiler et al. (2011)	Weiler et al. (2011)
SN 1998bw	38	Kulkarni et al. (1998)	Kulkarni et al. (1998)
SN 2003bg	19.6	Soderberg et al. (2006)	Soderberg et al. (2006)
SN 2003L	92	Soderberg et al. (2005)	Soderberg et al. (2005)
SN 2004cc	18	Wellons et al. (2012)	Wellons et al. (2012)
SN 2004dk	23		
SN 2004gq	26		
SN 2008ax	9.6	Roming et al. (2009)	Pastorello et al. (2008)
SN 2008iz	3.5	Marchili et al. (2010)	Marchili et al. (2010)
SN 2011dh	8.4	Krauss et al. (2012)	Krauss et al. (2012)

Table 4.4 Gamma Ray Bursts used in the analysis.

Source	Distance (Mpc)	Reference	Distance reference
GRB 970508	5299	Frail et al. (2000)	Frail et al. (2000)
GRB 030329	802	Mesler et al. (2012)	van der Horst et al. (2008)
GRB 060418	10917	Cenko et al. (2010)	Ellison et al. (2006)
GRB 110709B	36523	Zauderer et al. (2013a)	Zauderer et al. (2013a)

Table 4.5 Classical / dwarf / recurrent novae used in the analysis.

Source	Distance (Mpc)	Reference	Distance reference
RS Oph	0.0016	O'Brien et al. (2006)	O'Brien et al. (2006)
Sco 2012	0.0067	Weston et al. (2014)	Weston et al. (2014)
SS Cyg	0.000114	Körding et al. (2008)	Miller-Jones et al. (2013)
T Pyx	0.0048	Nelson et al. (2014)	Nelson et al. (2014)
V407 Cyg	0.003	Chomiuk et al. (2012)	Chomiuk et al. (2012)
V1500 Cyg	0.00135	Roy et al. (2012)	Slavin et al. (1995)
V1723 Aql	0.005	Krauss et al. (2011)	Krauss et al. (2011)
V1974 Cyg	0.0018	Hjellming (1996)	Kato and Hachisu (2005)

Table 4.6 A sample of X-ray binaries, including black hole X-ray binaries (BHXRB), neutron star X-ray binaries (NSXRB), binary pulsar and ultraluminous X-ray source (ULX) used in the analysis.

Source	Distance (Mpc)	Reference	Distance reference
Aql X-1	0.005	GBI	Galloway et al. (2008)
B1259-63	0.0023	Johnston et al. (1999)	Shannon et al. (2014)
CI Cam	0.01	GBI	Bartlett et al. (2013)
Cir X-1	0.0078	Soleri et al. (2009)	D'Aì et al. (2012)
Cyg X-1	0.00186	GBI	Miller-Jones (2014)
Cyg X-2	0.011	GBI	Galloway et al. (2008)
Cyg X-3	0.0072	Molnar et al. (1988), GBI	Ling et al. (2009)
GRO J1655-40	0.0032	Hannikainen et al. (2000)	Miller-Jones (2014)
GRS 1915+105	0.011	GBI	Miller-Jones (2014)
GX13+1	0.007	Homan et al. (2004)	Homan et al. (2004)
GX17+2	0.0075	GBI	Church et al. (2012)
GX 339-4	0.008	Gallo et al. (2004)	Gandhi et al. (2010)
LS 5039	0.0029	Ribó et al. (1999)	Moldón et al. (2012)
LSI+61°303	0.002	GBI	Dhawan et al. (2006)
MAXIJ1836-194	0.008	Trushkin et al. (2011)	Russell et al. (2013)
Sco X-1	0.0028	GBI	Bradshaw et al. (1999)
SGR 1806-20	0.009	Gaensler et al. (2005)	Tendulkar et al. (2012)
SS 433	0.0055	Trushkin et al. (2008), GBI	Blundell and Bowler (2004)
XTE J1550-564	0.00438	Hannikainen et al. (2001)	Steiner et al. (2011)
XTE J1748-288	0.008	Rodriguez and Prat (2008)	Brocksopp et al. (2007)
XTE J1859+226	0.0042	Rodriguez and Prat (2008)	Shaposhnikov and Titarchuk (2009)
M31 ULX	0.78	Middleton et al. (2013)	Middleton et al. (2013)

Table 4.7 RSCVn used in the analysis.

Source	Distance (Mpc)	Reference	Distance reference
CF Oct	0.000194	Slee et al. (1987)	Borisova et al. (2005)
HR1099	0.00003068	GBI	Huenemoerder et al. (2013)
UX Ari	0.00005	GBI	Peterson et al. (2011)

Table 4.8 Algol systems used in the analysis.

Source	Distance (Mpc)	Reference	Distance reference
Algol	0.000029	GBI	Peterson et al. (2011)
δ Lib	0.000095	GBI	Bakış et al. (2006)
RZ Cas	0.000063	Audard et al. (2005)	Audard et al. (2005)

Table 4.9 T Tauri included in the analysis.

Source	Distance (Mpc)	Reference	Distance reference
V773 Tau	0.0001328	Massi et al.	Torres et al. (2012)

Table 4.10 Magnetic CVs used in the analysis.

Source	Distance (Mpc)	Reference	Distance reference
AE Aqr	0.000102	Bastian et al. (1988), Abada-Simon et al. (1993)	Duerbeck (1999)
V834 Cen	0.000086	Wright et al. (1988)	Araujo-Betancor et al. (2005)

Table 4.11 Flare stars used in the analysis.

Source	Distance (Mpc)	Reference	Distance reference
AD Leo	0.0000047	Smith et al. (2005)	Smith et al. (2005)
AU Mic	0.00001	Smith et al. (2005)	Smith et al. (2005)
UV Ceti	0.0000026	Smith et al. (2005)	Smith et al. (2005)
YZ CMi	0.0000059	Smith et al. (2005)	Smith et al. (2005)

Table 4.12 Sample of sources observed at 1.4 GHz frequency used in the analysis (with exeption of SS 433 and Cyg X-3, which were observed at 1 GHz).

Source	Type	Distance (Mpc)	Reference	Distance reference
0235+164	Blazar	6142	Altschuler et al. (1984)	MOJAVE / NED
0333+32	Blazar	8848	Altschuler et al. (1984)	MOJAVE / NED
GRB 030329	GRB	802	Mesler et al. (2012)	van der Horst et al. (2008)
GRB 110328	GRB	1899.3	Wiersema et al. (2012)	Wiersema et al. (2012)
SN 1994I	SN	8.9	Weiler et al. (2011)	Weiler et al. (2011)
SN 2001gd	SN	20	Stockdale et al. (2007)	Stockdale et al. (2007)
SN 1993J	SN	3.6	Pérez-Torres et al. (2001)	Pérez-Torres et al. (2001)
SN 2001ig	SN	11.5	Ryder et al. (2003)	Ryder et al. (2003)
SN 1998bw	SN	38	Kulkarni et al. (1998)	Kulkarni et al. (1998)
V407 Cyg	Nova	0.003	Chomiuk et al. (2012)	Chomiuk et al. (2012)
RS Oph	Nova	0.0016	Hjellming et al. (1986)	O'Brien et al. (2006)
SS 433	BHXRB	0.0055	Trushkin et al. (2006); Trushkin et al. (2008)	Blundell and Bowler (2004)
Cyg X-3	XRB	0.008	Trushkin et al. (2006)	Ling et al. (2009)
B1259-63	Binary pulsar	0.0023	Johnston et al. (1999)	Shannon et al. (2014)
SGR 1806-20	Magnetar	0.009	Gaensler et al. (2005)	Tendulkar et al. (2012)
HR 1099	RSCVn	0.00003068	Jones et al. (1996)	Huenemoerder et al. (2013)
AE Aqr	Magnetic CV	0.000102	Bastian et al. (1988)	Duerbeck (1999)

Chapter 5

Method of Classifying Radio Transients

This work has been submitted to the MNRAS journal as Pietka, Fender, Staley & Pretorius

5.1 Introduction

5.1.1 Motivation

In the coming years, the next generation of radio telescopes are expected to survey large areas of sky to a sensitivity which could see the discovery of hundreds of transient sources (Fender et al., 2015). Previous discoveries of radio transients proved that relying solely on radio data makes it extremely difficult to validate both the nature, as well as the reality of the source (Bower et al. 2007, Stewart et al. 2016) and that it is vital they are supported by simultaneous multiwavelength observations or rapid follow up. On the other hand, with a rate of transient candidates as high as expected, it will not be possible to follow up each event with other multiwavelength instruments. However, if the nature of the source is constrained as early as possible, decision-making strategies can be created to follow up the type of events relevant to specific science goals.

5.1.2 Previous Automatic Classification Attempts

The importance of the automatic classification of light-curves has been discussed before in the context of deep surveys carried out at optical wavelengths, with attempts to include automatic classification of transients into optical surveys (Djorgovski et al. 2012; Saglia et al. 2012). Extended investigations of different ways to approach this task include developing classification techniques based on machine learning methods (Richards et al., 2011), Bayesian theory (Pichara and Protopapas, 2013), density approach (eliminating direct measurements of features such as magnitude or color; Kügler et al. 2015), fitting non-complete light-curves (Lo et al., 2014b) and other non-parametric techniques (Varughese et al., 2015). Those methods have been developed using archival optical light-curves as training datasets, as well as X-ray transients (Lo et al. 2014a, with a supervised learning technique implemented). For radio data, Rebbapragada et al. (2012) test different classification algorithms on simulated light-curves in preparation for the ASKAP VAST survey. Most of these methods, although they work effectively on sparse and noisy datasets, require the light-curve/flare to be (mostly) complete. In this work, however, we are focused on making an initial classification of the source, based on the early information about its radio light-curve.

5.1.3 Method

For any transient candidate discovered in a blind radio survey, the most basic measurable property of the light-curve is its variability time-scale. In Chapter 4 we have shown that a broad correlation between the peak radio luminosity L and the variability time-scales τ, approximately $L \propto \tau^5$, exists for variable synchrotron emitting sources, with each individual class occupying a constrained range in luminosity and time-scale space. This correlation offers an opportunity to classify new sources based on the radio data only. The method of classification presented here is based upon the assumption that at the time of discovery of a radio transient, its distance is unknown (unless a counterpart at other wavelengths is immediately identified). This means that the information about the luminosity is lost, and the discussed relation (Figures 4.7 and 4.8) is reduced to a distribution of the variability time-scales. This distribution provides a reference point against which we can compare the measurements of time-scales taken for any newly discovered transient candidate.

It should be noted that the results presented in Chapter 4 were based on the analysis of a sample of single flaring events manually selected from various radio light-curves. However, if we were to create an early transient classification tool based on those results, the analysis should be done in a reproducible way, such that the bias introduced by identifying flares by eye as it was done before is minimized. In order to do that, we have developed software which automatically identifies and selects flaring events from radio light-curves. Our routine is based on a simple thresholding approach, where any variability of the light-curve above a chosen flux density threshold is defined as a ’flare’. Having a set of flaring events selected this way, we have re-analysed the data as in Chapter 4.

5.1.4 Incompleteness of the Data

An important aspect of the presented analysis which needs to be carefully addressed is the bias associated with our sample of radio light-curves. The number of objects analysed within each class reflects the frequency and quality of observations rather than the actual sky density of those sources. Therefore, in order to accurately predict the probability of finding a given class of object, this effect needs to be accounted for. Although the exact areal densities of analysed classes of objects are not well known, we attempt to estimate those values and convolve them with the obtained distribution of rise/decline rates. This allows us to create an early classification tool, which makes it possible to narrow down the potential class of the radio transient candidate.

5.2 Automatic Selection of Flares

This section was written with contribution from Tim Staley (University of Oxford)

5.2.1 Overview of Flare Identification Methods

There are a number of possible approaches to measuring time-scales, and in particular flaring time-scales, in time-series data. Perhaps the simplest and most intuitive approach is to adopt a given threshold and designate any contiguous sections of the time-series above that threshold as a 'flare'. A time-scale measurement can then be obtained by measuring the time spent above the threshold level, but of course this requires that we wait for the flare to subside. Alternatively we may attempt to fit a model of some kind to any data points already recorded. This approach has often been adopted in the past (Lo et al., 2014b) due to its relative simplicity, robustness, and ease of implementation. Depending on the model-fitting requirements the thresholding approach can also be extremely computationally efficient, and hence suitable for real-time applications.

However, there are several disadvantages to the basic thresholding approach. First, finding a suitable threshold level can be a subjective process. If sources of noise are well characterised then a threshold can be chosen on the basis of a calculated false-positive rate, but this may not be possible in all cases. Even if instrument characteristics are well known, an astronomical source may display low-level intrinsic variability which is qualitatively different to the rapid flux-rise-and-decay characteristic of a flaring event. As such it may be necessary to devise some kind of calibration technique (as we do in this work) or even to manually pick a suitable threshold level. The second problem is that of choosing a suitable model for flare-fitting, which again is often somewhat arbitrary, although hopefully motivated by knowledge of the physical processes at work. Additionally, simple thresholding provides no means of separating multiple-superimposed flares, which degrades the accuracy of any model fits. Finally, a point-wise threshold will always lose some sensitivity compared to more sophisticated approaches, if enough is known about the flare-morphology to apply an effective matched-filter.

In the more general context of time-scale measurement, model-free metrics such as autocorrelation time and other metrics for aperiodic variability (Findeisen et al., 2015) can be applied, but typically require a large amount of variable time-series data to work effectively. Since we are interested in time-scales as an early-time classification tool, we do not consider these approaches further here.

More advanced change-or-flare-detection techniques typically take a probabilistic approach. As such they give a more rigorous and informative measure of the time-series data, at the cost of additional computational time and complexity. One possibility might be application of the Bayesian Blocks algorithm (Scargle, 1998) for a model-free probabilistic method of change-detection. This side-steps the problem of threshold-determination, but again does not provide an early-time estimate of characteristic time-scale. If a reasonable model can be chosen, then Monte-Carlo methods can be applied to estimate the likelihood of a flare presence with excellent sensitivity (Pitkin et al., 2014), or even to dissect the time-series into multiple superimposed flares (Huppenkothen et al., 2015), though this requires significant computational time. A thorough investigation of the relative accuracy and efficacy of such methods would be interesting, but is outside the scope of this work.

For this study we apply a thresholding approach with a simple exponential model. This provides a reasonably robust time-scale estimation for modest computational effort, albeit with some limitations to applicability, as detailed below.

5.2.2 Automatic Flare Finder (AFF)

The flare-identification routine we tested is relatively unsophisticated, but nonetheless provided a reproducible means of characterising flare time-scales for this work. It uses a simple thresholding approach, as follows: given a pre-determined quiescent or background flux level estimate, b, and an estimate of the signal variation due to noise, σ (rms), the routine first steps through the data looking for datapoints x where the flux f_x is more than 5σ above the quiescent flux:

$$x : \qquad f_x > b + 5\sigma ; \tag{5.1}$$

these are referred to as the 'trigger' points. Once a trigger is found, the algorithm searches for the nearest datapoints before and after the trigger which have flux less than 1.5σ above the quiescent flux-level, these are designated as the flare start and end.

The problematic part of this process is determining a suitable quiescent / background flux level, and estimating the levels of signal variation present when the source is not undergoing an outburst. For a source which has a well-sampled long-term light-curve encompassing extended periods of quiescence, the first problem – 'background' flux-level estimation – is straightforward; simply taking the median flux level provides a reasonable estimate. However, when analysing a light-curve which displays flares for a significant fraction of data-period, the median may overestimate the background level. The second problem, estimating the quiescent low-level variance, is harder. Again considering the ideal case of a well-sampled long-baseline light-curve, at some level we could simply use the formal errors on the datapoints and designate anything greater than 5σ above the median a flare. However, many of the light-curves analysed for this work display low-level variation which does not subjectively qualify as a flare, but which is nonetheless larger than would be expected from the formal errors, and appears persistent over multiple datapoints (e.g. SS 433, as shown in Figure 5.1) – we designate this as intrinsic quiescent variation (though varying telescope systematic noise-levels cannot be ruled out without access to the original raw data). To avoid the need to manually change the σ-threshold for each dataset according to the level of quiescent variation, we required an alternative method of estimating the low-level variation. For this purpose, we employed the sigma-clipping routine from the *astropy* library (Astropy

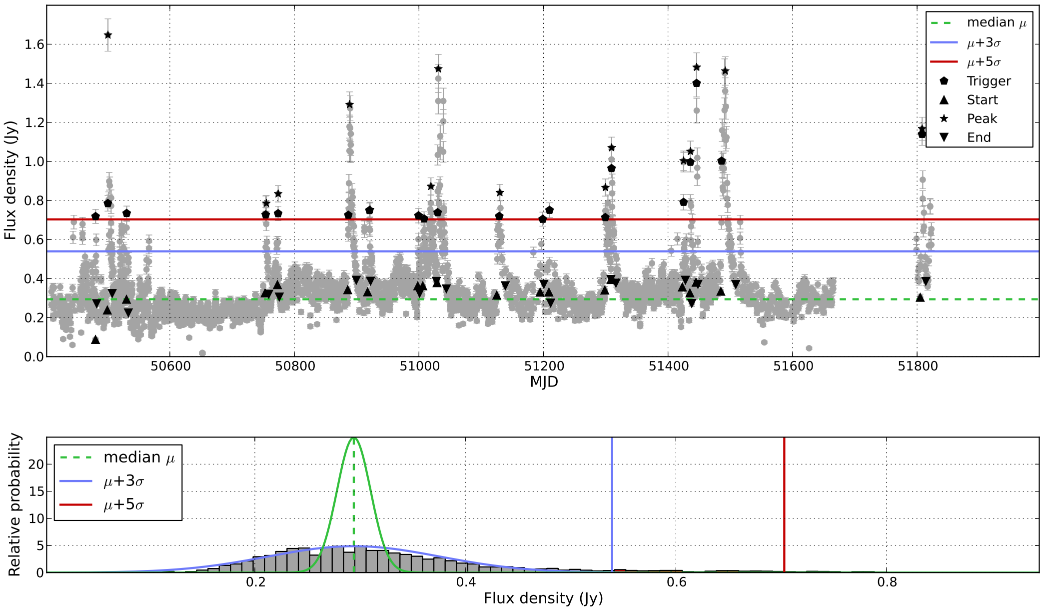

Fig. 5.1 An example of the detection of flaring events in the radio light-curve of the binary SS 433 (GBI). *Upper panel*: the light-curve of the source and flaring events selected by the Automatic Flare Finder (AFF). Marked with the dashed green line is the estimated quiescent flux level (labelled "median" in the key). The blue and red lines indicate the variation above the quiescent level by 3σ and 5σ respectively. The black symbols on each flare mark: start/end of the flare (triangles), datapoint triggering the flare detection (pentagons) and the peak of the flare (stars). *Lower panel*: histogram of the flux density values for the light-curve after sigma clipping has been applied. Flare-threshold values of 3σ and 5σ are marked by the blue and red vertical lines respectively. The curve overplotted in blue represents a Gaussian distribution with median and standard deviation matched to the sigma-clipped data. Curve overplotted in green represents a Gaussian distribution of the same median, but with standard deviation matched to the formal errorbars on the flux-density measurements, clearly showing that the formal errorbars underestimate the low-level variability in this light-curve.

Collaboration et al., 2013), using the default clipping-threshold of 3 standard deviations, and iterating until convergence. This means estimating the median value of the whole light-curve, clipping all the points which are above 3 standard deviations and repeating the procedure until no more points are rejected. For some of the light-curves we analysed this does a good job of masking the high-flux outlier datapoints representing flares, however, alternative methods of finding the background and low-level variation for light-curves which require a more specific approach are discussed in Section 5.4.1. We then estimate the median and standard deviation of the remaining unmasked ‘quiescent’ data, and use these quantities for the values of b and σ in equation 5.1. Figure 5.1 shows an example of the flares identified in a GBI light-curve for the X-ray binary SS 433.

The flare identification routine described in this section was initially developed by Tim Staley (University of Oxford). Work presented in this chapter is based on this method, which was further developed (as will be discussed in the following sections).

5.3 Data

The list of objects included in the following analysis span a broad range of radio variable sources and is the same as the one described in Chapter 4 (a detailed list can be found in Tables 4.2 – 4.11 at the end of Chapter 4). In this chapter, I also discuss the effect scintillating sources and extreme scattering events (Section 1.5.2) will have on our ability to classify transients based on their variability time-scales. Those additional sources, which were not included in the previous analysis (Chapter 4), are summarised in Tables 5.5 and 5.6 at the end of this chapter. As mentioned in Sections 5.1 and 5.2.2 in order to minimize the bias associated with the manual selection of flares, I use the complete light-curves available for each object/event and select individual outbursts using the flare finding routine. However, the automated method requires both flux density and the associated error measurements to be available for each light-curve (Section 5.2.2). Obtaining those was straightforward for the GBI data sets, thanks to the easy access to archival data. Detailed measurements were also specifically stated for some of the light-curves compiled from the literature. In all the other cases where the uncertainties of the flux density measurements were not available, I have estimated them based on the published figures (usually as ten per cent of flux density measurement).

5.4 Analysis

The routine for selecting flaring events from radio light-curves presented in Section 5.2.2 sets a number of restrictions on the analysed datasets. It requires the light-curve to be long enough in relation to the duration of the flare, such that the background flux level (excluding flares) can be accurately estimated. The light-curve also needs to be sufficiently noise-free in order to avoid false detections. While in an ideal case, periods of both quiescent emission as well as flaring events would be well sampled, the quality of the real data varies significantly across the sample. Data provided by the GBI consists of noisy light-curves for both slowly (AGN) and rapidly varying sources (XRBs, RSCVn), observed on time-scale of years. Data compiled from the literature, although much less noisy, in many cases shows pre-selected flares (GRBs, SNe), sometimes with background emission subtracted and often with no information about the quiescent flux level. The goal of this work was to create software that would automatically reproduce previous, manually obtained results (Chapter 4, Section 4.3.1). However, designing complex software that could directly detect flaring events with no manual intervention during the process for any type of the light-curve may be computationally inefficient (Section 5.2.1). On the other hand, the use of the simple flare finding routine developed is not always straightforward due to the diversity of available data sample. Testing the AFF on all the available light-curves have instantly revealed a set of difficulties which allowed us to divide the whole data sample into four groups, based on the type of the problem. The following section describes the details of the analysis for each of those groups.

5.4.1 Preparing Datasets

Short Duration Flares Selected from GBI

8% of all light-curves; 70% of all selected flares

The best quality light-curves in the sample are those of the GBI observations of Galactic binaries, showing multiple short duration ($\approx$ days) flares, monitored on a time-scale of years. For those datasets the flare finding software works well, successfully identifying a number of outbursts. Figure 5.2 shows an example of such light-curve, with a number of identified flaring events for an X-ray binary LS I +63°303.

Flares Compiled from the Literature

39% of all light-curves; 17% of all selected flares

This group consists of light-curves for the cataclysmic events as well as repeating outbursts compiled from the literature. However, information about the background level in this sample is limited to the close vicinity of the flares, and therefore is insufficient for the correct estimation of the quiescent emission and the low-level variability. In most cases, the automatic estimates of those values are too high when compared to the peak flux of the outbursts, and as a result, the flares are not recognized as varying above chosen (5σ) threshold. In order to resolve that problem, we have estimated the quiescent flux level b of the light-curve as the 10^{th} percentile of the flux density measurements F_{all}

$$b = p^{10\text{th}}\left(F_{\text{all}}\right). \tag{5.2}$$

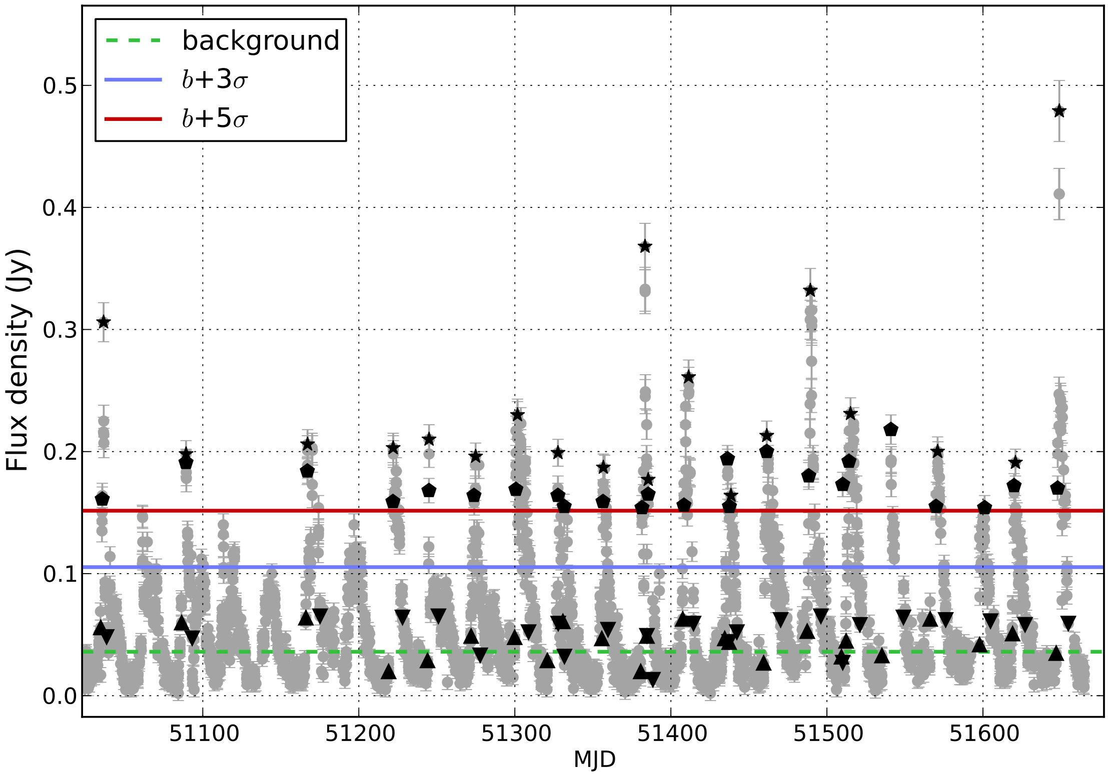

Fig. 5.2 An example of a light-curve showing multiple short flares for a periodic X-ray binary LS I +63°303. Flaring events selected from this 8.3 GHz GBI light-curve by the AFF are marked with the black stars. The background level has been estimated using the sigma clipping method described in Section 5.2.2.

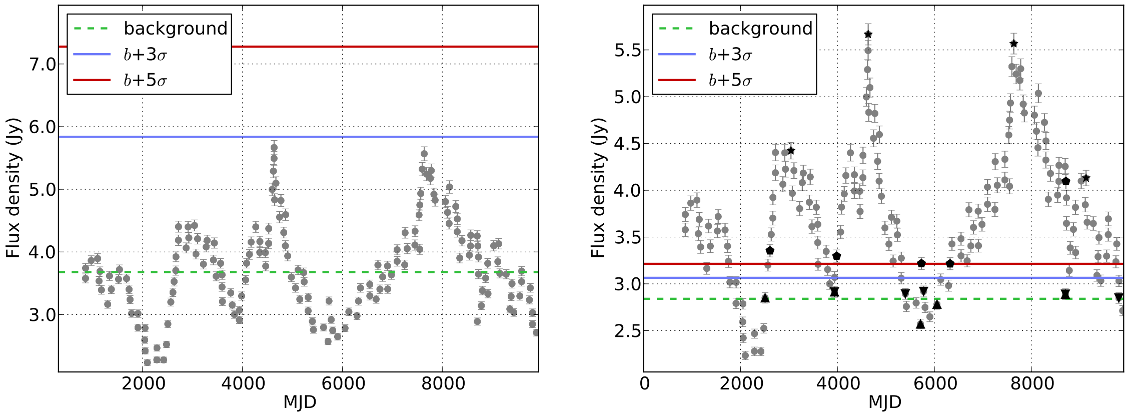

Fig. 5.3 *Left*: An example of a light-curve showing multiple flares with the quiescent level insufficiently well characterised for the automatic software to identify flares. (3C120, Volvach et al. 2010). *Right*: The same light-curve, where the quiescent flux level has been estimated as the 10th percentile of the flux measurements, and, for calculating the flare-detection-trigger amplitude, σ was set to equal the mean of the formal errorbars on the flux density measurements.

For calculating the flare-detection-trigger amplitude, I set σ equal to the mean μ of the formal error bars on the flux density measurements

$$\sigma = \mu\left(\Delta F_{\rm all}\right). \tag{5.3}$$

An example of such a light-curve, showing both original attempt to select flares by AFF, as well as flares selected with the alternative approach is shown in Figure 5.3.

Long Duration Flares Selected from GBI

14% of all light-curves; 5% of all selected flares

This group of light-curves consists of long duration ($\approx$ months) flares, collected from the GBI database. As in the previous group, datasets did not provide enough information to estimate the background level and the quiescent variability. Instead, both parameters have been calculated the same way as described above. The additional difficulty was introduced by scattered noise in the data. Some of the noisy datapoints have been falsely recognised

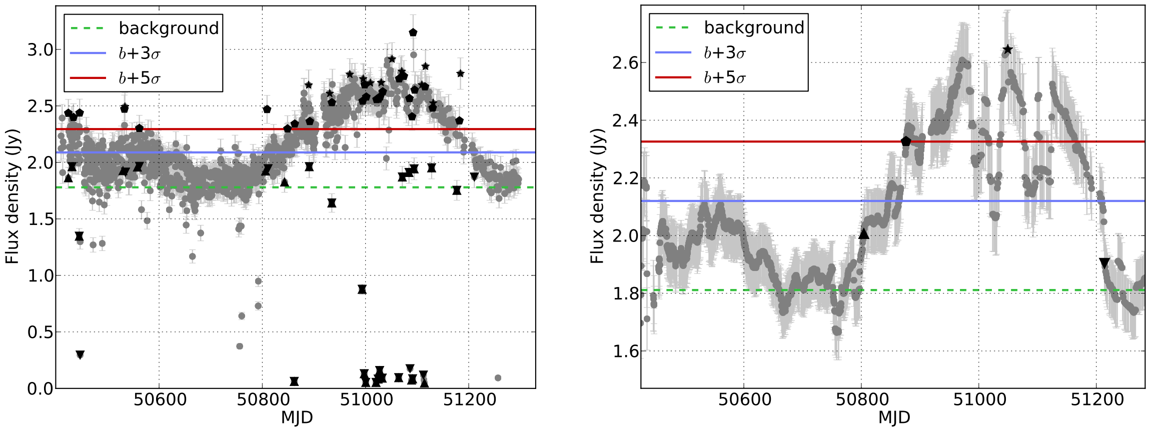

Fig. 5.4 *Left*: An example of a light-curve showing long time-scale flares (0224+671, GBI). With the background and the quiescent low-level variability estimated as in lower panel of Figure 5.3, some odd noisy datapoints are falsely identified as flares. *Right*: The same light-curve smoothed, with one major flare recognized by the software.

by the AFF as the beginning and/or end of the flare. The left panel of Figure 5.4 shows an example of such false detections. This problem was solved by smoothing the data. The smoothing has been performed with an approximately 20 days Gaussian window. This size of the window has been chosen based on the expected time-scale of the intrinsic AGN variability. Variabilities in those types of objects, observed on time-scales shorter than 20 days are more likely to be associated with scintillation (Section 1.5.2). The right panel of Figure 5.4 shows the result of smoothing, with flaring events identified by the AFF.

Pre-selected Flares Compiled From the Literature

39% of all light-curves; 8% of all selected flares

This group of datasets contains single, pre-selected flaring events, with the background emission subtracted, and no information about the light-curve before and after the outburst. Because estimating the background level the way as it was done above might create additional uncertainties, for this group of flares I decided to measure rise and decline time-scales directly (Figure 5.5), using the method described in Section 5.4.2.

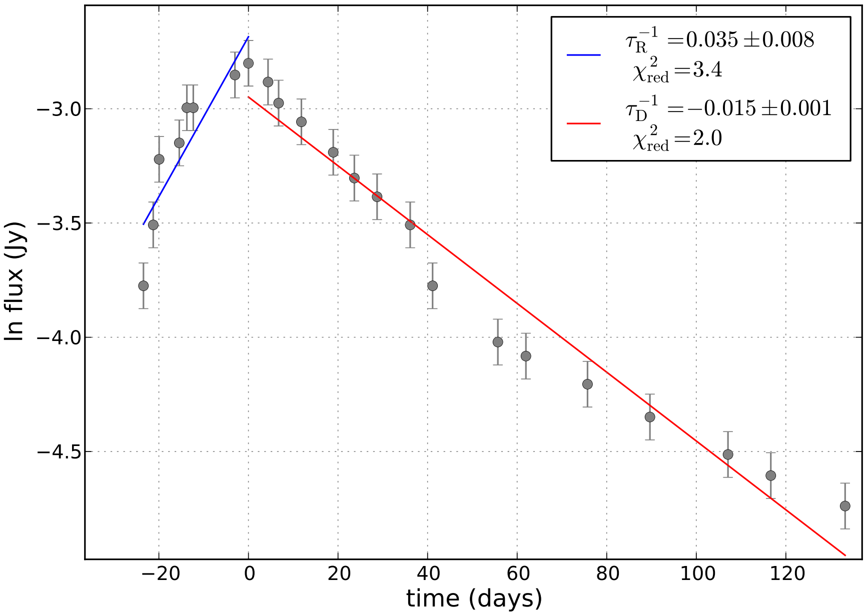

Fig. 5.5 Example of a light-curve (RS Oph, O'Brien et al. 2006) limited to the flaring event, with no information about the background flux density.

5.4.2 Measuring Variability Time-scales

The flare finding routine was applied to the whole sample of light-curves adjusted as described in Section 5.4.1 (excluding pre-selected flares) once more. The software selected 397 single outbursts which, together with 37 pre-selected flares, give the total number of 434 flaring events from 105 distinct objects. In order to measure rise and decline rates for each of the selected flares, I attempted fitting exponential functions to the data

$$F(t) = A \times \exp\left(\frac{t}{\tau}\right) + B, \tag{5.4}$$

where the amplitude A, background B and characteristic time-scale τ are the free parameters of the fit. However, I found that in most cases the exponential fit would fail. One of the likely reasons for that is the quality of the data, where the time sampling is often insufficient for fitting the three parameters model. Therefore, a similar approach as in the analysis described in Section 4.2.3 was adopted, that is, fitting a linear function to the natural logarithm of the flux plotted against linear time. In this case the background level is estimated separately and subtracted from the flux density measurements prior to the fit

$$\ln\left(F\left(t\right)-B\right)=\frac{t}{\tau}+const. \tag{5.5}$$

One obvious choice of this background is the quiescent flux density level b estimated earlier for each of the light-curves (Sections 5.2.2 and 5.4.1). Unfortunately, in many cases this value was so high, that, when subtracted from single flaring event resulted in negative flux density measurements. Those negative measurements had to be excluded from further analysis (involving calculating the logarithm of the flux density) and caused significant data loss. Instead, for each flare selected by AFF, I decided to calculate a separate background level b_{flare} either as the first percentile $p^{1\text{st}}$ of the flux values of the light-curve (F_{all}) or the minimum flux density measurement of the flare (F_{flare})

$$b_{\text{flare}}=\min\left(p^{1\text{st}}\left(F_{\text{all}}\right);\min\left(F_{\text{flare}}\right)\right). \tag{5.6}$$

The background emission calculated this way is then subtracted from the flux density measurements of every flare selected by the AFF. This approach minimizes the number of excluded data points to – at most – one for a given flare (this is the case for ≈ 5 per cent of all the flares).

For each single flare the rise (τ_{R}) and decline (τ_{D}) rates are measured, as fit with the linear function in the log-lin space (Fig 4.6, Eq. 5.5). No measurements have been taken for rise/decline phases consisting of three data points or less. Fits to the data have been done using the *curve fit* routine from the python *scipy.optimize* package, and include error bars of the flux measurements. Figure 5.6 shows the distribution of χ^2_{red} values for measurements of rise and decline phases of the selected flares. Having a set of measurements for each flare, consisting of peak flux density, rise/decline time-scales and reduced χ^2_{red}, we can map those

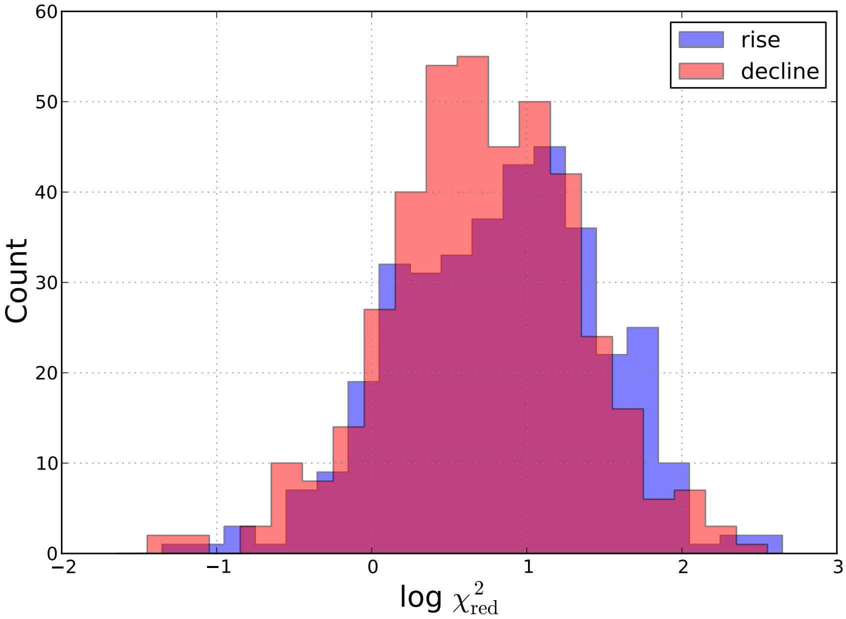

Fig. 5.6 Distribution of the $\log \chi^2_{\rm red}$ values for rise and decline rates calculated as in Equation 5.5. High values of the observed $\log \chi^2_{\rm red}$ distribution are caused by underestimating the error bars of the flux density measurements, as well as using a simple two parameter model for fitting the data which in some cases shows more complex structure.

results with a corresponding class to which the source belongs, its distance and the observed frequency. This enables us to calculate the peak radio luminosity of each flare.

5.5 Results

Out of the total number of 434 flares, the measurements for 364 rising and 412 declining phases have been taken, with the remaining data rejected due to number of datapoints being insufficient for the fit. Figure 5.7 shows the relation between the peak radio luminosities and rise/decline rates, measured for the sample of synchrotron flares selected by AFF (scintillating sources and ESEs are not included in this relation). The overall correlations of the form $L \propto \tau^{5.6}$ and $L \propto \tau^{6.5}$ (for rise and decline phase respectively) are slightly steeper than the corresponding relations $L \propto \tau^{5.2}$ and $L \propto \tau^{5.1}$ reported in Chapter 4 (Figures 4.7 and 4.8). In particular, the relation presented here shows more scatter for relatively lower-luminosity

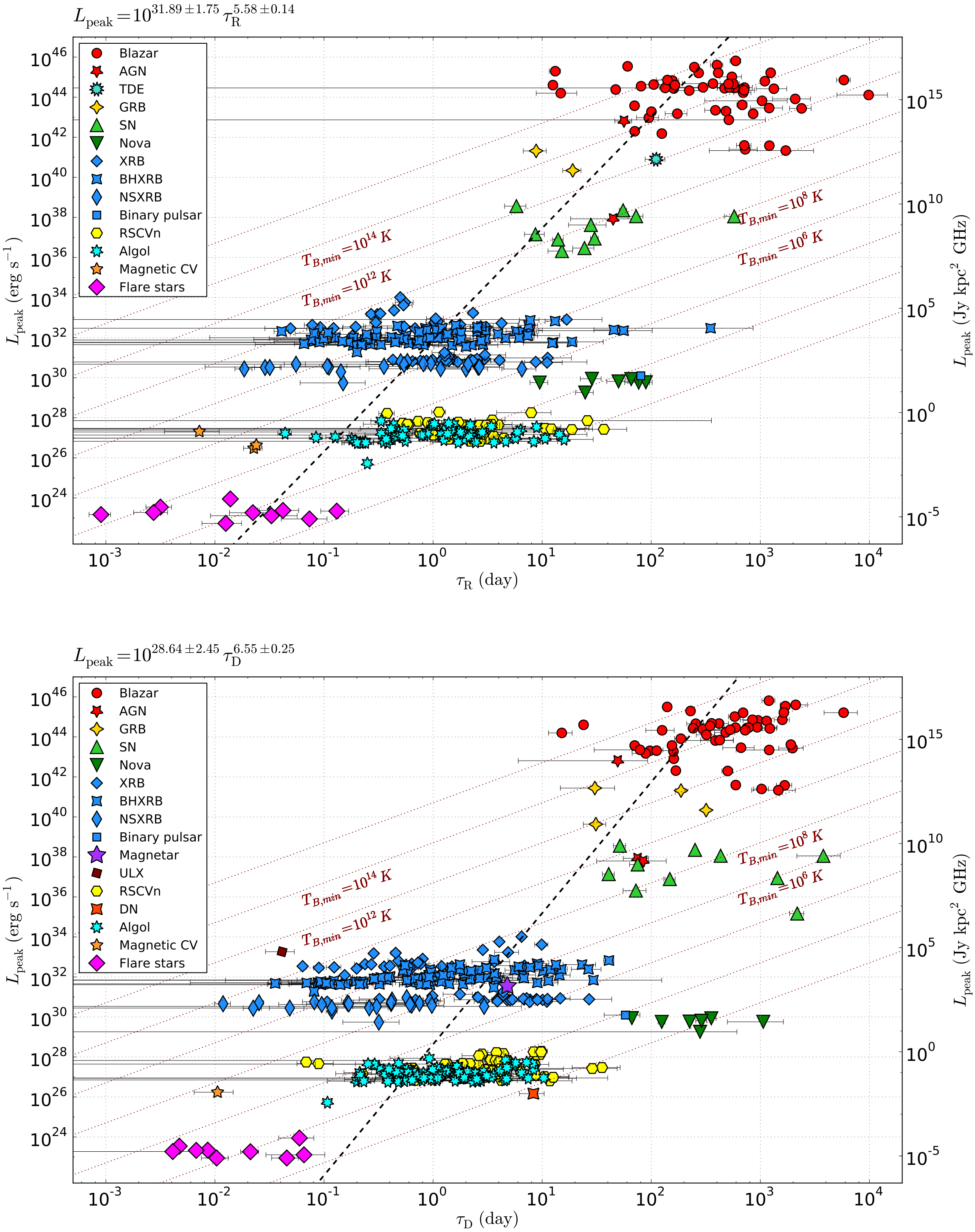

Fig. 5.7 Peak radio luminosity plotted against exponential rise (*upper panel*) and decline (*lower panel*) time-scales for a range of synchrotron emitting sources, selected automatically from the radio light-curves. This relation is slightly steeper compared to the corresponding manual results presented in Chapter 4 (Figures 4.7 and 4.8) and shows higher scatter in the time-scales of the low luminosity sources. Those differences are associated with the methods used to select flaring events (manual vs automatic) and are discussed in more detail in Section 5.8.3.

classes such as XRBs or RSCVn, than in Chapter 4. A clear comparison is presented in Figure 5.8, where histograms of the automatically measured time-scales distribution are overlaid with the manual measurements. By definition, the automated selection of flares is less biased than the one done by hand. However, it can also introduce bad measurements, which would have been rejected if data had been inspected by eye. It should be noted that for $\approx$ 30-40 per cent of measurements the χ^2_{red} is higher than 10 (Figure 5.6). This might partly be caused by underestimating the error bars of flux measurements. However, we expect that the main reason is that the simple two parameter model used in the analysis often fails to accurately fit the data, which may require a more complex approach. Therefore, it made sense to test whether eliminating measurements with high and/or low χ^2_{red} will decrease the scatter in the obtained time-scales. I have considered the following cuts on the allowed range of the χ^2_{red}. First, I have created a variation of Figure 5.7 for a number of cases where the allowed range of the χ^2_{red} was gradually changed from the lower, 10^{-2} limit, up to ≈ 0.5 value, while the upper limit was kept as 10^3. Second, I have kept the lower limit of 10^{-2} constant, slowly narrowing down the maximum value of χ^2_{red} instead, from 10^3 to ≈ 5. Finally, I have produced a simulation of the changes in the luminosity-time relation while simultaneously decreasing a range of the allowed χ^2_{red} values from both lower and upper limits. None of these constraints resulted in any systematic improvement in the range of time-scales across analysed classes of object. The final overall time-luminosity relation has not been significantly changed either. Therefore, I have decided to include all the measurements in the analysis. This step is further supported by the fact that the χ^2_{red} values are calculated based on the errors associated with the flux density measurements, which, for a considerable fraction of our sample might not be defined accurately enough to set a reliable criteria for rejecting bad data. Possible reasons for the observed scatter in measured time-scales are discussed in more detail in Section 5.8.3 and summary of the manually and automatically obtained results can be found in Table 5.1.

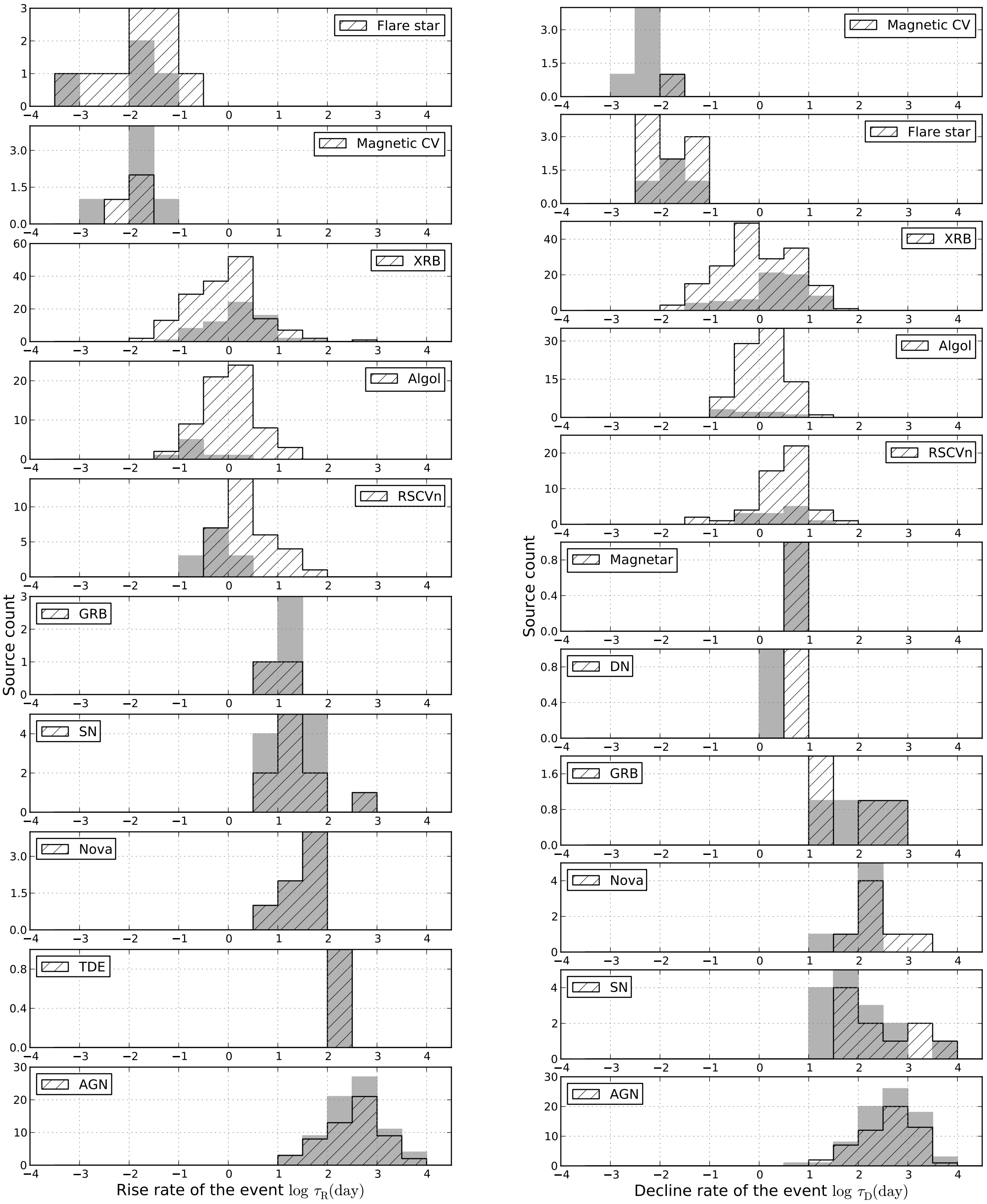

Fig. 5.8 Dashed histograms represent the distribution of the rise (left column) and decline (right column) rates measured for a range of automatically selected flares for different classes of objects. Grey histograms correspond to the previously reported (Chapter 4) manual measurements, overplotted for comparison. The measurements of time-scales for the automatically selected flares clearly show a higher level of scatter for both the rise and decline phases, especially for the lower luminosity classes of objects. Those differences are associated with the methods used to select flaring events and are discussed in more detail in Section 5.8.3.

Table 5.1 Parameters of the fits to the luminosity – time-scale data for rise and decline phases (with the following formula: $\log(L_{\text{peak}}) = a \times \log \tau + b$), for both manual ($\mathrm{a_M}$, b_{M}) and automatic ($\mathrm{a_A}$, b_{A}) methods.

	$\mathrm{a_M} \pm\delta\ \mathrm{a_M}$	$\mathrm{b_M} \pm\delta\ \mathrm{b_M}$	$\mathrm{a_A} \pm\delta\ \mathrm{a_A}$	$\mathrm{b_A} \pm\delta\ \mathrm{b_A}$
Rise	5.21 ± 0.15	31.08 ± 1.84	5.58 ± 0.14	31.89 ± 1.75
Decline	5.09 ± 0.22	29.44 ± 2.88	6.65 ± 0.25	28.64 ± 2.45

In the analysis described in this section, we have automatically reproduced results of the variability time-scales measurements reported in Chapter 4. From this point we will focus on converting those results into an early radio transients classification tool. The following analysis is focused on astrophysical events only, however, non-intrinsic variability will be further discussed in Section 5.8.2.

5.6 Sky Densities

The analysis presented in this chapter is based on a highly biased data sample. Compiled light-curves originate from various surveys, performed with a wide range of instruments with different sensitivities. A large fraction of the X-ray binaries and AGN light-curves have been compiled from the GBI archive. Those observations provide a considerable number of flares for XRBs, which misleadingly shows them as the most common objects in the sky. On the other hand, a small sample of the observed outbursts from other objects (SN, TDE, flare stars) might underestimate their underlying population. Before we can build the transient classification tool based on the distribution of the rise/decline rates presented in Figure 5.8, we need to estimate the expected sky densities of objects within each class. Only by convolving the distribution obtained in Section 5.5 with the areal densities of objects, can we get realistic prospects of finding a variable/transient source of a particular type. In this section we attempt to correct for the bias associated with the data sample by estimating the areal densities of objects within each class.

5.6.1 Methods of Estimating Areal Densities

The estimation of sky densities of events described below was done using various methods, such as extrapolating existing areal densities to different sensitivity limits as well as converting known space densities/source counts into a surface density. In this work the areal density R of objects is defined as the number of sources per square degree present in the sky at any given time. As discussed by Williams et al. 2013, the calculation of such densities does hide important characteristics between the different surveys used to derive the values, and between the populations of objects. These include different time-scales probed by the surveys as well as spectral information of different classes. While we do not account for such characteristics, it should be noted that these distinctions could affect the chances of detecting certain classes of object. Additionally, as the light-curves in our sample also originate from different surveys, they do not have a common sensitivity limit. To account for this we choose the flux density limit of the detection to be 0.1 mJy, and scale all of our calculations to this value.

The method of estimating areal densities depends on the nature of the considered source. For extragalactic sources we can assume an isotropic distribution within a spherically symmetric volume of space. This however is not the case for the Galactic objects, for which the expected density depends on the position in the Galaxy and decreases as we move in a direction away from Galactic plane. From this point I will consider extragalactic and galactic events separately. First, I will describe the methods of estimating sky densities for each group. Then, I will move on to details of the estimation of areal densities for individual classes in the sample.

Extragalactic

If we consider a uniformly distributed set of sources, the volume V of space probed can be expressed as

$$V = \frac{4}{3}\pi d^3, \tag{5.7}$$

where d is the distance to which the objects can be detected. The observed flux density S changes with the distance to the object as

$$S \propto d^{-2}. \tag{5.8}$$

Combining equations 5.7 and 5.8 gives the following relation between the flux density and the volume of space for a considered class of sources

$$V \propto S^{-3/2}. \tag{5.9}$$

For a uniformly distributed set of sources, the expected number N of objects within a given space is proportional to the volume of that space $N \propto V$, therefore the Equation 5.9 gives

$$N \propto S^{-3/2}, \tag{5.10}$$

which is an expression for the total number of sources expected to be found above given flux density. From this point, the flux S in the relation 5.10 is replaced by the flux density limit F_{lim} of 0.1 mJy assumed in the following analysis, which gives the maximum volume of space and, correspondingly, the number of sources expected to be seen above this limit. Areal density estimates for most of the extragalactic classes of objects can be found in the literature. Assuming that the relation 5.10 is valid for extragalactic classes of objects, those results can be easily scaled from the flux density limit given in publications to the one of 0.1 mJy.

Galactic

Space densities of Galactic objects have been studied previously and are available in the literature. In order to convert the spatial distribution (ρ) into areal density (R), we need to multiply the space density by the volume of space populated by the considered class of objects, and divide by the area of the sky (41 253 deg^2).

First, we calculate the maximum distance at which a source belonging to considered class can be observed, with an assumed flux density limit. We estimate a typical radio luminosity of the class and use the following relation to evaluate the distance

$$d_{\rm max} = \sqrt{\frac{L}{4\pi F_{\rm lim}}}. \tag{5.11}$$

Unlike for extragalactic sources, the space density of galactic sources depends on their position in the Galaxy and drops as we move out of the Galactic plane and away from the Galactic center. It can be described as

$$\rho(z) = \rho_0 {\rm e}^{(-|z|/h)}, \tag{5.12}$$

where $z = d \sin b$ is the distance from the Galactic plane (d is the distance to the source, b is the Galactic latitude), h is the scale height (describing a distance over which the number of sources drops by factor of e) and $\rho_0 = \rho(0)$ is the local space density of objects (we assume that the radial dependence of ρ is negligible). With this assumption we calculate the volume of space occupied by a given class of objects within distance d (details of the calculation of generalised volume of space depending on the density profile can be found in Tinney et al. 1993).

Finally, including a duty cycle estimate for each class of object gives the actual number of sources visible in the sky in a single snapshot. Table 5.2 summarises areal densities evaluated for each class. Details of the calculations are described in the following section.

5.6.2 Estimating Areal Densities for Individual Classes of Objects

Tidal Disruption Event

Currently there is only one well sampled radio observation of a Tidal Disruption Event (TDE) available – the recently discovered Swift J1644+57 (Zauderer et al., 2011). Frail et al. (2012) estimates the sky density of such events to be 0.1 deg^{-2} at the 0.3 mJy flux density limit. Using the method described in Section 5.6.1 we estimate that at the 0.1 mJy limit, the areal density of TDEs is ≈ 0.52 deg^{-2}.

Gamma-Ray Burst

The areal density of Orphan GRB Afterglows – classical GRBs with the explosion axis directed away from the line of sight, which should dominate, is derived by Frail et al. (2012) at the 0.3 mJy flux limit for a 10° beam opening angle. Their result of 0.01 deg^{-2} scaled down to 0.1 mJy gives the sky density of 0.052 deg^{-2}.

Supernovae

Frail et al. (2012) state areal densities for SNII, SNIbc and SN 1998bg-like sources. Summing all those sky densities and extrapolating the results to our flux density limit gives the surface density of 0.21 deg^{-2}.

Active Galactic Nuclei

In order to estimate the surface density of radio-variable AGN, we looked at the number of all variable objects found in the FIRST survey data. Out of 1600 variable sources reported by Thyagarajan et al. (2011), 489 were identified to be AGN and variable galaxies. Another 120 are believed to be highly variable quasars. The analysed observations covered 8444 deg^2, at the sensitivity of 0.15 mJy. The source detection threshold chosen for the analysis was 1 mJy. Extrapolating this result to 0.1 mJy with the spherical approximation described in

Section 5.6.1, gives the AGN sky density of 2.3 deg^{-2}.

X-ray Binaries

There are approximately 1000 X-ray binaries within our Galaxy, which, when above the flux density limit of 0.1 mJy chosen in this work, are in outburst and can be detected in a radio survey (e.g. Gallo et al., 2003). With the estimated duty cycle of XRBs of ≈ 1 per cent we expect ≈ 10 sources in the sky at any given moment. This gives a sky density of approximately 2.4 $\times 10^{-4}$ deg^{-2} objects at the 0.1 mJy flux density limit.

Non-magnetic CVs

Dwarf Novae. Having only one radio light curve of a Dwarf Nova (SS Cyg), we use the peak radio luminosity measured for that source in order to estimate the maximum distance to which objects of this class can be detected at the 0.1 mJy flux density limit. Following the steps described in (5.6.1) we get $\mathrm{d}_{\mathrm{max}}$= 380 pc . Pretorius and Knigge (2012) derive the space density of non-magnetic cataclysmic variables to be 4×10^{-6} pc^{-3} with the scale height of 260 pc. The estimated duty cycle of Dwarf Novae is 1-15 per cent (Servillat et al. 2011) – here we assume it is ≈ 10 per cent. Applying the method discussed in Section 5.6.1 we get the areal density of 0.0013 deg^{-2}.

Nova-likes. Nova-like CVs were until recently not thought to be radio sources. However, Körding et al. (2011) and Coppejans et al. (2015) have now shown that several of these systems are radio sources at a level of less than about 0.2 mJy, with variability detected in two systems. Nova-likes will therefore show up as variable sources in sensitive radio surveys. We will not consider them here, however, because we don't expect to see many of them as transients. The reasons are their low space density (more than an order of magnitude less than DNe) and the fact that Nova-likes do not show frequent large amplitude variability.

RSCVns

The space density of RSCVns is approximately 6×10^{-5} pc^{-3} (Favata et al., 1995). The duty cycle of the class is estimated to be $\approx$ 10 per cent and the typical monochromatic radio luminosity of sources 10^{16} erg s^{-1} Hz^{-1} (Williams et al., 2013). Converting space density into areal density as in Section 5.6.1, with the scale height of 325 pc for RSCVns (Ottmann, 1992), we get the sky density of 0.011 deg^{-2}.

Algols

We use a value of $\approx 5\times10^{-6}$ pc^{-3} for the space density of algol binaries, as defined by Duerbeck (1984). To calculate the maximum distance of detection at the 0.1 mJy flux density limit we use the average monochromatic luminosity of objects in the sample (2.14×10^{17} erg s^{-1} Hz^{-1}). There are no good estimations of duty cycle for algol binaries – for the purpose of our calculations we assume the typical value of $\approx$ 10 per cent. Correcting for the scale height of algols, which is $\approx$ 400 pc (Duerbeck, 1984), we get the final areal density of 0.046 deg^{-2}.

Novae

The rate of novae in the Milky Way is estimated to be $\approx$ 35 year^{-1} (Roy et al., 2012). In order to calculate the maximum distance at which a nova could be detected, with a limiting flux density of 0.1 mJy, we assume that the typical radio luminosity it can reach in an outburst is $\approx 1.1 \times 10^{20}$erg s^{-1} Hz^{-1}, that is, the average peak radio luminosity of novae in the sample. With the derived distance of 30 kpc, we can estimate that approximately all 35 novae per year in our Galaxy could be detected at the assumed flux limit. Because the rate of novae is given in number of events per year, we can estimate the areal density of novae at any given instant of time by multiplying that rate by the duration of nova. Based on the properties of light curves in our sample, we expect to detect a typical nova in outburst for $\approx$ 1000 days at

Table 5.2 Estimated areal densities of the studied classes of object at the 0.1 mJy flux density limit, together with the mean and standard deviation parameters calculated for each class and used to estimate their gaussian distribution, for both rise and decline phases.

Class	Areal density (deg^{-2})	References	$\log\mu_{\mathrm{R}}$ (day)	$\log\sigma_{\mathrm{R}}$ (day)	$\log\mu_{\mathrm{D}}$ (day)	$\log\sigma_{\mathrm{D}}$ (day)
AGN	2.3	Thyagarajan et al. (2011)	2.51	0.60	2.60	0.53
TDE	0.52	Frail et al. (2012)	2.04	0.42	–	–
GRB afterglow	0.052	Frail et al. (2012)	1.11	0.17	1.94	0.46
SN	0.21	Frail et al. (2012)	1.47	0.54	2.43	0.68
SGR	10^{-8}	Olausen and Kaspi (2014), Ofek (2007)	–	–	0.68	0.38
XRB	2.4×10^{-4}	Gallo et al. (2003)	-0.04	0.71	0.02	0.75
Dwarf Nova	0.0013	Pretorius and Knigge (2012), Servillat et al. (2011)	–	–	0.92	0.38
Classical nova	0.0021	Roy et al. (2012)	1.60	0.32	2.39	0.35
RSCVn	0.011	Williams et al. (2013), Favata et al. (1995), Ottmann and Schmitt (1992)	0.40	0.49	0.45	0.54
Algol	0.046	Duerbeck (1984)	0.001	0.54	0.08	0.44
Flare star	0.0067	Reid et al. (2007), Osten (2008)	-1.84	0.65	-1.82	0.45
Magnetic CV:						
Polar	0.038	Ramsay et al. (2004), Pretorius et al. (2013)	–	–	–	–
IP	0.0011	Pretorius and Mukai (2014), Pretorius et al. (2013)	–	–	–	–
Polar + IP	0.039	–	-1.80	0.24	-1.98	0.38

a frequency of 5-8 GHz. For the parameters listed above, we estimate that the areal density of novae is 0.0021 deg^{-2}.

Soft Gamma-ray Repeaters

The sky density of SGRs is not well constrained. Ofek (2007) gives the upper limit for the rate of giant flares (similar to SGR 1806-20 event) of 5×10^{-4} year^{-1} per SGR. With the number of SGR sources in the Galaxy reported by Olausen and Kaspi (2014) of 15[1], and the duration of the radio flare analysed in our sample ($\sim$ 20 days) we get the areal density of approximately 10^{-8} deg^{-2}.

Magnetic CVs

Polars. One of the two magnetic CVs in our sample – V834 Cen – belongs to the subclass of

---

[1] http://www.physics.mcgill.ca/~pulsar/magnetar/main.html

polar magnetic CVs. With the luminosity measured in the analysis (2.45×10^{17} erg s^{-1} Hz^{-1}), we estimate the maximum distance of $d_{\rm max}$ = 1.43 kpc. For the space density of 10^{-6} pc^{-3} (Pretorius et al., 2013), duty cycle of 0.5 (Ramsay et al., 2004) and the scale height equal to 260 pc (Pretorius et al., 2013), we estimate the sky density for these types of objects of 0.038 deg^{-2}.

Intermediate polars. Sky density of IPs calculated based on the AE Aqr. With the average measured luminosity of that source (7.45×10^{16} erg s^{-1} Hz^{-1}), the estimated maximum distance for the detection is $\rm d_{max}$ = 790 pc. With a space density of 10^{-7} pc^{-3} (Pretorius and Mukai, 2014), scale height 120 pc (Pretorius et al., 2013) and duty cycle of 1 (persistent sources) we get the estimated sky density of 0.0011 deg^{-2}.

Flare Stars

Space density of flare stars given by (Reid et al., 2007) is 0.08 pc^{-3}. The average luminosity of flare stars in our sample is $4{\times}10^{13}$ erg s^{-1} Hz^{-1}. With such low luminosities, at the 0.1 mJy flux limited survey they can be detected up to a distance of $d_{\rm max} \approx 20$ pc. Within that distance, which is relatively small compared to the size of the Galaxy, we can assume a uniform, spherical distribution of sources (Equation 5.7). The duty cycle of flare stars is not well constrained (Osten 2008, Hilton et al. 2010) – assuming the upper limit of 10 per cent, we get the areal density of 0.0067 deg^{-2}.

Flare stars can also produce bright coherent bursts, which at the sub-milijansky detection threshold can be detected from a distance of several hundred parsecs (Osten, 2008). Although these types of events are quite rare (duty cycle less than 1 per cent), because of their high brightness, the areal density of coherent flares can reach approximately 1.2 deg^{-1} at the 0.1 mJy flux density limit. On the other hand, they are expected to evolve rapidly ($\sim$ 60 s) and should only be common in surveys exploring very short time-scales.

5.7 Probability Distribution of Variability Time-scales

For a transient candidate discovered in a blind radio survey, it is very unlikely that the information about its distance, and therefore the luminosity, will be known (at least immediately). This means that all of the earliest information will be contained in the variability of the light-curve and spectral distribution of the source. In consequence, if we can not take into account information about the luminosity of the source, the relation shown in Figure 5.7 is reduced to a one dimensional histogram of the variability time-scales (as shown in Figure 5.8). Although this makes the previously clear separation between different classes of objects much more uncertain, we can still convert those results into the probability distribution and convolve them with the expected areal densities of radio sources.

In order to represent the variability time-scales as a probability distribution, for each of the analysed classes of objects, we calculate the mean $\mu_{\rm R}$, $\mu_{\rm D}$ and the standard deviation $\sigma_{\rm R}$, $\sigma_{\rm D}$ (listed in Table 5.2) of their measured rise and decline rates respectively. Several classes in the sample are represented by single source/event (e.g. TDE, DN). In those cases, the mean value of the distribution has been approximated by the value of the rise/decline rate measured for that source, while their standard deviation was calculated as the mean value of the standard deviations measured for all the other classes of objects. Using those values, we have assigned the following Gaussian function to each class

$$P(\tau) = \frac{1}{\sqrt{2\pi}\sigma} \exp\left(-\frac{(\tau-\mu)^2}{2\sigma^2}\right). \tag{5.13}$$

Figure 5.9 shows the probability distribution of the rise/decline rates for all the classes of objects in our sample, normalized to 100 per cent. Calculation of the normalized probability distribution $P_{\rm norm}(\tau)$ has been done in the following way. The value of the probability distribution for a class k in each time step $\tau_{\rm n}$ is divided by the sum of the probabilities of all the classes in that time step

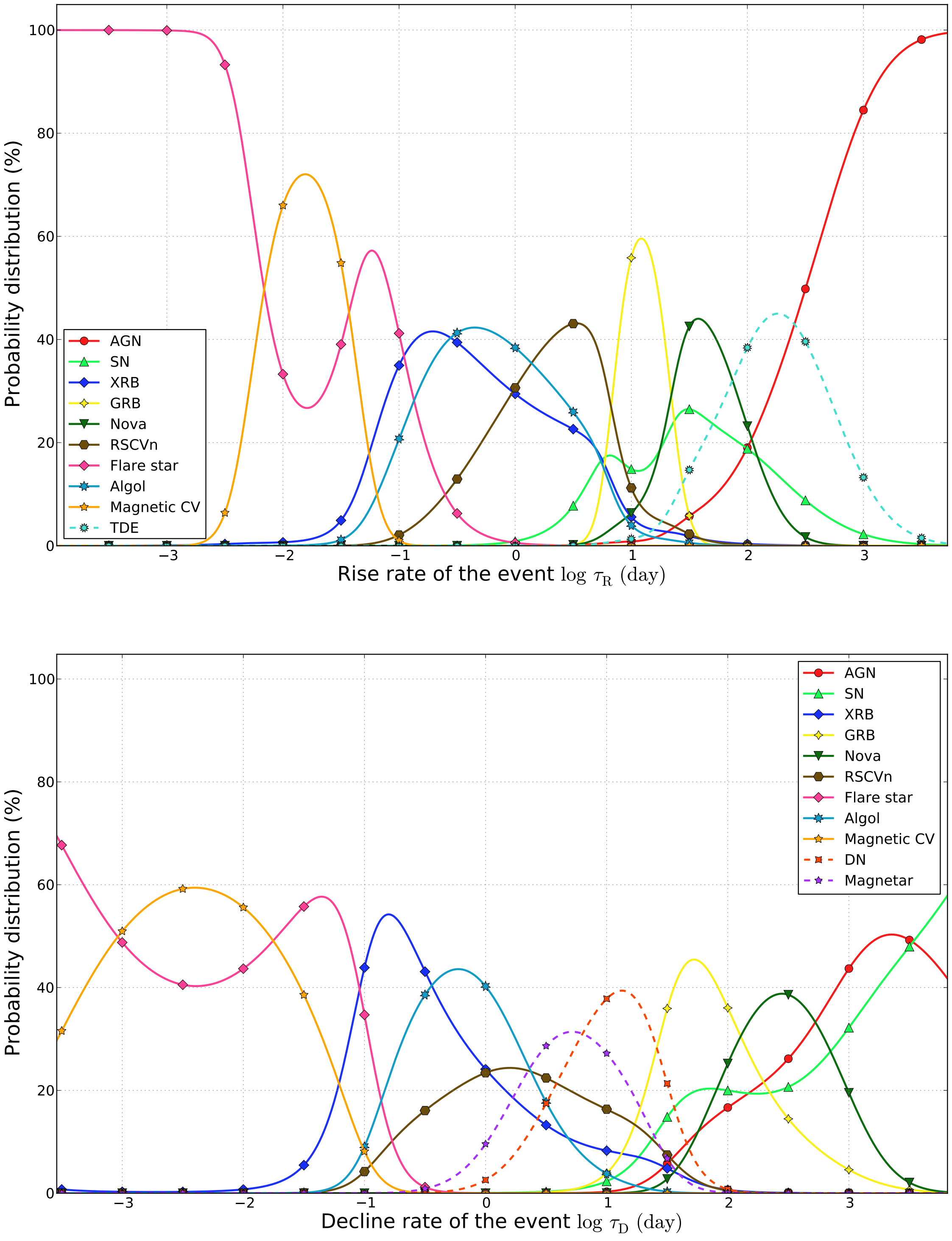

Fig. 5.9 *Upper:* Relation shown in Figure 5.7 converted into the probability distribution of a source belonging to a given class of objects based on the rise time-scale, normalised to 100 per cent. *Lower:* The same relation, calculated for the declining phases.

$$P_{k,\mathrm{norm}}(\tau_\mathrm{n}) = \frac{P_\mathrm{k}(\tau_\mathrm{n})}{\sum\limits_i P_i(\tau_\mathrm{n})}. \tag{5.14}$$

Therefore, adding up all the normalized probabilities calculated this way will give 1 in each time-step. This normalisation is the reason for the 'double peaked' structures in the Gaussian distribution of some classes (e.g. the distribution of supernovae rise rate). The dashed lines in Figure 5.9 represent distributions of sources for which only one flare was available (e.g. TDE). Given the small number of light-curves representing each subclass of magnetic CVs, I have decided to add their sky densities and calculate their combined probability distribution instead of considering them separately. If we take into account the broad scatter of the variability time-scales observed across all the classes of objects, we note that the separation of these two subcategories of magnetic CVs based on just the radio data is unlikely. Additionally, with this approach, we avoid adding the uncertainties associated with assigning a Gaussian distribution based on approximated parameters.

To this point, we have calculated the probability distribution of the observed variability time-scales of the radio sources (Equation 5.13) based on the available sample of light-curves. Now, these results need to be convolved with the actual sky densities of objects before they can be used to assign probabilities to unknown sources. In order to calculate the corrected probabilities $P_\mathrm{corr}(\tau)$, we multiply the distribution obtained in Equation 5.13 by the estimated areal density R for each class of objects (Table 5.2)

$$P_\mathrm{corr}(\tau) = P(\tau) \times R = \frac{R}{\sqrt{2\pi}\sigma} \exp\left(-\frac{(\tau-\mu)^2}{2\sigma^2}\right), \tag{5.15}$$

which is further normalised to 100 per cent as in Equation 5.14. The results of the probability distribution of all the types of sources in the sample, corrected for the estimated sky densities are shown in Figure 5.10. It is worth noting, that sources like XRBs or Novae, even though they make up a significant fraction of the original sample, due to their low sky densities

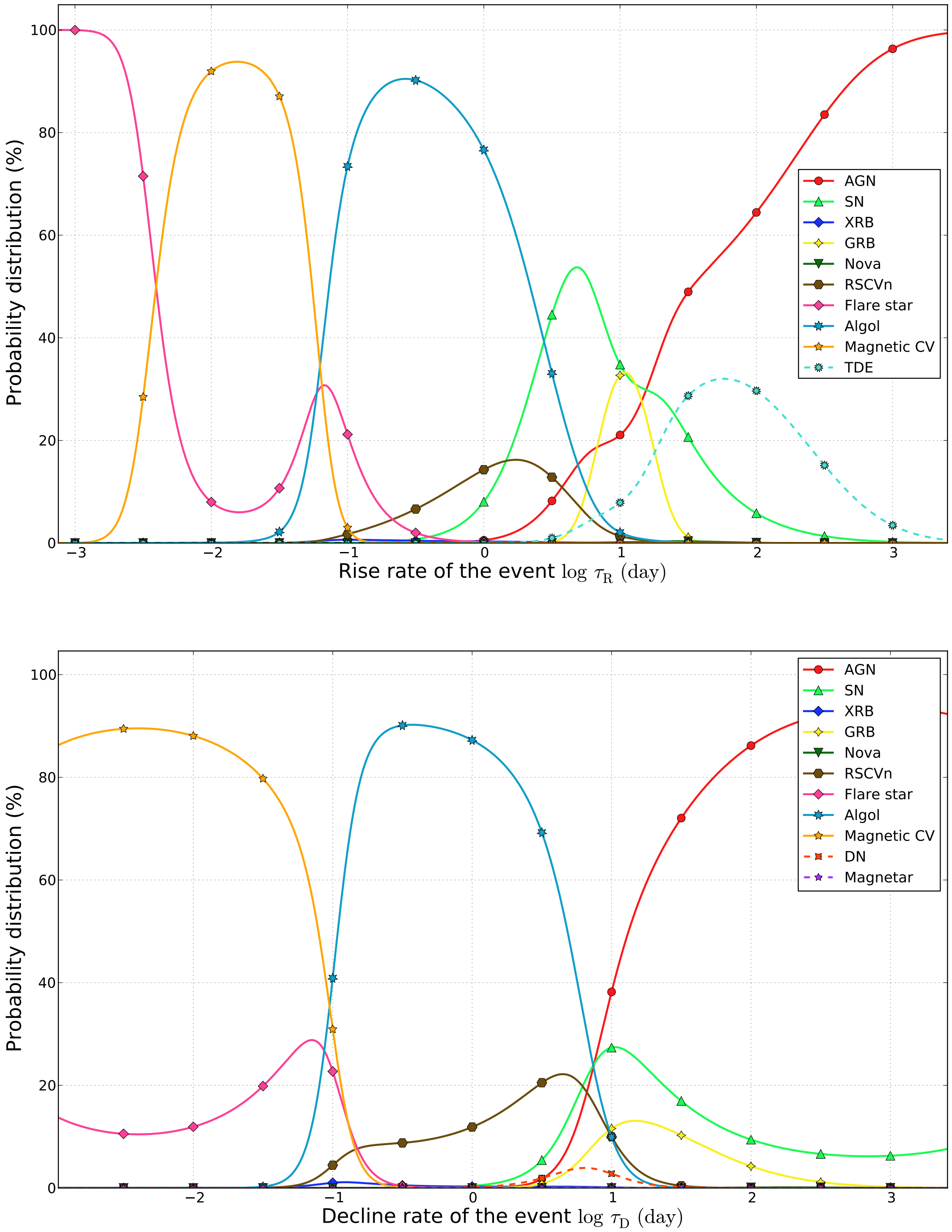

Fig. 5.10 Relation shown in Figure 5.9 convolved with the estimated sky densities of objects (Table 5.2) for rising (upper panel) and declining phases (lower panel). These estimated distributions are calculated for the flux density limit of 0.1 mJy.

are very unlikely to be found in blind radio transient surveys. These figures can ultimately be used to read the probability of source belonging to a given class of objects, based on its measured rise/decline rates.

Having built the template of variability time-scales distribution encompassing a wide range of synchrotron flaring sources, we can now determine what is the probability that a newly discovered transient candidate belongs to a given class of objects, by providing its characteristic rise and/or decline time-scale. Tables 5.3, 5.4 give the probability distribution values for each of the classes of objects (for rise and decline phases respectively) on a time-scale $\approx 10^{-4}$–10^{4} days, averaged over a logarithmic time-step of 0.5.

5.8 Discussion

5.8.1 Early Radio Transients Classification Tool

In this chapter, I have presented a radio transient classification tool, created based on measurements of the variability time-scales of synchrotron flares originating from a wide range of known objects. The tool has a form of a template of probability distributions of the rise/decline rates with time-scales ranging from less than days to longer than years. These probabilities have been convolved with the expected areal densities of sources (down to a 0.1 mJy flux density limit) in order to compensate for the biases in the data sample. By measuring the rise and/or decline rates of new transient candidates and comparing them against this template, we are now able to determine – with a given probability – their most likely nature.

The diagram shown in Figure 5.11 gives an overview of steps included in the analysis described in this chapter. While the entire process aims to automate the selection of flares as well as rise/decline rate measurements, several steps have been done 'by eye' (listed in rectangular frames in Figure 5.11). Those include splitting the complete sample of

Table 5.3 Probabilities distribution of variability time-scales for the rising phase of a flare, for a range of measured rise rates (time given on a logarithmic scale).

log τ (day)	AGN	SN	XRB	GRB	Nova	RSCVn	Flare stars	Algol	Magnetic CV	TDE
-4.0 -3.5	2.6e-17	3e-15	0.0003	5.8e-162	2.4e-54	1.3e-11	100.0	5e-06	5.7e-08	2.7e-33
-3.5 -3.0	1.5e-14	2.2e-12	0.0013	5.9e-129	1.1e-44	5.5e-09	100.0	0.00025	0.0037	1.2e-27
-3.0 -2.5	6.2e-12	1e-09	0.0059	1.1e-99	6.1e-36	1.3e-06	94.0	0.0082	5.8	2e-22
-2.5 -2.0	4e-10	5.9e-08	0.0073	8.2e-75	7.8e-29	3.3e-05	29.0	0.044	71.0	2.3e-18
-2.0 -1.5	1.3e-07	1.4e-05	0.016	1.7e-52	1.5e-21	0.0024	7.1	0.52	92.0	1e-13
-1.5 -1.0	0.00014	0.01	0.34	1.5e-33	1e-14	0.52	23.0	30.0	46.0	5.3e-09
-1.0 -0.5	0.0062	0.26	0.56	1.7e-19	4.6e-10	3.9	8.5	86.0	0.37	5.3e-06
-0.5 0.0	0.16	3.1	0.37	4.2e-09	2.8e-06	10.0	0.74	85.0	1e-05	0.0019
0.0 0.5	3.0	24.0	0.24	0.02	0.0019	15.0	0.059	58.0	6.9e-12	0.24
0.5 1.0	16.0	47.0	0.068	13.0	0.069	6.2	0.0023	13.0	7.5e-20	4.0
1.0 1.5	34.0	28.0	0.0061	18.0	0.28	0.49	2e-05	0.67	4e-30	18.0
1.5 2.0	57.0	12.0	0.0006	0.13	0.2	0.026	1.9e-07	0.027	5.5e-42	31.0
2.0 2.5	74.0	3.1	4.8e-05	4e-07	0.024	0.00063	1.2e-09	0.00061	1.2e-55	23.0
2.5 3.0	91.0	0.65	4.5e-06	4.1e-16	0.00057	1.1e-05	8.7e-12	1.1e-05	6.8e-71	8.5
3.0 3.5	98.0	0.1	4.5e-07	1.1e-28	2.3e-06	1.1e-07	5.9e-14	1.6e-07	9.6e-88	1.4
3.5 4.0	100.0	0.012	5.1e-08	8.2e-45	1.6e-09	7.5e-10	4e-16	1.8e-09	3.3e-106	0.12

Table 5.4 Probabilities distribution of variability time-scales for the declining phase of a flare, for a range of measured decline rates (time given on a logarithmic scale).

log τ (day)		AGN	SN	XRB	GRB	Nova	RSCVn	Flare star	Algol	Magnetic CV	DN	Magnetar
-4.0	-3.5	2.7e-23	9e-12	0.037	6.5e-27	4.9e-60	6.2e-08	41.0	2e-10	59.0	4.2e-27	4.2e-29
-3.5	-3.0	1.2e-20	4.5e-11	0.0054	2.2e-23	9.2e-52	4e-07	19.0	1.5e-08	81.0	1.1e-22	4.8e-25
-3.0	-2.5	1.1e-17	6.6e-10	0.0024	1.1e-19	1.1e-43	5.2e-06	12.0	1.6e-06	88.0	2.5e-18	4.8e-21
-2.5	-2.0	2.1e-14	3.1e-08	0.004	8.9e-16	8.7e-36	0.00016	11.0	0.00024	89.0	5.4e-14	4.5e-17
-2.0	-1.5	8.9e-11	4.7e-06	0.025	1.1e-11	4.6e-28	0.011	15.0	0.05	85.0	1.1e-09	3.9e-13
-1.5	-1.0	4.7e-07	0.0014	0.41	1.3e-07	8.5e-21	1.2	25.0	9.8	63.0	1.1e-05	1.9e-09
-1.0	-0.5	8.2e-05	0.026	0.88	3.6e-05	1.3e-15	7.6	7.0	77.0	7.1	0.0018	1.5e-07
-0.5	0.0	0.0051	0.17	0.36	0.0028	3e-11	10.0	0.084	89.0	0.018	0.05	1.8e-06
0.0	0.5	0.39	1.9	0.26	0.2	2.7e-07	16.0	0.00068	81.0	1.8e-05	0.75	1.2e-05
0.5	1.0	15.0	17.0	0.22	5.4	0.00033	19.0	4.1e-06	40.0	8.7e-09	3.3	2.7e-05
1.0	1.5	58.0	23.0	0.039	12.0	0.012	3.3	3.4e-09	2.3	4.1e-13	1.1	4.7e-06
1.5	2.0	80.0	13.0	0.0021	7.1	0.074	0.12	2.4e-13	0.015	9.1e-19	0.039	7.9e-08
2.0	2.5	90.0	7.8	0.00013	2.5	0.14	0.0035	8e-18	5e-05	6e-25	0.00048	4.4e-10
2.5	3.0	93.0	6.3	1.1e-05	0.59	0.081	9.5e-05	1.7e-22	9.9e-08	1.5e-31	2.4e-06	9.9e-13
3.0	3.5	93.0	7.0	1.5e-06	0.1	0.016	2.6e-06	2.3e-27	1.3e-10	1.6e-38	5.1e-09	9.3e-16
3.5	4.0	89.0	11.0	2.9e-07	0.012	0.0011	7e-08	2.2e-32	1e-13	7.4e-46	4.6e-12	3.8e-19

light-curves into four distinct groups (each of which required a different method of estimating the quiescent flux level) and applying smoothing for one of them. The remaining steps (listed in rounded frames in Figure 5.11), such as selecting flaring events from the data and measuring rise/decline rates (including background subtraction) have been done automatically. It should be noted that all the manual adjustments made to the datasets were only required due to the nature of the compiled sample and should not be necessary in any future transient survey. An iteration of the flare finding routine presented here could be used in a near-real time search for transients, where long term monitoring of the background prior to a potential outburst will provide sufficient information for the software to recognise and measure variability above the quiescent flux level.

5.8.2 Scintillation and ESEs

One of the main challenges we might come across while classifying a newly discovered source by its variability rates is scintillation. Figure 5.12 shows the relation between the time-scales and peak radio luminosities for our extended sample of objects, where scintillating sources and extreme scattering events are plotted along with the previously shown (Figure 5.7) synchrotron events. It shows that the parameter space of rise/decline rates for scintillating sources and ESEs overlaps strongly with that occupied by most of the analysed astrophysical flares. It may be possible to distinguish between them based on their spectral properties – while the amplitude of synchrotron flares is lower at lower frequencies, Rickett et al. (2006) show that the observed variability due to interstellar scintillation can be stronger at lower frequencies. Similarly, if originating from intrinsic variability, the light-curve should evolve on longer time-scales at lower frequencies, which is not the case for ESEs, where the peak flux density is observed simultaneously at all wavelengths (Fiedler et al., 1987). Another way of separating them lies in the shape of the flare – those originating from astrophysical

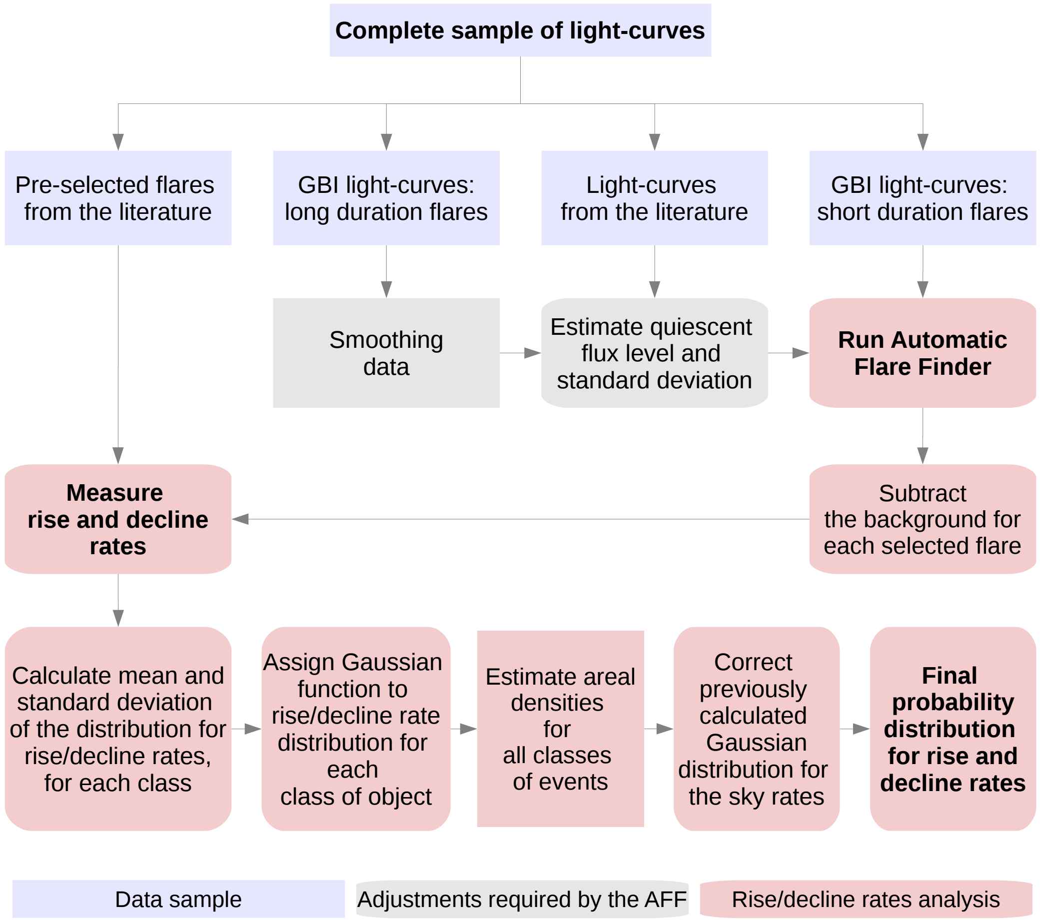

Fig. 5.11 Illustration of the process flow showing the main steps of the analysis, from the compiled sample of the data to obtaining the probability distribution for variability time-scales. Steps in rectangular frames correspond to parts of the analysis done manually. Automatic steps are listed in rounded frames.

explosions are usually characterised by longer decaying times comparing to their rise times, while in scintillation both phases are more symmetrical.

5.8.3 Comparison with the Manual Results

This work builds upon the results presented previously in Chapter 4, which showed broad correlation between the luminosity and time-scale of variable radio objects, ranging from nearby, intrinsically faint to distant and luminous sources. Creating an automatic flare finder allowed us to include a larger number of flares in the analysis and made the result easy to reproduce, reducing the bias associated with selecting data by hand. Figure 5.8 illustrates the distribution of rise (left) and decline (right) rates measured both automatically (dashed lines) and manually (shaded). As mentioned in Section 5.5, although there is an overall agreement between both methods, the comparison of results shows a higher degree of scatter for several classes of objects in the automatic approach. Light-curves corresponding to these sources (XRB, RSCVn, Algol) consist of tens of single outbursts (examples of those light-curves are shown in Figure 5.13). In the manual analysis, the sample of flares selected from these light-curves has been limited to those with the best data quality. The flare finding software, however, had identified all of the flaring events in the same datasets, increasing the range of time-scales measured for each source. Most of the measurements correspond to real flares, as in Figure 5.14, which shows snapshots for several flaring events identified in a GBI light-curve of the X-ray binary SS 433. However, in marginal cases a false detection has also been included. For example, an odd noisy datapoint within a flare can be mistaken for the end of the respective flare which results in underestimating the measured decline time. In other extreme cases, several outbursts superimposed such that the flux level does not drop low enough for the AFF to separate them, will be measured as one long flare rather than single events, and make the rise/decline times appear longer than they really are (Figure 5.15). Because several of those exceptions identified in the analysis could not be removed other

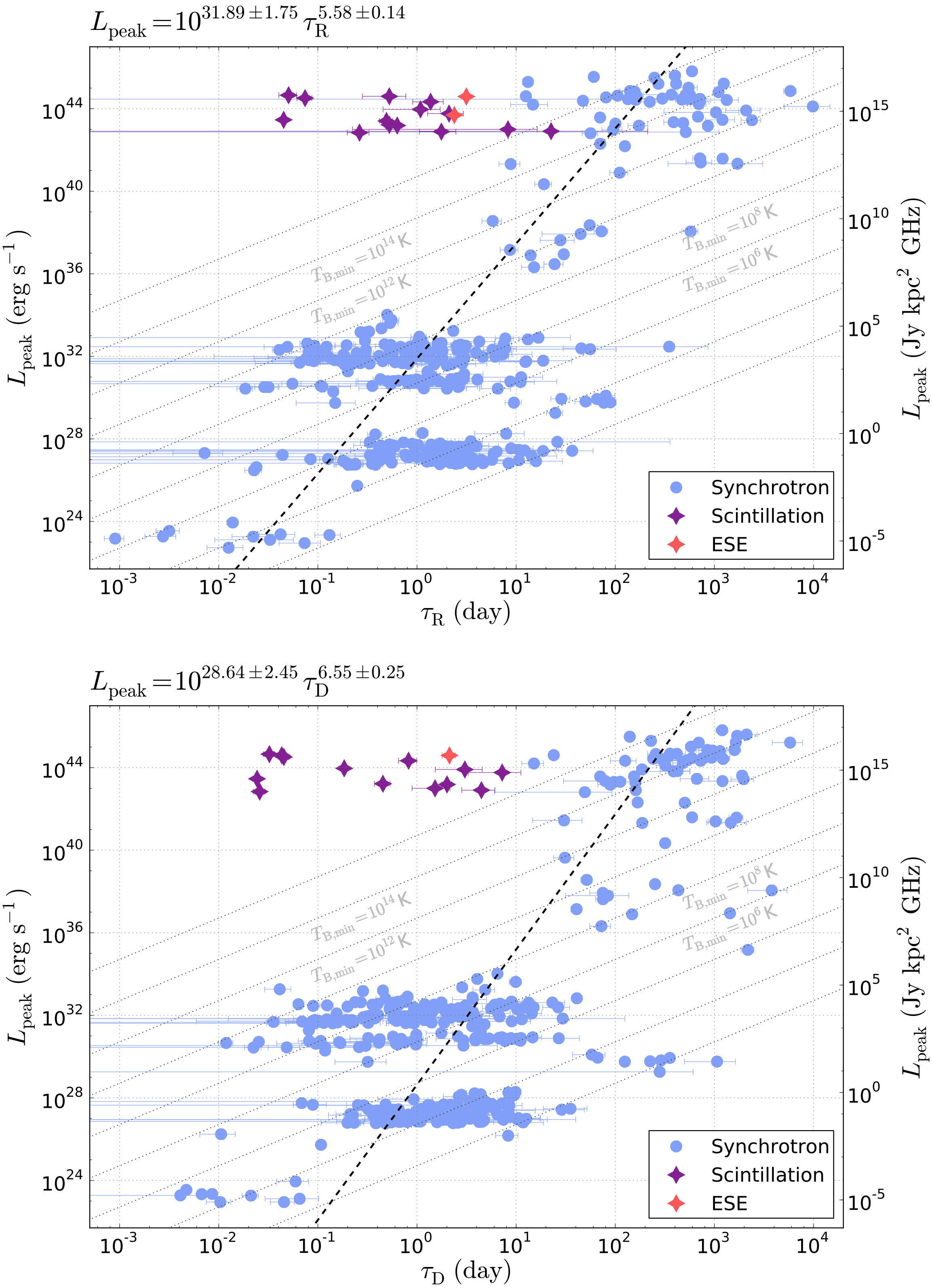

Fig. 5.12 Variation of Figure 5.7 for rise (upper panel) and decline (lower panel) phases, where all events originating from synchrotron emission are marked with blue circles, and additional measurements corresponding to scintillating sources and extreme scattering events are plotted in purple and red respectively. As discussed in Section 5.8.2, scintillating sources together with extreme scattering events appear to populate most of the time-scale parameter space and cover the range of rise (upper panel) and decline rates (lower panel) typical for all the classes, from low luminosity stars to AGN.

than by manually excluding them, I have decided to include them in the final results in order to keep the process purely automatic.

5.8.4 Future Work

Currently, the number of available flares used in designing the classification tool is uneven across a range of objects included. However, it can be gradually improved with new sources detected in future transient surveys, where additional data could help to limit the uncertainties of the initial classification. This would be especially desirable in the case of classes which have few well-studied light-curves to date, such as tidal disruption events, for which at this point, the variability time-scales are not well constrained.

In the future, this tool or a derivative could be incorporated into an automated transient detection pipeline (e.g. Swinbank et al., 2015) as the earliest classification step. This would set initial constraints on the class of any newly discovered sources, which can be further verified and narrowed down by, for example, an optical flux measurement (Stewart et al. *in prep*). Every newly detected and classified radio object can then be added to the input data of the original classifier, improving its accuracy.

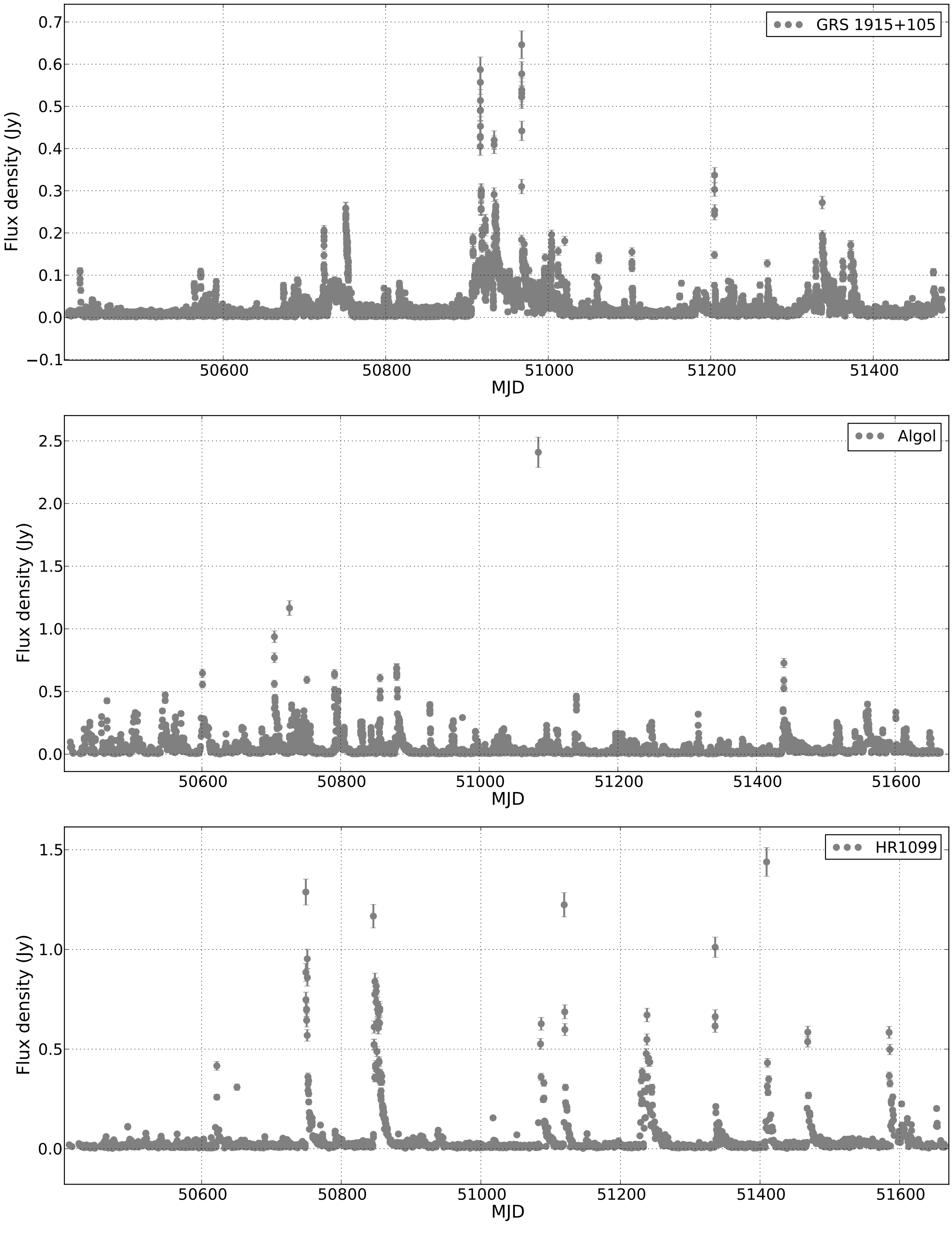

Fig. 5.13 Examples of the light-curves used in the analysis. All light-curves have been compiled from the GBI archive and show flares observed at 8.3 GHz from an X-ray binary (GRS 1915+105), Algol system, and an RSCVn (HR1099).

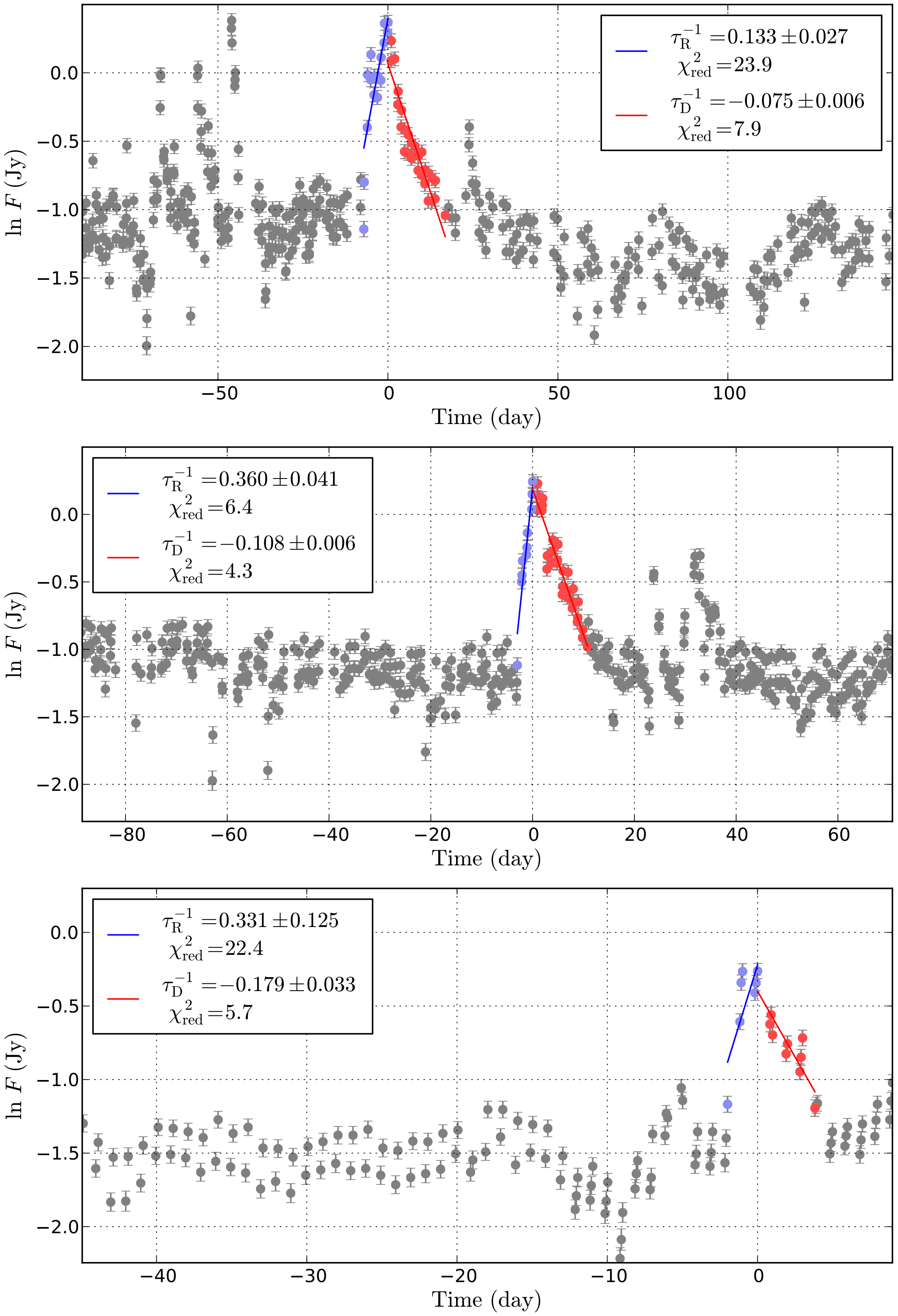

Fig. 5.14 Examples of the fits done to the rise and decline phases of the flares selected from an XRB radio light-curve (SS 433, 8.3 GHz GBI data). For clarity, each of the panels shows one flare with the obtained parameters of the fits.

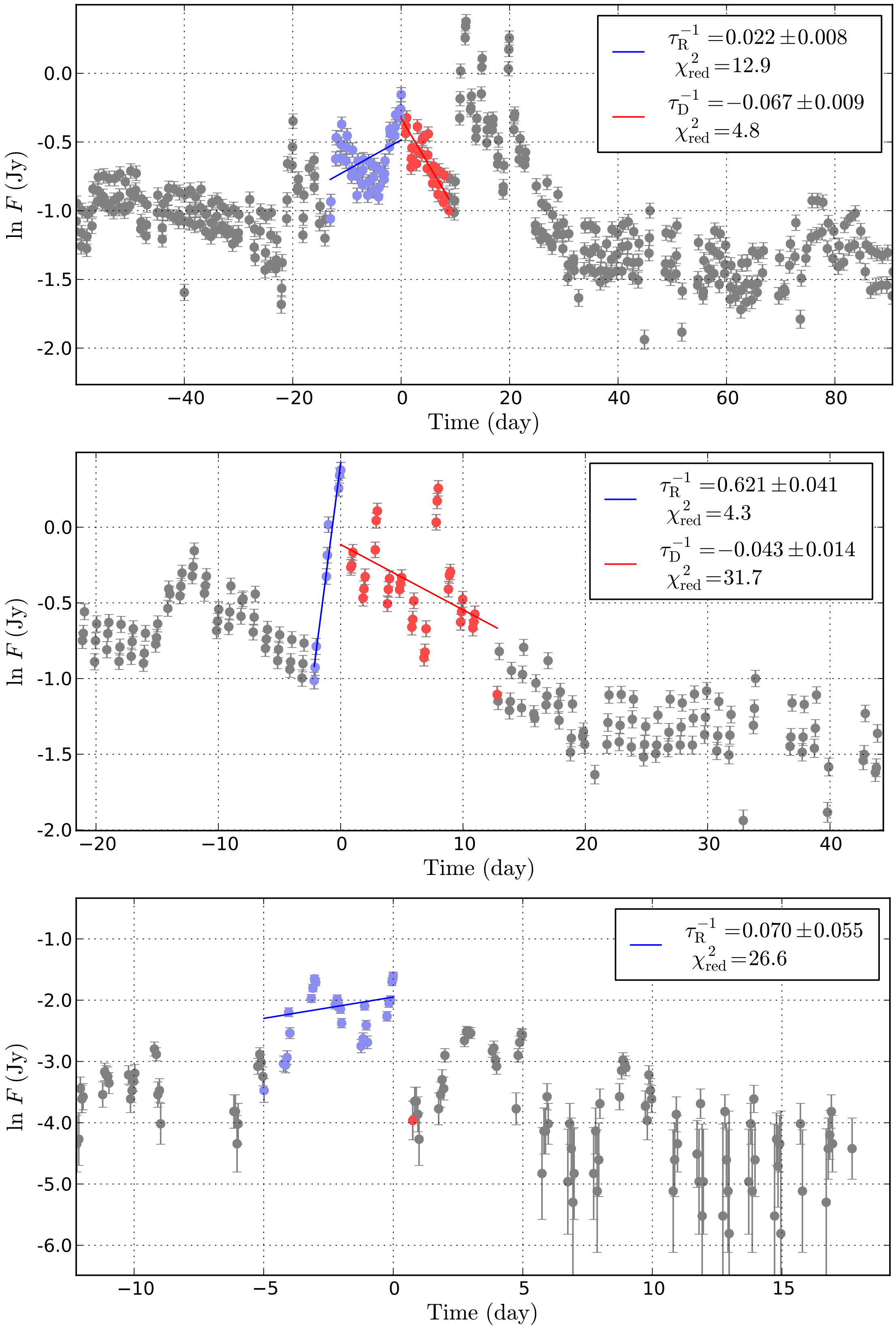

Fig. 5.15 Examples of inaccurate selection of flares from the 8.3 GHz GBI light-curves (top two panels: X-ray binary SS 433; lower panel: Algol). In this case, outbursts have been superimposed on each other such that the flare finding routine did not recognise them as separate events. As a result, the measured slope is shallower, and, in consequence, the obtained time-scales appear to be slower than they really are.

Table 5.5 Sample of scintillating sources included in the analysis

Source	Distance [Mpc]	Reference	Distance reference
0917+624	10581	Rickett et al. (1995)	MOJAVE [1]/NED [2]
0405-385	9151.6	Rickett (2007)	NED
1257-326	8895.6	Jauncey et al. (2003)	NED
1328+6221	8573	Koay et al. (2011a)	NED
1819+3845	3141.8	Dennett-Thorpe and de Bruyn (2003)	de Bruyn and Macquart (2015)
J0510+1800	2297.8	Koay et al. (2011b)	NED
J0958+6533	1951	Koay et al. (2011b)	MOJAVE/NED
J0920+4441	17588	Koay et al. (2011b)	MOJAVE/NED
J1734+3857	6452.6	Koay et al. (2011b)	NED
J1128+5925	13846.4	Gabányi et al. (2007)	NED
1144-379	7103.1	Turner et al. (2012)	NED

[1] http://www.physics.purdue.edu/astro/MOJAVE/index.html
[2] http://ned.ipac.caltech.edu/

Table 5.6 Sample of extreme scattering events included in the analysis

Source	Distance [Mpc]	Reference	Distance reference
0954 + 658	1951	Fiedler et al. (1987)	MOJAVE/NED
AO 0235+164	6142	Senkbeil et al. (2008)	MOJAVE/NED

Chapter 6

Conclusions

6.1 Radio Transients with LOFAR

With the majority of radio observations carried out at gigahertz frequencies, the low frequency transient sky has been poorly explored. LOFAR with its large field of view and broad spectral coverage provided an opportunity to search extensive areas of the sky across a wide bandwidth. However, as shown in this work, finding radio transients in LOFAR data proved to be extremely challenging. In Chapter 3 I presented work focused on searching for short duration radio transients in the LOFAR Radio Sky Monitor observations covering 440 deg^2. While a number of promising transient candidates have been found, a set of verification tests assigned their appearance in the images to RFI and imaging artefacts. Taking a conservative approach and assuming that none of those candidates were of an astrophysical origin, an upper limit of $\rho_{\rm RSM} < 2.7 \times 10^{-5}$ deg^{-2} was put on the areal density of transient events. I was also able to set constraints on the spectral index value of the first LOFAR transient detected in the NCP field (Stewart et al., 2016) with the upper limit of -1.4. Finally, this work highlighted the difficulties associated with the analysis of LOFAR data. In particular, it was shown that the short time-scale imaging is especially sensitive to various artefacts, which can strongly resemble real sources, and requires a careful and detailed approach.

6.2 Luminosity – Time-scale Correlation for Synchrotron Emitting Sources

In Chapter 4 I investigated the relation between the rise/decline time-scales and the peak radio luminosities across a wide range of flares originating from synchrotron emitting sources. It has been known for years that more massive, luminous sources are associated with flaring events evolving on longer time-scales than outbursts observed from nearby objects, however, it has not been quantitatively measured before. This work has shown that a broad correlation of the form $L \propto \tau^5$ exists for these types of events.

The sample of analysed objects was limited to those observed at the frequencies between 5 and 8 GHz due to the wavelength dependency of the light-curve profile. This effect was clearly demonstrated by the example of a 1.4 GHz dataset analysed for comparison, which showed that – as expected for synchrotron emission – lower frequencies correspond to lower luminosities and longer time-scales. Overall, the obtained correlation is steeper than expected, if compared to the relation between luminosities and time-scales for a set of events with approximately constant brightness temperatures. This discrepancy can be partially explained by reviewing the assumption about the size of the emitting region. In the analysis, this value is set to the maximum physical size possible. However, for some types of objects the actual size might be smaller, which means that the estimation of the brightness temperature in those cases is highly underestimated. Furthermore, emission observed from sources such as blazars – which make up a significant fraction of our sample – appears to be brighter and vary on shorter time-scales than it really does due to relativistic beaming. Correcting for this effect would shift high luminosity sources towards lower luminosities and longer time-scales, making the overall correlation less steep.

The results were illustrated in the more general context of radio transients phase space by extending the data sample to include the (previously known) measurements of coherent events. This comparison showed that the correlation between luminosities and time-scales does not apply to flares originating from coherent emission.

The outcome of the analysis proved to be promising in terms of exploring variability time-scales as a potential tool for early classification of synchrotron transient events.

6.3 Radio Transients Classification

The problem of near-real time classification of transient sources detected in radio surveys is crucial in terms of optimising the strategy for follow up observations. There are a number of methods which allow us to diagnose the nature of the source, however, they often require detailed multivawelength monitoring. In Chapter 5 I developed a method for classifying radio transients based on the earliest information contained in their rise and/or decline rates. The idea of the discussed technique is based on the results presented in Chapter 4, which showed a correlation between fast nearby sources and slow distant events.

Working towards the goal of complete automation of the classification process, we have developed a relatively simple software which automatically selects flaring events from the provided radio light-curves and takes all the necessary measurements. This method gave results which are in reasonable agreement with previous manual approach, additionally increasing the number of analysed flares and reducing the bias associated with manually editing the data.

Because the compiled sample of flares is highly biased and does not give an accurate account of the number of transient events expected to be found in the sky, I have estimated their areal densities within individual classes of objects. These estimations have been convolved with Gaussian representations of the variability time-scales distribution measured for each class in order to give the final distribution. As a result, to each of the rise/decline rate measurement of the transient candidate, we can assign parameters describing probabilities that the flare belongs to a particular class of objects.

We recognized that the main difficulty in using radio variability of a source as its classification feature might be introduced by scintillating sources, as well as extreme scattering events. Although the variability observed for these events reflects the way in which the interstellar medium affects the signal propagation, rather than intrinsic properties of objects, the corresponding time-scales seem to occupy the range characteristic for synchrotron events across all the classes. Additional information, such as spectral analysis, can help to differentiate between the synchrotron and non-intrinsic variability. However, this aspect of the proposed classification method might require further investigation.

6.4 Future Work

6.4.1 Finding Flares in V404 Cygni 2015 Outburst

The recent outburst of the nearby black hole V404 Cygni ($\approx$ 2.4 kpc away) has triggered extensive multiwavelength observations carried out across the world. One of the instruments monitoring this activity of V404 Cyg was the Arcminute Microkelvin Imager Large Array (AMI-LA; Zwart et al., 2008) – a synthesis radio telescope observing between 13-18 GHz. In 2012 AMI-LA was upgraded to enable an automatic response mode, which allows for fully robotised scheduling of follow up monitoring to well-localized *Swift* events, delivering some of the earliest radio observations of transients to date (Staley et al. 2013; Anderson et al. 2014).

Having the opportunity to analyse this rare, well sampled event, we chose one set of AMI-LA observations of the V404 Cyg in order to test the functionality of our flare finding routine. The data corresponds to observations carried out on a time-scale of ten days at the frequency of 13.9 GHz. The error bars have been estimated as ten per cent of the flux density measurements. Figure 6.1 shows the results of the analysis, with a total number of nine flares identified by the AFF. Marked with the green dashed line is the estimated background

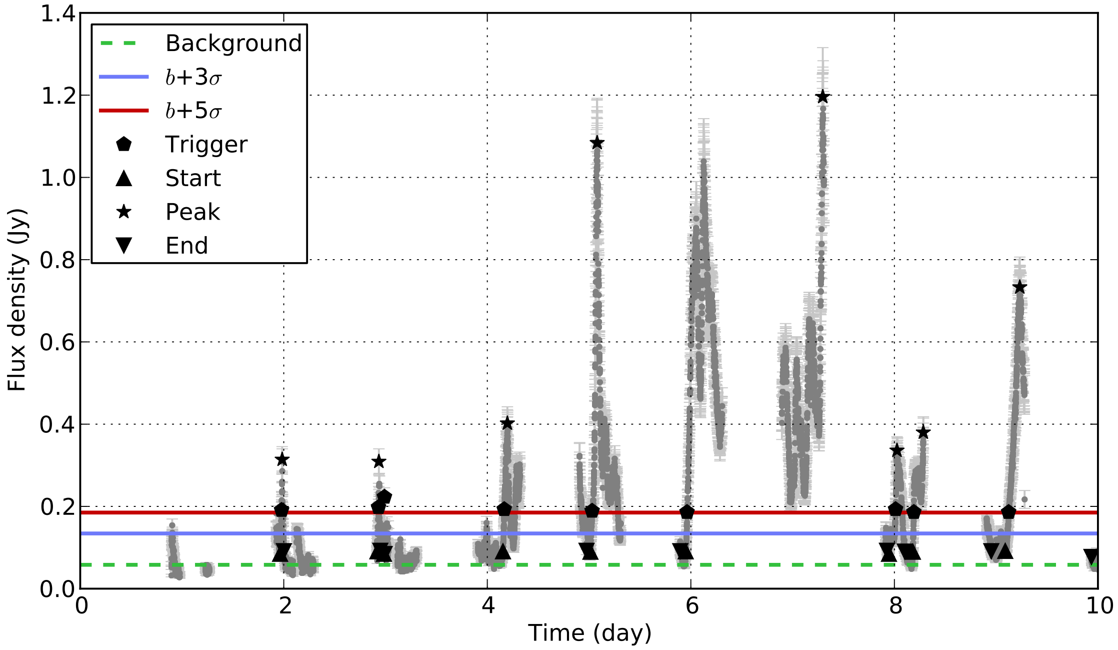

Fig. 6.1 Example of the Automatic Flare Finding (AFF) routine applied to the Arcminute Microkelvin Imager (AMI) observations of the V404 Cyg black hole. The data corresponds to 13.9 GHz observing frequency. We have run an AFF on the light-curve with the background estimated as described in Section 5.4.1, selecting nine flares.

level (which has been calculated as described in Section 5.4.1) and the blue and red lines correspond to 3 and 5σ levels above the background respectively.

A more detailed overview of the selected flaring events is presented in Figure 6.2, with four examples of the individual flares selected by the AFF. It shows that, overall, the thresholding approach works well in selecting single flaring events (left panel), however, as discussed in Sections 5.2.1 and 5.8.3, fails to separate super-imposed outbursts (right panel). Fits to the rise and decline phases of the individual flares shown in Figure 6.2 have been calculated as described in Section 5.4.2.

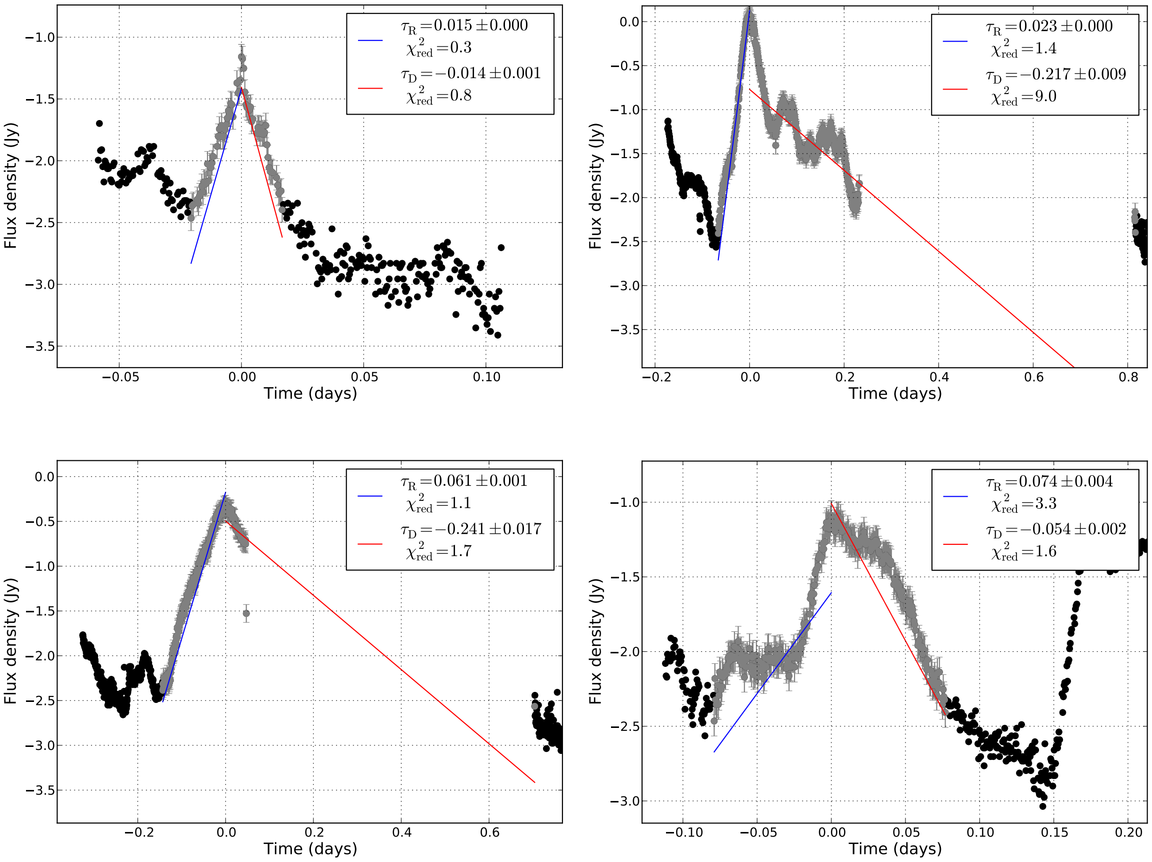

Fig. 6.2 Examples of the individual flares selected by the AFF from the AMI observation of V404 Cyg. Flares presented in the left panel show single outbursts correctly identified by the flare finding routine. Plots in the right panel show examples where the main flare has been identified by the AFF, however, additional super-imposed outbursts were not detected by the simple thresholding technique. Fits to the rise and decline phases of the individual flares have been calculated as described in Section 5.4.2.

6.4.2 Estimation of the Minimum Kinetic Energy

One of the interesting aspects of the discussed explosive events observed across a wide range of classes of objects is the estimation of their kinetic energy. While the calculation of the exact energy output associated with the event requires complex modelling, following the method described by Burbidge (1959) we can find its lower limit (Section 1.3.1). This is done by minimising the total energy associated with the event as a function of the magnetic field, assuming that the total energy consists of the energy in the electrons and the magnetic field.

In their overview, Fender and Muñoz-Darias (2015) discuss the general formula which can be used in order to estimate the minimum kinetic power of any synchrotron source. It shows that the lower limit of the energy associated with the synchrotron emitting plasma can be expressed as a function of the volume V in which the matter is contained and the monochromatic luminosity L_ν of the event

$$E_{\min} \sim 8 \times 10^6 \eta^{4/7} \left(\frac{V}{\mathrm{cm}^3}\right)^{3/7} \left(\frac{\nu}{\mathrm{Hz}}\right)^{2/7} \left(\frac{L_\nu}{\mathrm{erg\,s^{-1}Hz^{-1}}}\right)^{4/7} \mathrm{erg}, \tag{6.1}$$

where $\eta = \beta + 1$. Parameter $\beta << 1$ describes the energy in protons to electrons ratio, which allows us to assume that $\eta \approx 1$. This formula, independent of complex models applicable to individual classes of objects, can be used to estimate the minimum energy for the sample of flares selected in our analysis (Chapter 5), for which the monochromatic luminosity is known. Having measured the time-scale τ of the event we can estimate the volume of the emitting region (as it was done in Chapter 4), assuming that the expansion velocity of the relativistic plasma can not exceed $c/\sqrt{3}$. This allows us to use the Equation 6.4.2 in order to estimate the minimum kinetic energy associated with each of the analysed flares.

Figure 6.3 shows the minimum energy output estimated for rising (upper panel) and declining (lower panel) phases for a sample of synchrotron events, plotted against the

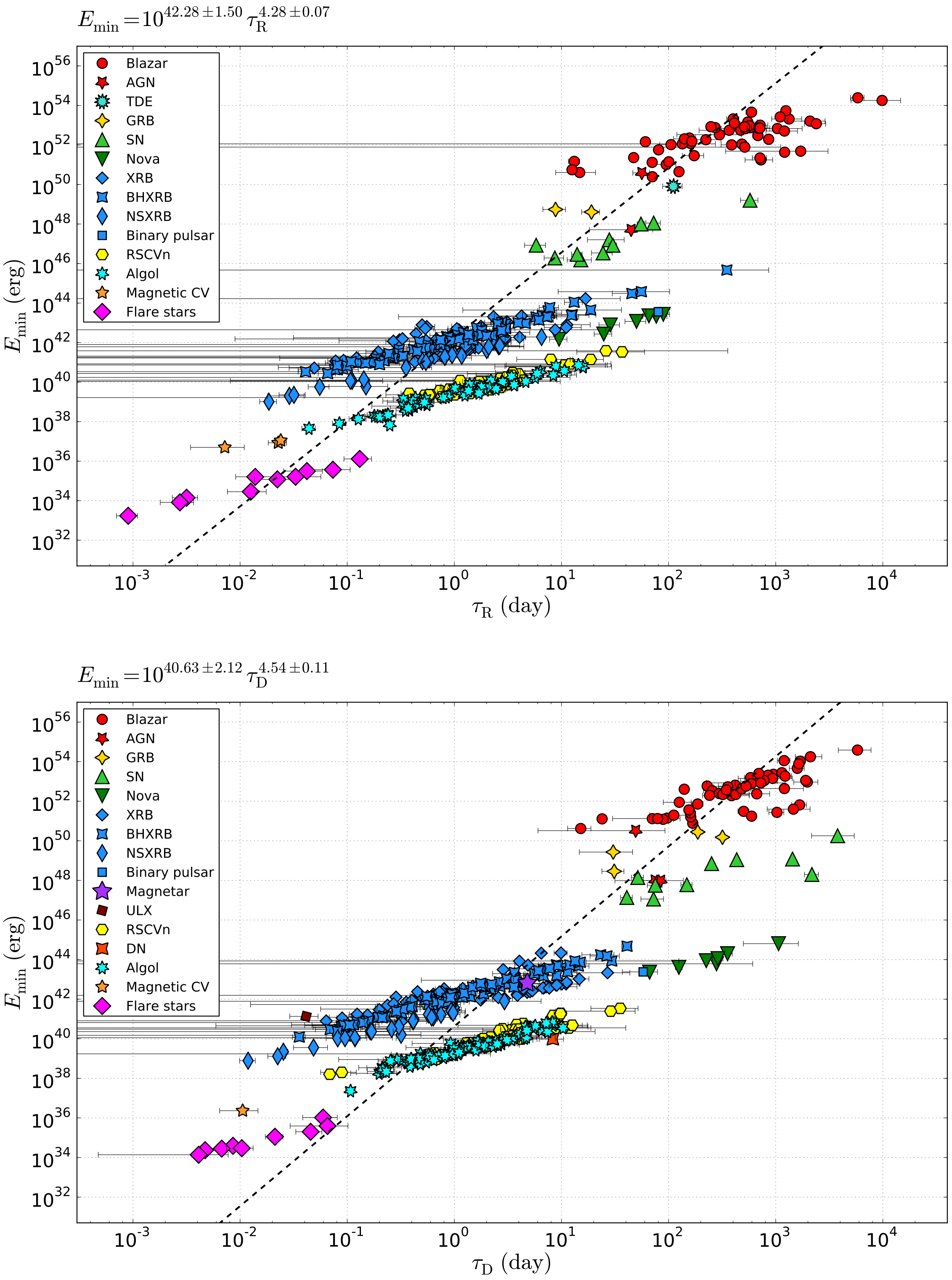

Fig. 6.3 The estimated minimum energy associated with synchrotron flares plotted against their rise and decline rates (upper and lower panel respectively). The correlation between the minimum energy and time-scale is of the form $E_{\rm min} \sim \tau^{4.5}$, with clear rising trend within individual classes corresponding to the time-scale dependence of the energy (Equation 6.4.2). The sample of sources is the same as in Chapter 4.

Table 6.1 Example comparison of the minimum kinetic power estimated based on the measured luminosity and time-scale of the events with the estimates found in the literature for several classes/objects.

Class/Objects	$P_{\mathrm{k,\,min}}$ (erg s^{-1}) This work	$P_{\mathrm{k,\,min}}$ (erg s^{-1}) Literature	References
Blazars[1]	1.5×10^{45}	7×10^{47}	López-Corredoira and Perucho (2012)
XRB: GRS 1915+105[2]	1.9×10^{37}	1.4×10^{41}	Zdziarski (2014)

[1] This work estimation of the minimum energy for blazars calculated as the average value of all blazars in our sample.

[2] Kinetic power $P_{\mathrm{k,\,min}}$ for the GRS 1915+105 estimated in this work was calculated as an average of $P_{\mathrm{k,\,min}}$ measured for all the flares included in the analysis.

rise/decline rates respectively. The overall correlation as fitted across all types of objects has the form of $E_{\mathrm{min}} \sim \tau^{4.5}$. Additionally, the minimum energy is clearly rising with time as observed within individual classes of events – this trend reflects the dependence of the estimation of the energy on time-scale, $E_{\mathrm{min}} \sim \tau^{9/7}$ (Equation 6.4.2). Tables 6.1 and 6.2 show a comparison between the minimum kinetic power and energy respectively calculated in this work and the estimations based on more complex approach found in the literature, for several classes of objects. Although the lower limit on the ejected energy calculated based on the luminosity and time-scale of the observed events is systematically lower than estimates taking into account more detailed processes, this simple method gives a relatively good and quick initial constraint.

6.4.3 Final Comments

This thesis presented the results of searching for low frequency radio transients in LOFAR observations, as well as new methods for early classification of synchrotron events based on their radio light-curves.

Table 6.2 Comparison of the minimum kinetic energy estimated based on the measured luminosity and time-scale of the events with the estimates found in the literature for several classes/objects.

Class/Objects	E_{min} (erg) This work	E_{min} (erg) Literature	References
SNe[1]	2.2×10^{47}	2.3×10^{51}	Lyman et al. (2016)
GRBs[2]	5×10^{48}	1.3×10^{51}	Bloom et al. (2003)

[1] Both this work as well as the literature based estimation of the supernovae energy was calculated as the average value of the following sources: SN 1993J, SN 1994I, SN 1998bw, SN 2003bg, SN 2004gq, SN 2008ax, SN 2011dh.

[2] This work estimation of the minimum energy for GRBs calculated as the average value of all GRBs in our sample.

While not many transients have been found with LOFAR to date, at this stage we can not completely rule them out. However, as shown in this work, finding a confident candidate might be challenging. As for searching for fast radio transients in image plane, at this point the efforts should be focused on learning more about short time-scale imaging and, in particular, better understanding of the origin of artefacts. These aspects are crucial if we want to avoid the risk of misinterpreting the data and make the verification process more efficient.

For the future development in classification of radio transients, the technique proposed in this work could be incorporated into a robotised transient detection pipeline and used as an early indicator of the nature of a candidate. The uncertainties associated with a small sample of flares representing individual classes of objects can be gradually reduced during the upcoming surveys carried out with e.g. MeerKAT and SKA, which will provide a more complete view of the transient and variable radio sky.

References

M. Abada-Simon, A. Lecacheux, T. S. Bastian, J. A. Bookbinder, and G. A. Dulk. The spectrum and variability of radio emission from AE Aquarii. *ApJ*, 406:692–700, Apr. 1993. doi: 10.1086/172479.

D. R. Altschuler, J. J. Broderick, B. Dennison, K. J. Mitchell, S. L. Odell, J. J. Condon, and H. E. Payne. Multifrequency light curves of low-frequency variable radio sources. *AJ*, 89: 1784–1798, Dec. 1984. doi: 10.1086/113687.

G. E. Anderson, A. J. van der Horst, T. D. Staley, R. P. Fender, R. A. M. J. Wijers, A. M. M. Scaife, C. Rumsey, D. J. Titterington, A. Rowlinson, and R. D. E. Saunders. Probing the bright radio flare and afterglow of GRB 130427A with the Arcminute Microkelvin Imager. *MNRAS*, 440:2059–2065, May 2014. doi: 10.1093/mnras/stu478.

S. Araujo-Betancor, B. T. Gänsicke, K. S. Long, K. Beuermann, D. de Martino, E. M. Sion, and P. Szkody. Far-Ultraviolet Spectroscopy of Magnetic Cataclysmic Variables. *ApJ*, 622:589–601, Mar. 2005. doi: 10.1086/427914.

Astropy Collaboration, T. P. Robitaille, E. J. Tollerud, P. Greenfield, M. Droettboom, E. Bray, T. Aldcroft, M. Davis, A. Ginsburg, A. M. Price-Whelan, W. E. Kerzendorf, A. Conley, N. Crighton, K. Barbary, D. Muna, H. Ferguson, F. Grollier, M. M. Parikh, P. H. Nair, H. M. Unther, C. Deil, J. Woillez, S. Conseil, R. Kramer, J. E. H. Turner, L. Singer, R. Fox, B. A. Weaver, V. Zabalza, Z. I. Edwards, K. Azalee Bostroem, D. J. Burke, A. R. Casey, S. M. Crawford, N. Dencheva, J. Ely, T. Jenness, K. Labrie, P. L. Lim, F. Pierfederici, A. Pontzen, A. Ptak, B. Refsdal, M. Servillat, and O. Streicher. Astropy: A community Python package for astronomy. *A&A*, 558:A33, Oct. 2013. doi: 10.1051/0004-6361/201322068.

M. Audard, J. R. Donisan, and M. Güdel. A multiwavelength study of RZ Cassiopeiae: the XMM-Newton/VLA campaign. In F. Favata, G. A. J. Hussain, and B. Battrick, editors, *13th Cambridge Workshop on Cool Stars, Stellar Systems and the Sun*, volume 560 of *ESA Special Publication*, page 407, Mar. 2005.

J. W. M. Baars and B. G. Hooghoudt. The Synthesis Radio Telescope at Westerbork. General Lay-out and Mechanical Aspects. *A&A*, 31:323, Mar. 1974.

V. Bakış, E. Budding, A. Erdem, H. Bakış, O. Demircan, and P. Hadrava. Analysis of δ Librae including Hipparcos astrometry. *MNRAS*, 370:1935–1945, Aug. 2006. doi: 10.1111/j.1365-2966.2006.10619.x.

K. W. Bannister, T. Murphy, B. M. Gaensler, R. W. Hunstead, and S. Chatterjee. A 22-yr southern sky survey for transient and variable radio sources using the Molonglo Observatory Synthesis Telescope. *MNRAS*, 412:634–664, Mar. 2011. doi: 10.1111/j.1365-2966.2010.17938.x.

E. S. Bartlett, J. S. Clark, M. J. Coe, M. R. Garcia, and P. Uttley. Timing and spectral analysis of the unusual X-ray transient XTE J0421+560/CI Camelopardalis. *MNRAS*, 429: 1213–1220, Feb. 2013. doi: 10.1093/mnras/sts411.

T. S. Bastian, G. A. Dulk, and G. Chanmugam. Radio flares from AE Aquarii - A low-power analog to Cygnus X-3? *ApJ*, 324:431–440, Jan. 1988. doi: 10.1086/165906.

M. E. Bell, T. Tzioumis, P. Uttley, R. P. Fender, P. Arévalo, E. Breedt, I. McHardy, D. E. Calvelo, O. Jamil, and E. Körding. X-ray and radio variability in the low-luminosity active galactic nucleus NGC 7213. *MNRAS*, 411:402–410, Feb. 2011. doi: 10.1111/j.1365-2966.2010.17692.x.

M. E. Bell, T. Murphy, D. L. Kaplan, P. Hancock, B. M. Gaensler, J. Banyer, K. Bannister, C. Trott, N. Hurley-Walker, R. B. Wayth, J.-P. Macquart, W. Arcus, D. Barnes, G. Bernardi, J. D. Bowman, F. Briggs, J. D. Bunton, R. J. Cappallo, B. E. Corey, A. Deshpande, L. deSouza, D. Emrich, R. Goeke, L. J. Greenhill, B. J. Hazelton, D. Herne, J. N. Hewitt, M. Johnston-Hollitt, J. C. Kasper, B. B. Kincaid, R. Koenig, E. Kratzenberg, C. J. Lonsdale, M. J. Lynch, S. R. McWhirter, D. A. Mitchell, M. F. Morales, E. Morgan, D. Oberoi, S. M. Ord, J. Pathikulangara, T. Prabu, R. A. Remillard, A. E. E. Rogers, A. Roshi, J. E. Salah, R. J. Sault, N. Udaya Shankar, K. S. Srivani, J. Stevens, R. Subrahmanyan, S. J. Tingay, M. Waterson, R. L. Webster, A. R. Whitney, A. Williams, C. L. Williams, and J. S. B. Wyithe. A survey for transients and variables with the Murchison Widefield Array 32-tile prototype at 154 MHz. *MNRAS*, 438:352–367, Feb. 2014. doi: 10.1093/mnras/stt2200.

N. Blagorodnova, S. E. Koposov, Ł. Wyrzykowski, M. Irwin, and N. A. Walton. GS-TEC: the Gaia spectrophotometry transient events classifier. *MNRAS*, 442:327–342, July 2014. doi: 10.1093/mnras/stu837.

J. S. Bloom, D. A. Frail, and S. R. Kulkarni. Gamma-Ray Burst Energetics and the Gamma-Ray Burst Hubble Diagram: Promises and Limitations. *ApJ*, 594:674–683, Sept. 2003. doi: 10.1086/377125.

J. S. Bloom, J. W. Richards, P. E. Nugent, R. M. Quimby, M. M. Kasliwal, D. L. Starr, D. Poznanski, E. O. Ofek, S. B. Cenko, N. R. Butler, S. R. Kulkarni, A. Gal-Yam, and N. Law. Automating Discovery and Classification of Transients and Variable Stars in the Synoptic Survey Era. *PASP*, 124:1175–1196, Nov. 2012. doi: 10.1086/668468.

K. M. Blundell and M. G. Bowler. Symmetry in the Changing Jets of SS 433 and Its True Distance from Us. *ApJL*, 616:L159–L162, Dec. 2004. doi: 10.1086/426542.

R. S. Booth, W. J. G. de Blok, J. L. Jonas, and B. Fanaroff. MeerKAT Key Project Science, Specifications, and Proposals. *ArXiv e-prints*, Oct. 2009.

A. P. Borisova, J. L. Innis, D. W. Coates, M. K. Tsvetkov, K.-P. Schröder, and I. Bues. Light curves of the active star CF Oct from the Bamberg Observatory Southern Sky Survey. In F. Favata, G. A. J. Hussain, and B. Battrick, editors, *13th Cambridge Workshop on Cool Stars, Stellar Systems and the Sun*, volume 560 of *ESA Special Publication*, page 453, Mar. 2005.

G. C. Bower, D. Saul, J. S. Bloom, A. Bolatto, A. V. Filippenko, R. J. Foley, and D. Perley. Submillijansky Transients in Archival Radio Observations. *ApJ*, 666:346–360, Sept. 2007. doi: 10.1086/519831.

C. F. Bradshaw, E. B. Fomalont, and B. J. Geldzahler. High-Resolution Parallax Measurements of Scorpius X-1. *ApJL*, 512:L121–L124, Feb. 1999. doi: 10.1086/311889.

H. Brink, J. W. Richards, D. Poznanski, J. S. Bloom, J. Rice, S. Negahban, and M. Wainwright. Using machine learning for discovery in synoptic survey imaging data. *MNRAS*, 435: 1047–1060, Oct. 2013. doi: 10.1093/mnras/stt1306.

S. Britzen, N. A. Kudryavtseva, A. Witzel, R. M. Campbell, E. Ros, M. Karouzos, A. Mehta, M. F. Aller, H. D. Aller, T. Beckert, and J. A. Zensus. The kinematics in the pc-scale jets of AGN. The case of S5 1803+784. *A&A*, 511:A57, Feb. 2010. doi: 10.1051/0004-6361/20079267.

C. Brocksopp, J. C. A. Miller-Jones, R. P. Fender, and B. W. Stappers. A highly polarized radio jet during the 1998 outburst of the black hole transient XTE J1748-288. *MNRAS*, 378:1111–1117, July 2007. doi: 10.1111/j.1365-2966.2007.11846.x.

J. W. Broderick, R. P. Fender, R. P. Breton, A. J. Stewart, A. Rowlinson, J. D. Swinbank, J. W. T. Hessels, T. D. Staley, A. J. van der Horst, M. E. Bell, D. Carbone, Y. Cendes, S. Corbel, J. Eislöffel, H. Falcke, J.-M. Grießmeier, T. E. Hassall, P. Jonker, M. Kramer, M. Kuniyoshi, C. J. Law, S. Markoff, G. J. Molenaar, M. Pietka, L. H. A. Scheers, M. Serylak, B. W. Stappers, S. ter Veen, J. van Leeuwen, R. A. M. J. Wijers, R. Wijnands, M. W. Wise, and P. Zarka. Low-radio-frequency eclipses of the redback pulsar J2215+5135 observed in the image plane with LOFAR. *MNRAS*, 459:2681–2689, July 2016. doi: 10.1093/mnras/stw794.

G. R. Burbidge. Estimates of the Total Energy in Particles and Magnetic Field in the Non-Thermal Radio Sources. *ApJ*, 129:849–852, May 1959. doi: 10.1086/146680.

S. Burke-Spolaor and K. W. Bannister. The Galactic Position Dependence of Fast Radio Bursts and the Discovery of FRB011025. *ApJ*, 792:19, Sept. 2014. doi: 10.1088/0004-637X/792/1/19.

T. Canosa, R. P. Fender, and G. G. Pooley. The decay phase of radio flares from GRS1915 + 105. *Vistas in Astronomy*, 41:21–26, 1997. doi: 10.1016/S0083-6656(96)00057-8.

Y. Cao, M. M. Kasliwal, J. D. Neill, S. R. Kulkarni, Y.-Q. Lou, S. Ben-Ami, J. S. Bloom, S. B. Cenko, N. M. Law, P. E. Nugent, E. O. Ofek, D. Poznanski, and R. M. Quimby. Classical Novae in Andromeda: Light Curves from the Palomar Transient Factory and GALEX. *ApJ*, 752:133, June 2012. doi: 10.1088/0004-637X/752/2/133.

D. Carbone, A. J. van der Horst, R. A. M. J. Wijers, J. D. Swinbank, A. Rowlinson, J. W. Broderick, Y. N. Cendes, A. J. Stewart, M. E. Bell, R. P. Breton, S. Corbel, J. Eislöffel, R. P. Fender, J.-M. Grießmeier, J. W. T. Hessels, P. Jonker, M. Kramer, C. J. Law, J. C. A. Miller-Jones, M. Pietka, L. H. A. Scheers, B. W. Stappers, J. van Leeuwen, R. Wijnands, M. Wise, and P. Zarka. New methods to constrain the radio transient rate: results from a survey of four fields with LOFAR. *MNRAS*, 459:3161–3174, July 2016. doi: 10.1093/mnras/stw539.

Y. Cendes, R. A. M. J. Wijers, J. D. Swinbank, A. Rowlinson, A. J. van der Horst, D. Carbone, J. W. Broderick, T. D. Staley, A. J. Stewart, G. Molenaar, F. Huizinga, A. Alexov, M. E. Bell, T. Coenen, S. Corbel, J. Eislöffel, R. Fender, J. Grießmeier, J. Hessel, P. Jonker, M. Kramer, M. Kuniyoshi, C. J. Law, S. Markoff, M. Pietka, B. Stappers, M. Wise, and P. Zarka. LOFAR Observations of Swift J1644+57 and Implications for Short-Duration Transients. *ArXiv e-prints*, Dec. 2014.

S. B. Cenko, D. A. Frail, F. A. Harrison, S. R. Kulkarni, E. Nakar, P. C. Chandra, N. R. Butler, D. B. Fox, A. Gal-Yam, M. M. Kasliwal, J. Kelemen, D.-S. Moon, E. O. Ofek, P. A. Price, A. Rau, A. M. Soderberg, H. I. Teplitz, M. W. Werner, D. C.-J. Bock, J. S. Bloom, D. A. Starr, A. V. Filippenko, R. A. Chevalier, N. Gehrels, J. N. Nousek, and T. Piran. The Collimation and Energetics of the Brightest Swift Gamma-ray Bursts. *ApJ*, 711:641–654, Mar. 2010. doi: 10.1088/0004-637X/711/2/641.

P. Chandra and D. A. Frail. A Radio-selected Sample of Gamma-Ray Burst Afterglows. *ApJ*, 746:156, Feb. 2012. doi: 10.1088/0004-637X/746/2/156.

Y.-J. Chen, D.-R. Jiang, and F.-J. Zhang. Multi-frequency VLBI Observations of NRAO 150. , 1:507–513, Dec. 2001.

R. A. Chevalier. Are young supernova remnants interacting with circumstellar gas. *ApJL*, 259:L85–L89, Aug. 1982a. doi: 10.1086/183853.

R. A. Chevalier. The radio and X-ray emission from type II supernovae. *ApJ*, 259:302–310, Aug. 1982b. doi: 10.1086/160167.

R. A. Chevalier and Z.-Y. Li. Gamma-Ray Burst Environments and Progenitors. *ApJL*, 520: L29–L32, July 1999. doi: 10.1086/312147.

L. Chomiuk, M. I. Krauss, M. P. Rupen, T. Nelson, N. Roy, J. L. Sokoloski, K. Mukai, U. Munari, A. Mioduszewski, J. Weston, T. J. O'Brien, S. P. S. Eyres, and M. F. Bode. The Radio Light Curve of the Gamma-Ray Nova in V407 CYG: Thermal Emission from the Ionized Symbiotic Envelope, Devoured from within by the Nova Blast. *ApJ*, 761:173, Dec. 2012. doi: 10.1088/0004-637X/761/2/173.

M. J. Church, A. Gibiec, M. Bałucińska-Church, and N. K. Jackson. Spectral investigations of the nature of the Scorpius X-1 like sources. *A&A*, 546:A35, Oct. 2012. doi: 10.1051/0004-6361/201218987.

B. G. Clark. An efficient implementation of the algorithm 'CLEAN'. *A&A*, 89:377, Sept. 1980.

J. J. Condon, W. D. Cotton, E. W. Greisen, Q. F. Yin, R. A. Perley, G. B. Taylor, and J. J. Broderick. The NRAO VLA Sky Survey. *AJ*, 115:1693–1716, May 1998. doi: 10.1086/300337.

D. L. Coppejans, E. G. Körding, J. C. A. Miller-Jones, M. P. Rupen, C. Knigge, G. R. Sivakoff, and P. J. Groot. Novalike cataclysmic variables are significant radio emitters. *MNRAS*, 451:3801–3813, Aug. 2015. doi: 10.1093/mnras/stv1225.

J. M. Cordes and T. J. W. Lazio. NE2001.I. A New Model for the Galactic Distribution of Free Electrons and its Fluctuations. *ArXiv Astrophysics e-prints*, July 2002.

J. M. Cordes, T. J. W. Lazio, and M. A. McLaughlin. The dynamic radio sky. *NewA Rev.*, 48: 1459–1472, Dec. 2004. doi: 10.1016/j.newar.2004.09.038.

D. Cseh, S. Corbel, P. Kaaret, C. Lang, F. Grisé, Z. Paragi, A. Tzioumis, V. Tudose, and H. Feng. Black Hole Powered Nebulae and a Case Study of the Ultraluminous X-Ray Source IC 342 X-1. *ApJ*, 749:17, Apr. 2012. doi: 10.1088/0004-637X/749/1/17.

A. D'Aì, E. Bozzo, A. Papitto, R. Iaria, T. Di Salvo, L. Burderi, A. Riggio, E. Egron, and N. R. Robba. A complete X-ray spectral coverage of the 2010 May-June outbursts of Circinus X-1. *A&A*, 543:A20, July 2012. doi: 10.1051/0004-6361/201118577.

C. De Breuck, W. van Breugel, H. J. A. Röttgering, and G. Miley. A sample of 669 ultra steep spectrum radio sources to find high redshift radio galaxies. , 143:303–333, Apr. 2000. doi: 10.1051/aas:2000181.

A. G. de Bruyn and J.-P. Macquart. The intra-hour variable quasar J1819+3845: 13-year evolution, jet polarization structure, and interstellar scattering screen properties. *A&A*, 574:A125, Feb. 2015. doi: 10.1051/0004-6361/201220522.

J. Dennett-Thorpe and A. G. de Bruyn. Annual modulation in the scattering of J1819+3845: Peculiar plasma velocity and anisotropy. *A&A*, 404:113–132, June 2003. doi: 10.1051/0004-6361:20030329.

P. E. Dewdney, P. J. Hall, R. T. Schilizzi, and T. J. L. W. Lazio. The Square Kilometre Array. *IEEE Proceedings*, 97:1482–1496, Aug. 2009. doi: 10.1109/JPROC.2009.2021005.

V. Dhawan, A. Mioduszewski, and M. Rupen. LS I +61 303 is a Be-Pulsar binary, not a Microquasar. In *VI Microquasar Workshop: Microquasars and Beyond*, page 52, 2006.

S. G. Djorgovski, A. J. Drake, A. A. Mahabal, M. J. Graham, C. Donalek, R. Williams, E. C. Beshore, S. M. Larson, J. Prieto, M. Catelan, E. Christensen, and R. H. McNaught. The Catalina Real-Time Transient Survey (CRTS). *ArXiv e-prints*, Feb. 2011.

S. G. Djorgovski, A. A. Mahabal, C. Donalek, M. J. Graham, A. J. Drake, B. Moghaddam, and M. Turmon. Flashes in a Star Stream: Automated Classification of Astronomical Transient Events. *ArXiv e-prints*, Sept. 2012.

L. du Buisson, N. Sivanandam, B. A. Bassett, and M. Smith. Machine learning classification of SDSS transient survey images. *MNRAS*, 454:2026–2038, Dec. 2015. doi: 10.1093/mnras/stv2041.

H. W. Duerbeck. Constraints for cataclysmic binary evolution as derived from space distributions. , 99:363–385, Feb. 1984. doi: 10.1007/BF00650260.

H. W. Duerbeck. Hipparcos parallaxes of cataclysmic binaries and the quest for their absolute magnitudes. *Information Bulletin on Variable Stars*, 4731:1, July 1999.

S. L. Ellison, P. Vreeswijk, C. Ledoux, J. P. Willis, A. Jaunsen, R. A. M. J. Wijers, A. Smette, J. P. U. Fynbo, P. Møller, J. Hjorth, and A. Kaufer. Three intervening galaxy absorbers towards GRB 060418: faint and dusty? *MNRAS*, 372:L38–L42, Oct. 2006. doi: 10.1111/j.1745-3933.2006.00221.x.

D. Emmanoulopoulos, I. E. Papadakis, F. Nicastro, and I. M. McHardy. X-ray spectral analysis of the low-luminosity active galactic nucleus NGC 7213 using long XMM-Newton observations. *MNRAS*, 429:3439–3448, Mar. 2013. doi: 10.1093/mnras/sts610.

F. Favata, G. Micela, and S. Sciortino. The space density of active binaries from X-ray surveys. *A&A*, 298:482, June 1995.

R. Fender. Jets From X-ray Binaries: A Brief Overview and Comparison with Active Galactic Nuclei. In P. A. Hughes and J. N. Bregman, editors, *Relativistic Jets: The Common Physics of AGN, Microquasars, and Gamma-Ray Bursts*, volume 856 of *American Institute of Physics Conference Series*, pages 23–32, Sept. 2006. doi: 10.1063/1.2356382.

R. Fender and T. Muñoz-Darias. The balance of power: accretion and feedback in stellar mass black holes. *ArXiv e-prints*, May 2015.

R. Fender, R. Wijers, B. Stappers, and t. LOFAR Transients Key Science Project. LOFAR Transients and the Radio Sky Monitor. *ArXiv e-prints*, May 2008a.

R. Fender, R. Wijers, B. Stappers, and t. LOFAR Transients Key Science Project. LOFAR Transients and the Radio Sky Monitor. *ArXiv e-prints*, May 2008b.

R. Fender, A. Stewart, J.-P. Macquart, I. Donnarumma, T. Murphy, A. Deller, Z. Paragi, and S. Chatterjee. Transient Astrophysics with the Square Kilometre Array. *ArXiv e-prints*, July 2015.

R. P. Fender and M. E. Bell. Radio transients: an antediluvian review. *Bulletin of the Astronomical Society of India*, 39:315–332, Sept. 2011.

H. Feng and P. Kaaret. Optical Counterpart of the Ultraluminous X-Ray Source IC 342 X-1. *ApJ*, 675:1067–1075, Mar. 2008. doi: 10.1086/527353.

R. Fiedler, B. Dennison, K. J. Johnston, E. B. Waltman, and R. S. Simon. A summary of extreme scattering events and a descriptive model. *ApJ*, 430:581–594, Aug. 1994. doi: 10.1086/174432.

R. L. Fiedler, B. Dennison, K. J. Johnston, and A. Hewish. Extreme scattering events caused by compact structures in the interstellar medium. *Nature*, 326:675–678, Apr. 1987. doi: 10.1038/326675a0.

K. Findeisen, A. M. Cody, and L. Hillenbrand. Simulated Performance of Timescale Metrics for Aperiodic Light Curves. *ApJ*, 798:89, Jan. 2015. doi: 10.1088/0004-637X/798/2/89.

D. A. Frail, S. R. Kulkarni, L. Nicastro, M. Feroci, and G. B. Taylor. The radio afterglow from the γ-ray burst of 8 May 1997. *Nature*, 389:261–263, Sept. 1997. doi: 10.1038/38451.

D. A. Frail, E. Waxman, and S. R. Kulkarni. A 450 Day Light Curve of the Radio Afterglow of GRB 970508: Fireball Calorimetry. *ApJ*, 537:191–204, July 2000. doi: 10.1086/309024.

D. A. Frail, S. R. Kulkarni, E. O. Ofek, G. C. Bower, and E. Nakar. A Revised View of the Transient Radio Sky. *ApJ*, 747:70, Mar. 2012. doi: 10.1088/0004-637X/747/1/70.

R. H. Frater, J. W. Brooks, and J. B. Whiteoak. The Australia Telescope - Overview. *Journal of Electrical and Electronics Engineering Australia*, 12:103–112, June 1992.

K. É. Gabányi, N. Marchili, T. P. Krichbaum, S. Britzen, L. Fuhrmann, A. Witzel, J. A. Zensus, P. Müller, X. Liu, H. G. Song, J. L. Han, and X. H. Sun. The IDV source J 1128+5925, a new candidate for annual modulation? *A&A*, 470:83–95, July 2007. doi: 10.1051/0004-6361:20067033.

B. M. Gaensler, C. Kouveliotou, J. D. Gelfand, G. B. Taylor, D. Eichler, R. A. M. J. Wijers, J. Granot, E. Ramirez-Ruiz, Y. E. Lyubarsky, R. W. Hunstead, D. Campbell-Wilson, A. J. van der Horst, M. A. McLaughlin, R. P. Fender, M. A. Garrett, K. J. Newton-McGee, D. M. Palmer, N. Gehrels, and P. M. Woods. An expanding radio nebula produced by a giant flare from the magnetar SGR 1806-20. *Nature*, 434:1104–1106, Apr. 2005. doi: 10.1038/nature03498.

E. Gallo, R. P. Fender, and G. G. Pooley. A universal radio-X-ray correlation in low/hard state black hole binaries. *MNRAS*, 344:60–72, Sept. 2003. doi: 10.1046/j.1365-8711.2003.06791.x.

E. Gallo, S. Corbel, R. P. Fender, T. J. Maccarone, and A. K. Tzioumis. A transient large-scale relativistic radio jet from GX 339-4. *MNRAS*, 347:L52–L56, Jan. 2004. doi: 10.1111/j.1365-2966.2004.07435.x.

L. C. Gallo, P. G. Edwards, E. Ferrero, J. Kataoka, D. R. Lewis, S. P. Ellingsen, Z. Misanovic, W. F. Welsh, M. Whiting, T. Boller, W. Brinkmann, J. Greenhill, and A. Oshlack. The spectral energy distribution of PKS 2004-447: a compact steep-spectrum source and possible radio-loud narrow-line Seyfert 1 galaxy. *MNRAS*, 370:245–254, July 2006. doi: 10.1111/j.1365-2966.2006.10482.x.

D. K. Galloway, M. P. Muno, J. M. Hartman, D. Psaltis, and D. Chakrabarty. Thermonuclear (Type I) X-Ray Bursts Observed by the Rossi X-Ray Timing Explorer. *ApJS*, 179:360–422, Dec. 2008. doi: 10.1086/592044.

P. Gandhi, V. S. Dhillon, M. Durant, A. C. Fabian, A. Kubota, K. Makishima, J. Malzac, T. R. Marsh, J. M. Miller, T. Shahbaz, H. C. Spruit, and P. Casella. Rapid optical and X-ray timing observations of GX339-4: multicomponent optical variability in the low/hard state. *MNRAS*, 407:2166–2192, Oct. 2010. doi: 10.1111/j.1365-2966.2010.17083.x.

D. Giannios and B. D. Metzger. Radio transients from stellar tidal disruption by massive black holes. *MNRAS*, 416:2102–2107, Sept. 2011. doi: 10.1111/j.1365-2966.2011.19188.x.

M. Giroletti, G. B. Taylor, and G. Giovannini. The Two-sided Parsec-Scale Structure of the Low-Luminosity Active Galactic Nucleus in NGC 4278. *ApJ*, 622:178–186, Mar. 2005. doi: 10.1086/427898.

T. H. Hankins, J. S. Kern, J. C. Weatherall, and J. A. Eilek. Nanosecond radio bursts from strong plasma turbulence in the Crab pulsar. *Nature*, 422:141–143, Mar. 2003.

D. Hannikainen, K. Wu, D. Campbell-Wilson, R. Hunstead, J. Lovell, V. McIntyre, J. Reynolds, R. Soria, and T. Tzioumis. Radio emission from the X-ray transient XTE J1550-564. In A. Gimenez, V. Reglero, and C. Winkler, editors, *Exploring the Gamma-Ray Universe*, volume 459 of *ESA Special Publication*, pages 291–294, Sept. 2001.

D. C. Hannikainen, R. W. Hunstead, D. Campbell-Wilson, K. Wu, D. J. McKay, D. P. Smits, and R. J. Sault. Radio Emission from GRO J1655-40 during the 1994 Jet Ejection Episodes. *ApJ*, 540:521–534, Sept. 2000. doi: 10.1086/309294.

T. E. Hassall, E. F. Keane, and R. P. Fender. Detecting highly dispersed bursts with next-generation radio telescopes. *MNRAS*, 436:371–379, Nov. 2013. doi: 10.1093/mnras/stt1598.

G. H. Heald, R. F. Pizzo, E. Orrú, R. P. Breton, D. Carbone, C. Ferrari, M. J. Hardcastle, W. Jurusik, G. Macario, D. Mulcahy, D. Rafferty, A. Asgekar, M. Brentjens, R. A. Fallows, W. Frieswijk, M. C. Toribio, B. Adebahr, M. Arts, M. R. Bell, A. Bonafede, J. Bray, J. Broderick, T. Cantwell, P. Carroll, Y. Cendes, A. O. Clarke, J. Croston, S. Daiboo, F. de Gasperin, J. Gregson, J. Harwood, T. Hassall, V. Heesen, A. Horneffer, A. J. van der Horst, M. Iacobelli, V. Jelić, D. Jones, D. Kant, G. Kokotanekov, P. Martin, J. P. McKean, L. K. Morabito, B. Nikiel-Wroczyński, A. Offringa, V. N. Pandey, M. Pandey-Pommier, M. Pietka, L. Pratley, C. Riseley, A. Rowlinson, J. Sabater, A. M. M. Scaife, L. H. A. Scheers, K. Sendlinger, A. Shulevski, M. Sipior, C. Sobey, A. J. Stewart, A. Stroe, J. Swinbank, C. Tasse, J. Trüstedt, E. Varenius, S. van Velzen, N. Vilchez, R. J. van Weeren, S. Wijnholds, W. L. Williams, A. G. de Bruyn, R. Nijboer, M. Wise, A. Alexov, J. Anderson, I. M. Avruch, R. Beck, M. E. Bell, I. van Bemmel, M. J. Bentum, G. Bernardi, P. Best, F. Breitling, W. N. Brouw, M. Brüggen, H. R. Butcher, B. Ciardi, J. E. Conway, E. de Geus, A. de Jong, M. de Vos, A. Deller, R.-J. Dettmar, S. Duscha, J. Eislöffel, D. Engels, H. Falcke, R. Fender, M. A. Garrett, J. Grießmeier, A. W. Gunst, J. P. Hamaker, J. W. T. Hessels, M. Hoeft, J. Hörandel, H. A. Holties, H. Intema, N. J. Jackson, E. Jütte, A. Karastergiou, W. F. A. Klijn, V. I. Kondratiev, L. V. E. Koopmans, M. Kuniyoshi, G. Kuper, C. Law, J. van Leeuwen, M. Loose, P. Maat, S. Markoff, R. McFadden, D. McKay-Bukowski, M. Mevius, J. C. A. Miller-Jones, R. Morganti, H. Munk, A. Nelles, J. E. Noordam, M. J. Norden, H. Paas, A. G. Polatidis, W. Reich, A. Renting, H. Röttgering, A. Schoenmakers, D. Schwarz, J. Sluman, O. Smirnov, B. W. Stappers, M. Steinmetz, M. Tagger, Y. Tang, S. ter Veen, S. Thoudam, R. Vermeulen, C. Vocks, C. Vogt, R. A. M. J. Wijers, O. Wucknitz, S. Yatawatta, and P. Zarka. The LOFAR Multifrequency Snapshot Sky Survey (MSSS). I. Survey description and first results. *A&A*, 582:A123, Oct. 2015. doi: 10.1051/0004-6361/201425210.

A. Hewish, S. J. Bell, J. D. H. Pilkington, P. F. Scott, and R. A. Collins. Observation of a Rapidly Pulsating Radio Source. *Nature*, 217:709–713, Feb. 1968. doi: 10.1038/217709a0.

E. J. Hilton, A. A. West, S. L. Hawley, and A. F. Kowalski. M Dwarf Flares from Time-resolved Sloan Digital Sky Survey Spectra. *AJ*, 140:1402–1413, Nov. 2010. doi: 10.1088/0004-6256/140/5/1402.

R. M. Hjellming. A Unified Model Approach to Interpreting Radio and Optical Images and Spectra for Classical Novae. In A. R. Taylor and J. M. Paredes, editors, *Radio Emission from the Stars and the Sun*, volume 93 of *Astronomical Society of the Pacific Conference Series*, page 174, 1996.

R. M. Hjellming and K. J. Johnston. Radio emission from conical jets associated with X-ray binaries. *ApJ*, 328:600–609, May 1988. doi: 10.1086/166318.

R. M. Hjellming, J. H. van Gorkom, A. R. Taylor, E. R. Sequist, S. Padin, R. J. Davis, and M. F. Bode. Radio observations of the 1985 outburst of RS Ophiuchi. *ApJL*, 305:L71–L75, June 1986. doi: 10.1086/184687.

J. A. Högbom. Aperture Synthesis with a Non-Regular Distribution of Interferometer Baselines. , 15:417, June 1974.

D. C. Homan, Y. Y. Kovalev, M. L. Lister, E. Ros, K. I. Kellermann, M. H. Cohen, R. C. Vermeulen, J. A. Zensus, and M. Kadler. Intrinsic Brightness Temperatures of AGN Jets. *ApJL*, 642:L115–L118, May 2006. doi: 10.1086/504715.

J. Homan, R. Wijnands, M. P. Rupen, R. Fender, R. M. Hjellming, T. di Salvo, and M. van der Klis. Simultaneous radio and X-ray observations of the low-mass X-ray binary GX 13+1. *A&A*, 418:255–263, Apr. 2004. doi: 10.1051/0004-6361:20034258.

D. P. Huenemoerder, K. J. H. Phillips, J. Sylwester, and B. Sylwester. Stellar Coronae, Solar Flares: A Detailed Comparison of σ GEM, HR 1099, and the Sun in High-resolution X-Rays. *ApJ*, 768:135, May 2013. doi: 10.1088/0004-637X/768/2/135.

D. Huppenkothen, B. J. Brewer, D. W. Hogg, I. Murray, M. Frean, C. Elenbaas, A. L. Watts, Y. Levin, A. J. van der Horst, and C. Kouveliotou. Dissecting Magnetar Variability with Bayesian Hierarchical Models. *ApJ*, 810:66, Sept. 2015. doi: 10.1088/0004-637X/810/1/66.

S. D. Hyman, T. J. W. Lazio, N. E. Kassim, and A. L. Bartleson. Low-Frequency Radio Transients in the Galactic Center. *AJ*, 123:1497–1501, Mar. 2002. doi: 10.1086/338905.

S. D. Hyman, T. J. W. Lazio, N. E. Kassim, P. S. Ray, C. B. Markwardt, and F. Yusef-Zadeh. A powerful bursting radio source towards the Galactic Centre. *Nature*, 434:50–52, Mar. 2005. doi: 10.1038/nature03400.

S. D. Hyman, T. J. W. Lazio, S. Roy, P. S. Ray, N. E. Kassim, and J. L. Neureuther. A New Radio Detection of the Transient Bursting Source GCRT J1745-3009. *ApJ*, 639:348–353, Mar. 2006. doi: 10.1086/499294.

S. D. Hyman, R. Wijnands, T. J. W. Lazio, S. Pal, R. Starling, N. E. Kassim, and P. S. Ray. GCRT J1742-3001: A New Radio Transient Toward the Galactic Center. *ApJ*, 696: 280–286, May 2009. doi: 10.1088/0004-637X/696/1/280.

T. R. Jaeger, S. D. Hyman, N. E. Kassim, and T. J. W. Lazio. Discovery of a Meter-wavelength Radio Transient in the SWIRE Deep Field: 1046+59. *AJ*, 143:96, Apr. 2012. doi: 10.1088/0004-6256/143/4/96.

D. L. Jauncey, H. E. Bignall, J. E. J. Lovell, L. Kedziora-Chudczer, A. K. Tzioumis, J.-P. Macquart, and B. J. Rickett. Interstellar Scintillation and Radio Intra-Day Variability. In J. A. Zensus, M. H. Cohen, and E. Ros, editors, *Radio Astronomy at the Fringe*, volume 300 of *Astronomical Society of the Pacific Conference Series*, page 199, 2003.

S. Johnston, R. N. Manchester, D. McConnell, and D. Campbell-Wilson. Transient radio emission from the PSR B1259-63 system near periastron. *MNRAS*, 302:277–287, Jan. 1999. doi: 10.1046/j.1365-8711.1999.02133.x.

S. Johnston, M. Bailes, N. Bartel, C. Baugh, M. Bietenholz, C. Blake, R. Braun, J. Brown, S. Chatterjee, J. Darling, A. Deller, R. Dodson, P. G. Edwards, R. Ekers, S. Ellingsen, I. Feain, B. M. Gaensler, M. Haverkorn, G. Hobbs, A. Hopkins, C. Jackson, C. James, G. Joncas, V. Kaspi, V. Kilborn, B. Koribalski, R. Kothes, T. L. Landecker, E. Lenc, J. Lovell, J.-P. Macquart, R. Manchester, D. Matthews, N. M. McClure-Griffiths, R. Norris, U.-L. Pen, C. Phillips, C. Power, R. Protheroe, E. Sadler, B. Schmidt, I. Stairs, L. Staveley-Smith, J. Stil, R. Taylor, S. Tingay, A. Tzioumis, M. Walker, J. Wall, and M. Wolleben. Science with the Australian Square Kilometre Array Pathfinder. , 24:174–188, Dec. 2007. doi: 10.1071/AS07033.

S. Johnston, R. Taylor, M. Bailes, N. Bartel, C. Baugh, M. Bietenholz, C. Blake, R. Braun, J. Brown, S. Chatterjee, J. Darling, A. Deller, R. Dodson, P. Edwards, R. Ekers, S. Ellingsen, I. Feain, B. Gaensler, M. Haverkorn, G. Hobbs, A. Hopkins, C. Jackson, C. James, G. Joncas, V. Kaspi, V. Kilborn, B. Koribalski, R. Kothes, T. Landecker, A. Lenc, J. Lovell, J.-P. Macquart, R. Manchester, D. Matthews, N. McClure-Griffiths, R. Norris, U.-L. Pen, C. Phillips, C. Power, R. Protheroe, E. Sadler, B. Schmidt, I. Stairs, L. Staveley-Smith, J. Stil, S. Tingay, A. Tzioumis, M. Walker, J. Wall, and M. Wolleben. Science with ASKAP. The Australian square-kilometre-array pathfinder. *Experimental Astronomy*, 22:151–273, Dec. 2008. doi: 10.1007/s10686-008-9124-7.

K. L. Jones, A. Brown, R. T. Stewart, and O. B. Slee. Extended multifrequency observations of radio emission from the RS CVn binary HR 1099. *MNRAS*, 283:1331–1339, Dec. 1996.

P. Kaaret, S. Corbel, A. H. Prestwich, and A. Zezas. Radio Emission from an Ultraluminous X-ray Source. *Science*, 299:365–368, Jan. 2003. doi: 10.1126/science.1079610.

M. M. Kasliwal. Transients in the local Universe: systematically bridging the gap between novae and supernovae. *Bulletin of the Astronomical Society of India*, 39:375–385, Sept. 2011.

M. Kato and I. Hachisu. A Modeling of the Super-Eddington Luminosity in Nova Outbursts: V1974 Cygni. *ApJL*, 633:L117–L120, Nov. 2005. doi: 10.1086/498300.

E. F. Keane. Radio pulsar variability. In J. van Leeuwen, editor, *IAU Symposium*, volume 291 of *IAU Symposium*, pages 295–300, Mar. 2013. doi: 10.1017/S1743921312023927.

E. F. Keane, M. Kramer, A. G. Lyne, B. W. Stappers, and M. A. McLaughlin. Rotating Radio Transients: new discoveries, timing solutions and musings. *MNRAS*, 415:3065–3080, Aug. 2011. doi: 10.1111/j.1365-2966.2011.18917.x.

K. I. Kellermann and I. I. K. Pauliny-Toth. The Spectra of Opaque Radio Sources. *ApJL*, 155:L71, Feb. 1969. doi: 10.1086/180305.

J. Y. Koay, H. E. Bignall, J.-P. Macquart, D. L. Jauncey, B. J. Rickett, and J. E. J. Lovell. Detection of six rapidly scintillating active galactic nuclei and the diminished variability of J1819+3845. *A&A*, 534:L1, Oct. 2011a. doi: 10.1051/0004-6361/201117805.

J. Y. Koay, J.-P. Macquart, B. J. Rickett, H. E. Bignall, J. E. J. Lovell, C. Reynolds, D. L. Jauncey, T. Pursimo, L. Kedziora-Chudczer, and R. Ojha. Dual-frequency Observations of 140 Compact, Flat-spectrum Active Galactic Nuclei for Scintillation-induced Variability. *AJ*, 142:108, Oct. 2011b. doi: 10.1088/0004-6256/142/4/108.

E. Körding, M. Rupen, C. Knigge, R. Fender, V. Dhawan, M. Templeton, and T. Muxlow. A Transient Radio Jet in an Erupting Dwarf Nova. *Science*, 320:1318–, June 2008. doi: 10.1126/science.1155492.

E. G. Körding, C. Knigge, T. Tzioumis, and R. Fender. Detection of radio emission from a nova-like cataclysmic variable: evidence of jets? *MNRAS*, 418:L129–L132, Nov. 2011. doi: 10.1111/j.1745-3933.2011.01158.x.

M. I. Krauss, L. Chomiuk, M. Rupen, N. Roy, A. J. Mioduszewski, J. L. Sokoloski, T. Nelson, K. Mukai, M. F. Bode, S. P. S. Eyres, and T. J. O'Brien. Expanded Very Large Array Nova Project Observations of the Classical Nova V1723 Aquilae. *ApJL*, 739:L6, Sept. 2011. doi: 10.1088/2041-8205/739/1/L6.

M. I. Krauss, A. M. Soderberg, L. Chomiuk, B. A. Zauderer, A. Brunthaler, M. F. Bietenholz, R. A. Chevalier, C. Fransson, and M. Rupen. Expanded Very Large Array Observations of the Radio Evolution of SN 2011dh. *ApJL*, 750:L40, May 2012. doi: 10.1088/2041-8205/750/2/L40.

N. A. Kudryavtseva and T. B. Pyatunina. A search for periodicity in the light curves of selected blazars. *Astronomy Reports*, 50:1–11, Jan. 2006. doi: 10.1134/S106377290601001X.

N. A. Kudryavtseva, S. Britzen, A. Witzel, E. Ros, M. Karouzos, M. F. Aller, H. D. Aller, H. Teräsranta, A. Eckart, and J. A. Zensus. A possible jet precession in the periodic quasar B0605-085. *A&A*, 526:A51, Feb. 2011. doi: 10.1051/0004-6361/201014968.

S. D. Kügler, N. Gianniotis, and K. L. Polsterer. Featureless classification of light curves. *MNRAS*, 451:3385–3392, Aug. 2015. doi: 10.1093/mnras/stv1181.

S. R. Kulkarni, D. A. Frail, M. H. Wieringa, R. D. Ekers, E. M. Sadler, R. M. Wark, J. L. Higdon, E. S. Phinney, and J. S. Bloom. Radio emission from the unusual supernova 1998bw and its association with the γ-ray burst of 25 April 1998. *Nature*, 395:663–669, Oct. 1998. doi: 10.1038/27139.

P. Kumar and A. Panaitescu. Steepening of Afterglow Decay for Jets Interacting with Stratified Media. *ApJL*, 541:L9–L12, Sept. 2000. doi: 10.1086/312888.

W. M. Lane, W. D. Cotton, S. van Velzen, T. E. Clarke, N. E. Kassim, J. F. Helmboldt, T. J. W. Lazio, and A. S. Cohen. The Very Large Array Low-frequency Sky Survey Redux (VLSSr). *MNRAS*, 440:327–338, May 2014. doi: 10.1093/mnras/stu256.

T. J. W. Lazio, T. E. Clarke, W. M. Lane, C. Gross, N. E. Kassim, P. S. Ray, D. Wood, J. A. York, A. Kerkhoff, B. Hicks, E. Polisensky, K. Stewart, N. Paravastu Dalal, A. S. Cohen, and W. C. Erickson. Surveying the Dynamic Radio Sky with the Long Wavelength Demonstrator Array. *AJ*, 140:1995–2006, Dec. 2010. doi: 10.1088/0004-6256/140/6/1995.

A. J. Levan, N. R. Tanvir, S. B. Cenko, D. A. Perley, K. Wiersema, J. S. Bloom, A. S. Fruchter, A. d. U. Postigo, P. T. O'Brien, N. Butler, A. J. van der Horst, G. Leloudas, A. N. Morgan, K. Misra, G. C. Bower, J. Farihi, R. L. Tunnicliffe, M. Modjaz, J. M. Silverman, J. Hjorth, C. Thöne, A. Cucchiara, J. M. C. Cerón, A. J. Castro-Tirado, J. A. Arnold, M. Bremer, J. P. Brodie, T. Carroll, M. C. Cooper, P. A. Curran, R. M. Cutri, J. Ehle, D. Forbes, J. Fynbo,

J. Gorosabel, J. Graham, D. I. Hoffman, S. Guziy, P. Jakobsson, A. Kamble, T. Kerr, M. M. Kasliwal, C. Kouveliotou, D. Kocevski, N. M. Law, P. E. Nugent, E. O. Ofek, D. Poznanski, R. M. Quimby, E. Rol, A. J. Romanowsky, R. Sánchez-Ramírez, S. Schulze, N. Singh, L. van Spaandonk, R. L. C. Starling, R. G. Strom, J. C. Tello, O. Vaduvescu, P. J. Wheatley, R. A. M. J. Wijers, J. M. Winters, and D. Xu. An Extremely Luminous Panchromatic Outburst from the Nucleus of a Distant Galaxy. *Science*, 333:199–, July 2011. doi: 10.1126/science.1207143.

Z.-Y. Li and R. A. Chevalier. Radio Supernova SN 1998bw and Its Relation to GRB 980425. *ApJ*, 526:716–726, Dec. 1999. doi: 10.1086/308031.

Z. Ling, S. N. Zhang, and S. Tang. Determining the Distance of Cyg X-3 with its X-Ray Dust Scattering Halo. *ApJ*, 695:1111–1120, Apr. 2009. doi: 10.1088/0004-637X/695/2/1111.

M. Livio. Astrophysical jets: a phenomenological examination of acceleration and collimation. , 311:225–245, Apr. 1999. doi: 10.1016/S0370-1573(98)00102-1.

K. K. Lo, S. Farrell, T. Murphy, and B. M. Gaensler. Automatic Classification of Time-variable X-Ray Sources. *ApJ*, 786:20, May 2014a. doi: 10.1088/0004-637X/786/1/20.

K. K. Lo, T. Murphy, U. Rebbapragada, and K. Wagstaff. Online classification for time-domain astronomy. *ArXiv e-prints*, Feb. 2014b.

M. López-Corredoira and M. Perucho. Kinetic power of quasars and statistical excess of MOJAVE superluminal motions. *A&A*, 544:A56, Aug. 2012. doi: 10.1051/0004-6361/201219410.

D. R. Lorimer, A. J. Faulkner, A. G. Lyne, R. N. Manchester, M. Kramer, M. A. McLaughlin, G. Hobbs, A. Possenti, I. H. Stairs, F. Camilo, M. Burgay, N. D'Amico, A. Corongiu, and F. Crawford. The Parkes Multibeam Pulsar Survey - VI. Discovery and timing of 142 pulsars and a Galactic population analysis. *MNRAS*, 372:777–800, Oct. 2006. doi: 10.1111/j.1365-2966.2006.10887.x.

D. R. Lorimer, M. Bailes, M. A. McLaughlin, D. J. Narkevic, and F. Crawford. A Bright Millisecond Radio Burst of Extragalactic Origin. *Science*, 318:777–, Nov. 2007. doi: 10.1126/science.1147532.

J.-C. Lu, J.-Y. Wang, T. An, J.-M. Lin, and H.-B. Qiu. Periodic radio variability in NRAO 530: phase dispersion minimization analysis. *Research in Astronomy and Astrophysics*, 12:643–650, June 2012. doi: 10.1088/1674-4527/12/6/004.

J. D. Lyman, D. Bersier, P. A. James, P. A. Mazzali, J. J. Eldridge, M. Fraser, and E. Pian. Bolometric light curves and explosion parameters of 38 stripped-envelope core-collapse supernovae. *MNRAS*, 457:328–350, Mar. 2016. doi: 10.1093/mnras/stv2983.

A. A. Mahabal, S. G. Djorgovski, A. J. Drake, C. Donalek, M. J. Graham, R. D. Williams, Y. Chen, B. Moghaddam, M. Turmon, E. Beshore, and S. Larson. Discovery, classification, and scientific exploration of transient events from the Catalina Real-time Transient Survey. *Bulletin of the Astronomical Society of India*, 39:387–408, Sept. 2011.

N. Marchili, I. Martí-Vidal, A. Brunthaler, T. P. Krichbaum, P. Müller, X. Liu, H.-G. Song, U. Bach, R. Beswick, and J. A. Zensus. The radio lightcurve of SN 2008iz in M82 revealed by Urumqi observations. *A&A*, 509:A47, Jan. 2010. doi: 10.1051/0004-6361/200913126.

N. Marchili, T. P. Krichbaum, X. Liu, H.-G. Song, K. É. Gabányi, L. Fuhrmann, A. Witzel, and J. A. Zensus. A seasonal cycle and an abrupt change in the variability characteristics of the intraday variable source S4 0954+65. *A&A*, 542:A121, June 2012. doi: 10.1051/0004-6361/201218977.

H. Marlowe, P. Kaaret, C. Lang, H. Feng, F. Grisé, N. Miller, D. Cseh, S. Corbel, and R. F. Mushotzky. Spectral state transitions of the Ultraluminous X-ray Source IC 342 X-1. *MNRAS*, 444:642–650, Oct. 2014. doi: 10.1093/mnras/stu1471.

M. Massi, K. Menten, and J. Neidhöfer. Periodic radio flaring on the T Tauri star V 773 Tauri. *A&A*.

M. A. McLaughlin, A. G. Lyne, D. R. Lorimer, M. Kramer, A. J. Faulkner, R. N. Manchester, J. M. Cordes, F. Camilo, A. Possenti, I. H. Stairs, G. Hobbs, N. D'Amico, M. Burgay, and J. T. O'Brien. Transient radio bursts from rotating neutron stars. *Nature*, 439:817–820, Feb. 2006. doi: 10.1038/nature04440.

R. A. Mesler, Y. M. Pihlström, G. B. Taylor, and J. Granot. VLBI and Archival VLA and WSRT Observations of the GRB 030329 Radio Afterglow. *ApJ*, 759:4, Nov. 2012. doi: 10.1088/0004-637X/759/1/4.

B. D. Metzger, P. K. G. Williams, and E. Berger. Extragalactic Synchrotron Transients in the Era of Wide-field Radio Surveys. I. Detection Rates and Light Curve Characteristics. *ApJ*, 806:224, June 2015. doi: 10.1088/0004-637X/806/2/224.

M. J. Middleton, J. C. A. Miller-Jones, S. Markoff, R. Fender, M. Henze, N. Hurley-Walker, A. M. M. Scaife, T. P. Roberts, D. Walton, J. Carpenter, J.-P. Macquart, G. C. Bower, M. Gurwell, W. Pietsch, F. Haberl, J. Harris, M. Daniel, J. Miah, C. Done, J. S. Morgan, H. Dickinson, P. Charles, V. Burwitz, M. Della Valle, M. Freyberg, J. Greiner, M. Hernanz, D. H. Hartmann, D. Hatzidimitriou, A. Riffeser, G. Sala, S. Seitz, P. Reig, A. Rau, M. Orio, D. Titterington, and K. Grainge. Bright radio emission from an ultraluminous stellar-mass microquasar in M 31. *Nature*, 493:187–190, Jan. 2013. doi: 10.1038/nature11697.

D. Milisavljevic, R. A. Fesen, R. A. Chevalier, R. P. Kirshner, P. Challis, and M. Turatto. Late-time Optical Emission from Core-collapse Supernovae. *ApJ*, 751:25, May 2012. doi: 10.1088/0004-637X/751/1/25.

N. A. Miller, R. F. Mushotzky, and S. G. Neff. Radio Emission Associated with the Ultraluminous X-Ray Source in Holmberg II. *ApJL*, 623:L109–L112, Apr. 2005. doi: 10.1086/430112.

J. C. A. Miller-Jones. Astrometric Observations of X-ray Binaries Using Very Long Baseline Interferometry. , 31:e016, Mar. 2014. doi: 10.1017/pasa.2014.7.

J. C. A. Miller-Jones, G. R. Sivakoff, C. Knigge, E. G. Körding, M. Templeton, and E. O. Waagen. An Accurate Geometric Distance to the Compact Binary SS Cygni Vindicates Accretion Disc Theory. *Science*, 340:950–952, May 2013. doi: 10.1126/science.1237145.

U. Mitra-Kraev, L. K. Harra, D. R. Williams, and E. Kraev. The first observed stellar X-ray flare oscillation: Constraints on the flare loop length and the magnetic field. *A&A*, 436: 1041–1047, June 2005. doi: 10.1051/0004-6361:20052834.

J. Moldón, M. Ribó, J. M. Paredes, W. Brisken, V. Dhawan, M. Kramer, A. G. Lyne, and B. W. Stappers. On the origin of LS 5039 and PSR J1825-1446. *A&A*, 543:A26, July 2012. doi: 10.1051/0004-6361/201219205.

L. A. Molnar, M. J. Reid, and J. E. Grindlay. VLBI observations of expansion in Cygnus X-3. *ApJ*, 331:494–508, Aug. 1988. doi: 10.1086/166575.

T. Nelson, L. Chomiuk, N. Roy, J. L. Sokoloski, K. Mukai, M. I. Krauss, A. J. Mioduszewski, M. P. Rupen, and J. Weston. The 2011 Outburst of Recurrent Nova T Pyx: Radio Observations Reveal the Ejecta Mass and Hint at Complex Mass Loss. *ApJ*, 785:78, Apr. 2014. doi: 10.1088/0004-637X/785/1/78.

K. S. Obenberger, J. M. Hartman, G. B. Taylor, J. Craig, J. Dowell, J. F. Helmboldt, P. A. Henning, F. K. Schinzel, and T. L. Wilson. Limits on Gamma-Ray Burst Prompt Radio Emission Using the LWA1. *ApJ*, 785:27, Apr. 2014a. doi: 10.1088/0004-637X/785/1/27.

K. S. Obenberger, G. B. Taylor, J. M. Hartman, J. Dowell, S. W. Ellingson, J. F. Helmboldt, P. A. Henning, M. Kavic, F. K. Schinzel, J. H. Simonetti, K. Stovall, and T. L. Wilson. Detection of Radio Emission from Fireballs. *ApJL*, 788:L26, June 2014b. doi: 10.1088/2041-8205/788/2/L26.

T. O'Brien, M. F. Bode, R. W. Porcas, T. W. B. Muxlow, R. J. Beswick, S. T. Garrington, S. P. S. Eyres, J. P. Osborne, K. L. Page, A. P. Beardmore, M. R. Goad, S. Starrfield, J. U. Ness, A. Evans, G. K. Skinner, and R. J. Davis. The 2006 explosion of the recurrent nova RS Ophiuchi. In *Proceedings of the 8th European VLBI Network Symposium*, page 52, 2006.

T. J. O'Brien. Novae and other Cataclysmic Variables (invited). In *8th International e-VLBI Workshop*, page 3, 2009.

E. O. Ofek. Soft Gamma-Ray Repeaters in Nearby Galaxies: Rate, Luminosity Function, and Fraction among Short Gamma-Ray Bursts. *ApJ*, 659:339–346, Apr. 2007. doi: 10.1086/511147.

E. O. Ofek, I. Arcavi, D. Tal, M. Sullivan, A. Gal-Yam, S. R. Kulkarni, P. E. Nugent, S. Ben-Ami, D. Bersier, Y. Cao, S. B. Cenko, A. De Cia, A. V. Filippenko, C. Fransson, M. M. Kasliwal, R. Laher, J. Surace, R. Quimby, and O. Yaron. Interaction-powered Supernovae: Rise-time versus Peak-luminosity Correlation and the Shock-breakout Velocity. *ApJ*, 788: 154, June 2014. doi: 10.1088/0004-637X/788/2/154.

A. R. Offringa, A. G. de Bruyn, M. Biehl, S. Zaroubi, G. Bernardi, and V. N. Pandey. Post-correlation radio frequency interference classification methods. *MNRAS*, 405:155–167, June 2010. doi: 10.1111/j.1365-2966.2010.16471.x.

S. A. Olausen and V. M. Kaspi. The McGill Magnetar Catalog. *ApJS*, 212:6, May 2014. doi: 10.1088/0067-0049/212/1/6.

R. A. Osten. Transient Emissions from Radio-Active Stars: Implications for Wide-Field Radio Surveys. *ArXiv e-prints*, Jan. 2008.

R. A. Osten and T. S. Bastian. Wide-Band Spectroscopy of Two Radio Bursts on AD Leonis. *ApJ*, 637:1016–1024, Feb. 2006. doi: 10.1086/498410.

R. A. Osten, S. L. Hawley, J. C. Allred, C. M. Johns-Krull, and C. Roark. From Radio to X-Ray: Flares on the dMe Flare Star EV Lacertae. *ApJ*, 621:398–416, Mar. 2005. doi: 10.1086/427275.

R. Ottmann and J. H. M. M. Schmitt. The contributions of RSCVn systems to the diffuse X-ray background. *A&A*, 256:421–427, Mar. 1992.

A. Pastorello, M. M. Kasliwal, R. M. Crockett, S. Valenti, R. Arbour, K. Itagaki, S. Kaspi, A. Gal-Yam, S. J. Smartt, R. Griffith, K. Maguire, E. O. Ofek, N. Seymour, D. Stern, and W. Wiethoff. The Type IIb SN 2008ax: spectral and light curve evolution. *MNRAS*, 389: 955–966, Sept. 2008. doi: 10.1111/j.1365-2966.2008.13618.x.

A. A. Penzias and R. W. Wilson. A Measurement of Excess Antenna Temperature at 4080 Mc/s. *ApJ*, 142:419–421, July 1965. doi: 10.1086/148307.

M. A. Pérez-Torres, A. Alberdi, and J. M. Marcaide. The role of synchrotron self-absorption in the late radio emission from SN 1993J. *A&A*, 374:997–1002, Aug. 2001. doi: 10.1051/0004-6361:20010774.

R. A. Perley, C. J. Chandler, B. J. Butler, and J. M. Wrobel. The Expanded Very Large Array: A New Telescope for New Science. *ApJL*, 739:L1, Sept. 2011. doi: 10.1088/2041-8205/739/1/L1.

W. M. Peterson, R. L. Mutel, J.-F. Lestrade, M. Güdel, and W. M. Goss. Radio Astrometry of the Triple Systems Algol and UX Arietis. *ApJ*, 737:104, Aug. 2011. doi: 10.1088/0004-637X/737/2/104.

E. Petroff, M. Bailes, E. D. Barr, B. R. Barsdell, N. D. R. Bhat, F. Bian, S. Burke-Spolaor, M. Caleb, D. Champion, P. Chandra, G. Da Costa, C. Delvaux, C. Flynn, N. Gehrels, J. Greiner, A. Jameson, S. Johnston, M. M. Kasliwal, E. F. Keane, S. Keller, J. Kocz, M. Kramer, G. Leloudas, D. Malesani, J. S. Mulchaey, C. Ng, E. O. Ofek, D. A. Perley, A. Possenti, B. P. Schmidt, Y. Shen, B. Stappers, P. Tisserand, W. van Straten, and C. Wolf. A real-time fast radio burst: polarization detection and multiwavelength follow-up. *MNRAS*, 447:246–255, Feb. 2015. doi: 10.1093/mnras/stu2419.

E. Petroff, E. D. Barr, A. Jameson, E. F. Keane, M. Bailes, M. Kramer, V. Morello, D. Tabbara, and W. van Straten. FRBCAT: The Fast Radio Burst Catalogue. *ArXiv e-prints*, Jan. 2016.

K. Pichara and P. Protopapas. Automatic Classification of Variable Stars in Catalogs with Missing Data. *ApJ*, 777:83, Nov. 2013. doi: 10.1088/0004-637X/777/2/83.

M. Pietka, R. P. Fender, and E. F. Keane. The variability time-scales and brightness temperatures of radio flares from stars to supermassive black holes. *MNRAS*, 446:3687–3696, Feb. 2015. doi: 10.1093/mnras/stu2335.

M. Pitkin, D. Williams, L. Fletcher, and S. D. T. Grant. A Bayesian method for detecting stellar flares. *MNRAS*, 445:2268–2284, Dec. 2014. doi: 10.1093/mnras/stu1889.

M. L. Pretorius and C. Knigge. The space density and X-ray luminosity function of non-magnetic cataclysmic variables. *MNRAS*, 419:1442–1454, Jan. 2012. doi: 10.1111/j.1365-2966.2011.19801.x.

M. L. Pretorius and K. Mukai. Constraints on the space density of intermediate polars from the Swift-BAT survey. *MNRAS*, 442:2580–2585, Aug. 2014. doi: 10.1093/mnras/stu990.

M. L. Pretorius, C. Knigge, and A. D. Schwope. The space density of magnetic cataclysmic variables. *MNRAS*, 432:570–583, June 2013. doi: 10.1093/mnras/stt499.

T. B. Pyatunina, N. A. Kudryavtseva, D. C. Gabuzda, S. G. Jorstad, M. F. Aller, H. D. Aller, and H. Teräsranta. Frequency-dependent time-delays for strong outbursts in selected blazars from the Metsähovi and the University of Michigan Radio Astronomy Observatory monitoring databases - I. *MNRAS*, 373:1470–1482, Dec. 2006. doi: 10.1111/j.1365-2966.2006.11068.x.

G. Ramsay, M. Cropper, K. Wu, K. O. Mason, F. A. Córdova, and W. Priedhorsky. XMM-Newton observations of polars in low accretion states. *MNRAS*, 350:1373–1384, June 2004. doi: 10.1111/j.1365-2966.2004.07732.x.

A. Rau, S. R. Kulkarni, N. M. Law, J. S. Bloom, D. Ciardi, G. S. Djorgovski, D. B. Fox, A. Gal-Yam, C. C. Grillmair, M. M. Kasliwal, P. E. Nugent, E. O. Ofek, R. M. Quimby, W. T. Reach, M. Shara, L. Bildsten, S. B. Cenko, A. J. Drake, A. V. Filippenko, D. J. Helfand, G. Helou, D. A. Howell, D. Poznanski, and M. Sullivan. Exploring the Optical Transient Sky with the Palomar Transient Factory. *PASP*, 121:1334–1351, Dec. 2009. doi: 10.1086/605911.

V. Ravi, R. M. Shannon, and A. Jameson. A Fast Radio Burst in the Direction of the Carina Dwarf Spheroidal Galaxy. *ApJL*, 799:L5, Jan. 2015. doi: 10.1088/2041-8205/799/1/L5.

U. Rebbapragada, K. Lo, K. L. Wagstaff, C. Reed, T. Murphy, and D. R. Thompson. Classification of ASKAP VAST Radio Light Curves†. In E. Griffin, R. Hanisch, and R. Seaman, editors, *IAU Symposium*, volume 285 of *IAU Symposium*, pages 397–399, Apr. 2012. doi: 10.1017/S1743921312001196.

M. J. Rees. A better way of searching for black-hole explosions. *Nature*, 266:333, Mar. 1977. doi: 10.1038/266333a0.

I. N. Reid, K. L. Cruz, and P. R. Allen. Meeting the Cool Neighbors. XI. Beyond the NLTT Catalog. *AJ*, 133:2825–2840, June 2007. doi: 10.1086/517914.

R. B. Rengelink, Y. Tang, A. G. de Bruyn, G. K. Miley, M. N. Bremer, H. J. A. Roettgering, and M. A. R. Bremer. The Westerbork Northern Sky Survey (WENSS), I. A 570 square degree Mini-Survey around the North Ecliptic Pole. , 124:259–280, Aug. 1997. doi: 10.1051/aas:1997358.

M. Ribó, J. M. Paredes, and J. Martí. VLA/GBI observations of the new high mass X-ray binary LS 5039. *NewA Rev.*, 43:545–547, Nov. 1999. doi: 10.1016/S1387-6473(99)00051-2.

J. W. Richards, D. L. Starr, N. R. Butler, J. S. Bloom, J. M. Brewer, A. Crellin-Quick, J. Higgins, R. Kennedy, and M. Rischard. On Machine-learned Classification of Variable Stars with Sparse and Noisy Time-series Data. *ApJ*, 733:10, May 2011. doi: 10.1088/0004-637X/733/1/10.

B. Rickett. The Role of Interstellar Scintillation in Intraday Variations at Centimetre Wavelengths. , 19:100–105, 2002. doi: 10.1071/AS01120.

B. J. Rickett. Refractive interstellar scintillation of radio sources. *ApJ*, 307:564–574, Aug. 1986. doi: 10.1086/164444.

B. J. Rickett. Probing the Cores of Radio Jets through Interstellar Scintillation. In *Revista Mexicana de Astronomia y Astrofisica, vol. 27*, volume 27 of *Revista Mexicana de Astronomia y Astrofisica, vol. 27*, pages 129–139, Mar. 2007.

B. J. Rickett, A. Quirrenbach, R. Wegner, T. P. Krichbaum, and A. Witzel. Interstellar scintillation of the radio source 0917+624. *A&A*, 293:479–492, Jan. 1995.

B. J. Rickett, T. J. W. Lazio, and F. D. Ghigo. Interstellar Scintillation Observations of 146 Extragalactic Radio Sources. *ApJS*, 165:439–460, Aug. 2006. doi: 10.1086/504897.

J. Rodriguez and L. Prat. Is the ejection of the corona a general phenomenom in microquasars? In *Proceedings of the 7th INTEGRAL Workshop*, page 96, 2008.

P. W. A. Roming, T. A. Pritchard, P. J. Brown, S. T. Holland, S. Immler, C. J. Stockdale, K. W. Weiler, N. Panagia, S. D. Van Dyk, E. A. Hoversten, P. A. Milne, S. R. Oates, B. Russell, and C. Vandrevala. Multi-Wavelength Properties of the Type IIb SN 2008ax. *ApJL*, 704: L118–L123, Oct. 2009. doi: 10.1088/0004-637X/704/2/L118.

A. Rowlinson, M. E. Bell, T. Murphy, C. M. Trott, N. Hurley-Walker, S. Johnston, S. J. Tingay, D. L. Kaplan, D. Carbone, P. J. Hancock, L. Feng, A. R. Offringa, G. Bernardi, J. D. Bowman, F. Briggs, R. J. Cappallo, A. A. Deshpande, B. M. Gaensler, L. J. Greenhill, B. J. Hazelton, M. Johnston-Hollitt, C. J. Lonsdale, S. R. McWhirter, D. A. Mitchell, M. F. Morales, E. Morgan, D. Oberoi, S. M. Ord, T. Prabu, N. Udaya Shankar, K. S. Srivani, R. Subrahmanyan, R. B. Wayth, R. L. Webster, A. Williams, and C. L. Williams. Limits on Fast Radio Bursts and other transient sources at 182 MHz using the Murchison Widefield Array. *ArXiv e-prints*, Feb. 2016.

M. Roy, I. E. Papadakis, E. Ramos-Colón, R. Sambruna, K. Tsinganos, J. Papamastorakis, and M. Kafatos. The Recent High State of the BL Lacertae Object AO 0235 and Cross-Correlations between Optical and Radio Bands. *ApJ*, 545:758–771, Dec. 2000. doi: 10.1086/317842.

N. Roy, L. Chomiuk, J. L. Sokoloski, J. Weston, M. P. Rupen, T. Johnson, M. I. Krauss, T. Nelson, K. Mukai, A. Mioduszewski, M. F. Bode, S. P. S. Eyres, and T. J. O'Brien. Radio studies of novae: a current status report and highlights of new results. *Bulletin of the Astronomical Society of India*, 40:293–310, Sept. 2012.

D. M. Russell, T. D. Russell, J. C. A. Miller-Jones, K. O'Brien, R. Soria, G. R. Sivakoff, T. Slaven-Blair, F. Lewis, S. Markoff, J. Homan, D. Altamirano, P. A. Curran, M. P. Rupen, T. M. Belloni, M. Cadolle Bel, P. Casella, S. Corbel, V. Dhawan, R. P. Fender,

E. Gallo, P. Gandhi, S. Heinz, E. G. Körding, H. A. Krimm, D. Maitra, S. Migliari, R. A. Remillard, C. L. Sarazin, T. Shahbaz, and V. Tudose. An Evolving Compact Jet in the Black Hole X-Ray Binary MAXI J1836-194. *ApJL*, 768:L35, May 2013. doi: 10.1088/2041-8205/768/2/L35.

S. D. Ryder, E. Sadler, R. Subrahmanyan, K. W. Weiler, N. Panagia, and C. Stockdale. Radio Monitoring of Supernova 2001ig: The First Year. *ArXiv Astrophysics e-prints*, Sept. 2003.

M. Ryle and A. Hewish. The synthesis of large radio telescopes. *MNRAS*, 120:220, 1960. doi: 10.1093/mnras/120.3.220.

M. Ryle, G. Hine, J. Shakeshaft, and J. L. Caswell. A new class of radio star. *Nature*, 276: 571–573, Dec. 1978. doi: 10.1038/276571a0.

R. P. Saglia, J. L. Tonry, R. Bender, N. Greisel, S. Seitz, R. Senger, J. Snigula, S. Phleps, D. Wilman, C. A. L. Bailer-Jones, R. J. Klement, H.-W. Rix, K. Smith, P. J. Green, W. S. Burgett, K. C. Chambers, J. N. Heasley, N. Kaiser, E. A. Magnier, J. S. Morgan, P. A. Price, C. W. Stubbs, and R. J. Wainscoat. The Photometric Classification Server for Pan-STARRS1. *ApJ*, 746:128, Feb. 2012. doi: 10.1088/0004-637X/746/2/128.

N. J. Salvi, M. J. Page, J. A. Stevens, K. Wu, K. O. Mason, M. F. Aller, H. D. Aller, H. Teräsranta, E. Romero-Colmenero, F. A. Cordova, and W. C. Priedhorsky. Correlated multiwavelength emission from the X-ray-bright Seyfert galaxy III Zw 2. *MNRAS*, 335: 177–188, Sept. 2002. doi: 10.1046/j.1365-8711.2002.05603.x.

R. Sari, T. Piran, and J. P. Halpern. Jets in Gamma-Ray Bursts. *ApJL*, 519:L17–L20, July 1999. doi: 10.1086/312109.

J. D. Scargle. Studies in Astronomical Time Series Analysis. V. Bayesian Blocks, a New Method to Analyze Structure in Photon Counting Data. *ApJ*, 504:405–418, Sept. 1998. doi: 10.1086/306064.

L. H. A. Scheers. *Transient and variable radio sources in the LOFAR sky: an architecture for a detection framework*. PhD thesis, University of Amsterdam, 2011.

E. M. Schlegel and R. Petre. A Chandra ACIS Observation of the X-Ray-luminous SN 1988Z. *ApJ*, 646:378–384, July 2006. doi: 10.1086/504890.

C. E. Senkbeil, S. P. Ellingsen, J. E. J. Lovell, J.-P. Macquart, G. Cimò, and D. L. Jauncey. A Compact Extreme Scattering Event Cloud toward AO 0235+164. *ApJL*, 672:L95–L98, Jan. 2008. doi: 10.1086/527300.

M. Servillat, N. A. Webb, F. Lewis, C. Knigge, M. van den Berg, A. Dieball, and J. Grindlay. A Dwarf Nova in the Globular Cluster M13. *ApJ*, 733:106, June 2011. doi: 10.1088/0004-637X/733/2/106.

B. Sesar, Ž. Ivezić, R. H. Lupton, M. Jurić, J. E. Gunn, G. R. Knapp, N. DeLee, J. A. Smith, G. Miknaitis, H. Lin, D. Tucker, M. Doi, M. Tanaka, M. Fukugita, J. Holtzman, S. Kent, B. Yanny, D. Schlegel, D. Finkbeiner, N. Padmanabhan, C. M. Rockosi, N. Bond, B. Lee, C. Stoughton, S. Jester, H. Harris, P. Harding, J. Brinkmann, D. P. Schneider, D. York, M. W. Richmond, and D. Vanden Berk. Exploring the Variable Sky with the Sloan Digital Sky Survey. *AJ*, 134:2236–2251, Dec. 2007. doi: 10.1086/521819.

R. M. Shannon, S. Johnston, and R. N. Manchester. The kinematics and orbital dynamics of the PSR B1259-63/LS 2883 system from 23 yr of pulsar timing. *MNRAS*, 437:3255–3264, Feb. 2014. doi: 10.1093/mnras/stt2123.

N. Shaposhnikov and L. Titarchuk. Determination of Black Hole Masses in Galactic Black Hole Binaries Using Scaling of Spectral and Variability Characteristics. *ApJ*, 699:453–468, July 2009. doi: 10.1088/0004-637X/699/1/453.

A. J. Slavin, T. J. O'Brien, and J. S. Dunlop. A deep optical imaging study of the nebular remnants of classical novae. *MNRAS*, 276:353–371, Sept. 1995.

O. B. Slee, G. J. Nelson, R. T. Stewart, A. E. Wright, J. L. Innis, S. G. Ryan, and A. E. Vaughan. A microwave survey of southern active stars. *MNRAS*, 229:659–677, Dec. 1987.

K. Smith, M. Güdel, and M. Audard. Flares observed with XMM-Newton and the VLA. *A&A*, 436:241–251, June 2005. doi: 10.1051/0004-6361:20042054.

A. M. Soderberg, S. R. Kulkarni, E. Berger, R. A. Chevalier, D. A. Frail, D. B. Fox, and R. C. Walker. The Radio and X-Ray-Luminous Type Ibc Supernova 2003L. *ApJ*, 621:908–920, Mar. 2005. doi: 10.1086/427649.

A. M. Soderberg, R. A. Chevalier, S. R. Kulkarni, and D. A. Frail. The Radio and X-Ray Luminous SN 2003bg and the Circumstellar Density Variations around Radio Supernovae. *ApJ*, 651:1005–1018, Nov. 2006. doi: 10.1086/507571.

P. Soleri, V. Tudose, R. Fender, M. van der Klis, and P. G. Jonker. Linking jet emission and X-ray properties in the peculiar neutron star X-ray binary Circinus X-1. *MNRAS*, 399: 453–464, Oct. 2009. doi: 10.1111/j.1365-2966.2009.15297.x.

J. N. Spreeuw. *Search and detection of low frequency radio transients*. PhD thesis, University of Amsterdam, 2010.

T. D. Staley, D. J. Titterington, R. P. Fender, J. D. Swinbank, A. J. van der Horst, A. Rowlinson, A. M. M. Scaife, K. J. B. Grainge, and G. G. Pooley. Automated rapid follow-up of Swift gamma-ray burst alerts at 15 GHz with the AMI Large Array. *MNRAS*, 428: 3114–3120, Feb. 2013. doi: 10.1093/mnras/sts259.

J. F. Steiner, R. C. Reis, J. E. McClintock, R. Narayan, R. A. Remillard, J. A. Orosz, L. Gou, A. C. Fabian, and M. A. P. Torres. The spin of the black hole microquasar XTE J1550-564 via the continuum-fitting and Fe-line methods. *MNRAS*, 416:941–958, Sept. 2011. doi: 10.1111/j.1365-2966.2011.19089.x.

A. J. Stewart, R. P. Fender, J. W. Broderick, T. E. Hassall, T. Muñoz-Darias, A. Rowlinson, J. D. Swinbank, T. D. Staley, G. J. Molenaar, B. Scheers, T. L. Grobler, M. Pietka, G. Heald, J. P. McKean, M. E. Bell, A. Bonafede, R. P. Breton, D. Carbone, Y. Cendes, A. O. Clarke, S. Corbel, F. de Gasperin, J. Eislöffel, H. Falcke, C. Ferrari, J.-M. Grießmeier, M. J. Hardcastle, V. Heesen, J. W. T. Hessels, A. Horneffer, M. Iacobelli, P. Jonker, A. Karastergiou, G. Kokotanekov, V. I. Kondratiev, M. Kuniyoshi, C. J. Law, J. van Leeuwen, S. Markoff, J. C. A. Miller-Jones, D. Mulcahy, E. Orru, M. Pandey-Pommier, L. Pratley, E. Rol, H. J. A. Röttgering, A. M. M. Scaife, A. Shulevski, C. A. Sobey, B. W. Stappers, C. Tasse, A. J. van der Horst, S. van Velzen, R. J. van Weeren, R. A. M. J. Wijers,

R. Wijnands, M. Wise, P. Zarka, A. Alexov, J. Anderson, A. Asgekar, I. M. Avruch, M. J. Bentum, G. Bernardi, P. Best, F. Breitling, M. Brüggen, H. R. Butcher, B. Ciardi, J. E. Conway, A. Corstanje, E. de Geus, A. Deller, S. Duscha, W. Frieswijk, M. A. Garrett, A. W. Gunst, M. P. van Haarlem, M. Hoeft, J. Hörandel, E. Juette, G. Kuper, M. Loose, P. Maat, R. McFadden, D. McKay-Bukowski, J. Moldon, H. Munk, M. J. Norden, H. Paas, A. G. Polatidis, D. Schwarz, J. Sluman, O. Smirnov, M. Steinmetz, S. Thoudam, M. C. Toribio, R. Vermeulen, C. Vocks, S. J. Wijnholds, O. Wucknitz, and S. Yatawatta. LOFAR MSSS: detection of a low-frequency radio transient in 400 h of monitoring of the North Celestial Pole. *MNRAS*, 456:2321–2342, Mar. 2016. doi: 10.1093/mnras/stv2797.

C. J. Stockdale, C. L. Williams, K. W. Weiler, N. Panagia, R. A. Sramek, S. D. Van Dyk, and M. T. Kelley. The Radio Evolution of SN 2001gd. *ApJ*, 671:689–694, Dec. 2007. doi: 10.1086/522584.

J. D. Swinbank, T. D. Staley, G. J. Molenaar, E. Rol, A. Rowlinson, B. Scheers, H. Spreeuw, M. E. Bell, J. W. Broderick, D. Carbone, H. Garsden, A. J. van der Horst, C. J. Law, M. Wise, R. P. Breton, Y. Cendes, S. Corbel, J. Eislöffel, H. Falcke, R. Fender, J.-M. Grießmeier, J. W. T. Hessels, B. W. Stappers, A. J. Stewart, R. A. M. J. Wijers, R. Wijnands, and P. Zarka. The LOFAR Transients Pipeline. *Astronomy and Computing*, 11:25–48, June 2015. doi: 10.1016/j.ascom.2015.03.002.

C. Tasse, S. van der Tol, J. van Zwieten, G. van Diepen, and S. Bhatnagar. Applying full polarization A-Projection to very wide field of view instruments: An imager for LOFAR. *A&A*, 553:A105, May 2013. doi: 10.1051/0004-6361/201220882.

S. P. Tendulkar, P. B. Cameron, and S. R. Kulkarni. Proper Motions and Origins of SGR 1806-20 and SGR 1900+14. *ApJ*, 761:76, Dec. 2012. doi: 10.1088/0004-637X/761/1/76.

D. Thornton, B. Stappers, M. Bailes, B. Barsdell, S. Bates, N. D. R. Bhat, M. Burgay, S. Burke-Spolaor, D. J. Champion, P. Coster, N. D'Amico, A. Jameson, S. Johnston, M. Keith, M. Kramer, L. Levin, S. Milia, C. Ng, A. Possenti, and W. van Straten. A Population of Fast Radio Bursts at Cosmological Distances. *Science*, 341:53–56, July 2013. doi: 10.1126/science.1236789.

N. Thyagarajan, D. J. Helfand, R. L. White, and R. H. Becker. Variable and Transient Radio Sources in the FIRST Survey. *ApJ*, 742:49, Nov. 2011. doi: 10.1088/0004-637X/742/1/49.

S. J. Tingay, R. Goeke, J. D. Bowman, D. Emrich, S. M. Ord, D. A. Mitchell, M. F. Morales, T. Booler, B. Crosse, R. B. Wayth, C. J. Lonsdale, S. Tremblay, D. Pallot, T. Colegate, A. Wicenec, N. Kudryavtseva, W. Arcus, D. Barnes, G. Bernardi, F. Briggs, S. Burns, J. D. Bunton, R. J. Cappallo, B. E. Corey, A. Deshpande, L. Desouza, B. M. Gaensler, L. J. Greenhill, P. J. Hall, B. J. Hazelton, D. Herne, J. N. Hewitt, M. Johnston-Hollitt, D. L. Kaplan, J. C. Kasper, B. B. Kincaid, R. Koenig, E. Kratzenberg, M. J. Lynch, B. Mckinley, S. R. Mcwhirter, E. Morgan, D. Oberoi, J. Pathikulangara, T. Prabu, R. A. Remillard, A. E. E. Rogers, A. Roshi, J. E. Salah, R. J. Sault, N. Udaya-Shankar, F. Schlagenhaufer, K. S. Srivani, J. Stevens, R. Subrahmanyan, M. Waterson, R. L. Webster, A. R. Whitney, A. Williams, C. L. Williams, and J. S. B. Wyithe. The Murchison Widefield Array: The Square Kilometre Array Precursor at Low Radio Frequencies. , 30:e007, Jan. 2013. doi: 10.1017/pasa.2012.007.

C. G. Tinney, I. N. Reid, and J. R. Mould. The faintest stars - From Schmidt plates to luminosity functions. *ApJ*, 414:254–278, Sept. 1993. doi: 10.1086/173074.

R. M. Torres, L. Loinard, A. J. Mioduszewski, A. F. Boden, R. Franco-Hernández, W. H. T. Vlemmings, and L. F. Rodríguez. VLBA Determination of the Distance to nearby Star-forming Regions. V. Dynamical Mass, Distance, and Radio Structure of V773 Tau A. *ApJ*, 747:18, Mar. 2012. doi: 10.1088/0004-637X/747/1/18.

S. Trushkin, N. N. Bursov, N. A. Nizhelskij, E. K. Majorova, and P. A. Voitsik. What do we understand from multi-frequency monitoring of microquasars? In *VI Microquasar Workshop: Microquasars and Beyond*, page 15, 2006.

S. A. Trushkin, N. A. Nizhelskij, and N. N. Bursov. Longterm multi-frequency monitoring of microquasars. In *Microquasars and Beyond*, page 32, 2008.

S. A. Trushkin, N. A. Nizhelskij, and G. V. Zhekanis. First radio light curve of MAXIJ1836-194 at 4.8 GHz with RATAN-600. *The Astronomer's Telegram*, 3656:1, Sept. 2011.

R. J. Turner, S. P. Ellingsen, S. S. Shabala, J. Blanchard, J. E. J. Lovell, J. N. McCallum, and G. Cimò. BL Lac Object PKS B1144-379: An Extreme Scintillator. *ApJL*, 754:L19, Aug. 2012. doi: 10.1088/2041-8205/754/2/L19.

C. Usher, D. A. Forbes, L. R. Spitler, J. P. Brodie, A. J. Romanowsky, J. Strader, and K. A. Woodley. The SLUGGS Survey: wide field imaging of the globular cluster system of NGC 4278. *MNRAS*, 436:1172–1190, Dec. 2013. doi: 10.1093/mnras/stt1637.

A. J. van der Horst, A. Kamble, L. Resmi, R. A. M. J. Wijers, D. Bhattacharya, B. Scheers, E. Rol, R. Strom, C. Kouveliotou, T. Oosterloo, and C. H. Ishwara-Chandra. Detailed study of the GRB 030329 radio afterglow deep into the non-relativistic phase. *A&A*, 480: 35–43, Mar. 2008. doi: 10.1051/0004-6361:20078051.

H. van der Laan. A Model for Variable Extragalactic Radio Sources. *Nature*, 211:1131, Sept. 1966. doi: 10.1038/2111131a0.

S. . van der Tol, B. D. Jeffs, and A.-J. . van der Veen. Self-Calibration for the LOFAR Radio Astronomical Array. *IEEE Transactions on Signal Processing*, 55:4497–4510, Sept. 2007. doi: 10.1109/TSP.2007.896243.

S. D. van Dyk, K. W. Weiler, R. A. Sramek, and N. Panagia. SN 1988Z: The Most Distant Radio Supernova. *ApJL*, 419:L69, Dec. 1993. doi: 10.1086/187139.

M. P. van Haarlem, M. W. Wise, A. W. Gunst, G. Heald, J. P. McKean, J. W. T. Hessels, A. G. de Bruyn, R. Nijboer, J. Swinbank, R. Fallows, M. Brentjens, A. Nelles, R. Beck, H. Falcke, R. Fender, J. Hörandel, L. V. E. Koopmans, G. Mann, G. Miley, H. Röttgering, B. W. Stappers, R. A. M. J. Wijers, S. Zaroubi, M. van den Akker, A. Alexov, J. Anderson, K. Anderson, A. van Ardenne, M. Arts, A. Asgekar, I. M. Avruch, F. Batejat, L. Bähren, M. E. Bell, M. R. Bell, I. van Bemmel, P. Bennema, M. J. Bentum, G. Bernardi, P. Best, L. Bîrzan, A. Bonafede, A.-J. Boonstra, R. Braun, J. Bregman, F. Breitling, R. H. van de Brink, J. Broderick, P. C. Broekema, W. N. Brouw, M. Brüggen, H. R. Butcher, W. van Cappellen, B. Ciardi, T. Coenen, J. Conway, A. Coolen, A. Corstanje, S. Damstra, O. Davies, A. T. Deller, R.-J. Dettmar, G. van Diepen, K. Dijkstra, P. Donker, A. Doorduin,

J. Dromer, M. Drost, A. van Duin, J. Eislöffel, J. van Enst, C. Ferrari, W. Frieswijk, H. Gankema, M. A. Garrett, F. de Gasperin, M. Gerbers, E. de Geus, J.-M. Grießmeier, T. Grit, P. Gruppen, J. P. Hamaker, T. Hassall, M. Hoeft, H. A. Holties, A. Horneffer, A. van der Horst, A. van Houwelingen, A. Huijgen, M. Iacobelli, H. Intema, N. Jackson, V. Jelic, A. de Jong, E. Juette, D. Kant, A. Karastergiou, A. Koers, H. Kollen, V. I. Kondratiev, E. Kooistra, Y. Koopman, A. Koster, M. Kuniyoshi, M. Kramer, G. Kuper, P. Lambropoulos, C. Law, J. van Leeuwen, J. Lemaitre, M. Loose, P. Maat, G. Macario, S. Markoff, J. Masters, R. A. McFadden, D. McKay-Bukowski, H. Meijering, H. Meulman, M. Mevius, E. Middelberg, R. Millenaar, J. C. A. Miller-Jones, R. N. Mohan, J. D. Mol, J. Morawietz, R. Morganti, D. D. Mulcahy, E. Mulder, H. Munk, L. Nieuwenhuis, R. van Nieuwpoort, J. E. Noordam, M. Norden, A. Noutsos, A. R. Offringa, H. Olofsson, A. Omar, E. Orrú, R. Overeem, H. Paas, M. Pandey-Pommier, V. N. Pandey, R. Pizzo, A. Polatidis, D. Rafferty, S. Rawlings, W. Reich, J.-P. de Reijer, J. Reitsma, G. A. Renting, P. Riemers, E. Rol, J. W. Romein, J. Roosjen, M. Ruiter, A. Scaife, K. van der Schaaf, B. Scheers, P. Schellart, A. Schoenmakers, G. Schoonderbeek, M. Serylak, A. Shulevski, J. Sluman, O. Smirnov, C. Sobey, H. Spreeuw, M. Steinmetz, C. G. M. Sterks, H.-J. Stiepel, K. Stuurwold, M. Tagger, Y. Tang, C. Tasse, I. Thomas, S. Thoudam, M. C. Toribio, B. van der Tol, O. Usov, M. van Veelen, A.-J. van der Veen, S. ter Veen, J. P. W. Verbiest, R. Vermeulen, N. Vermaas, C. Vocks, C. Vogt, M. de Vos, E. van der Wal, R. van Weeren, H. Weggemans, P. Weltevrede, S. White, S. J. Wijnholds, T. Wilhelmsson, O. Wucknitz, S. Yatawatta, P. Zarka, A. Zensus, and J. van Zwieten. LOFAR: The LOw-Frequency ARray. *A&A*, 556:A2, Aug. 2013. doi: 10.1051/0004-6361/201220873.

M. M. Varughese, R. von Sachs, M. Stephanou, and B. A. Bassett. Non-parametric transient classification using adaptive wavelets. *MNRAS*, 453:2848–2861, Nov. 2015. doi: 10.1093/mnras/stv1816.

R. C. Vermeulen and M. H. Cohen. Superluminal motion statistics and cosmology. *ApJ*, 430:467–494, Aug. 1994. doi: 10.1086/174424.

M. Villata, C. M. Raiteri, H. D. Aller, M. F. Aller, H. Teräsranta, P. Koivula, S. Wiren, O. M. Kurtanidze, M. G. Nikolashvili, M. A. Ibrahimov, I. E. Papadakis, G. Tosti, F. Hroch, L. O. Takalo, A. Sillanpää, V. A. Hagen-Thorn, V. M. Larionov, R. D. Schwartz, J. Basler, L. F. Brown, and T. J. Balonek. The WEBT campaigns on <ASTROBJ>BL Lacertae</ASTROBJ>. Time and cross-correlation analysis of optical and radio light curves 1968-2003. *A&A*, 424:497–507, Sept. 2004. doi: 10.1051/0004-6361:20040439.

A. E. Volvach, M. I. Ryabov, L. N. Volvach, A. I. Suharev, H. D. Aller, and M. F. Aller. The catalog of periods of the variability of blazars 3C120, 3C273, 3C279, 3C345 and 3C454.3 at centimeter and millimeter wavelengths. In S. K. Chakrabarti, A. I. Zhuk, and G. S. Bisnovatyi-Kogan, editors, *American Institute of Physics Conference Series*, volume 1206 of *American Institute of Physics Conference Series*, pages 360–367, Jan. 2010. doi: 10.1063/1.3292541.

M. A. Walker. Extreme Scattering Events: Insights into the Interstellar Medium on AU-Scales. In M. Haverkorn and W. M. Goss, editors, *SINS - Small Ionized and Neutral Structures in the Diffuse Interstellar Medium*, volume 365 of *Astronomical Society of the Pacific Conference Series*, page 299, July 2007.

K. W. Weiler, S. D. van Dyk, N. Panagia, and R. A. Sramek. Full evolution of the 6 and 20 centimeter radio emission from SN 1980K. *ApJ*, 398:248–253, Oct. 1992. doi: 10.1086/171852.

K. W. Weiler, N. Panagia, M. J. Montes, and R. A. Sramek. Radio Emission from Supernovae and Gamma-Ray Bursters. *ARA&A*, 40:387–438, 2002. doi: 10.1146/annurev.astro.40.060401.093744.

K. W. Weiler, N. Panagia, C. Stockdale, M. Rupen, R. A. Sramek, and C. L. Williams. Radio Emission from SN 1994I in NGC 5194 (M 51): The Best-studied Type Ib/c Radio Supernova. *ApJ*, 740:79, Oct. 2011. doi: 10.1088/0004-637X/740/2/79.

S. Wellons, A. M. Soderberg, and R. A. Chevalier. Radio Observations Reveal Unusual Circumstellar Environments for Some Type Ibc Supernova Progenitors. *ApJ*, 752:17, June 2012. doi: 10.1088/0004-637X/752/1/17.

J. H. S. Weston, J. L. Sokoloski, Y. Zheng, L. Chomiuk, A. Mioduszewski, K. Mukai, M. P. Rupen, M. I. Krauss, N. Roy, and T. Nelson. Shocks and Ejecta Mass: Radio Observations of Nova V1723 Aql. In P. A. Woudt and V. A. R. M. Ribeiro, editors, *Stell Novae: Past and Future Decades*, volume 490 of *Astronomical Society of the Pacific Conference Series*, page 339, Dec. 2014.

K. Wiersema, A. J. van der Horst, A. J. Levan, N. R. Tanvir, R. Karjalainen, A. Kamble, C. Kouveliotou, B. D. Metzger, D. M. Russell, I. Skillen, R. L. C. Starling, and R. A. M. J. Wijers. Polarimetry of the transient relativistic jet of GRB 110328/Swift J164449.3+573451. *MNRAS*, 421:1942–1948, Apr. 2012. doi: 10.1111/j.1365-2966.2011.20379.x.

P. K. G. Williams, G. C. Bower, S. Croft, G. K. Keating, C. J. Law, and M. C. H. Wright. ASGARD: A Large Survey for Slow Galactic Radio Transients. I. Overview and First Results. *ApJ*, 762:85, Jan. 2013. doi: 10.1088/0004-637X/762/2/85.

A. E. Wright, R. T. Stewart, G. J. Nelson, O. B. Slee, and M. Cropper. Detection of the AM HER type cataclysmic variable V834 CEN at radio wavelengths. *MNRAS*, 231:319–324, Mar. 1988.

B. A. Zauderer, E. Berger, A. M. Soderberg, A. Loeb, R. Narayan, D. A. Frail, G. R. Petitpas, A. Brunthaler, R. Chornock, J. M. Carpenter, G. G. Pooley, K. Mooley, S. R. Kulkarni, R. Margutti, D. B. Fox, E. Nakar, N. A. Patel, N. H. Volgenau, T. L. Culverhouse, M. F. Bietenholz, M. P. Rupen, W. Max-Moerbeck, A. C. S. Readhead, J. Richards, M. Shepherd, S. Storm, and C. L. H. Hull. Birth of a relativistic outflow in the unusual γ-ray transient Swift J164449.3+573451. *Nature*, 476:425–428, Aug. 2011. doi: 10.1038/nature10366.

B. A. Zauderer, E. Berger, R. Margutti, A. J. Levan, F. Olivares E., D. A. Perley, W. Fong, A. Horesh, A. C. Updike, J. Greiner, N. R. Tanvir, T. Laskar, R. Chornock, A. M. Soderberg, K. M. Menten, E. Nakar, J. Carpenter, P. Chandra, A. J. Castro-Tirado, M. Bremer, J. Gorosabel, S. Guziy, D. Pérez-Ramírez, and J. M. Winters. Illuminating the Darkest Gamma-Ray Bursts with Radio Observations. *ApJ*, 767:161, Apr. 2013a. doi: 10.1088/0004-637X/767/2/161.

B. A. Zauderer, E. Berger, R. Margutti, G. G. Pooley, R. Sari, A. M. Soderberg, A. Brunthaler, and M. F. Bietenholz. Radio Monitoring of the Tidal Disruption Event Swift J164449.3+573451. II. The Relativistic Jet Shuts Off and a Transition to Forward Shock X-Ray/Radio Emission. *ApJ*, 767:152, Apr. 2013b. doi: 10.1088/0004-637X/767/2/152.

A. A. Zdziarski. The jet kinetic power, distance and inclination of GRS 1915+105. *MNRAS*, 444:1113–1118, Oct. 2014. doi: 10.1093/mnras/stu1525.

J. T. L. Zwart, R. W. Barker, P. Biddulph, D. Bly, R. C. Boysen, A. R. Brown, C. Clementson, M. Crofts, T. L. Culverhouse, J. Czeres, R. J. Dace, M. L. Davies, R. D'Alessandro, P. Doherty, K. Duggan, J. A. Ely, M. Felvus, F. Feroz, W. Flynn, T. M. O. Franzen, J. Geisbüsch, R. Génova-Santos, K. J. B. Grainge, W. F. Grainger, D. Hammett, R. E. Hills, M. P. Hobson, C. M. Holler, N. Hurley-Walker, R. Jilley, M. E. Jones, T. Kaneko, R. Kneissl, K. Lancaster, A. N. Lasenby, P. J. Marshall, F. Newton, O. Norris, I. Northrop, D. M. Odell, G. Petencin, J. C. Pober, G. G. Pooley, M. W. Pospieszalski, V. Quy, C. Rodríguez-Gonzálvez, R. D. E. Saunders, A. M. M. Scaife, J. Schofield, P. F. Scott, C. Shaw, T. W. Shimwell, H. Smith, A. C. Taylor, D. J. Titterington, M. Velić, E. M. Waldram, S. West, B. A. Wood, G. Yassin, and AMI Consortium. The Arcminute Microkelvin Imager. *MNRAS*, 391:1545–1558, Dec. 2008. doi: 10.1111/j.1365-2966.2008.13953.x.

Appendix A

Example parset files

AWIMAGER parset file used in imaging the RSM HBA data on a 30 second time-scale.

```
weight=briggs
robust=-2
npix=1280
cellsize=20arcsec
data=CORRECTED_DATA
padding=1.5
niter=5000
threshold=0.25Jy
stokes=I
operation=mfclark
oversample=5
wmax=8000
cyclefactor=1.5
gain=0.1
timewindow=300
```

```
ChanBlockSize=2
ApplyElement=0
UVmin=0.1
UVmax=3
```

Configuration parset used for the RSM 30 second images run through the TraP, containing settings of the source extraction and analysis parameters.

```
[persistence]
description = "RSM 30s PT01 mosaic QC 1.5sigma deep image"
dataset_id = -1
sigma = 4 ; sigma value used for iterave clipping image before RMS calculation
f = 8 ; determines size of subsection, result will be 1/fth of the image size

[quality_lofar]
low_bound = 0.0 ; multiplied with noise to define lower threshold
high_bound = 11.2 ; multiplied with noise to define upper threshold
oversampled_x = 30 ; threshold for oversampled check
elliptical_x = 5.0 ; threshold for elliptical check
min_separation = 0 ; minimum distance to a bright source (in degrees)

[source_extraction]
# extraction threshold (S/N)
detection_threshold = 10
analysis_threshold = 5
back_size_x = 181
```

```
back_size_y = 60
margin = 180
deblend_nthresh = 32 ; Number of subthresholds for deblending; 0 disables
extraction_radius_pix = 810
force_beam = True
box_in_beampix = 10
# ew/ns_sys_err: Systematic errors on ra & decl (units in arcsec)
ew_sys_err = 10
ns_sys_err = 10

[association]
deruiter_radius = 5.68

[transient_search]
new_source_sigma_margin = 15
```